UNIVERSITÉ DE RENNES 1

THESE DE DOCTORAT DE

L'UNIVERSITE DE RENNES 1

ECOLE DOCTORALE N° 601
Mathématiques et Sciences et Technologies de l'Information et de la Communication
Spécialité : *Electronique*

Par
Petros BANTAVIS

Study and Design of Compact Quasi Optical Beam Forming Lens Antennas in a Parallel Plate Waveguide Technology for on Board Satellite Constellation Missions

Thèse présentée et soutenue à Rennes, le dateUnité de recherche : IETR – UMR CNRS 6164, Institut d'Électronique et des Technologies numéRique, Université de Rennes 1.

Rapporteurs avant soutenance :

Thierry MONEDIERE Professeur des universités, Université de Limoges
Ashraf UZ ZAMAN Associate Professeur, Chalmers University of Technology, Gothenburg, Suède

Composition du Jury :

Examinateurs :	Thierry MONEDIERE	Professeur des universités, Université de Limoges
	Ashraf UZ ZAMAN	Associate Professeur, Chalmers University of Technology, Gothenburg, Suède
	Astrid ALGABA BRAZALEZ	Chercheur Ingénieur, Ericsson, Suède
	Ségolène TUBEAU	Chercheur Ingénieur, Thales Alenia Space, France
Dir. de thèse :	Ronan SAULEAU	Professeur des universités, Université de Rennes 1
Co-dir. de thèse :	George GOUSSETIS	Professeur des universités, Heriot Watt University, Edimbourg, Ecosse

Στους γονείς μου, Γιάννη, Δέσποινα,
στην αδερφή μου Κωνσταντίνα,
και στο Ρονάκι.

The Ph. D thesis has been funded by the European Commission (H2020 project REVOLVE, MSCA-ITN-2016-722840)

Acknowledgments

I would like to deeply thank my supervisors Professor Ronan Sauleau, Dr Hervé Legay and Professor George Goussetis. I truly appreciate your guidance and support through these 3 years of the thesis. I would like to thank my co-supervisors Segolene Tubau and Dr Cebrian Garcia Gonzalez for their additional technical support.

I would like to thank Mario López Marlasca and Luis Ignacio Suárez Rios from Idonial for their support on the manufacturing aspects.

I want to thank Dr Laurent Le Coq for his continuous support of the measurement campaign and Frederic Boutet, Xavier Morvan for the additional help in the soldering parts of the manufacturing. I feel lucky that I had the chance to meet you and cooperate with you.

I would like to thank Dr Mauro Ettorre for his crucial role in my recruitment in the project and for our fruitful discussions though my short period in IETR.

I couldn't forget the continuous efforts from the secretaries of Idonial, Monica Arenal Zapico and Susana Llaneza concerning my complex administrative situation. Special thanks to the secretaries of IETR Noelle le Ber, Natalie Blanchard, Martine Boublil. Your presence in IETR gives additional credits in the ambience of the lab.

I had the chance to meet and cooperate with exceptional friends and researchers through theses 3 years of my thesis. Nicola Bartolomei, Michele del Mastro, Thomas Strober, Srdjan Pacovics, Antoine Calleau, Alvaro Jose Pascual Garcia, Francois Doucet, it was a real pleasure to meet you, you are my friends for life. Yann chao-oger, Tuyen Pham, Rosa Orlacchio, Attaja Nicolas, Jorge Ruis Garcia, Zain Haider, thank you for our discussions and your special energy.

I would like to thank the revolvers Charalampos Stoumpos, Thomas Strober, Andrea Guarriello, Claire Benteyn, Florian Vidal, Luis Dufour. It was a pleasure to cooperate with you.

I wish deeply to thank Marc le Roy, Raafat Lababidi, Andre Perennec, Denis Le Jeune, from Lab-STICC for our short cooperation in my first research activity in France. Thank you for your trust, our cooperation and your welcome in Brest. You know better than anybody else that you are very well appreciated.

I would like to present my profound gratitude to my mentor Professor George Kyriacou from Democritus university of Thrace and my supervisor of my internship Vasili Kassouras from KEMEA. You have my respect and I was very lucky to cooperate with you. I wish to thank my friend and colleague Dr Christos Kolitsidas from Ericsson for our rare friendship and his vital support through my master thesis.

I wish to thank my lovely family. Father, mother, sister, you are the pure inspiration of all my achievements. Please, let me dedicate the thesis to you.

Résumé

Actuellement, la demande croissante de bande passante, de faible latence et de connectivité rapide dans l'industrie spatiale, appelle au développement de systèmes d'antennes multifaisceaux intelligents. L'industrie spatiale font récemment appel aux missions spatiales de constellation. Le but d'une configuration de mission de constellation est de placer un très grand nombre de satellites miniaturisés et à faible coût sur des orbites très basses. Ce dernier, conduit à une connectivité à haute vitesse et à une faible latence, car le satellite est placé à des altitudes plus basses par rapport aux orbites GEO traditionnelles.

En ce qui concerne le besoin supplémentaire de capacité élevée du réseau et le trafic élevé, les systèmes d'antennes multifaisceaux augmentent le débit du réseau et exploitent effectivement le spectre disponible. Un faisceau à directivité élevée est nécessaire pour augmenter encore la capacité du réseau. Ce dernier, a conduit l'industrie spatiale à étudier en profondeur la possibilité d'utiliser la bande Ka comme bande de fréquence de fonctionnement. La bande Ku a été largement utilisée pour fournir des services de diffusion large bande. Cependant, les avantages majeurs de la bande Ka résident dans la taille compacte des antennes et de leurs faisceaux à directivité élevée. D'autre part, la bande Ku est presque immunisée contre les phénomènes atmosphériques tels que la pluie, la neige, etc. et donc les pertes de signal sont plus basses.

Les antennes à lentilles multifaisceaux offrent une solution très fructueuse pour l'intégration des satellites dans les missions de constellation en orbite basse. En comparaison avec les systèmes d'antennes à réseau phasé traditionnels qui utilisent des déphaseurs pour dépointer le faisceau, les lentilles fournissent simultanément plusieurs faisceaux et permettent de les dépointer en produisant des retards. Ce dernier facilite la conception des lentilles, car il n'est pas nécessaire de créer des réseaux de formation de faisceau complexes. Les lentilles qui ont été développées dans la présente thèse sont les lentilles métasurface à index progressif multifaisceaux fixes et des lentilles à ligne de retard continu, toutes deux dans une technologie PPW. Ils sont composés uniquement de matériaux métalliques pour éviter les pertes indésirables ce qui les rendent adaptés aux missions spatiales.

L'inspiration initiale de ce travail est dérivée d'une thèse de doctorat précédente [92] où une antenne à lentilles de Lunebourg utilisant des métasurfaces a été développée dans une technologie PPW, Fig. 1(a-d). La lentille a été synthétisée en utilisant la cellule « fakir bed of nails » et fonctionne en bande Ku. La lentille offre un large champ de vision, de très bonnes performances en termes d'adaptation et elle est facile à fabriquer. Cependant, c'est une structure très lourde et la cellule a une dispersion élevée pour des valeurs élevées d'indice de réfraction effectif. Par conséquent, l'un des objectifs de la présente thèse repose sur l'étude des structures périodiques qui présentent des valeurs élevées d'indice de réfraction effectif afin de concevoir des lentilles plus compactes.

L'antenne à lentille GRIN Gutman entièrement métallique a été sélectionnée pour être étudiée, conçue et fabriquée dans cette activité, Fig. 2(a-d). La lentille Gutman est une lentille plus compacte que la Luneburg, bien qu'elle demande des valeurs plus élevées d'indice de réfraction effectif. Dans le Chapitre 3 de la thèse, une méthodologie de conception approfondie de la lentille a été introduite. La cellule à indice de glissement entrelacé a été examinée et a abouti à des valeurs élevées d'indice de réfraction effectif; il a été utilisé pour synthétiser la lentille. Une méthodologie de conception pour synthétiser la lentille Gutman a été analysée et peut être utilisée pour chaque lentille GRIN à symétrie circulaire utilisant des cellules entièrement métalliques. En outre, une méthodologie d'adaptation a été introduite pour adapter l'a lentille à un connecteur coaxial SMA commercial. De plus, une nouvelle conception mécanique qui stabilise la sensibilité de la transition de la lentille a été proposée.

La lentille Gutman à distance focale $f = R/2$ a été fabriquée et testée expérimentalement et est 19% plus compacte par rapport à la lentille Luneburg.

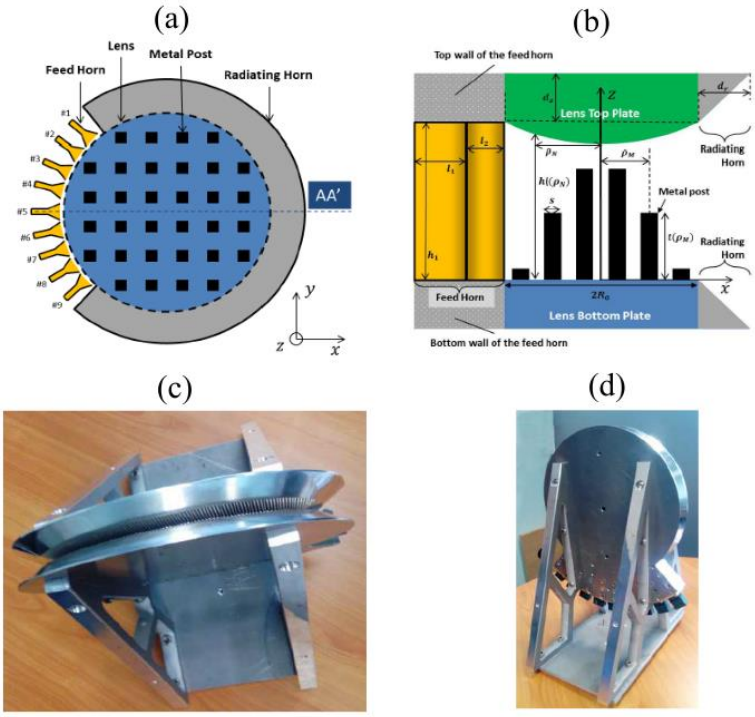

Figure 1: Antenne de lentille de Luneburg, [92] (a) disposition, vue de dessus, (b) vue en coupe 2D, (c) prototype, (d) prototype, vue en perspective.

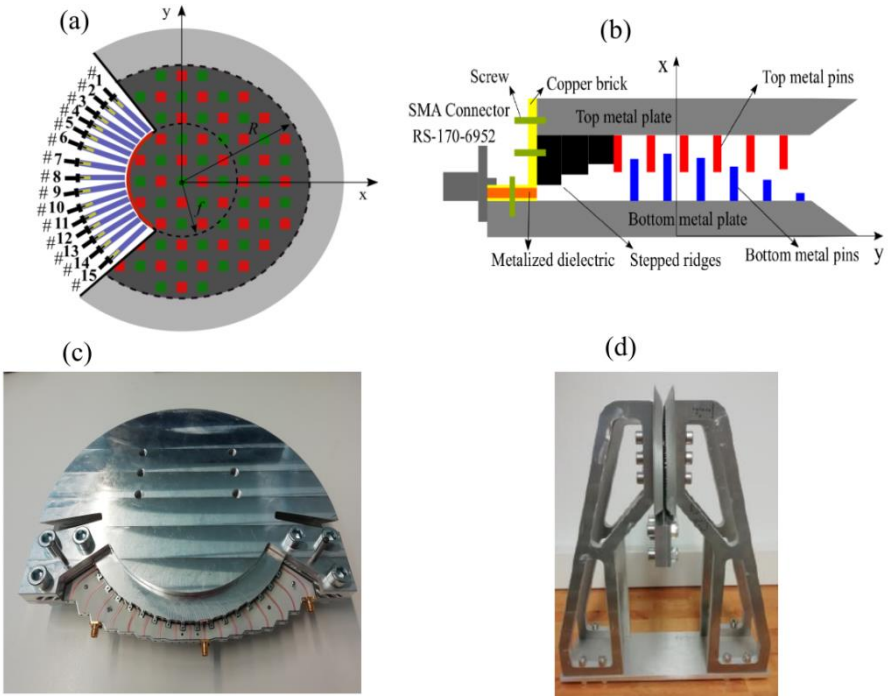

Figure 2: Antenne à lentille Gutman avec distance focale $f = R / 2$, (a) disposition, vue de dessus, (b) vue en coupe 2D, (c) prototype, (d) prototype, vue en perspective.

Ensuite, une antenne à lentille GRIN Gutman plus compacte qui a un arc focal plus petit égal à $f = R / 2.85$ a été conçue. La cellule à indice de glissement entrelacé a été utilisée pour synthétiser la lentille et présente une distribution distincte de l'indice de réfraction effectif le long de la surface de la lentille avec des valeurs maximales n_{eff}=3. La lentille a une taille 25% plus compacte que la lentille de Luneburg.

Les deux lentilles GRIN Gutman entièrement métalliques ont été comparées à la lentille GRIN Luneburg entièrement métallique pour évaluer leurs performances en termes de rayonnement, de réflexions et de masse. Il a été conclu qu'elles ont un champ de vision similaire, bien que les lentilles Gutman aient des pertes de dépointage légèrement plus élevées et un niveau SLL plus élevé, elles ont une taille très compacte. Les pertes de dépointage et le niveau SLL de la lentille Gutman proviennent de la surface supprimée de la lentille. En outre, les pertes de dépointage dans les lentilles de Luneburg et de Gutman sont dues au placement de toutes les sources d'excitation le long de l'arc focal des lentilles. De plus, la lentille Gutman nécessite des alimentations d'excitation compactes car son arc focal est très étroit. À cet effet, une transition compacte a été conçue pour exciter et correspondre à la lentille Gutman.

D'autres études ont été examinées dans les lentilles diélectriques équivalentes afin de comparer les performances des lentilles entièrement métalliques aux lentilles diélectriques et de tester l'influence de la dispersion des cellules dans le rayonnement des lentilles. Les lentilles diélectriques; la lentille de Luneburg, la lentille Gutman avec une distance focale $f = R / 2$ et la lentille Gutman avec $f = R / 2.85$ ont été conçues en utilisant des couches diélectriques non dispersives, Fig. 3.

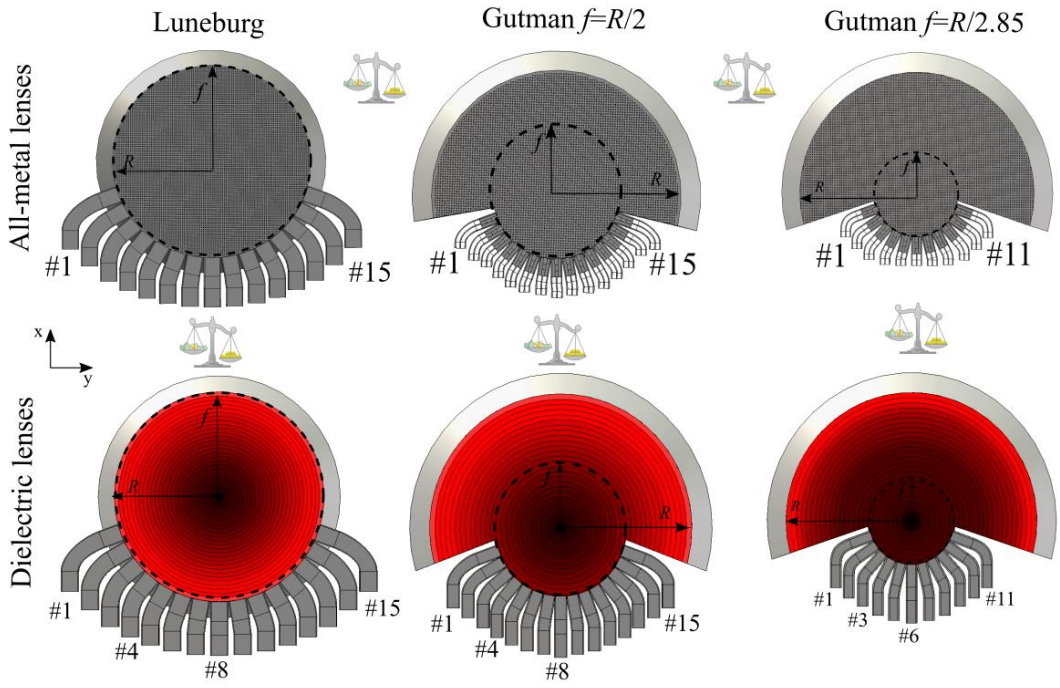

Figure 3: Antennes à lentille GRIN tout métal; lentille Luneburg, lentille Gutman avec distance focale $f = R / 2$ et lentille Gutman avec $f = R / 2.85$ Vs les lentilles diélectriques équivalents.

La dernière partie de la thèse porte sur le développement d'une antenne à lentille multifaisceaux optimisée afin de produire un masque d'enveloppe isoflux. L'antenne étudiée est la lentille à ligne à retard continue en PPW qui a été introduite dans [12]. Une

méthodologie de conception a été présentée qui est basée sur l'inversion d'axe de l'ellipse et a conduit à augmenter progressivement la directivité des faisceaux décalés par rapport au faisceau large.

Une technique d'optimisation a été développée pour optimiser la cavité transversale de la lentille à l'aide de profils elliptiques. Des modèles de masque de puissance différents ont été conçus dans l'optimiseur et des cibles distinctes ont été définies pour les modèles de masque de puissance simultanément pour des angles de pointage distincts. De plus, l'ouverture des sources d'excitation ainsi que leurs distances focales ont également été optimisées pour augmenter les degrés de liberté (DoF) dans le processus d'optimisation. Les meilleurs agents de l'optimiseur ont été importés dans le modèle de conception du HFSS pour vérifier les performances de rayonnement de la lentille. Les optimisations ont abouti à une lentille à ligne à retard continue optimisée avec un large champ de vision et des faisceaux de rayonnement de la lentille synthétisant un masque d'enveloppe isoflux, Fig. 4(a,b).

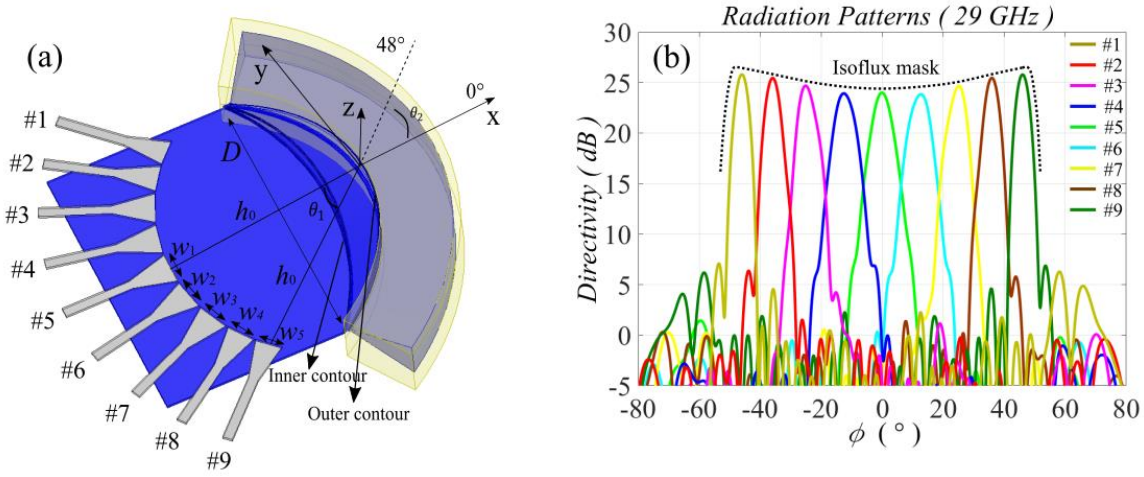

Figure 4: (a) Modèle d'antenne à lentille à ligne à retard continu 3D en HFSS, (b) diagrammes de directivité pour tous les faisceaux de l'antenne finale à 29 GHz.

Abstract

Nowadays, the increasing demand of bandwidth, low latency and fast connectivity in space industry, calls for the development of smart multi-beam antenna systems. Constellation space missions have recently appealed the interest of the space industry. The goal of a constellation mission configuration is to place a very high number of miniaturized and low cost satellites in very low orbits. This leads to high speed connectivity and low latency, since the satellite is placed in lower altitudes compared to traditional GEO orbits.

Concerning the additional need of high capacity of the network and the high traffic, multi-beam antennas increase the throughput of the network and exploit efficiently the available spectrum. High directive beams are needed to further increase the capacity of the network. Multi-beam lens antennas provide a very fruitful solution for on board payloads in low orbit constellation missions. In comparison with traditional phased array antenna systems which use phase shifters to scan the beam, lenses attain the desired scan shifts through time delays. This facilitates the design of lenses, since there is no need for complex beamforming networks. The type of lenses that have been developed in the present thesis is fixed multi-beam graded index metasurface lenses and continuous delay line lenses, both in a Parallel Plate Waveguide (PPW) technology. They are composed of merely metal materials to avoid undesired losses which make them suitable for on board satellite missions.

The initial inspiration of this work is derived from a previous Ph. D thesis [92] where a Luneburg lens antenna using metasurfaces developed in a PPW technology. The lens has been synthesized using the fakir bed of nails unit-cell and operates at Ku-band. The lens provides wide field of view, very good performance in terms of matching and it is easy to fabricate. However, it is very heavy structure and the unit-cell has high dispersions for high values of effective index of refraction. Hence, one of the objectives of the thesis lies on the investigation of periodic structures that present high values of effective index of refraction in order to design more compact lenses.

The all-metal Graded Index (GRIN) Gutman lens antenna has been selected to be investigated, designed, manufactured and experimentally tested. The Gutman lens is a more compact lens compared to the Luneburg, although it calls for higher values of effective index of refraction. The interleaved glide index unit-cell has been examined and ended up to high values of effective index of refraction; it has been used to synthesize the lens. A design methodology to synthesize the Gutman lens has been analysed which can be further used to every GRIN lens having circular symmetry utilizing all-metal unit-cells. In addition, a matching methodology introduced to adapt the lens in a commercial SMA coaxial connector. Additionally, a novel mechanical design for the transition of the lens proposed and stabilized the sensitivity of the transition. The Gutman lens with focal distance $f=R/2$ has been manufactured and experimentally tested and is 19% more compact than the Luneburg lens.

Going forward, a more compact GRIN Gutman lens antenna with smaller focal arc equal to $f=R/2.85$ has been designed. The interleaved glide index unit-cell has been utilized to synthesize the lens and it presents a distinct distribution of effective index of refraction along the surface of the lens with maximal value $n_{eff}=3$. The lens has 25% more compact size comparing to the size of the Luneburg lens. Both all-metal GRIN Gutman lenses have been compared to the all-metal GRIN Luneburg lens in terms of evaluating their performance in radiation, reflections and mass.

Additional studies have been realised in the equivalent dielectric lenses in order to compare the performance of the all-metal lenses to the dielectric lenses and test the influence of the dispersion of the unit-cells in the radiation of the lenses. The dielectric lenses, Luneburg lens,

Gutman lens with focal distance $f=R/2$ and Gutman lens with $f=R/2.85$ have been designed using non-dispersive dielectric layers.

The last part of the thesis, focuses on the development of an optimized multi-beam lens antenna in order to attain an isoflux envelope mask pattern. This particular antenna examined is the continuous delay line lens in a PPW housing introduced in [12]. A design methodology has been presented based on the axis inversion of the ellipse and it led to increasing progressively the directivity of the offset beams comparing to the broadside beam.

An optimization technique developed to optimize the transversal ridge of the lens using elliptical profiles. Segregate power mask patterns have been designed and separate targets have been defined to the power mask patterns simultaneously for distinct pointing angles. Apart from that, the aperture of the excitation feeds together with their focal distances have been likewise optimized to increase the DoFs in the optimization process. The best agents of the optimizer have been imported to the design model of the HFSS to verify the radiation performance of the lens. The optimizations ended up to an optimized continuous delay line lens with wide field of view and thus the radiation beams of the lens synthesized an isoflux envelope mask.

Table of Contents

Table of Figures

Chapter 1 Introduction

Contents

1.1 Multiple beam antenna

Multi-beam antenna systems enhance the throughput and the capacity of the network, since they provide flexibility on the re-use of the bandwidth and handle the dense traffic. The increase of the throughput of the network exploiting efficiently the available bandwidth leads on high speed internet services. Additionally, multi-beam antenna systems handle efficiently the traffic density of the network since they provide directive beam spots which can be oriented according to the demands of every separate user.

A multi-beam antenna configuration provides an increased capacity as compared to classical contoured beam coverage. To further decrease the cost of satellite communications, the trend is now to increase the number of radiating spots and on parallel to reduce their size. However, a drawback of the increased number of spots is the requirement of high number of getaways, as well as, large and high power spacecrafts. In order to achieve a system with high capacity we need to develop flexible multi-beam antenna configurations and also to consider the allocated bandwidth, as well as, the average efficiency of the system.

1.2 The Constellation Context

Nowadays, recent technological advances increase the demands in terms of bandwidth, throughput, capacity and low latency to provide services with fast connectivity. To address these challenges the space industry has proposed a different scenario of satellite configuration. The objective is to place compact satellites in LEO orbits or even in closer altitudes and increase the number of them. This scenario has been named as constellation

satellite missions. The major advantage of satellites that are placed in low altitudes is the fast connectivity since they perform low latency. The drawback is the high losses of the signal by virtue of atmospheric phenomena such as rain, snow, etc. Additionally, massive production calls for low cost satellites and concerning the need for massive number of launchers, the size and the mass of the payloads needs to be minimized. On the other hand, user's demands have to be satisfied.

Smart multi-beam antenna configurations embarked on the payloads can address the above mentioned challenges compared to conventional contoured beam antennas. The latter, increases the throughput of the network exploiting efficiently the available bandwidth and leads on high speed internet services. Additionally, multi-beam antenna systems handle efficiently the traffic density of the network since they provide directive beam spots which can be oriented according to the demands of every separate user.

1.2.1 Iridium NEXT

The Iridium NEXT is the world's highest performance constellation mission. It has been recently completed with 66 satellites in orbit by TAS, [3]. 6 distinct orbits have been strategically selected and 11 satellites have been placed on each orbit in an altitude of 780 Km. Iridium NEXT is independent from terrestrial infrastructures with no gateways and it provides 100% earth coverage. It has improved mobile services such as 3G and 4G, and finds further applications in maritime, aeronautics, governmental, connected objects, etc.

Antenna coverage

Each satellite embarks a principle multi-beam antenna to communicate with users in L-band (alternating Tx & Rx slots). It is equipped with 4 more antennas which are mechanically steerable antennas operating at Ka-band and provide inter-satellite links. The main mission multi-beam antenna configuration which is shown in Fig. 1.1(a, b) is a Direct Radiating Array (DRA) which is capable of generating 48 independent fixed beams (see Fig. 1.1(c)) in a constellation mission (see Fig. 1.1(c)). The antenna geometry consists of 120 radiating elements with 0.55 λ spacing with a Field Of View (FOV) of ±60°. Those 48 fixed beams are controlled by a passive BFN made of RF PCB multilayers as illustrated by the antenna block diagram.

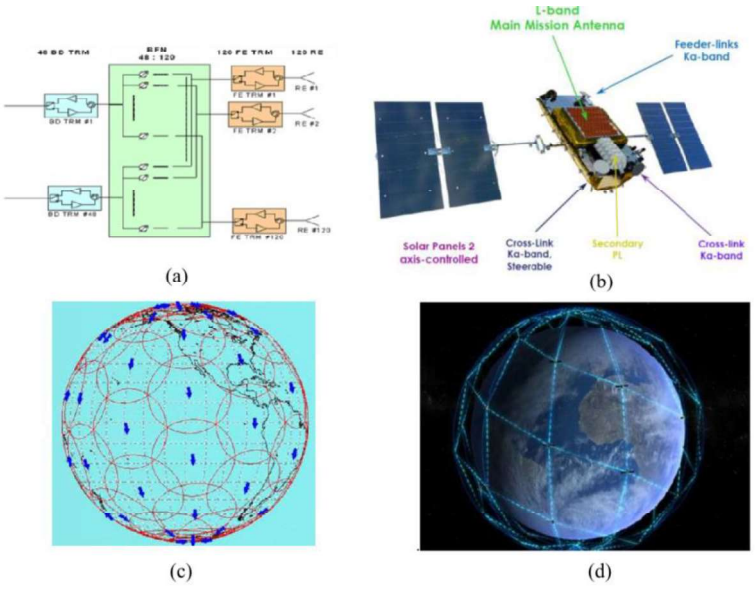

Figure 1.1: (a) Example of satellite constellations, (b) Iridium NEXT satellite with all the antenna parts.

1.2.2 Globalstar

Globalstar's second generation constellation belongs in the same family of constellation missions as the Iridium NEXT, although it operates at higher LEO orbit altitudes. Developed by TAS, Globalstar finds applications in mobile communications, [4]. It is composed of 48 satellites orbiting at 1.400km with an inclination of 52°. Globalstar compared to the Iridium NEXT does not cover polar areas, due to the lower orbit inclination.

Antenna coverage

The constellation is based on 24 satellites. The antenna sub-system provides 16 shaped beams, with an active Rx antenna, and 2 passive Tx antennas assemblies composed of a 6-panel pyramid, a 9-panel one and a horn for the central beams, (see Fig. 1.2(a-c)).

The Rx active antenna is a DRA capable of producing 16 distinct fixed beams. The antenna configuration consists of 52 radiating elements with 0.6 λ spacing for a FOV of ±54°. Those 16 fixed beams are controlled by a passive BFN which is made of an RF PCB multilayer as shown by the antenna block diagram.

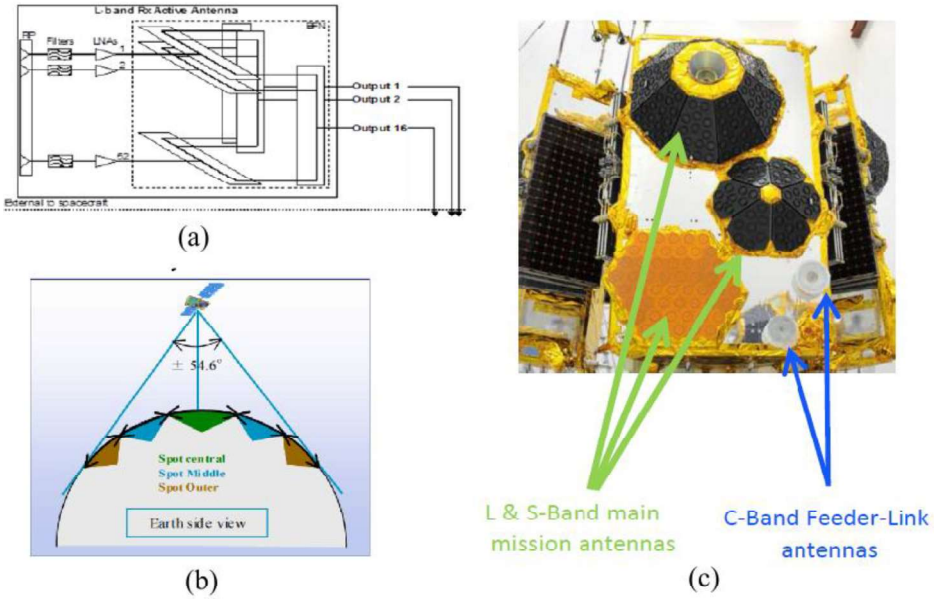

Figure 1.2: (a) Globalstar 2 satellite (b) antenna coverage over earth, (c) antenna system.

1.2.3 Mega-Constellations

Iridium NEXT and Globalstar 2 constellation missions have offered a new generation of telecommunication services. A new concept of mega-constellations recently proposed by a new era of entrepreneurs such as OneWeb and SpaceX target to disrupt the telecommunication market with broadband connectivity, affordable, low latency and high speed internet with global coverage. The advent of these mega-constellations managed to decrease the cost of the launch of the satellites which are more compact compared to the existing on orbit payloads of Iridium and Globalstar. The number of satellites in orbit is significant increased and thus cost saving is expected related to the mass production.

The Federal Communications Commission (FCC) has already approved the above mega-constellations:

- SpaceX, 4.425 satellites
- OneWeb, 720 satellites
- Telesat, 117 satellites

The challenge of these mega-constellation missions is the development of compact and flexible payloads with low mass. Since the satellites are in low orbits, high path losses exist between the users that are placed on the edge coverage of the earth and the satellite. These losses need to be compensated and thus antenna systems on board with isoflux coverage must be implemented. Precisely, for a LEO constellation orbit of 1.200 km scenario (see Fig. 1.3), for a user which is at scan angle 52° in the case of 20° elevation we have an extra path loss of 6.2 dB. Hence, it is obvious the need to not only compensate the scan losses of the antenna array but also to produce more directive beams at the edge scan angles.

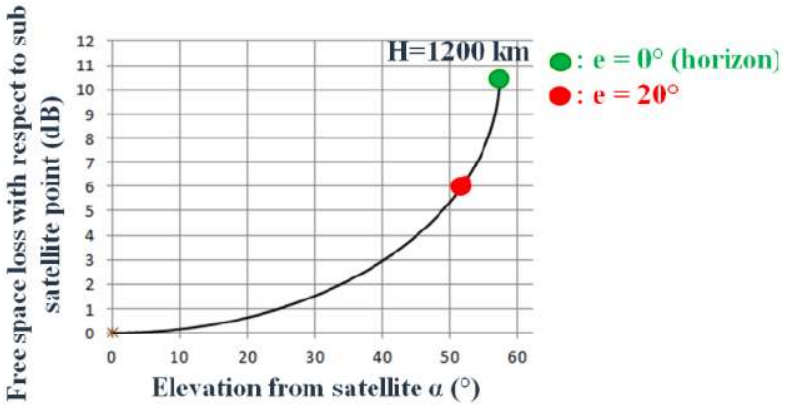

Figure 1.3: Free space loss vs users elevation angles for a satellite orbiting at 1200 km altitude.

1.2.4 Discussion on antenna sub-system solutions

Mainly 2 design approaches are considered for the payloads of mega-constellation missions which are divided on active and passive antennas. Passive phased array antennas reduce the on board complexity of the payload, although they don't provide enough flexibility. Active reconfigurable array antennas provide flexibility, although they introduce complexity in the payload. A compromise on the cost, size and the performance of the payload is evident to select the appropriate on board antenna solutions. Multi-beam antenna systems solutions are discussed below.

Active digitally controlled phased array antennas are a fruitful solution for high flexibility on the payload system. They can deliver a high number of flexible beams from the radiating elements. This technology has been used for ground applications, however Boeing space systems awarded the O3b mPOWER to deliver 4.000 beams using digital beamforming phased arrays integrated on the payload, [5]. The on board system is expected to be launched in 2021 and will operate at MEO orbits. This technology provides high flexibility, although it implies complex payload architectures. Fully flexible active phased array with digital beamforming embarked on LEO orbits is very challenging. Digital payloads with fully active phased arrays are very expensive solutions and mega-constellation missions require a massive number of satellites. LEO orbits imply wide FOV and small radiating elements. Hence, the development of compact active devices (integrated with the radiating elements) with embedded efficient thermal management is challenging.

A simpler payload solution which is partially flexible is the multiple coverage exploiting Beam Hopping (BH). BH provides flexibility to the satellite system since enables transmission which is divided in time slots accommodating time variant traffic. Precisely, BH allows the illumination of only a subset pair of spots in a specific time slot and the selection of the pairs is controlled by a switch. Fig. 1.4 shows an example of 256 beam coverage with isoflux characteristics using BH. Let's suppose that the BH switch period is Δt. The first pair of 16 spots is illuminated at t_0 and it is shown in Fig. 1.4. Then the second pair of spot is illuminated at $t_0 + \Delta t$, the third pair at $t_0 + 2\Delta t$, etc. The BH solution can 'replace' the full active antenna approach, it is less costly and it can be used in LEO orbits.

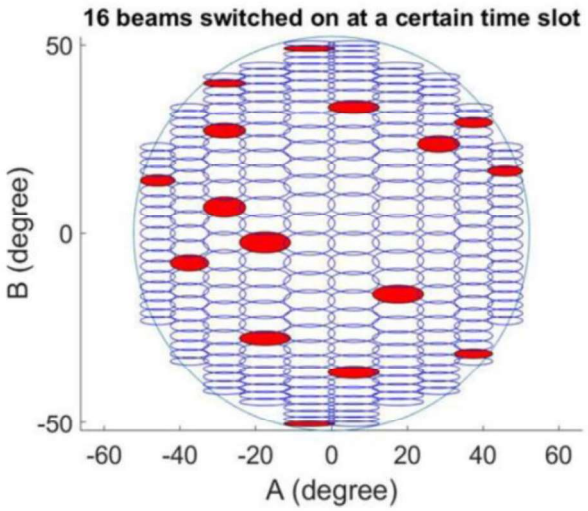

Figure 1.4: 256 beams coverage showing 16 beams switched on a certain time slot.

An alternative promising antenna solution for the payload system is the Hybrid Beam Forming Network (HBFN). The HBFN comprises a quasi-optical antenna beamformer combined with an analogue and reconfigurable layer. This technology provides reconfigurability and together with the quasi-optical antennas simplifies the complexity of the payload compared to fully active antenna solutions. This antenna solution is very promising since the whole antenna system can be easily integrated in the payload which will be more compact and also it is a low cost solution.

To conclude, passive antennas facilitate the development of the payload architecture and reduce its complexity. Apart from that, they can offer significant flexibility of the system exploiting the BH technique or the reconfigurable case of HBFN. QOBFs simplify the design of the antenna part providing a high number of beams and they are a very promising solution for on board payloads.

Quasi Optical Beam Formers (QOBF)

QOBFs are eminent antenna solutions for payloads. They are based on the optics theory and these lens type antennas provide beam steering without the need of the complex discrete beamforming networks. Hence, passive lens antennas have been selected to be examined in the present thesis and thus a brief description of 2 promising QOBF lens antennas are presented below.

The first antenna concept for on board satellite integration is the QOBF passive lens antenna which is shown in Fig. 1.5(a). The antenna technology is a continuous delay line lens which is fed by Parallel Plate Waveguide (PPWs). The antenna system consists of 2 identical lenses which radiate a high number of beams illuminating a cylindrical reflector. The reflector collimates the beams along the orthogonal axis and also produces a circular polarized wave by virtue of a periodic polarizing reflective surface coated on its surface. This combination of 2 QOBFs with a single polarizing reflector provides 2 rows of beams and the antennas operate in a Tx and Rx mode separately. This antenna design approach can lead to isoflux performance since the radiating beams can have progressively higher directivity for edge earth coverage (see Fig. 5(b)). This concept is being matured and is promising for next generation mega-constellation mission.

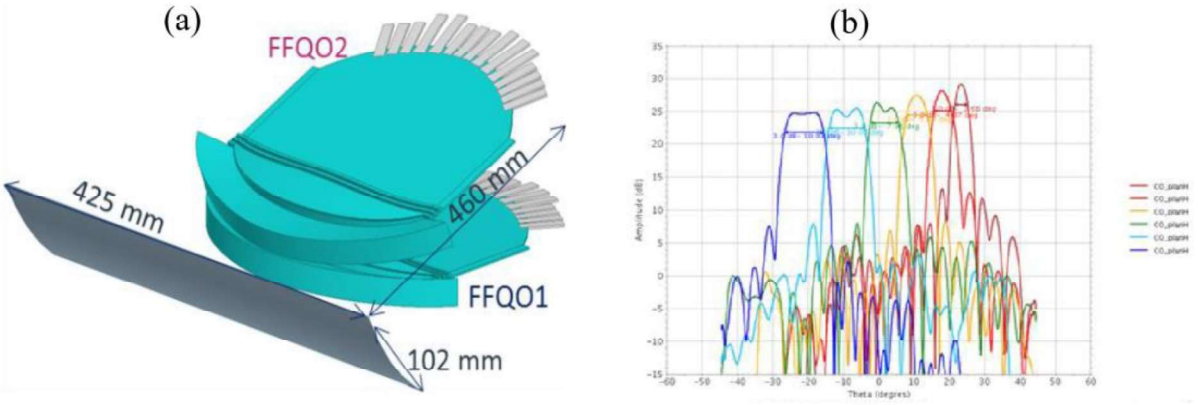

Figure 1.5: (a) Antenna subsystem made of a polarizing reflector illuminated by two QOBF (producing two rows of beams), (b) radiation patterns. [6].

An alternative promising antenna configurations is the Corporate Array of Quasi Optical Beamformer (CAQOB) that is illustrated in Fig. 1.6(a). The proposed concept aims to enlarge the radiating aperture producing more directive beams. The present development exploits the Continuous Transverse Stub (CTS) antenna which has been first introduced in [7] and further explored in [8]. The CTS is fed by a pillbox which generates plane waves that propagate in the PPW power divider and then the collimation of the waves is performed close to the radiation aperture. The latter, results on low losses, by virtue of the reduced propagation lengths of the propagating wave inside the antenna. Circular polarized wave can be also produced using linear to circular polarization (LP to CP) converters, [9]. Multiple blocks of this antenna technology aim to be placed strategically on the payload as shown in Fig. 1. 6(b) to produce 96 radiating beams.

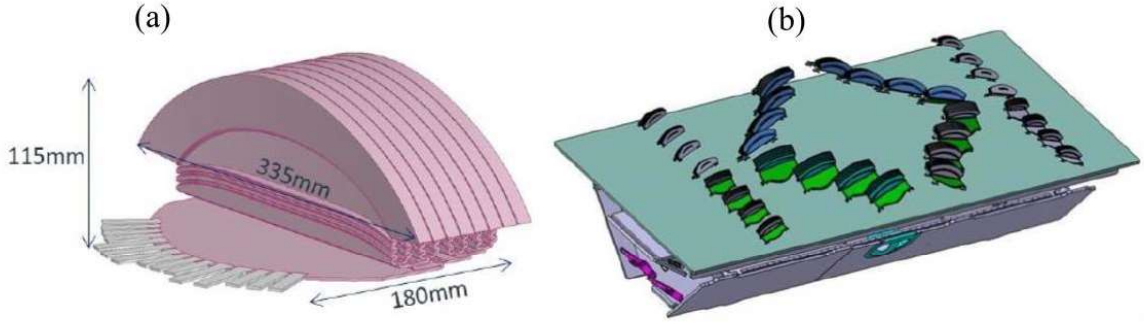

Figure 1.6: (a) The Corporate Array of Quasi Optical Beamformer (CAQOB), (b) accommodation of the antenna blocks based on CAQOB, [6].

1.3 Objectives of the Thesis

Concerning the high number of satellites in a low orbit mega-constellation mission, the antennas placed on the RF front end of the satellite need to fulfil the multiple criteria that have been highlighted in previous sections. QOBF networks such as lens antennas provide a fruitful solution compared to traditional phased array systems by virtue of the simplicity of their design and their wide FOV. Therefore, in this part of the thesis, lens antennas have been considered to be examined and analysed. Precisely, the technology of the lens is a 2D quasi-optical radiated lens configuration in PPW housing. This technology facilitates the final antenna demonstrator that can be integrated in the terminal of the satellite since multiple lenses can be stacked and eventually provide a 3D coverage to the surface of the earth.

The antenna examined in the present thesis is the Gutman lens antenna in a PPW technology utilizing all-metal artificial dielectrics and operates in Ku band. The Gutmnan lens presents wide FOV, low losses, compact size and the use of artificial dielectrics to synthesize the lens facilitates its fabrication. One of the goals of the thesis is to explore periodic structures that achieve very high values of effective index of refraction. The latter is a major challenge of this study since it leads to the design of very compact Gutman lenses. We target to produce the maximum amount of radiating beams and this can be achieved with the integration of multiple compact waveguides along the focal arc of the lens. Since the focal arc of the Gutman lens is very narrow, compact feeds need to be explored in order to be able to integrate many feeds. Moreover, matching techniques will be examined to match the effective index of refraction in the focal arc of the lens with traditional commercial feeds. The Gutman lens antenna is a more compact Luneburg lens, hence thorough comparison between the two lenses will be presented to evaluate their performance.

-The technical specifications of the multi-beam Gutman lens antenna are briefly highlighted below:

- Wide FOV up to ±70°
- Low scan losses
- Compact size
- Broadband performance
- Low cost
- Low weight
- Easy to fabricate

Thoroughly, we target to achieve a wide FOV of the Gutman lens up to ±70° since the antenna is aimed to be integrated to on board mega-constellation missions in very low orbits. For LEO missions, we need to compensate the high losses at the edge coverage of the earth. Hence, scan losses of the antenna array need to be compensated. Compact size is a major goal of our design since mega-constellation missions embark very compact payloads compared to the traditional constellations in higher orbits or MEO missions. Taking into account the massive expected production of multiple satellites the antenna technology needs to be easy to fabricate and to be tested in order to facilitate the production line.

Metasurface lenses that operate at higher frequencies such as Ka band are not preferred for on board satellite missions, by virtue of the small size of the periodic structures. High vibrations during the launcher can impact and even destroy the unit cells. Hence, a second antenna solution is proposed in the present thesis using a distinct technology operating at Ka band. The antenna is the continuous delay line lens and belong to the same family of QOBFs as the Gutman lens. It is a compact size lens antenna and easy to fabricate. It has more narrow FOV compared to the Gutman lens, although it can compensate the scan losses. In this design approach, optimization techniques will be explored using in-house softwares to compensate the high path losses of satellite with the edge coverage of the earth. The goal of the work with the continuous delay line lens is to optimize its profile and also its excitation feeds in order to progressively increase the directivity of the beams starting from the broadside beam till the extreme beam at 52°.

In the following sections we briefly present the principles of the antennas that have been studied in the present thesis. We start with the description of the Luneburg lens which is our reference antenna. Then, we illustrate the proposed Gutman lens, which is a more compact Luneburg lens antenna. Finally, we describe the continuous delay line lens antenna.

1.4 Proposed QOBF antenna solutions

1.4.1 Luneburg lens

The Luneburg lens antenna has been introduced in [10] where the Fermat's principle used in the geometrical theory of optics to analyse the performance of the lens. The lens has a spherical shape composed of inhomogeneous dielectric material and it is fully symmetric. A point source along the periphery of the lens creates parallel rays which are transmitted on the opposite direction of the lens. The point source can be rotated along the periphery of the lens and exploiting the symmetry of the lens identical performance is attained in all directions. By reciprocity, the Luneburg lens can operate likewise on the receiving case where incident parallel rays are focused on a point source on the opposite direction. In Fig. 1.7(a) an example is shown where a point source is excited on the periphery of the lens and the evolution of the rays inside the lens is depicted. In Fig. 1.7(b) the lens has been excited by a dipole and full-wave simulations resulted on the representation of the E-field of the lens; it is apparent the plane wave formed along the periphery on the opposite direction. The latter, leads to a pencil beam designated in Fig. 1.7(c). The pencil beam can be rotated by moving the point source along the periphery of the lens and therefore the Luneburg lens in a reconfigurable scenario is able to provide 360° coverage.

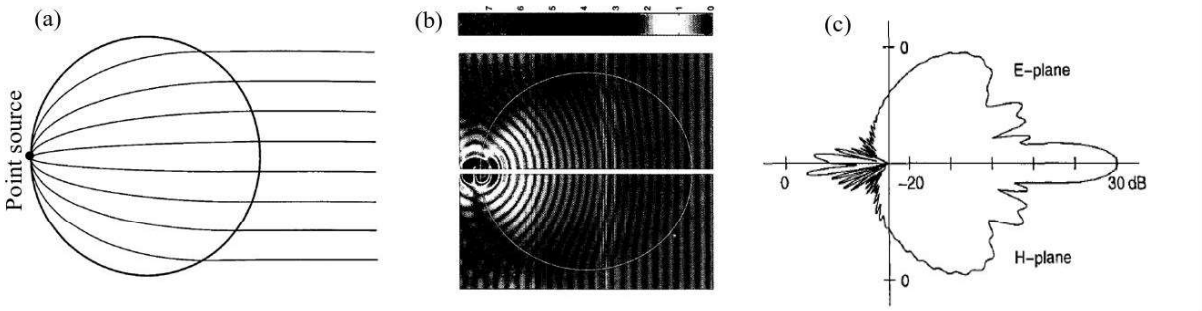

Figure 1.7: Luneburg lens [10], (a) ray tracing sketch, (b) E-field illustration, (c) pencil beam.

1.4.2 Gutman lens

The Gutman lens antenna is a modified Luneburg lens introduced in [11]. Hamiltonian optic techniques have been applied on the Luneburg lens profile which ended up in a new design of a transformed lens. It has been proved that the modification of the permittivity distribution along the surface of the lens results on segregate focal points which are placed inside the surface of the lens. Thoroughly, high permittivity values lead to focal points that are closer to the center of the lens. Hence, the feed excitation of the lens is moved inside the surface of the lens. Rays that are produced by a point source inside the lens can be transformed into parallel rays on the periphery of the lens on the opposite direction similar to the Luneburg lens. Hence, the lens provides pencil beams which can be steered with the move of the feeds which are placed inside the lens. Similar to the Luneburg lens, inhomogeneous material comprises the lens which has circular symmetry. Three examples of the Gutman lens are depicted in Fig. 1.8(a-c). Fig. 1.8(a) shows a Gutman lens where a point source is placed on the focal distance $f=a/2$ where, a, is the radius of the lens. Fig. 1.8(b) shows a Gutman lens where a point source is placed on the focal distance, $f=a/4$ which is closer to the center of the lens and Fig. 1.8(c) a Gutman lens where the point source is placed on the minimal focal distance, $f=a/10$. In both paradigms, parallel rays have ended up on the periphery of the lens, although the performance of the radiated beams has not been examined to further evaluate the electromagnetic properties of the radiator. The advantages of the Gutman lens is its wide FOV with low losses and the compact size compared to the Luneburg lens. The drawback is the placement of the feeds inside the surface of the lens which creates practical challenges; the matching and the high required values of permittivity to synthesize the lens, adds more complexity in its implementation. The latter, has been engineered in the present thesis and two Gutman lenses with focal points $f=a/2$ and $f=a/2.85$ have been analysed and designed using all-metal artificial dielectrics, as well as homogeneous dielectric materials.

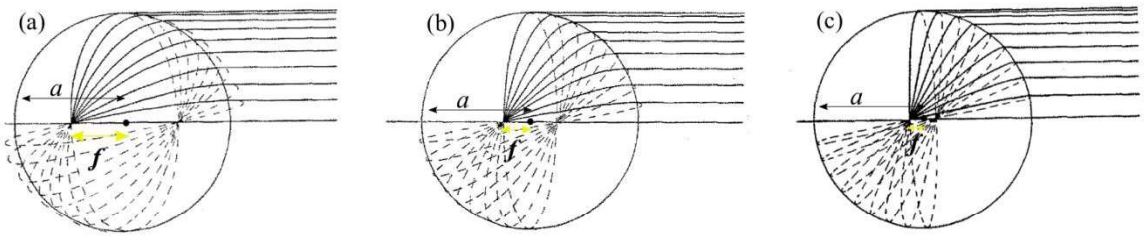

Figure 1.8: Gutman lens antenna with focal distance (a) $f=a/2$, (b) $f=a/4$ and (c) $f=a/10$.

1.4.3 Continuous delay line lens antenna

The approach adopted in a wide part of the present thesis to find antenna solutions for low orbit constellation satellite missions was the design of the Gutman lens antenna using all-metal artificial dielectrics operated at Ku-band. A second approach has been further investigated in the thesis to design a lens for constellation satellites in low altitudes and it is presented in Chapter 6. The antenna technology that has been investigated is the continuous delay line lens in all-metal PPW housing at Ka-band (see Fig. 1.9(a, b)). Ku-band confronts high losses by virtue of atmospheric phenomena such as rain, wind, etc. Therefore, the major target of this part of the thesis is to produce high gain titled beams at wide scan angles. Thoroughly, the beams of the multi-beam antenna must form a mask which has an isoflux shape as designated in Fig. 1.9(a). Every consecutive spot beam transmits in segregate frequencies (see Fig. 1.9(b)) applying the Frequency Hopping Spread Spectrum (FHSS) technique and therefore we improve the carrier to interference (C/I) between the beams and thus we exploit efficiently the available spectrum.

The continuous delay line lens antenna has been introduced in [12] and provides excellent broadband performance and excellent radiation patterns. It is easy to fabricate and has a compact size. The drawback of this type of lens is its narrow FOV which is limited up to ±30°. The objective of this type of lens is first to increase its FOV and then attain higher directivity progressively for the offset beams in order to accomplish an isoflux mask. A modified design methodology is proposed together with optimization techniques in Chapter 6 of the thesis.

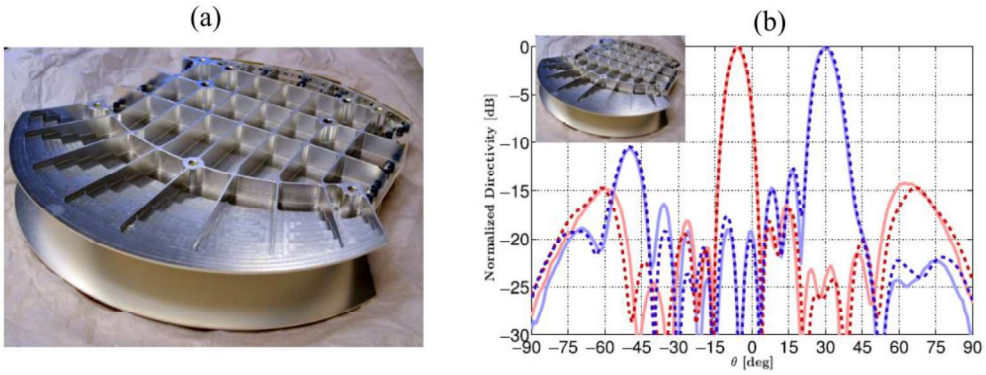

Figure 1.9: Manufactured continuous delay line PPW beamformer, (b) simulated (dash line) versus measured (continuous line) radiation pattern of the manufactured PPW beamformer in H-plane.

1.5 Chapters outline of the thesis

Chapter 2

The Chapter 2 presents discussions on state of the art multi-beam antennas that target in satellite integration missions for constellation orbits. The technology of the antennas lies on quasi-optical configurations and graded index lenses which present wide FOV and low losses. Additionally, novel compact lenses are presented utilizing transformation optic techniques. Moreover, antennas that provide isoflux patterns as well as novel 2D and 3D multi-beam dome lenses with wide coverage are highlighted.

Chapter 3

The Chapter 3 introduces the design of a multi-beam Gutman lens antenna with focal distance $f=R/2$ utilizing all-metal artificial dielectrics in a PPW technology. A novel interleaved glide index symmetry unit-cell is presented with high effective index of refraction and has been used to synthesize the lens. Comparison of unit-cells with high effective index of refraction is presented. A novel design methodology to synthesize the Gutman lens is analysed as well as the matching methodology. The radiation performance of the lens together with the reflections of its excitation source is tested.

Chapter 4

The Chapter 4 presents the prototype and the experimental tests of the Gutman lens antenna with focal distance $f=R/2$ that has been analysed in Chapter 3. The mechanical design of the lens is presented included the mechanical support, the screws, the dowels that have been used as well as, a novel mechanical design of the transition of the lens. Sensitivity tests are provided for the transition to test possible tolerances. Experimental results are shown to test the patterns and the reflections of the lens.

Chapter 5

The Chapter 5 introduces the design of the all-metal Gutman lens antenna with focal distance $f=R/2.85$ in a PPW technology. The lens is a more compact lens compared to the Gutman lens of Chapter 2. The all-metal Luneburg lens using the fakir bed of nails unit-cell is described. Additionally, the equivalent design of the dielectric Gutman lenses with focal distances $f=R/2$ and $f=R/2.85$ synthesized by non-dispersive homogeneous dielectric layers together with the dielectric Luneburg lens are presented. The all-metal Gutman lens with focal distance $f=R/2$, the all-metal Gutman lens with focal distance $f=R/2.85$ and all-metal Luneburg lens are comparted to the equivalent dielectric lenses to evaluate the performance of the lenses.

Chapter 6

The Chapter 6 presents a multi-beam optimized continuous delay line lens antenna in a PPW technology. The antenna topology together with the GO model tool and the optimizer that have been used, are described. A design method is presented and is based on the axis inversion of the elliptical profile of the transversal ridge of the lens. An optimization technique is analysed with all the Degrees of Freedom (DoFs) that are used to optimise the lens. An antenna demonstrator is presented which provides wide FOV and all the beams of the lens form an isoflux envelope mask.

Chapter 2 State of the art

Contents

2.1 Introduction

Lenses have been used for a wide range of applications such as radars, medical systems, space applications, acoustics, plasmonics and optics. Luneburg lenses, firstly introduced in [10], have been studied extensively because of their superior performance in terms of spherical aberrations regarding beam scanning. In particular, the radiated beam can be scanned over a wide FOV by displacing the feed mechanically along the lens periphery. However, Luneburg lenses require materials that can provide a graded index of refraction, which make their implementation complicated. To overcome such challenges, Luneburg lenses utilizing metasurfaces or metamaterials have been implemented [13]. This approach provides more flexibility as the index variation along the lens surface can be controlled by modulating the geometry of a periodic structure. The latter can lead to a simplified manufacturing process and potentially also to reduced mass. 2D and 3D Graded Index (GRIN) Luneburg lenses have been widely implemented using various periodic structures for a wide range of applications from microwave to optical frequencies, [14]–[19] including in plasmonics. For example, in [20] electron beam lithography has been used to fabricate a plasmonic Luneburg lens based on holes in a dielectric thin film. Luneburg lenses have also inspired various types of integrated photonic circuits such as waveguide tapers [20] and couplers [21].

For antenna applications in the microwave and mm-wave range, the bulkiness of traditional Luneburg lenses can be a disadvantage. An approach to reduce the physical volume of quasi-optical devices with media with variable refractive indices has been introduced in [23] and [24] and is referred to transformation optics (TO). This method exploits coordinate transformations between the initial reference mesh and a transformed mesh, which enables the calculation of new values of permittivity and permeability for the transformed design that leads to similar performance behaviour as the reference one [25]. This class of transformation techniques has been applied to design new lenses [26]-[29], including evolutions of the Luneburg lens towards more compact designs [30], [31]. In these works, a curved part of the focal surface of the Luneburg is transformed into a planar surface. The planar transformed surface of the new lens enables the integration of traditional planar feeds such as phased array configurations. However, these transformed lenses call for high values of refractive index, which can be difficult to implement. An alternative design consists in using materials that can be found in nature [32], [33]. However, as mentioned above, such approaches lead to more complex and less flexible designs.

An alternative transformation technique to reduce the volume of the traditional Luneburg lens has been presented in [11]. An asset of this radiator is that the focal point can be placed closer to the center of the lens and thus leading to a more compact lens. It has been proven that, similar to the Luneburg lens, the Gutman lens is free of spherical aberrations and achieves similar radiation performance. A first implementation of this type of lens presented in [34] where a Gutman lens with wide scan and broadband performance synthesized by multiple dielectric layers. In [35], a 3D GRIN Gutman lens has been designed and tested using additive manufacturing utilizing a dielectric cubic periodic cell. However, in both configurations a planar surface approximation of the lens is selected and resulted on aberrations for the offset beams.

2.2 Broadband multi-beam lens antennas with wide field of view

2.2.1 Geodesic Lenses

The concept of the Geodesic lens geometry introduced by Rinehart [36], [37] where he proved that a parallel pair of two conductive surfaces in a spherical form, provides similar performance as a planar Luneburg lens. This type of lens, which is named also as Rinehart Luneburg lens (see Fig. 2.1(a)), allows propagation in homogeneous medium such as air and therefore is suitable for space applications. Both conductive surfaces are spherical and they have common normal at all points along their surfaces. The space between the two surfaces is defined small in order to allow the propagation of only the fundamental TEM mode. The focusing properties depend on the various path lengths of every ray along the air gap. The shape of the conductive surfaces is defined appropriately and the equivalent index of refraction along the surfaces is distinct at every point and equal to the required values of the Luneburg lens. Therefore, focusing is achieved in 360° azimuth scanning when rotating the excitation source on the periphery of the lens. Thorough analysis of the geodesic Luneburg lens has been further investigated in [38]-[43].

In [44] a new concept of transformed geodesic lenses has been introduced. Conductive surfaces with non-identical shapes examined to design more compact geodesic lenses. A mean surface is defined and represents the curve that is formed between two conductive surfaces that have common normal at all points. The effective index of refraction along the formulated mean surface presents distinct values along the surface of the lens. A class of geodesic lenses with different profiles examined (see Fig. 2.1(b)) and lead to more compact size lenses compared to the Luneburg profile. The equations of the profile of the surfaces that have been examined, as well as, the equivalent distribution of the indices are depicted in the table of Fig. 2.1(c).

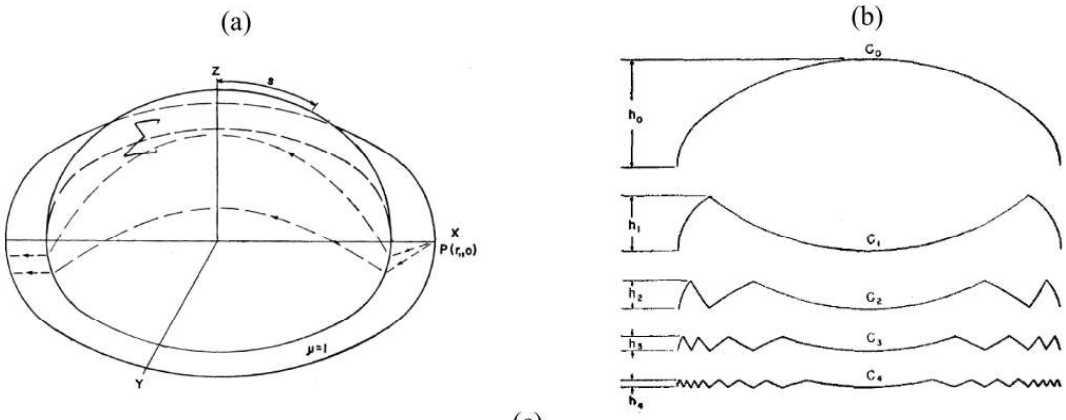

(c)

Surface	Generating curve	Index needed [$n(s)$ or $N(\rho)$]	Permissible range
1. Plane (Luneberg lens itself)	$s=\rho$	$[2-\rho^2]^{\frac{1}{2}}$	$0\leq\rho\leq1$
2. Cone	$s=k\rho$	$\rho^{k-1}[2-\rho^{2k}]^{\frac{1}{2}}$	$0\leq\rho\leq1$ if $k>0$ $\rho\geq1$ if $k<0$
3. Cylinder	$\rho=1$	$e^{-s}[2-e^{-2s}]^{\frac{1}{2}}$	$s\geq0$
4. Rinehart surface	$s=\frac{1}{2}(\rho+\sin^{-1}\rho)$	1	$0\leq\rho\leq1$
5. Generalized Rinehart surface	$s=(1-k)\rho+k\sin^{-1}\rho$	$\frac{\{2[1+(1-\rho^2)^{\frac{1}{2}}]^{2k}-\rho^2\}^{\frac{1}{2}}}{[1+(1-\rho^2)^{\frac{1}{2}}]^{2k}}$	$0\leq\rho\leq1$
6. Hemisphere	$s=\sin^{-1}\rho$	$\frac{\{2[1+(1-\rho^2)^{\frac{1}{2}}]^2-\rho^2\}^{\frac{1}{2}}}{[1+(1-\rho^2)^{\frac{1}{2}}]^2}$	$0\leq\rho\leq1$

Figure 2.1: (a) Geometry of the generalized geodesic Luneburg lens, [36], (b) family of curves of modified geodesic Luneburg lens, [44]. (c) Table with the generating curves of geodesic surfaces, [44].

In [45], [46], a compact geodesic Luneburg lens named also as the water drop lens, has been presented. Inspired by [44], a modified conductive surface has been designed and resulted on a compact lens. Extensive analysis of the water drop lens is introduced in [47], [48], where the analytical profile of the lens is presented together with experimental results (see Fig. 2.2(a-d)). The lens operates at Ka-band and presents wide FOV up to ±75° with maximum scan losses 3 dB.

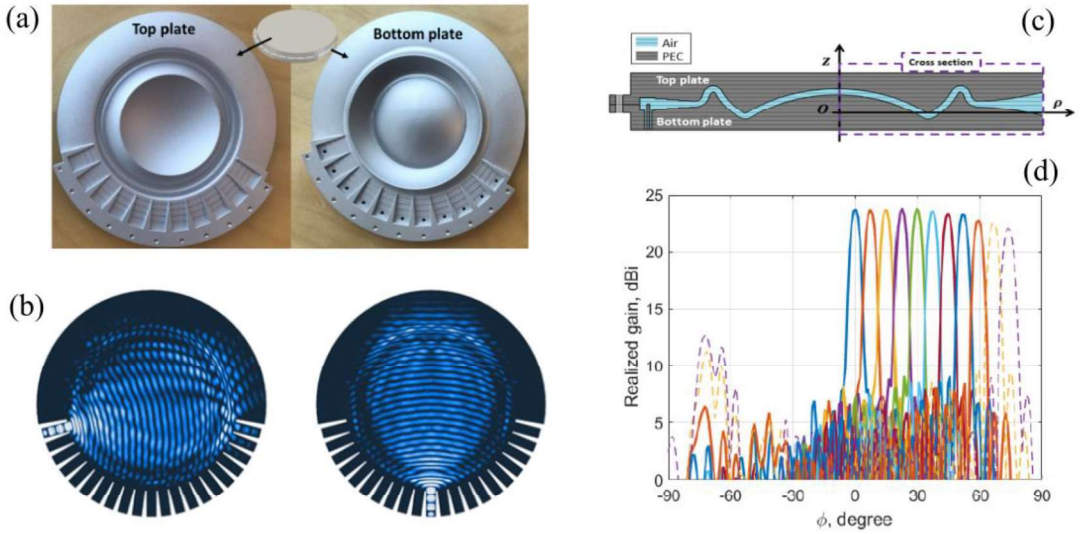

Figure 2.2: Water drop lens, (a) prototype (b) E-field of the broadside and the extreme beam, (c) 2D cut view of the geometry of the lens, (d) symmetric radiation patterns.

2.2.2 Rotman Lenses

The Rotman lens antenna, [49] is a constrained type lens which is also referred as bootlace lens [50], Fig. 2.3(a-d). The major advantage of this type of lens is its wide scan capabilities. The lens consists of a linear outer contour and a curved inner contour to provide focusing properties. The curved surface of the inner contour provides flexibility in the design and increased number of DoFs. The outer contour is linear in order to support radiated elements in an array form. Segregate time delay paths from the inner contour till the outer contour, form the lens. This type of lens consists of two symmetric focal points which are off-axis and one focal point on-axis and both are placed along the focal arc.

Rotman, [49] has proposed flexible coaxial cables with distinct electrical lengths to compose the delay lines between the inner and the outer contour of the lens. The lens designed in a PPW technology and input horns are placed along the focal arc of the lens to excite it. The cables have been connected to the terminated curved PPW region and provide focus on the linear output of the lens.

The Rotman lens antenna has been further investigated in [51], [52] using multiple configurations for the time delay paths between the inner and the outer contour of the lens. Fig. 2.4(a) shows a Rotman lens in a PPW technology where traditional waveguides has been used with distinct lengths in order to provide phase adjustment on the output linear contour of the lens. The discrete delay paths synthesized by cables with segregate electrical paths and a sectorial horn antenna connected to the linear contour of the lens to further increase the directivity of the lens (see Fig. 2.4(b)). In addition, the Rotman lens has been implemented in a full-dielectric configuration (see Fig. 2.4(c)).

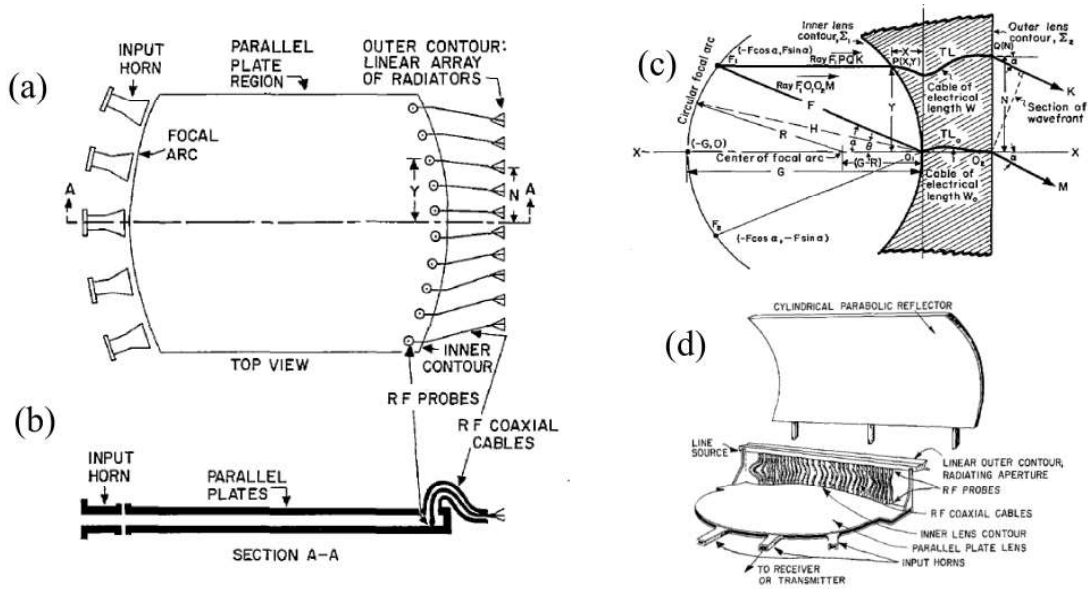

Figure 2.3: Rotman lens (a) geometry, (b) 2D cut view, (c) design parameters, (c) Rotman lens with parabolic reflector.

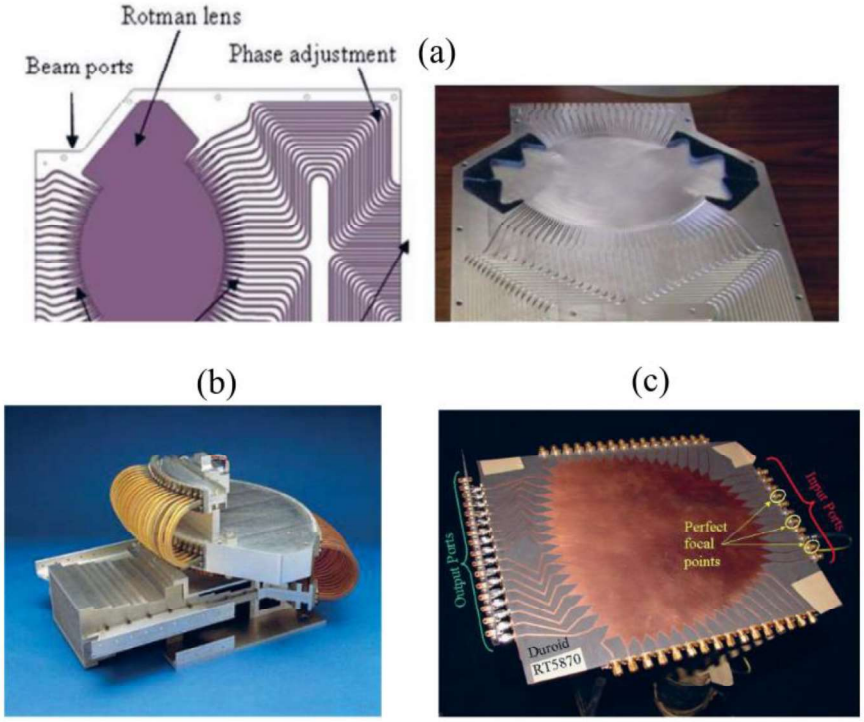

Figure 2.4: Rotman lens antenna (a) using discrete waveguide delay lines, (b) using cables with separate electrical lengths, (c) using microstrip lines as discrete delay lines.

2.3 Graded index lens antennas utilizing metasurfaces

2.3.1 2D Metasurface lenses

Metasurfaces are artificial surfaces composed of periodic structures that cannot be found in nature. Arranging properly these periodic structures we can control and manipulate the electromagnetic waves. Metasurfaces can be utilized to design GRIN lenses. The variation of

the effective index of refractive of the periodic structures, guide the electromagnetic waves and focus the beam. In [53] [54], multiple types of metasurfaces studied in a PPW technology to implement Luneburg lenses at UWB frequency band. The fakir bed of nails unit-cell is presented, as well as, the glide index symmetry unit-cell. The holey surface unit-cell shows low dispersion in the UWB band with maximum refractive index n=1.4 (see Fig. 2.5(a)). The periodic structures that are shown in Fig. 2.5(b) are all-metal structures and can be used to design 2D planar GRIN Luneburg lenses with focusing properties as depicted in Fig. 2.5(c).

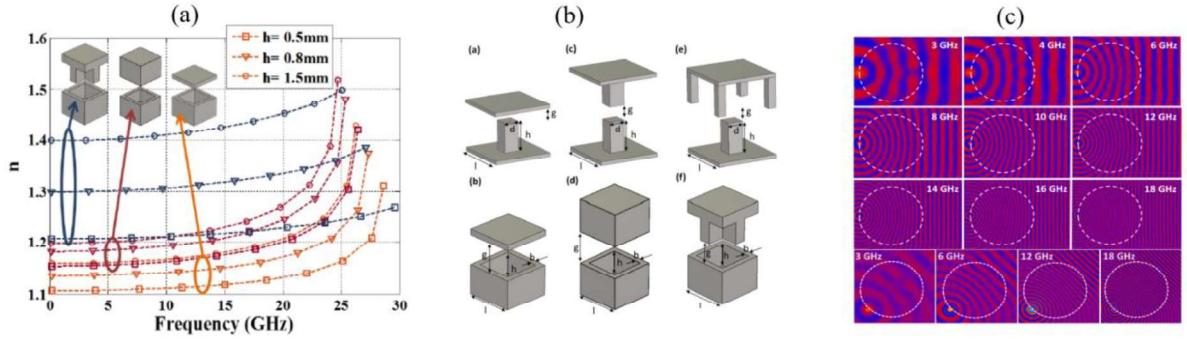

Figure 2.5: (a) Effective refractive index for holey surfaces unit cells, (b) 2D PPW metasurfaces, (c) E-field distribution of a 2D PPW lens.

A demonstrator of a 2D GRIN Lunenburg lens is depicted in Fig. 2.6(a-c) where the fakir cell has been utilized to synthesize the lens and shows low dispersion at the Ku-band, [55]. The lens is fed by all-metal rectangular waveguides producing nine beams in the same H-plane. The effective index of refraction of all the cells range from n=1 to n=1.4 to synthesize the PPW lens. In addition, a radiated horn aperture is designed at the edge of the lens to smoothly match the lens into free space.

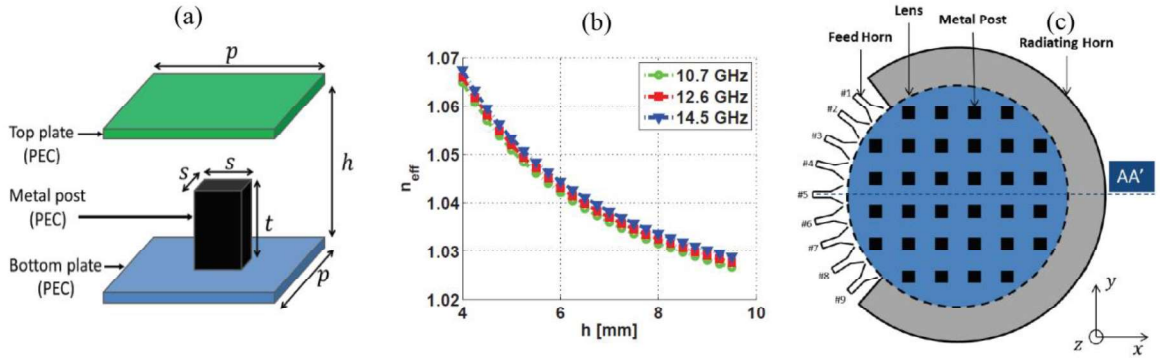

Figure 2.6: (a) PPW fakir bed of nail unit-cell, (b) effective refractive index variation vs height of post, (c) GRIN PPW lens, [55].

The fakir bed of nails unit-cell has been likewise used to design a PPW Luneburg lens at Ka-band, [56]. Fig. 2.7(a) shows the geometry of the lens in a 2D view where the above PPW metal plate is curved following a 2D spline. The latter, improves the dispersion of the unit-cell at higher frequencies. The demonstrator has been manufactured and tested and is depicted in Fig. 2.7(b).

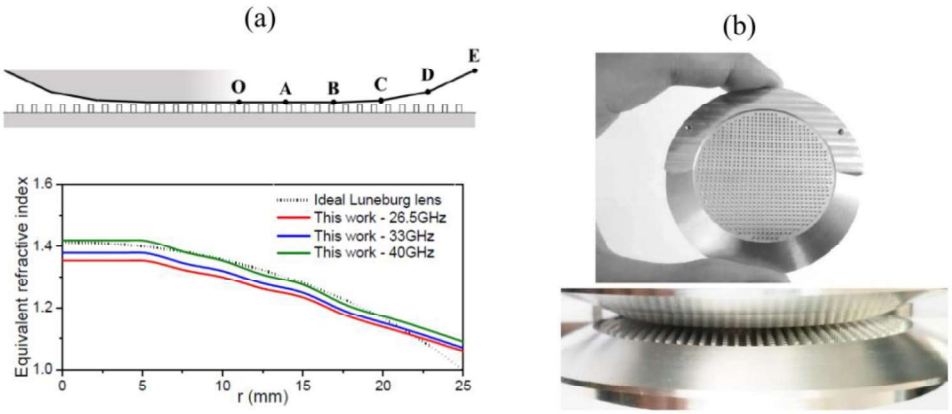

Figure 2.7: (a) Geometry of the GRIN Luneburg lens with the required effective index distribution, (b) prototype demonstrator.

The glide symmetry unit-cell appears lower dispersion compared to the fakir bed of nails unit-cell, by virtue of the higher number of DoFs and it can be used for the design of lenses in the challenging Ka-band. In [57] is shown that the combination of glide symmetry metal posts with holey surfaces can lead to a unit-cell which has low and linear dispersion in the Ka-band. Therefore, the glide symmetric pin loaded holey metasurface that is depicted in Fig. 2.8(a, b) is utilized to design and manufacture a GRIN Lunenburg lens (see Fig. 2.8(c)). For the excitation of the lens, a coaxial to parallel waveguide transition is designed. Despite the good performance in the radiation patterns, high reflections were inevitable, by virtue of the sensitivity of the transition that has been used.

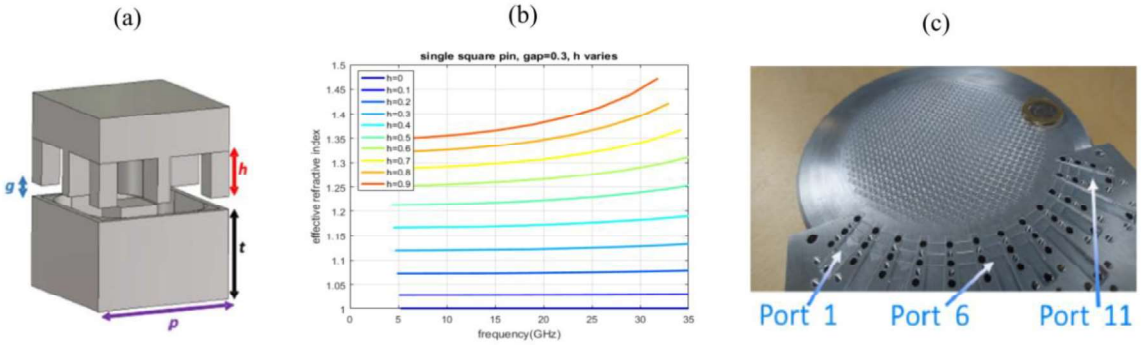

Figure 2.8: (a) Glide symmetric pin loaded holey metasurface, (b) effective refractive index variation vs frequency, (c) prototype of the Lens, [57].

The glide symmetry unit-cell has been further used to design a transformed Luneburg lens which calls for high values of effective index of refraction [58]. The unit-cell accomplishes a maximal value of effective index of refraction equal to n=1.8. The transformed lens antenna has a planar surface to excite its feeds and is shown in Fig. 2.9(a, b).

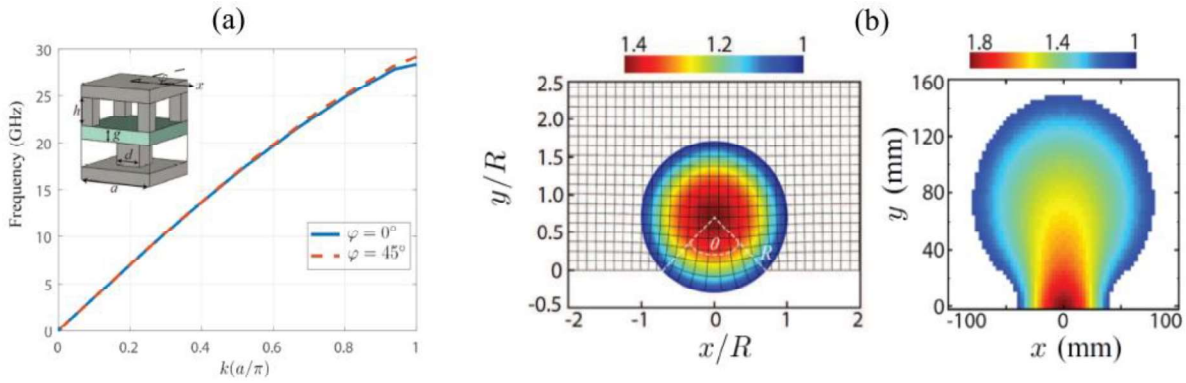

Figure 2.9: (a) Glide symmetry unit-cell, (b) transformed Luneburg lens.

2.3.2 3D Metasurface lenses

3D GRIN lenses recently have been implemented at microwave frequencies. That type of lenses provide beam steering in both E- and H-plane. However, all these type of lenses are composed of dielectric substrates and add losses. For space applications there is a need for 3D all-metal lenses, although there is no any documentation from any research group. The first 3D half-spherical dielectric GRIN Luneburg lens presented in [59]. A 3D GRIN half-spherical Luneburg lens is depicted in Fig. 2.10(a), where dielectric slabs with drilled holes which are nearly isotropic are used to design the lens. The synthesis of the required effective index of refraction of the lens is realized by multiple dielectric slabs that have been stacked. In the manufacturing process these slabs first drilled to shape the holes and then stacked to compose the lens.

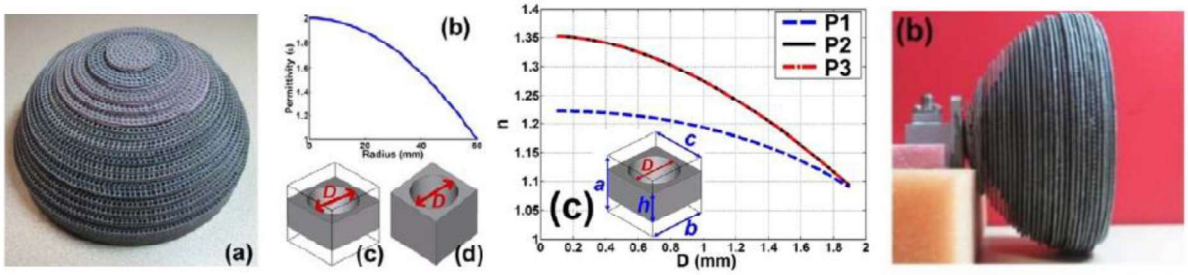

Figure 2.10: 3D half-spherical Luneburg lens utilizing a holey dielectric unit-cell, [59].

In [60] a 3D Luneburg lens is presented where unit-cells of polystyrene dielectric used to create a variable effective index of refraction along the total spherical surface of the lens. The polystyrene rods have been placed in the periphery of a sphere with segregate values of radii as shown in Fig. 2.11.

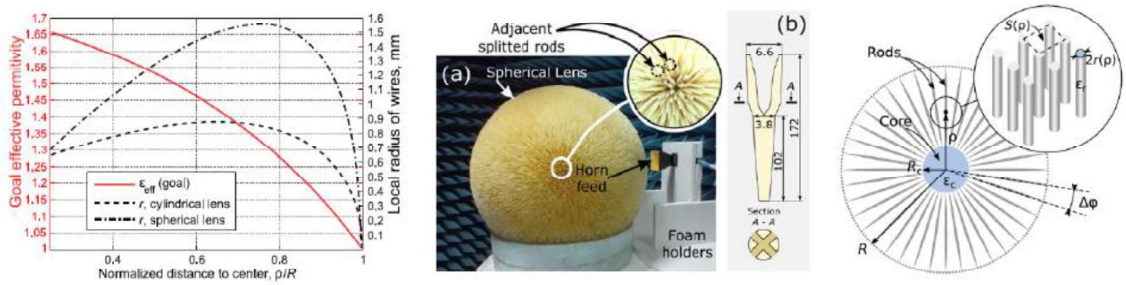

Figure 2.11: Polystyrene dielectric 3D spherical lens using a rod unit-cell, [60].

In [35] a 3D Gutman lens antenna using dielectric periodic structures has been designed and manufactured (see Fig. 2.12(a, b)). A modified planar focal arc is proposed to facilitate the rotation of the feeds, as well as, the incorporation of possible arrays as excitation feeds. However, the planar surface of the focal arc of the lens restricts the FOV of the lens, since the excitation feeds are out of the ideal circular focal arc of the lens. The dielectric unit-cell that has been used, provides the required values of effective index of refraction by varying the density of the structure inside its volume.

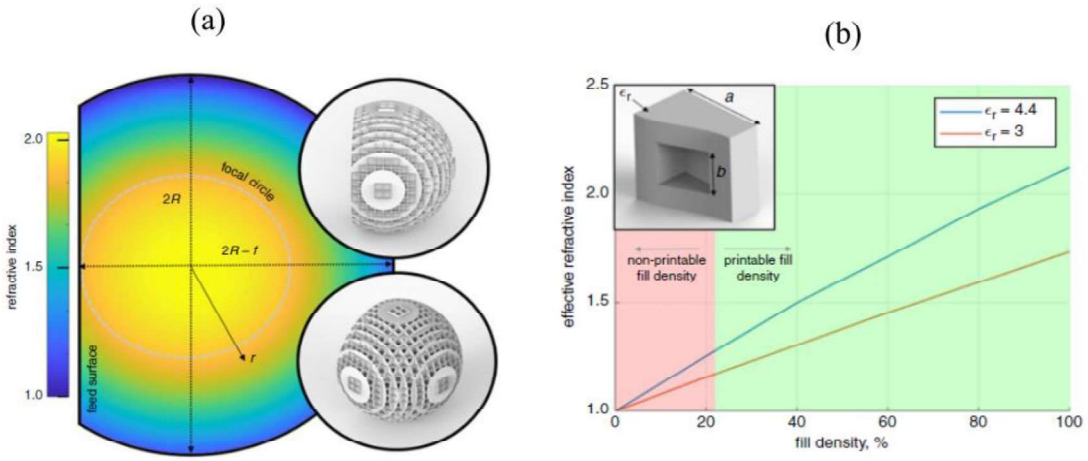

Figure 2.12: (a) Refractive index colour-map and representation of the 3D Gutman lens with flat focal arc, (b) effective refractive index versus fill density.

2.4 Lens antennas utilizing transformation optics

TO, recently have appealed the interest to quasi-optical devices. Applying quasi-conformal mapping techniques, we can transform and minimize the size of lenses. Hence, following the industrial trend to implement compact devices, TO techniques is a fruitful design approach to achieve this goal. In [61], a TO technique has been applied to re-shape the Luneburg lens into a more compact planar lens. It has been proved that squeezing the shape of the lens, higher values of effective index of refraction are required. Multiple materials used to synthesize and finally construct the final prototype. The required variation of the permittivity of the reshaped lens is ε_r:[1-12]. Therefore, to implement the reshaped lens, ceramic materials with different volume fractions of titanate fillers have been used and every ceramic layer represents distinct values of refractive index (see Fig. 2.13). In that work the use of materials with different permittivity was very critical to implement the final prototype. The design of the transformed lens can be implemented also with metasurfaces, although there is a need of unit-cells with high values of effective index of refraction (in this case n_{max}= 3.47). Therefore, there is a trade-off between the size of the transformed lens that we want to achieve and the highest value of the effective index of refraction that it can be achieved.

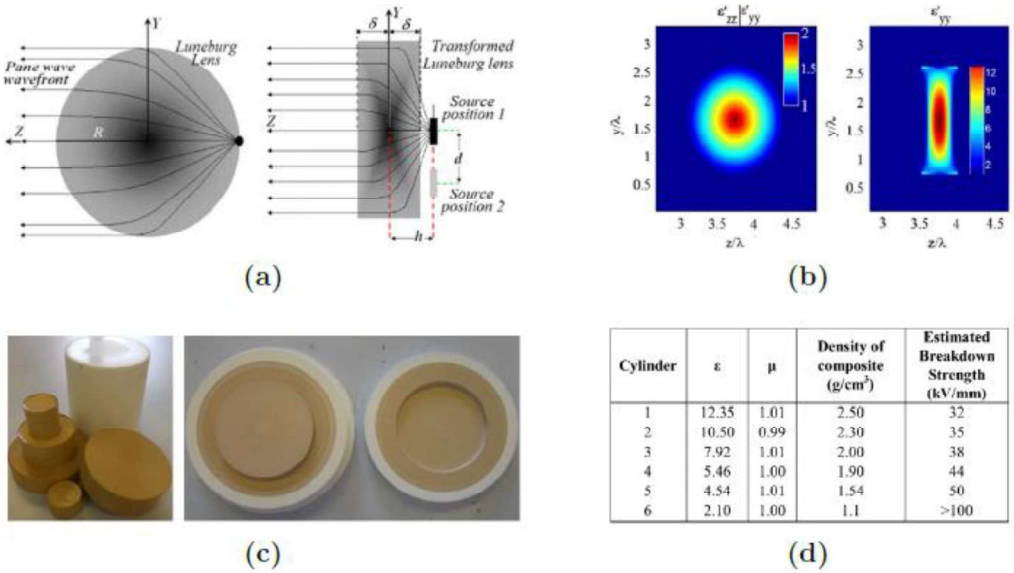

Cylinder	ε	μ	Density of composite (g/cm³)	Estimated Breakdown Strength (kV/mm)
1	12.35	1.01	2.50	32
2	10.50	0.99	2.30	35
3	7.92	1.01	2.00	38
4	5.46	1.00	1.90	44
5	4.54	1.01	1.54	50
6	2.10	1.00	1.1	>100

Figure 2.13: (a) Spherical Luneburg lens and transformed planar lens, (b) permittivity comparison of the two lenses, (c) ceramic material sheets, (d) permittivity values of the ceramic plates, [61].

In [32], TO have been likewise utilized to squeeze the Luneburg lens into a slimmer lens. The implementation was realized with multiple dielectric layers as shown in Fig 2.14(a-c). In that work, the offset beams have less directivity compared to the broadside one as depicted in Fig. 2.14(d). Six dielectric substrates stacked to synthesize the lens. The major advantages in that transformed lens, are its compact size and also the capability controlling the directivity of the patterns with the feed position. The present cylindrical transformed lens can be further analysed to achieve an isoflux envelope mask that was discussed in previous section.

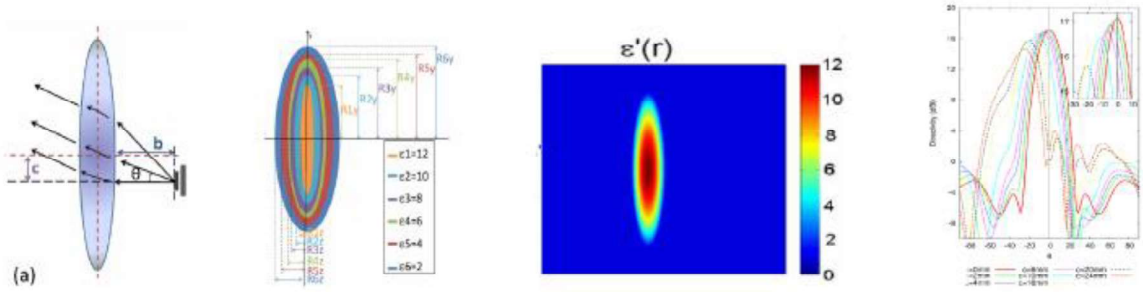

Figure 2.14: (a) Feed displacement, (b) permittivity values of the dielectric substrates, (c) permittivity distribution, (d) radiation patterns for different values of feed displacement, [32].

The works mentioned previously discuss the synthesis of the transformed lenses using multiple layers of dielectric slabs with the relevant permittivity values. An alternative method to synthesize transformed lenses is the use of artificial dielectric periodic materials with the required effective index of refraction distribution. Although, as previously mentioned, it is very challenging to achieve high values of effective index of refraction. In [31], quasi-conformal mapping utilized to transform the conventional spherical Luneburg lens to a more compact 3D lens. The part that was selected to be transformed is the circular arc of the traditional lens as depicted in Fig. 2.15(a). This part has been flattened resulting in higher values of effective refractive indices in the transformed area (see Fig.

2.15(b)). In that work, as we minimize the radius of the hole of the dielectric slab we can achieve higher values of refractive index. However, in that case we have manufacturing constraints. For instance, using milling machines or even with 3D printing machines, the finest width of surface or the finest hole diameter is 0.3 mm. Hence, the maximum hole diameter of the unit cell was 0.5 mm with index n = 2 as is depicted in Fig. 2.15(c). The prototype has been experimentally tested and is illustrated in Fig. 2.15(d).

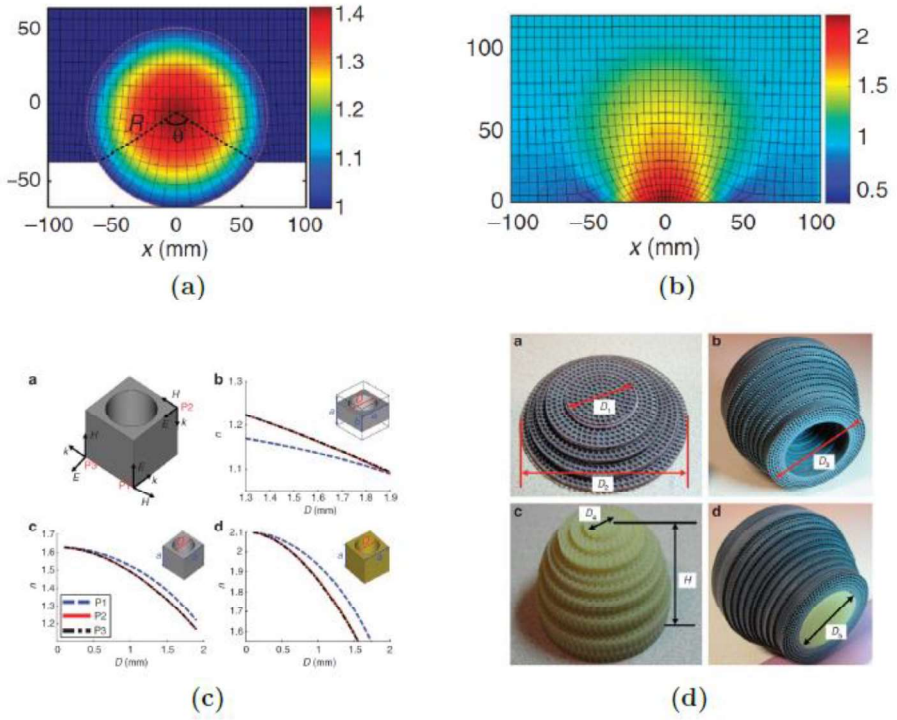

Figure 2.15: (a) 3D Luneburg lens, (b) 3D transformed lens, (c) unit-cells, (d) prototype parts, [31].

To conclude, transformation optic techniques is a very appealing process to produce compact lenses. However, the transformed lenses require very high values of effective index of refraction. Thus, a challenging topic is to design novel periodic structures that achieve low dispersion in high values of refractive index.

2.5 Isoflux single radiator pattern antennas

It is well known the need for isoflux patterns in space applications. Many research groups have been implemented antennas to provide that pattern [62]-[64] and they focus mainly on 3D dielectric single radiators. In Fig. 2.16(a), a 3D double dielectric shell lens is presented [65]. The main goal of this design is to achieve a compact lens with a single isoflux pattern. Therefore, two optimized low loss dielectric shells consists the inner and the outer contour of the lens, respectively. It has been proved that the usage of two dielectric shells reduces drastically the size of the lens in comparison with merely a single dielectric layer. Furthermore, a power mask template has been defined and by utilizing optimization techniques, the final isoflux pattern has been achieved and is depicted in Fig. 2.16(b).

In Fig 2.17(a), a circular polarized antenna in X-band for LEO satellites is proposed. It is a flat metasurface radiator utilizing metal patches in a ground dielectric slab. The strategic position and geometry of the patches provides the circular polarized wave. An isoflux pattern attained (see Fig. 2.17(b)) applying the relevant amplitudes and phases in every metal patch.

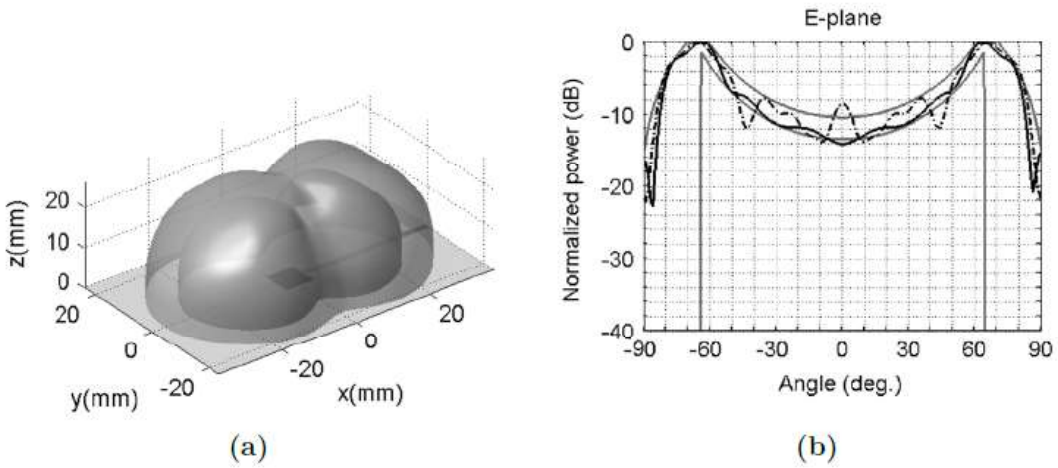

Figure 2.16: (a) 3D double dielectric shell lens and (b) isoflux pattern, [65].

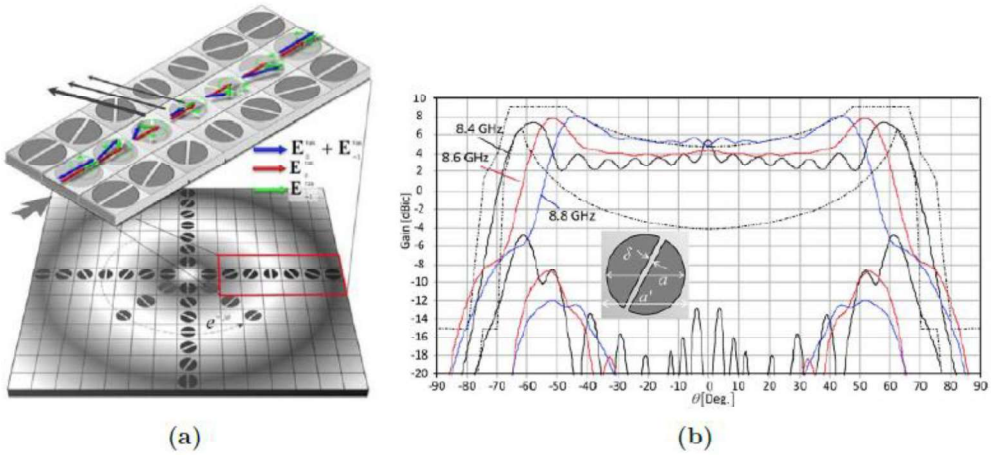

Figure 2.17: (a) Metasurface antenna design, (b) 2D isoflux pattern representation, [66]**.**

Helical antennas have been used widely in space missions by virtue of their low cost, low weight and their proper performance, [67], [68]. In Figure 2.18(a) a miniaturized circular polarized printed quadrifilar helical antenna (PQHA) is presented, [69]. The goal of that work is to provide a compact element and maintain the low cross polarization and the isoflux pattern of the antenna. Following that requirements, the metallic helices that are printed in the dielectric have been replaced by sinusoidal strips periods and finally a 50% miniaturization has been accomplished. The circular polarization achieved with a 90° progressive phase in the printed helices.

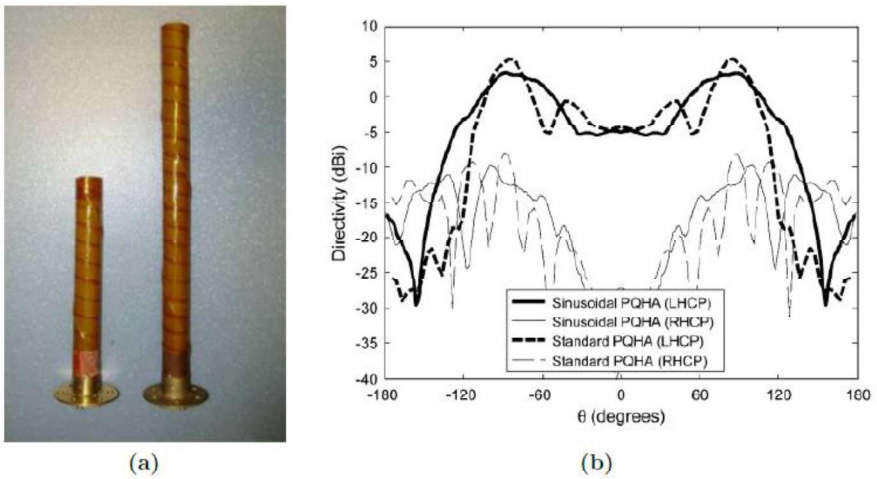

Figure 2.18: (a) Printed quadrifilar helical antennas initial design and compact one, (b) isoflux radiation pattern [69].

2.6 Multi-beam wide scan lens antennas

2.6.1 Multi-beam lenses with isoflux envelope performance

Few activities have been realised regarding to the isoflux envelope multi-beam patterns. As mentioned in Chapter 1, an isoflux envelope mask is formed by all the radiating beams of the antenna array; meaning that we need to progressively increase the directivity of the offset beams compared to the broadside beam. Mainly, the existing state of the art projects already published rely on the use of a single element antenna which produces the isoflux radiation pattern that we have highlighted in the previous Section 2.5.

The sunflower multi-beam antenna

A first antenna proposal to achieve the isoflux envelope mask producing multi-beam patterns has been introduced in [70]-[72]. To attain these patterns, sparced array elements have been used.

-The advantages of these aperiodic arrays compared to periodic elements are the following:

- First, SLL reduction can be achieved.
- Second, the beamwidth can remain stable as we reduce the number of elements on a specific predefined aperture.
- Last, grading lobes (GL) can be avoided.

Spaced tapering process in the aperiodic elements has implemented with uniform excitation to achieve amplitude tapering. Therefore, this density tapering that has been utilized, placing strategically the elements of the array (see Fig. 2.19(a)), provides a very flexible design and control of the SLL level. The final element position which is depicted in Fig. 2.19(b) resembles the sunflower and thus the antenna named as the sunflower antenna. Continuously, to achieve the isoflux envelope distribution the aperiodic elements are divided in subarrays covering different apertures. Therefore, a small subarray has been defined for the broadside beam. For the first offset beam, a larger subarray has been defined for the effective aperture which leads to a more directive beam. Hence, as we scan, we are able to provide beams with higher directivity because they exploit larger subarrays and consecutively larger effective apertures.

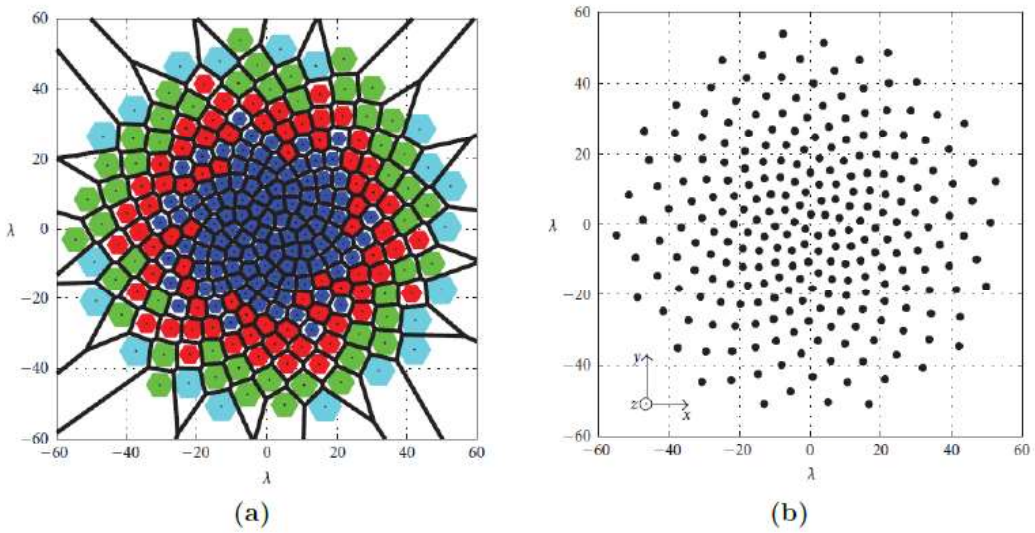

Figure 2.19: [70]-[72]. Sparse density tapering and (b) positioning of the radiated elements in a sunflower distribution.

3D Geodesic Hemispherical antenna array

In [73], a 3D hemispherical antenna array is presented. The array is composed of passive radiated elements which are connected with an active module beamforming network and targets to operate at Ku-band for aircraft in flight entertainment applications. The hemispherical profile of the antenna is divided in 40 triangles which each of them indicates a tile subarray and each array has the same number of radiated elements (see Fig. 2.20(a, b)). This active Tx/Rx system consists of two beam forming networks (see Fig. 2.20(c, d)). At the output of the beamforming networks there are active Tx/Rx modules which are connected to all the radiating elements in separate triangles. Hence, regarding to the target pointing angle, we switch the triangles to radiate the desired beam. However, in that configuration, every triangle has the same number of radiating elements which results on beams with the same beamwidth and directivity. An alternative design in that configuration to achieve more narrow beams in the offset beams is to divide the hemispherical array aperture into triangles which have different number of elements and with distinct sizes. The concept of that design is similar to the sunflower array in [71]. As we scan the beam, we need to define larger triangles which will lead to larger subarrays and thus larger effective radiating apertures and thus more directive beams; the number and the placement of every triangle (sub-array) is vital.

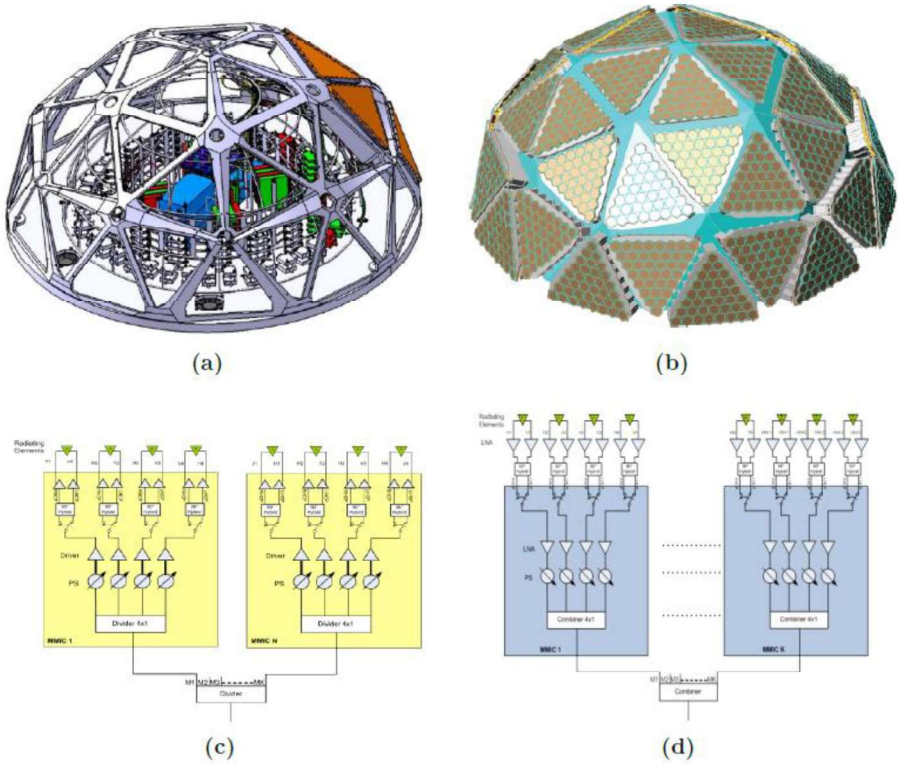

Figure 2.20: [73] (a) 3D Hemisphere with the integrating beamforming network, (b) radiating elements in pairs of triangles integrated in a hemisphere aperture, (c) Tx beamforming network, (d) Rx beamforming network.

2.6.2 Dome Lenses

Thales Alenia Space [74] has implemented a beamforming antenna system using the dome lens and it is very promising to achieve the isoflux envelope. As depicted in Fig. 2.21(a), the goal of the project was to achieve the relevant beam footprints. The dome lens has been designed and it consists of two dielectric layers with high permittivity values (see Fig. 2.21(b)). The excitation of the dome element is composed of an analogue beamforming network and an antenna array. Fig. 2.21(c) shows that the extreme beam at 50° has higher directivity compared to the broadside beam and the dB difference between the beams is equal to 1.5 dB. The extreme beam is narrower because the input wave exploits larger effective aperture of the lens compared to the wave of the broadside excitation, Fig. 2.21(d).

In [75] a metadome multi-beam antenna has been designed with an increased scanning range up to 80°. An antenna array is selected and designed for the excitation of the Dome. The array has been defined with equal amplitude excitation and the phase has been optimized in order to achieve the required beam angles in the output of the Dome. Therefore, the array that illuminates the Dome can scan the beam up to 60° and the effect of the Dome increases the scanning range up to 80° (see Fig. 2.22). However, in both cases there are high SLL levels which need to be eliminated.

In [76] an extensive design analysis is presented to the meta-dome lens of [75]. Geometrical optic (GO) techniques have been explored to design the Dome. Physical optics analysis has been implemented to define the required amplitude and phase distribution of the feed array. Fig. 2.22(a) shows the rays at the extreme angle were they illuminate a smaller effective aperture compared to the rays at the broadside direction. Thus, we have high losses in the

extreme beams that need to be compensated. Except from the high level of SLL, an additional challenge that we face on the present configuration, is the high cross over values.

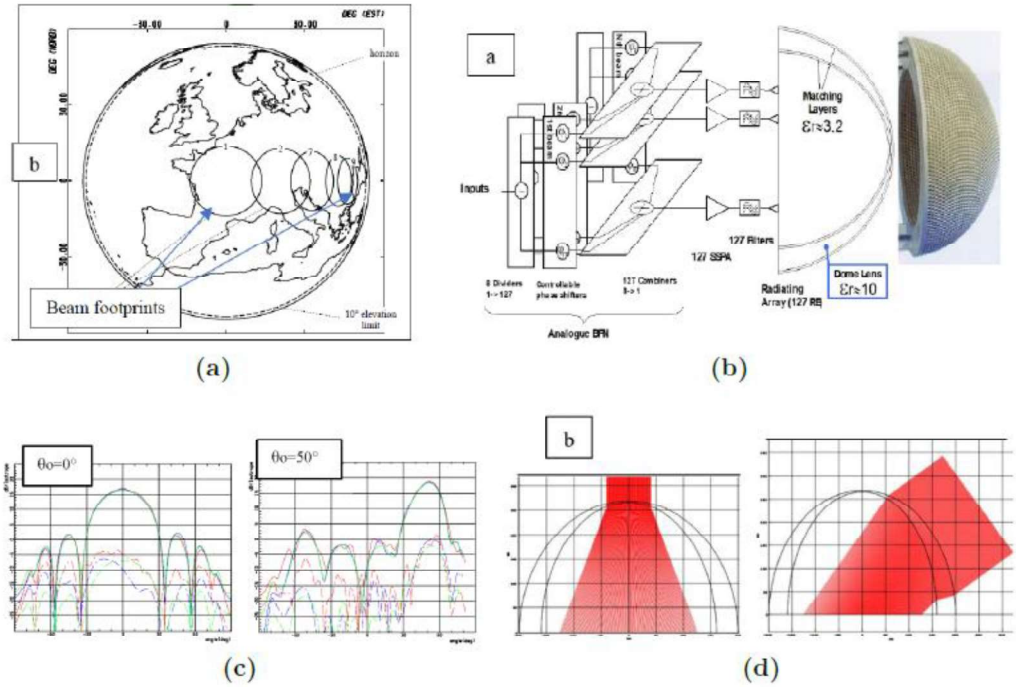

Figure 2.21: [74] (a) Beam footprints with isoflux pattern, (b) RF part of the satellite (analogue beamforming network and the dome lens element), (c) radiation patterns for the broadside and the 50° offset beam, (d) ray tracing for the broadside and the 50° offset beam.

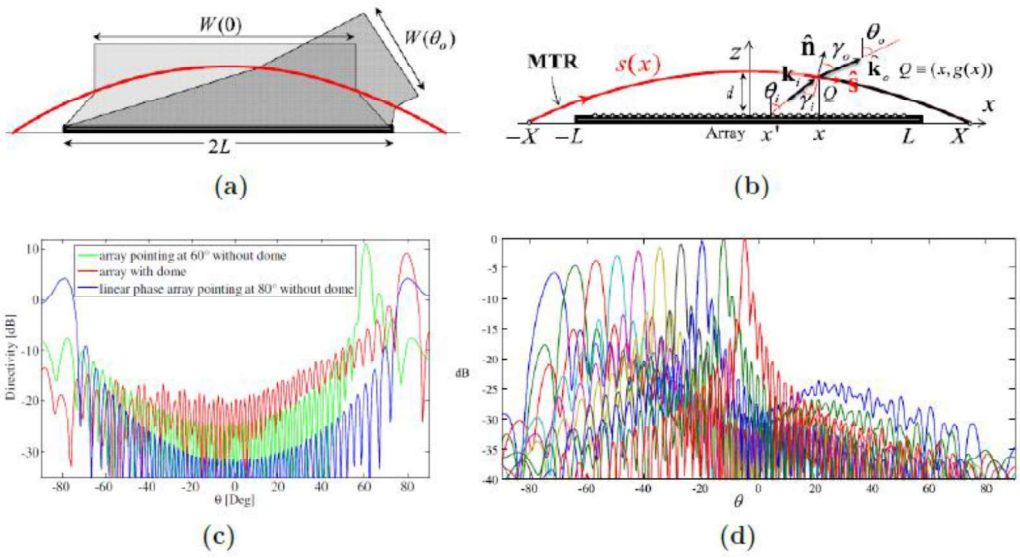

Figure 2.22: [75], [76] and (a) Effective aperture representation for the broadside and extreme beam, (b) dome profile with the antenna array excitation, (c) beam comparison of the array and the final beam, (d) radiation pattern in all the scanning range.

In [77] a dome lens with high scanning performance (up to 70°) is presented. This rotational dielectric Dome (see Fig. 2.23(a)) is composed of a dielectric with different inner and outer

profiles. Optimization techniques have been utilized on the inner and outer profile of the Dome based on a geometrical optics. The target of the optimization is to compensate the losses of the dome of the initial design that is depicted in Fig. 2.23(b). The goal has been achieved and the Dome resulted in scanning up to 70° with very low losses (up to solely 0.5 dB). However, there are two challenges that need to be addressed. First, the high level of side lobes which reaches the value of -11 dB and -10 dB in some beams. Second, there is high level of carrier to interference (C/I) which needs to be eliminated.

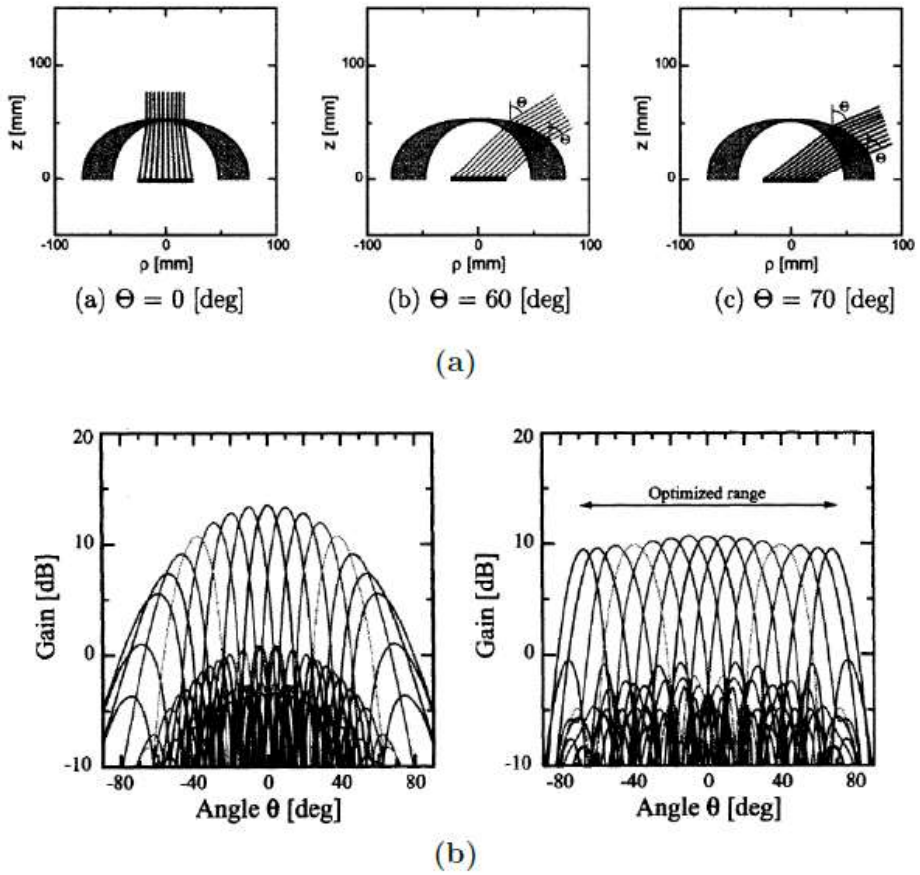

Figure 2.23: (a) [77] Rotational dielectric Dome (b) Radiation patterns of the initial design (left) and the final optimized one (right).

2.7 Advanced manufacturing technologies

Following the demanding specifications in the space industry for compact structures and 3D configuration designs, addictive manufacturing (AM) has appealed the interest the last years. AM is the process of joining materials to make objects from 3D model data, usually layer upon layer as opposed to traditional subtractive manufacturing technologies. AM is used to build physical models, prototypes, patterns, tooling components and production parts in metals, plastics, ceramics or composite materials. The main advantage of this manufacturing technique is that very complex 3D structures can be constructed layer by layer. In the following Table 2.1 we depict the pros and the cons of the AM process.

Table. 2.1: Pros and cons of additive manufacturing.

ADDITIVE MANUFACTURING	
Advantages	Disadvantages
Reduce time market: fast industrial manufacturing	Slow build rates
Build real parts	High production costs
Reduce costs for complicated shapes	Require post processing
Bring together different functionalities in one part	Discontinuous production process
Reduce assembly errors and hence costs	Small build volume
Free design from restrictions of traditional manufacturing processes: design and manufacture of complex 3D structures	Poor mechanical properties
Access new market niches	
Reduce costs for short series (mass customization, batch of one, custom made)	
Meet individual costumer needs	

In the satellite RF chain, AM provides manufacturing capability of complex geometries and low mass microwave components such as antennas, couplers, dividers, filters, etc.

-Using AM we can construct all metal components with two different ways.

- The first choice is to manufacture directly these components with the appropriate metals such as silver, aluminium or titanium.
- The second choice is to use plastic to construct the components and then to metalize the structure with copper coating. In this case, we result in low weight structures and improve the rough surfaces of the structure. However, we have low conductivity values which are very critical for space applications.

An example of the critical usage of 3D printing is the horn antennas. Horns are widely used in satellites because they provide high gain patterns. However, when using multiple elements with complex spline horn profiles, the whole array is very heavy and expensive. Utilizing 3D printing we can manufacture complex horn shapes with very light weight.

One example is presented by Thales Alenia Space in [78] where a spline horn antenna has been fabricated utilizing 3D printing (see Fig. 2.24(a)). Furthermore, an array with spline horn elements has been manufactured and is designated in Fig. 2.24(b)). The present array has low mass and low price and is proposed to be implemented for satellite missions in Ku-band.

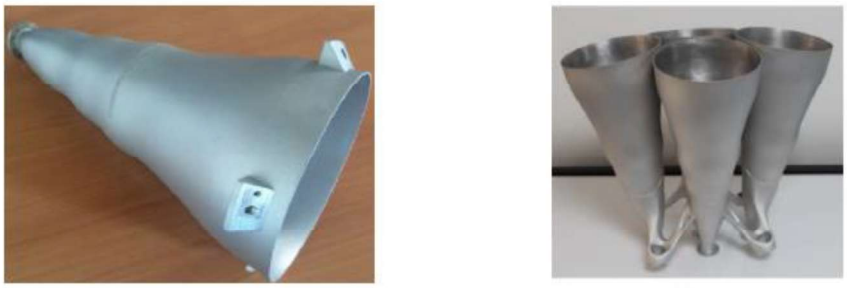

(a) (b)

Figure 2.24: 3D printing (a) spline horn antenna and (b) horn antenna array, [78].

In Idonial (partner of the Revolve project) the in-house machines that are available for 3D printing additive manufacturing and traditional milling are depicted in Table 2.2.

Table 2.2. In-house manufacturing machines in Idonial.

MANUFACTURING TECHNOLOGY	
3D printing machines	Milling machines
DMLS for metal parts: 2 machines EOS M270 and EOS M280	CNC 5 axis milling center:DECKEL MAHO
SLS for plastic parts (polyamide mainly): 2 machines EOS P100 and EOS P395	CNC 5 axis micro milling center:KERN EVO
LCM for technical ceramics: LITHOZ CERAFAB 8500	
Jetting for photosensitive resins (object technology): STRATASYS CONNEX and STRATASYS EDEN	

EOS M270 that is depicted in Fig. 2.25(a), builds metal parts using Direct Metal Laser-Sintering (DMLS). The technology fuses metal powder into a solid part by melting it locally using a focused laser beam and all the parts are built up additively layer by layer.

EOS P 100, produces plastic products from polyamide or polystyrene; it has been designed to produce vertical walls with maximum surface quality and is depicted in Fig. 2.25(b). Hence, a critical remark here is that utilizing plastics instead of metals we can avoid the rough surfaces in our components. However, we need to metalize the prototype and it creates more complexity in the manufacturing process.

LITHOZ CERAFAB 8500 in Fig 2.25(c), offers a process for the additive manufacturing of high-performance ceramics which is called Lithography-based Ceramic Manufacturing (LCM)-technology. The LCM-technology allows the production of high-performance ceramic parts with the same material properties as conventionally formed parts.

The STRATASYS CONNEX Objet260 in Fig. 2.25(d), allows the usage of wide range of material properties for its class, from rigid to flexible, transparent to opaque, neutral to vibrant, standard to bio-compatible and durable to high temperature. It is a Poly-Jet 3D printing technology and the main pros are the capability to achieve smooth surfaces, fine precision and the usage of the diverse material properties.

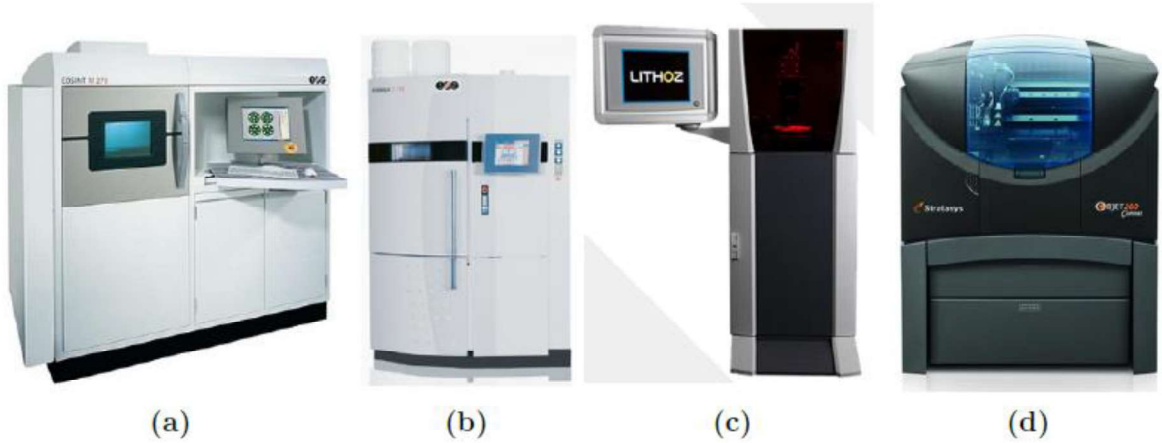

Figure 2.25: (a) DMLS for metal parts: machines EOS M270, (b) SLS for plastic parts (polyamide mainly): 2 machines EOS P100 and EOS P395, (c) LCM for technical ceramics: LITHOZ CERAFAB 8500, (d) Jetting for photosensitive resins (object technology): STRATASYS CONNEX and STRATASYS EDEN.

In Idonial, CNC milling centers are also available for traditional milling process. The CNC centers, CNC 5 axis milling center: DECKEL MAHO and CNC 5 axis micro milling center: KERN EVO are illustrated in Fig. 2.26(a, b).

Figure 2.26: (a) CNC 5 axis milling center: DECKEL MAHO, (b) CNC 5 axis micro milling center: KERN EVO.

For the purposes of the present thesis, the most appropriate machines that can be used are the EOS M270 for 3D printing and the CNC 5 axis center for milling. The first, realizes direct metal laser sintering (DMLS) and appears to be the best candidate to manufacture 3D or 2D GRIN lens antennas. The CNC machine also can be used mainly for 2D GRIN lenses. The rest 3D printing machines can be utilized to manufacture different types of lenses, however after the construction, the prototype needs to be metalized. It needs to be mentioned that the CNC 5 axis milling center, DECKEL MAHO has been selected to manufacture the prototype of the thesis by virtue of the high precision of the traditional milling technology.

2.8 Conclusions

Novel state of the art lens antennas have been highlighted in the present chapter. In the first subsection, all-metal lenses have been presented which have wide FOV and are fruitful solutions for space applications. Second subsection, has remarked novel all-metal GRIN lenses with wide FOV which are appealing candidates for constellation space missions. Third subsection has highlighted the power of TO where compact transformed lens antennas can be designed using techniques such as quasi-conformal mapping. Fifth subsection, has remarked helical single radiator antennas which provide an isoflux radiation pattern. Seventh subsection, has highlighted the sunflower antenna and similar array configurations together with the Dome lens which can be further examined in order to provide an isoflux envelope mask. Last, advanced manufacturing technologies briefly described such as, additive manufacturing and traditional milling technology.

Chapter 3 All-Metal Graded Index Gutman Lens Antennas in a PPW technology - A Design Methodology

Contents

3.1 Description of Gutman lens antenna with focal distance $f = R/2$

The Gutman lens is introduced in [11] as a modified Luneburg lens. It has the same dimensions and operating principles as the Luneburg lens, although the excitation source is moved to smaller focal circles. This, in turn, enables accommodating the feed network within

the region that would otherwise be occupied by a Luneburg lens. Consequently, the form factor of the lens with the associated feeds is reduced.

In order to calculate the required permittivity values along the surface of the lens, Hamiltonian TO have applied to the Luneburg lens based on ray tracing [11]. The corresponding distribution of the relative permittivity of the lens is provided by Eq. (3.1) where f is the focal distance, R the radius of the lens and r the spatial position from the origin.

$$\varepsilon_r = \frac{1+(f/R)^2-(r/R)^2}{(f/R)^2} \tag{3.1}$$

Based on Eq. (3.1), smaller focal distances, f (focal circles) are associated with higher permittivity values, ε_r and therefore higher values for the effective index of refraction, n_{eff}, since the latter is related to the dielectric permittivity according to $n_{eff}=\sqrt{\varepsilon_r}$. For the Luneburg lens, which is obtained at the limit $f=R$, the index distribution along the lens varies from $n_{eff}=1$ to $n_{eff}=1.4$ (see Fig. 3.1(a)). However, since smaller focal circles are selected, then the variable f in Eq. (3.1) is lower than R, unlike is the case for a Luneburg lens where $f= R$. Consequently the required index of refraction distribution is different. It is easy to notice that higher index of refraction values are required to synthesize the Gutman lens compared to a Luneburg lens. For instance, for the Gutman lens with focal circle $f=R/2$, the index values varies from $n_{eff}=1$ to $n_{eff}=2.2$ (see Fig. 3.1(b)) and with focal circle $f=R/2.85$ the index values varies from $n_{eff}=1$ to $n_{eff}=3$ (see Fig. 3.1(c)).

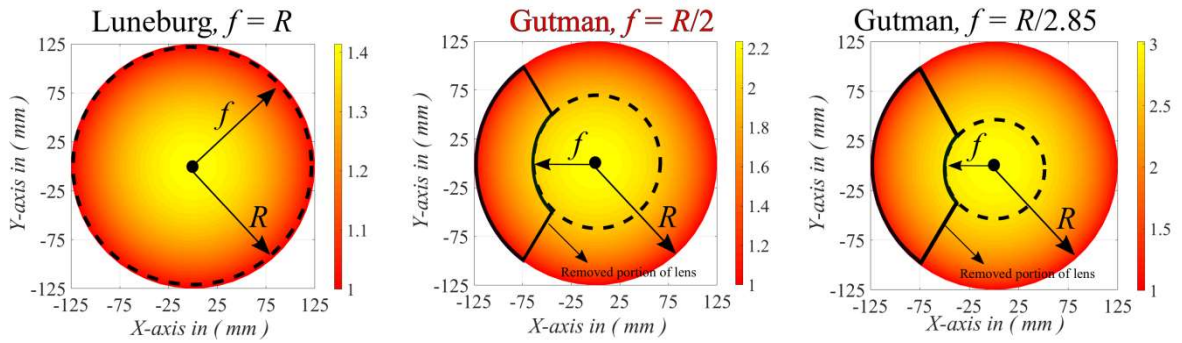

Figure 3.1: Index distribution along the total surface of the (a) Luneburg lens, (b) Gutman lens with focal distance $f=R/2$, (c) Gutman lens with focal distance $f=R/2.85$.

A comparison of the 2D index distribution between the Luneburg lens and the Gutman lens with focal distances $f=R/2$ and $f=R/2.85$ is illustrated also in the below Fig. 3.2. Both lenses call for materials that can provide relative graded index of refraction. These materials are difficult to be found in nature and their manufacturing is complex. As a consequence, artificial dielectrics have been examined to confer the appropriate indices and eventually synthesize the lenses. A main drawback of the artificial dielectrics is that for high effective index of refraction the structure has very high frequency dispersion. Besides, the Gutman lens calls for periodic structures with high effective index of refraction which have low frequency dispersion.

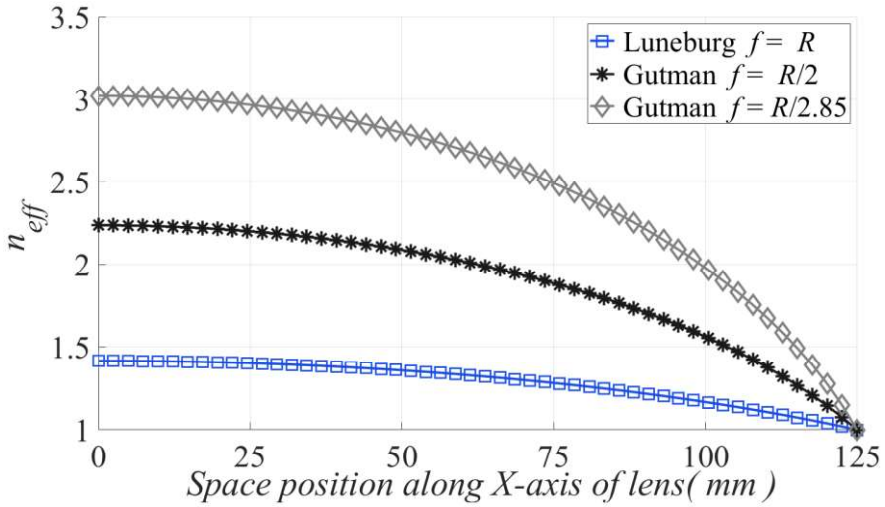

Figure 3.2: 2D effective index of refraction along axis X; Luneburg lens vs Gutman lens with focal distance f=R/2 vs Gutman lens with focal distance f=R/2.85.

3.1.1 Compact size

An asset of the Gutman lens antenna in comparison with the Luneburg lens antenna is its compact size. The smaller focal distance f is selected in the Gutman lens, the more compact size is achieved. The compactness of the Gutman is the portion that is subtracted from its surface (see Fig. 3.1(b, c)). We are obliged to extract this surface from the lens in order to settle the appropriate excitation sources along its focal arc. Based on the number of sources that we desire to integrate along the focal arc of the lens, the compactness of the Gutman lens differs compared to the Lunenburg. The bigger amount of sources that we place along its focal arc, the larger portion of the lens is removed and thus more compact size is achieved. An example is descripted in the below Fig. 3.3(a-d) for the Gutman lens with focal distance f=R/2. For a focal arc angle a= π/10, the portion that is depicted in Fig. 3.3(a) is removed and the Gutman lens with f=R/2 is 7% more compact compared to the Luneburg. Consecutively, for larger number of feeds, a largest portion of lens is subtracted when the focal arc angle equal to a= π/4 and 12% compactness is accomplished compared to the Luneburg (see Fig. 3.3(b)). Finally, for a maximal number of feeds, the largest portion is removed with a=π/2.6 and the maximum compact size that the Gutman lens with f=R/2 can reach in comparison with the Luneburg lens equal to 19% (see Fig. 3.3(c, d)).

The Gutman lens with focal circle equal to f = R/2.85 is more compact compared to the Gutman lens with focal circle equal to f=R/2 (see Fig. 3.3(d)). However, as larger portions are removed to reach this compactness, the radiation performance is degraded and it will be discussed in the further sections.

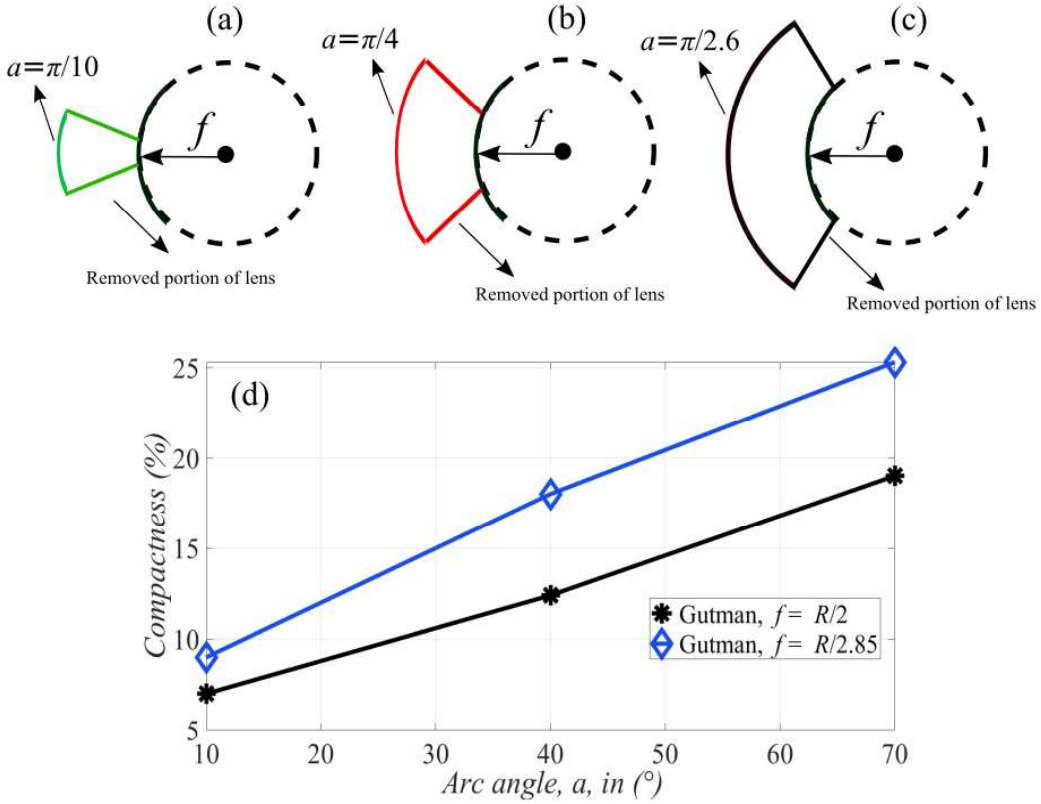

Figure 3.3: Removed portion of Gutman lens with f=R/2 when (a) a=π/10, (b) a=π/4, (c) a= π/2.6. (d) Compactness of the Gutman lens with f=R/2 and f=R/2.85 in comparison with the Luneburg lens.

3.1.2 Lens excitation

The next challenge that needs to be addressed on the Gutman lens antenna is the selection and placement of the excitation sources along its focal arc. The focal arc of Gutman lens with f=R/2 is smaller in comparison with the focal arc of Luneburg. It is thus needed to use compact feeds in a PPW technology that can be integrated along the focal arc of the Gutman. Common feeds that have been used to excite a PPW all-metal lens are traditional rectangular waveguides [79] or horn antennas [80]. However, the aperture of a WR75 standard waveguide at Ku-band is equal to 0.79 λ and its aperture is very large. For instance, in Fig. 3.4, 12 conventional WR75 waveguides are placed along the focal arc of the Luneburg lens, however the same amount of feeds cannot be placed along the focal arc of the Gutman but merely 5 feeds for the Gutman with focal circle f = R/2 and only 3 feeds for the Gutman with f = R/2.85. One of the goals of this thesis is to explore compact feeds with small apertures to integrate the maximum amount of feeds along the focal arc of the Gutman which is equal to 6.3 λ and it will be further analysed in next section.

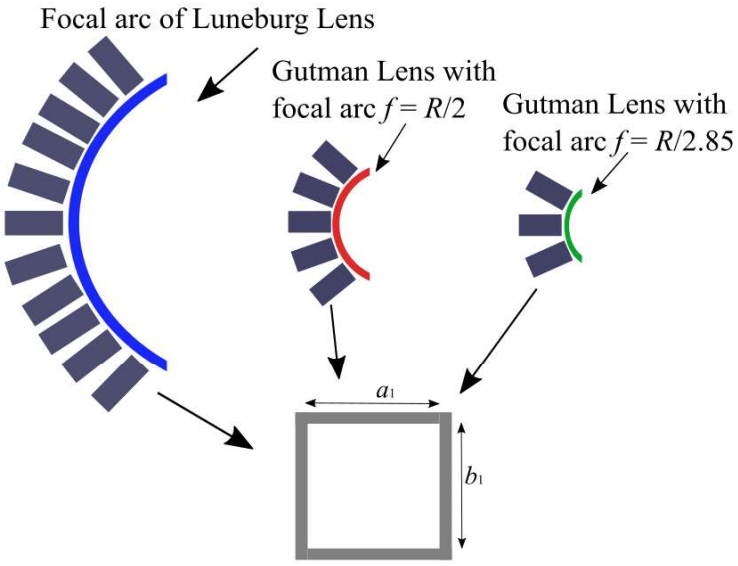

Figure 3.4: Rectangular waveguides integrated along the focal arcs of the Luneburg lens, the Gutman lens with f=R/2 and the Gutman lens with f=R/2.85.

3.1.3 Metasurface GRIN Gutman lens with f=R/2

In the present section, we employ an example of a GRIN metasurface Gutman lens with focal circle f=R/2. To synthesize the lens, modulated periodic structures comprised of metal pins in a PPW housing are utilized as depicted in Fig. 3.5(b, c). Achieving a range that covers the highest required index n_{eff}=2.2 with low dispersion is therefore requested to implement a lens with stable performance across the entire Ku-band. An interleaved unit-cell has been selected to modulate the required indices along the surface of the lens and will be extensively analysed in Subsection 3.2.1.

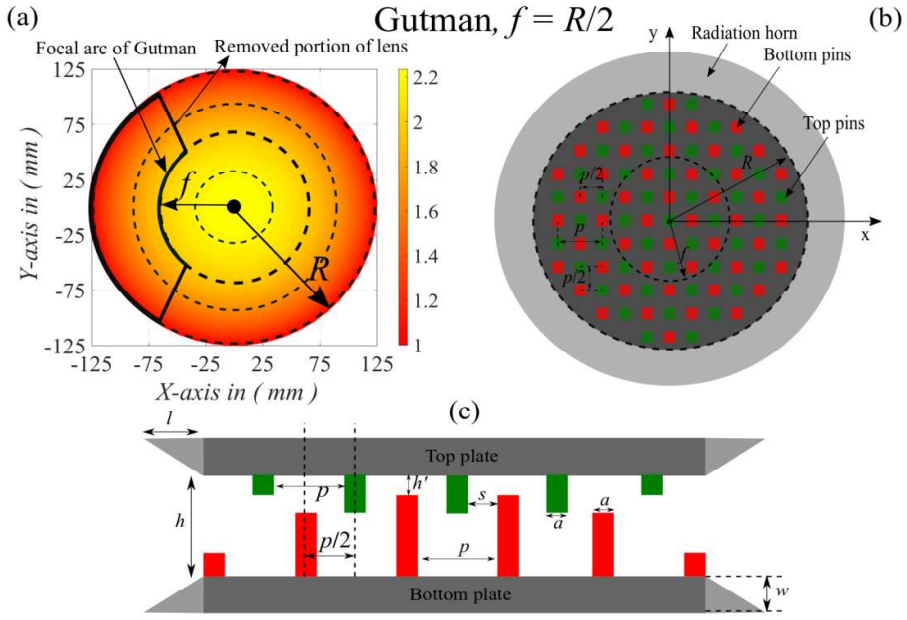

Figure 3.5: (a) Effective index of refraction n_{eff} of the Gutman lens with focal arc f=R/2. (b) PPW GRIN Gutman lens layout using an interleaved glide symmetry unit-cell (top view), (c) 2D cut view, p=2.4, a=0.8, s=0.4, h'=1.9, w=12, all dimensions in mm.

In order to provide efficient matching of the fields travelling from the feed to the edge of the lens such that they can radiate into free space, a radiation horn flare is accommodated along the periphery of the lens (see Fig. 3.5(b, c). The excitation sources along the focal arc of the lens are accommodated by virtue of removing a portion of the lens (see Fig. 3.5(a)). This allows for 19% compactness compared to the traditional Luneburg lens. Since the feeds are placed along a focal circle that is smaller than the radius of the lens R, at their interface with the lens they experience an effective index of refraction larger than unity. Consequently, impedance matching for the excitation feeds needs also to be addressed. An impedance matching methodology has been explored and it will be presented in Section 3.5.

3.2 High Index all-metal unit cells

All-metal periodic structures in a PPW technology have been extensively analysed in [81] where it is demonstrated that double-pin structures in a glide symmetry topology, and especially when interleaved, can provide artificial dielectrics with high index values and lower frequency dispersion in comparison with the single pin unit-cells. For instance, in [82] a horn lens is designed using the glide symmetry cell in gap waveguide technology where a very low dispersion is attained using the double-pin unit-cell. In [57], a Luneburg lens has been implemented using a glide symmetry unit-cell at Ka-band and resulted on a lens with a wide FOV up to 50°. A new degree of freedom (DoF) of the double pin topology glide symmetry cell consists in interleaving topology of the top and bottom pins of the PPW. This DoF leads to high index values with low dispersion and this will be further discussed in the above Subsection 3.2.1 and Subsection 3.2.2.

3.2.1 Interleaved glide symmetry unit cell

The maximum index value of the considered Gutman lens is n_{eff}=2.2 (at its center, r=0). It defines the highest value for the effective index of refraction that the artificial dielectric should provide. For operation of the lens across a wide bandwidth, low frequency dispersion of the artificial dielectric is also required. Glide symmetry double-pin all-metal structures in a PPW [53] provide favourably high effective index values with low dispersion. An interleaved glide symmetry (IGS) unit-cell is introduced here that results in maximum index values up to n_{eff}=2.2 with dispersion stability ±0.05 across the entire Ku-band.

The design of the unit-cell commence by defining the PPW height, which in Fig. 3.6(a) is noted as h. In particular, in order to avoid higher order modes, the PPW height should be selected to be less than $\lambda/2$, where λ is the free space wavelength at the highest operating frequency. Otherwise, larger values are preferred in terms of ohmic losses and manufacturing tolerances. In the example considered here we therefore define h=4 mm. We next select the dimensions of the square unit-cell, which in Fig. 3.6(a) is marked as, p. Lower values provide closer approximation to an artificial dielectric but increased ohmic losses, reduced design flexibility, as well as more demanding manufacturing tolerances. Here we select p=2.4 mm, which corresponds to $\lambda/10$ at center frequency f=12.5 GHz.

Once periodicity is introduced in the PPW housing by means of the pins, the phase velocity of the propagating mode is reduced [97], leading to an increase of the effective index of refraction. In order to calculate the effective index of refraction associated with a unit-cell, full wave electromagnetic simulations are conducted using CST microwave studio [98]. Periodic boundary conditions are applied to the unit-cell along the tangential plane with an appropriate phase shift imposed across opposing sides that corresponds to the propagation constant, β. The frequency associated with the given propagation constant is the calculated by

means of an eigenmode solution. Repeating the process for the range of propagation constants, β, along the irreducible Brillouin zone provides the dispersion curve associated with the unit-cell. Finally, the equivalent effective index n_{eff} is derived from $n_{eff}=c\beta/2\pi f$.

We next study the effective index of refraction as a function of the geometrical parameters of the unit-cell. In order to reduce the geometrical DoF, we fix the cross sectional edge of the pins to a suitable value in light of the unit-cell dimensions, here at a = 0.8 mm. With reference to Fig. 3.6(a), we then study the impact of the length, t, of the top metal post (green post in Fig. 3.6(b)) on the equivalent index of refraction. Simulated dispersion curves and extracted effective index of refraction are depicted in Fig. 3.6(c, d). The minimum height of the cell is t_{min}=0 mm and, in the absence of lower pins, this leads to a uniform parallel plate waveguide. The latter supports a pure TEM mode with dispersion coinciding with the line of light (LoL) and hence an equivalent index of refraction, n_{eff}=1. For large values of the pin height, t, that approaches the waveguide height, h, high dispersion is observed. Thus, the maximum height of the pin is selected at t=2.6 mm leading to n_{eff}=1.48, in Fig. 3.6(b).

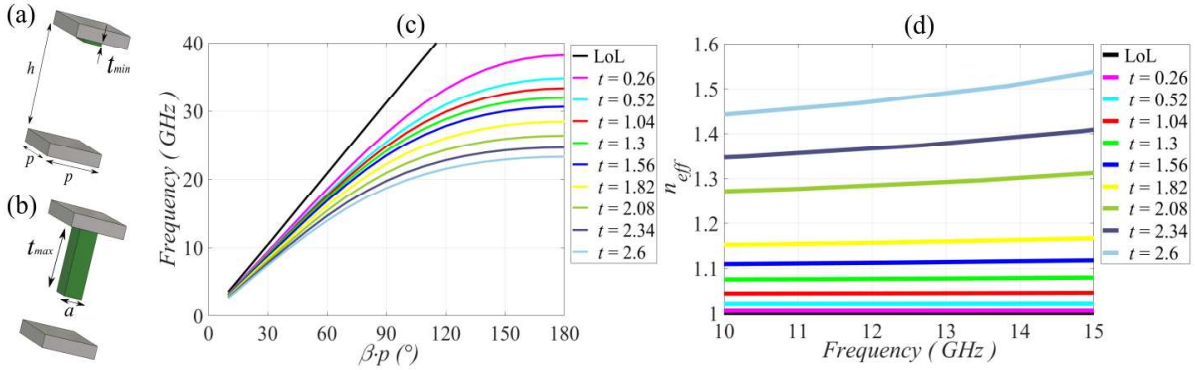

Figure 3.6: (a) LoL propagation (b) fakir unit cell - first DoF, (c) dispersion and (d) effective index of refraction values.

A supplementary degree of freedom arises from the metal posts on the bottom part of the PPW section placed in a glide symmetry position, Fig. 3.7(a) where g varies from g = 0 mm to g = 1.2 mm. Finally, the last DoF is the interleaving between the top and bottom metal posts, Fig. 3.7(b) where g varies from g=1.2 mm to g=2.09 mm. Simulated dispersion curves obtained for a fixed height of the top metal post is at t=2.6 mm and associated extracted effective index of refraction are depicted in Fig. 3.7(c, d). As shown, varying the height g of the bottom post (red posts) from g=0 mm to g=1.2 mm, leads to an increasing index of refraction up to n_{eff}=1.8. Then, from g > 1.2 mm to g=2.09 mm the metal posts of the top and bottom plate are interleaved and lead to maximum index of n_{eff}=2.2 . In conclusion, the combination of the fakir bed of nails and the interleaved glide symmetry cell lead to an index coverage from n_{eff}=1 to n_{eff}=2.2 and the unit-cell can be utilized to synthesize the Gutman lens.

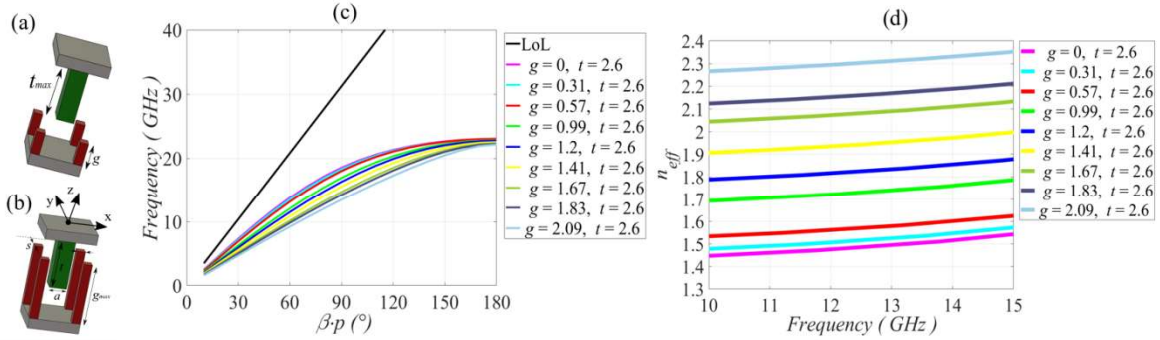

Figure 3.7: (a) Glide symmetry cell without interleaving (b) Glide symmetry cell with interleaving (c) dispersion and (d) effective index values.

3.2.2 Misalignments

A parametric study on the misalignments of the bottom and top pins is valuable to evaluate the impact of manufacturing imperfections. Here the sensitivity of the refractive index value is studied for its nominal maximum value of n_{eff}=2.2 associated with the dimensions, g=1.9 mm and t=2.6 mm. On one parametric setup, the top pin is shifted through the diagonal direction (see Fig. 3.8(a)). For the maximum shifted value of a=0.2 mm, the index increases and the dispersion of the cell slightly increases. On another parametric setup, the top pin is shifted through axis x (see Fig. 3.8(b)). On this configuration the impact of the shifting position of the cell on its index values is not significant in comparison with the diagonal shifting, except for the extreme shifting value of, t=0.2 mm.

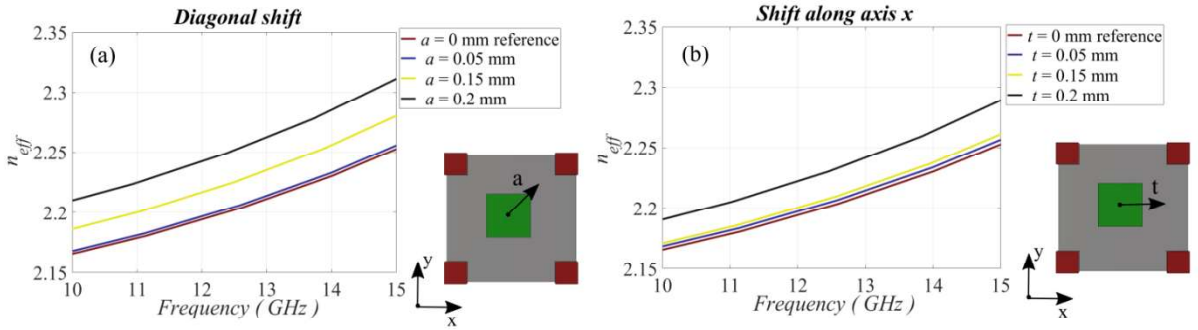

Figure 3.8: Parametric study on the misalignments of the interleaved unit-cell, (a) top pin diagonal shifting, (b) top pin shifting along axis x.

3.2.3 High index unit-cells with interleaving – A comparison

As discussed in Subsection 3.2.1, the unit-cell with interleaving pins and glide symmetry can accommodate for effective index values that reach n_{eff}=2.2 required in the Gutman lens design. In order to complete the study towards to even higher values and further confirm the choice of the selected glide symmetry cell, this section presents additional studies. In particular we study the selected unit-cell against its variant where the top and bottom pins do not interleave, as well as a unit-cell with a single pin. Results presented in Fig. 3.9(a), indicate that the refractive index value n_{eff}=1.4 of the single pin fakir unit-cell leads to high dispersion at Ku-band, while the double-pin cell with glide symmetry and no interleaving between the top and the bottom pins [53], reduces the dispersion. This is in agreement with

the conclusions of [81] where the double-pin cell in a glide symmetry topology is less dispersive compared to the single pin unit-cell.

Fig. 3.9(a) further indicates that higher values of the effective index of refraction for these unit-cells lead to high dispersion that can be impractical for lens applications. In contrast, the selected unit-cell leads to significantly lower dispersion even for higher values of the effective index of refraction. For instance, in Fig. 3.9(b) the interleaved double-pin glide symmetry cell with dimensions t=2.6 mm and g=1.8 mm shows maximum index value n_{eff}=2.2 with very low dispersion compared to the maximum value of the single pin cell. Moreover, if the height of the top and bottom pins increases (t=3.1 mm, g=3.1), a maximum value of n_{eff}=3 is reached with low dispersion.

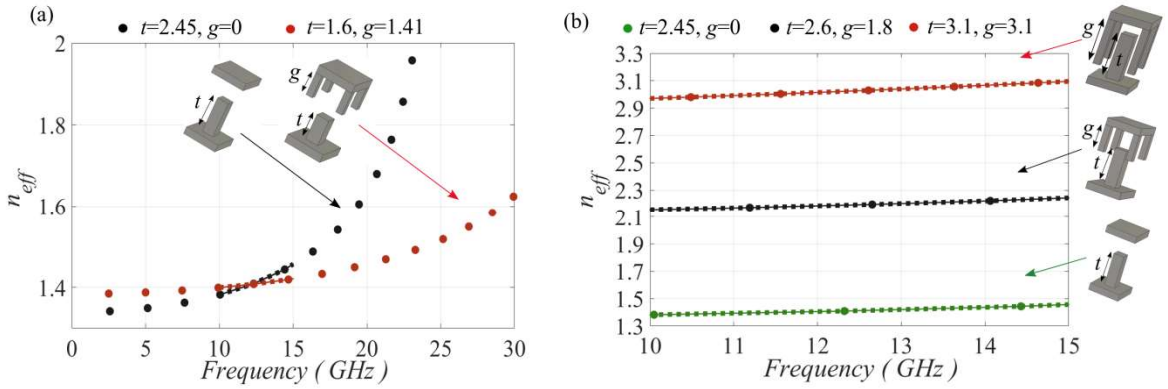

Figure 3.9: Index comparison of (a) single pin unit-cell vs glide symmetry cell without interleaving, (b) single pin unit cell vs glide symmetry cell with slight interleaving vs glide symmetry cell with maximum interleaving.

Glide symmetry unit-cells that can support interleaving topologies between metal posts can increase the effective index of refraction and on parallel have low dispersion. In the design procedure of any unit-cell the posts need to be settled strategically inside the PPW region in order to be interleaved. This interleaving DoF increases significantly the index of the unit-cell. An example of a glide symmetry unit-cell which consists of four metal posts in glide symmetry geometry is depicted in the inset 1 of Fig. 3.10(a).

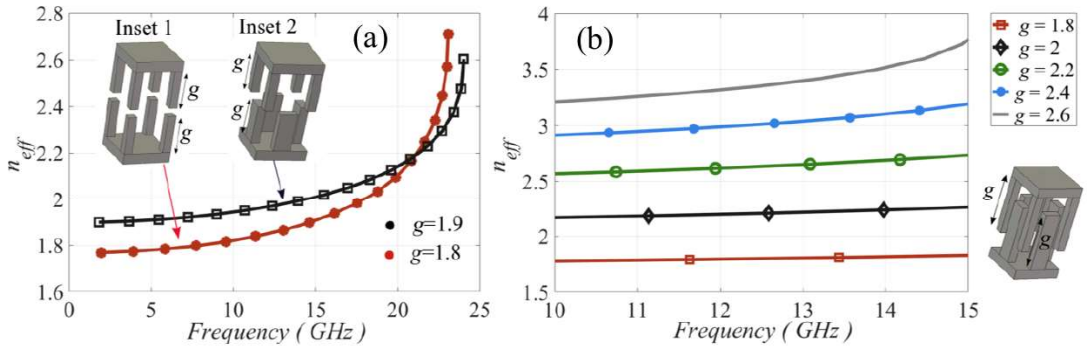

Figure 3.10: Index comparison of (a) glide symmetry unit-cell vs modified glide symmetry cell interleaving capabilities, (b) effective index of refraction of the interleaved glide symmetry unit-cell, simultaneously variation of height g.

A maximum index of refraction for the cell is up to n_{eff}=1.85 at Ku-band (see Fig. 3.10(a)). The distance, *s,* between the metal posts is equal to *s*=0.4 mm and is the smallest acceptance value for traditional manufacturing machines such as milling. The cell on the inset 2 of the Fig. 3.10(a) presents the same glide symmetry unit-cell with the difference that the bottom pins are placed strategically in order to be interleaved with the top posts. This design modification, allows the advent of the interleaving DoF and the index of refraction for the unit-cell of the inset 2 increases and has lower frequency dispersion compared to the unit-cell of the inset 1. Additionally, by varying simultaneously the height *g* of the both top and bottom posts which are always interleaved, we manage to reach even higher values of index up to n_{eff}=2.6 with low frequency dispersion. For values n_{eff}>2.6 the cell is more dispersive.

It has been proved that interleaved glide symmetry unit-cells can reach high index of refraction with low frequency dispersion. Multiple interleaved glide symmetries can be designed to reach high index values. One of the goals of this thesis was to explore unit-cells that can reach the highest indices. The result is the interleaved glide symmetry cell which has only one metal post on the bottom plate and four posts on the top plate. The proposed unit-cell is compared to the interleaved glide symmetry unit-cell with four metal posts in both top and bottom plate (see inset of Fig. 3.11) and reaches higher indices. It is shown that the interleaved unit-cell which has only one metal post on the bottom plate achieve a maximum effective index of refraction n_{eff}=3 with low frequency dispersion.

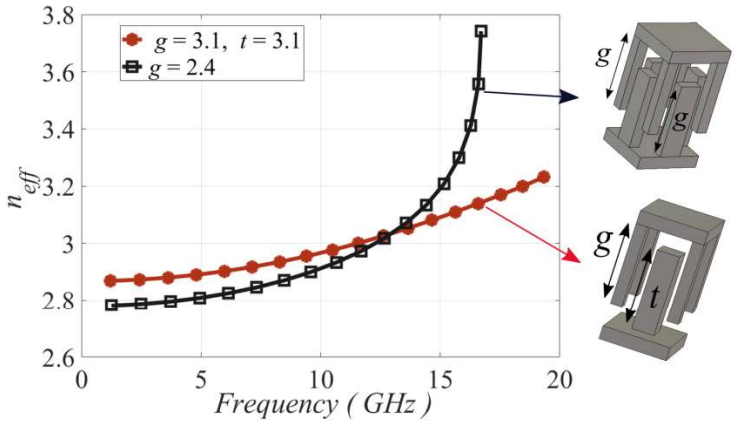

Figure 3.11: Maximum effective index of refraction comparison between the interleaved glide symmetry unit-cell with four pins on the bottom plate and the interleaved glide symmetry unit-cell with one pin on the bottom plate.

3.3 Synthesizing the lens

Following the methodology described in Subsection 3.2.1 a map of geometrical dimensions of the effective index of refraction is obtained. The next step is the definition of the geometrical dimensions to synthesize the lens. At this point, a design methodology is proposed which can be applied to every GRIN lens which has circular symmetry. The goal of the design is to place the metal posts of both top and bottom plates which represent the equivalent indices of the Gutman lens along its surface.

The first design step is the discretization of the lens and is depicted in Fig. 3.12(a). While the radius of the lens is equal to R=5.21 λ =125 mm and the periodicity of the unit-cell is p=2.4 mm, for $x \in$ A, where A={0, R} the discretization gives K=R/p=52 cells. Via exploiting the circular symmetry of the lens, the analysis of the discretization can converge upon the area A={X, Y} where X={0, R} and Y={-a/2, a/2}. Also, the design analysis can emphasized on the discretized data which correspond to n_{eff} values on the area A={X, Y} and are approximately depicted in Fig. 3.12(b). Each unit-cell represents separate n_{eff} values and K discretized values embody the positions of the cells along the surface of the lens. To mimic the required values of the effective index of refraction we use the interleaved glide symmetry unit-cell that has been presented in Subsection 3.2.1. The unit-cell has metal posts in both top and bottom PPW plates. Thus, K discretized values correspond only to the bottom metal posts and another K discretized values correspond to the top metal posts (see Fig. 3.12(b)).

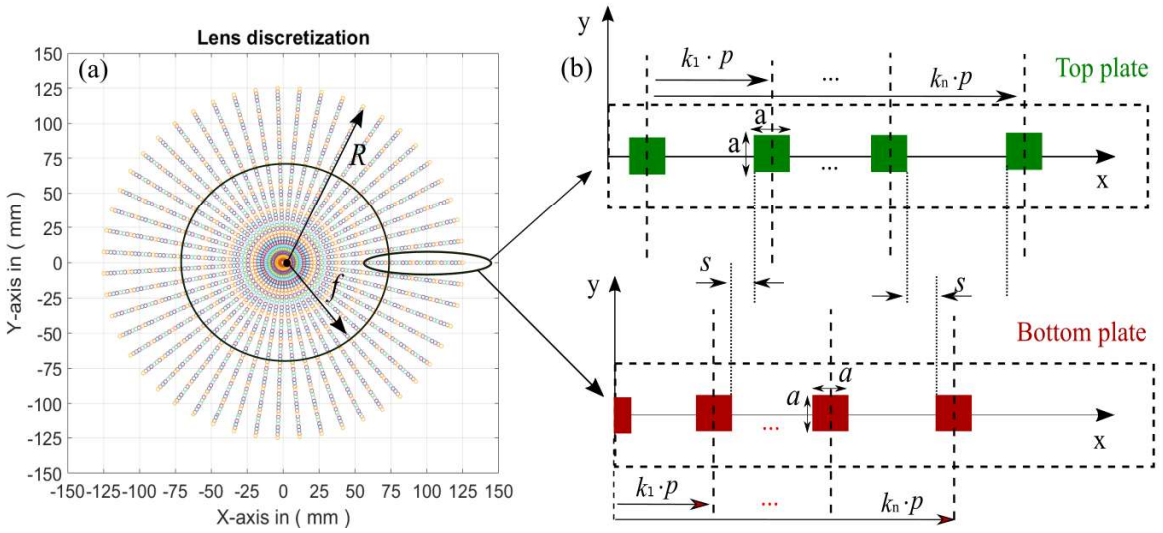

Figure 3.12: (a) Lens discretization, (b) K discretized values of the bottom and top metal posts.

The next step is to extract index values from the dispersion graphs that have been calculated and depicted in Fig. 3.6(d) and Fig. 3.7(d). For $x \in$ A based on Eq. (3.1), the index distribution of the Gutman lens is computed and depicted in Fig. 3.13(a). Based on the dispersion study of the previous section both top and bottom metal posts need to be placed on the surface of the lens to mimic the required indices of Fig. 3.13(a).

In Fig. 3.13(b) we depict a 2D layout of the lens (symmetric cut view) in order to illustrate approximately the height of the posts and the different unit-cells that are used on this circular symmetric surface of the lens. The precise position of both glide symmetry unit-cell and the fakir cell along axis x is necessary in order to define the exact heights of the posts. The latter, allows us to split the discretization into two ranges: the first for the glide symmetry index values and the second for the fakir bend of nails unit-cell.

Based on the values of the effective index of refraction of Fig. 3.7(d) and the required index values of the Gutman lens (see Fig. 3.13(a)) we find the initial and the last position of the glide symmetry cell along the symmetric axis x of Fig. 3.13(b). Thus, we define the first discretization range for the glide symmetry cell as $0 \leq \text{range}_{(\text{gli sym, cell})} \leq K_{42}$, where the value 0 corresponds to the center of the lens and the value K_{42} corresponds to the last position of the cell along the symmetric axis x of Fig. 3.13(b). These K_{42}=42 discretized data embody the

effective index range $1.48 \leq n_{eff} \leq 2.25$. Thus, 42 values of effective index of refraction have been calculated for the glide symmetry unit-cell by varying its height g and they are depicted in Fig. 3.14(a).

For the rest values of the effective index of refraction we define the second discretization range for the fakir unit-cell as $K_{43} \leq range_{(fakir\ cell)} \leq K_N$ where K_{43} is the first position of the fakir unit-cell along axis x and K_N=K_{52}=52 the last one which is on the periphery of the lens. These 10 discetized data represent the index range $1 \leq n_{eff} \leq 1.48$ and 10 values of effective index of refraction have been calculated for the fakir unit-cell by varying its height t and they are depicted in Fig. 3.14(b). As a result, the required database for the calculation of the equivalent heights of the metal posts on the surface of the lens is formed. It follows the methodology that has been adopted to calculate the height of the bottom plate metal post and their placement along the total surface of the bottom metal plate of the PPW.

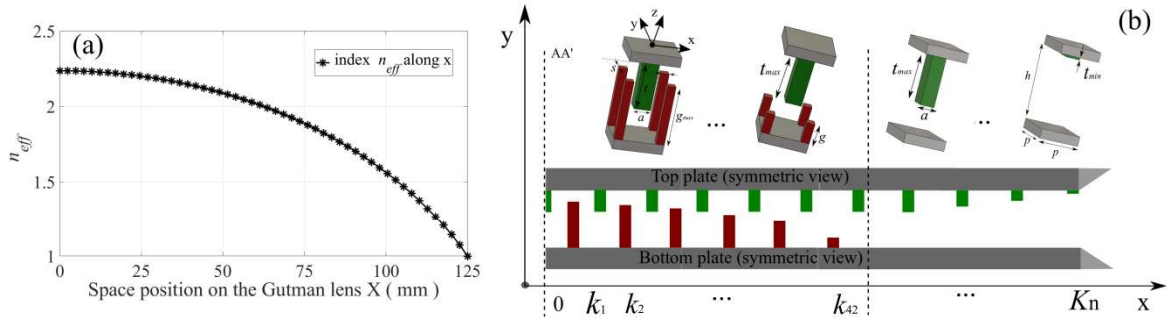

Figure 3.13: (a) Required effective index values of the Gutman lens for $x \in A$, (b) unit-cell design stages to form the required indices.

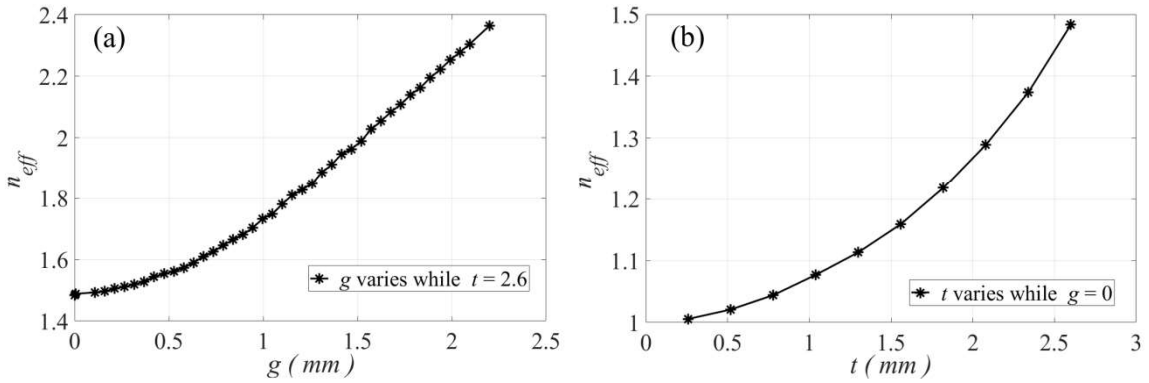

Figure 3.14: (a) Extracted index data from the dispersion of the glide symmetry cell, (b). extracted index data from the dispersion of the fakir cell.

3.3.1 Bottom metal posts height calculation

In the process of exploiting the circular symmetry of the lens, the next step is the design of a K×K matrix which corresponds to K=52 rectangular metal posts of equal heights and they are placed on the bottom metal surface of the PPW. This matrix is the quarter part of the full lens matrix surface that is depicted in Fig. 3.15(a). The values of the effective index of refraction of this matrix are depicted in Fig. 3.15(b) and its 3D view in Fig. 3.15(c). It is composed of K×K rectangular metal posts with post width a=0.8 mm, periodicity p=2.4 mm. The height of

all the posts is equal to h=2.1 mm and it is located through axis z. This is the maximum height of the metal post on the bottom part of the lens and bearing in mind the dispersion study of the previous section it will be placed on the center of the lens. The metal posts are placed on the surface of a circle which represents the bottom PPW plate and has a radius equal to R=125 mm.

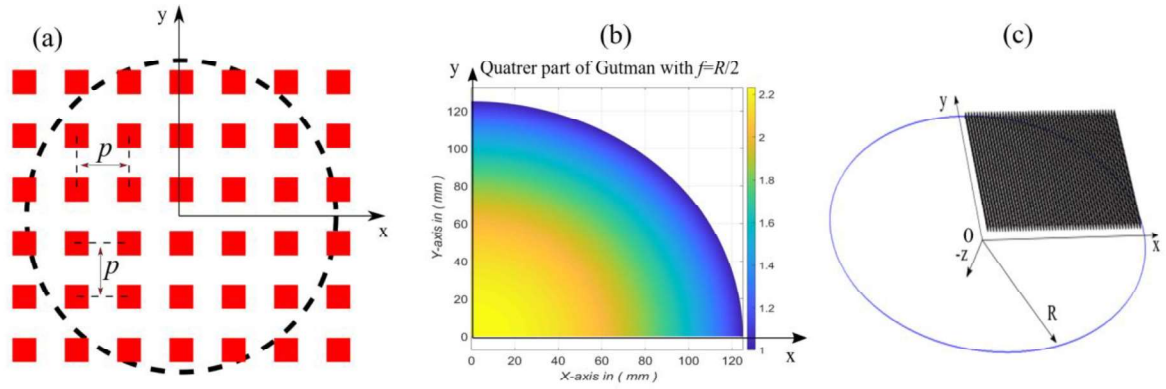

Figure 3.15: (a) $K\times K$ matrix designed for bottom metal pins with equal heights h top view (b) index distribution along its quarter symmetric surface (c) 3D $K\times K$ matrix with equal height bottom metal plates.

The following step is to calculate the required heights of the bottom metal posts that are placed on the bottom PPW metal plate (see Fig. 3.16(a)). The index values n_{eff} along the axis x of the lens for the glide symmetry unit-cell for the discretized range $0 \leq \text{range}_{(\text{gli sym cell})} \leq K_{42}$ are known (see Fig. 3.14(a)). Thus, by utilizing data extrapolation the data of Fig. 3.14(a) and Fig. 3.13(a), the bottom post heights g along the axis x of the lens are computed and are shown in Fig. 3.16(b). The rest discretized range $K_{43} \leq \text{range}_{(\text{fakir cell})} \leq K_N$ corresponds to the fakir unit-cell which consists of only a single metal post which is placed on the top plate of the PPW. Hence, the data vector is filled with zeros for the range $K_{43} \leq \text{range}_{(\text{fakir cell})} \leq K_N$, (see Fig. 3.16(b)).

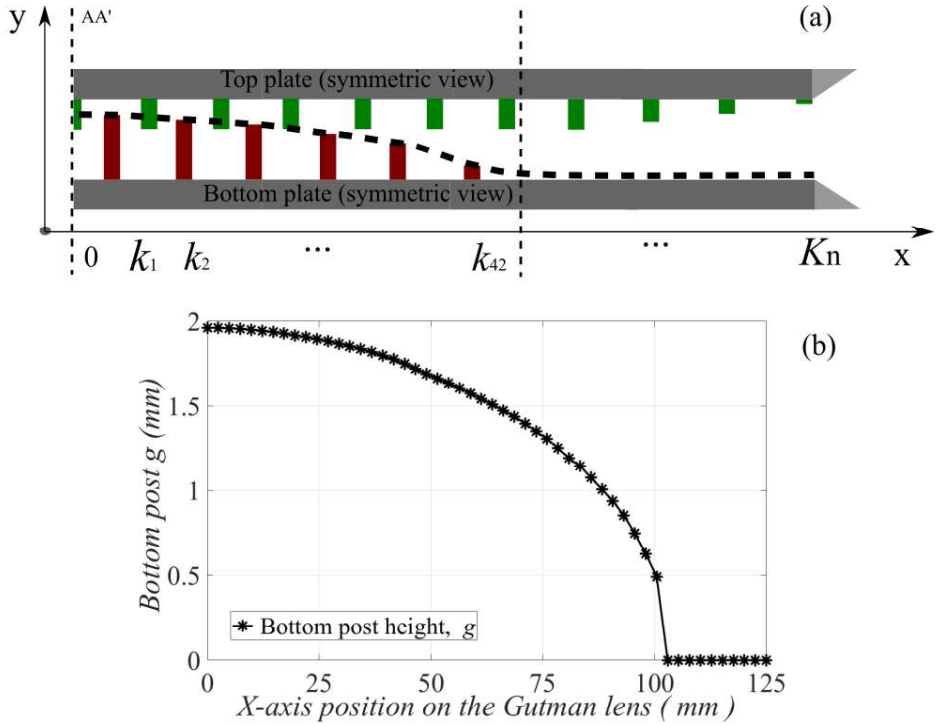

Figure 3.16: (a) Spline illustration that represents the height of the bottom plate posts. (b) Bottom metal post height g of the lens along axis x bottom plate.

Through extracting the data of Fig. 3.16(b), a 2D spline for the bottom plate pins is designed and imported to the $K\times K$ matrix that was designed with equal heights g of the bottom metal posts. For instance, in Fig. 3.17(a) the bottom plate pins with equal heights are depicted. The 2D spline with the data of Fig. 3.16(b) is imported and then was reproduced, rotated by 5° to create a surface. This surface represents the modulation of the bottom pins of the PPW. A 2D view is also depicted in Fig. 3.17(b). The elements that were out of the range of this surface were removed and the expected height of the bottom pins of Fig. 3.16(a) is reached. The final modulated metal posts are depicted in Fig. 3.17(c) where the pins are detached on the bottom circular metal plate of the PPW. The rest posts of the bottom part are added by mirroring three times the part of Fig. 3.17(c) to compose the final matrix of Fig. 3.15(a). It follows the design procedure that has been endorsed on the CST Microwave Studio to complete the design of the modulated bottom metal posts inside the PPW.

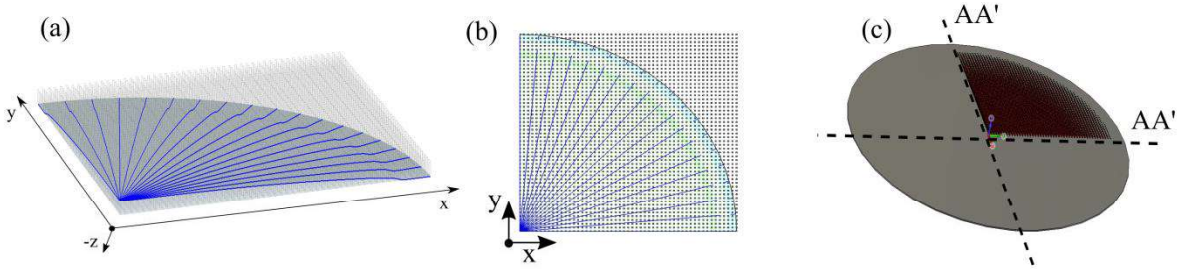

Figure 3.17: (a) 3D view of the imported splines over the $K\times K$ matrix of posts of equal heights, (b) 2D splines representation over the $K\times K$ matrix, (c) final modulated metal posts over the bottom metal plate of the PPW.

CST design scheme

The initial design step is the design of the bottom plate of the PPW with radius R=5.21λ that is depicted in Fig. 3.18(a); a 2D view is illustrated also in Fig; 3.18(b). Next, the K×K matrix of metal posts with equal heights has been designed (see Fig. 3.18(c)) and then the 2D spline has been imported and re-produced rotated by 5° to form the modulated surface (see Fig. 3.18(d)). Afterwards, the metal posts that are out of the range of the modulated surface have been extruded and the remained posts represent the ultimate modulated bottom metal posts of the quarter part of the lens. These posts have been placed on the bottom metal plate of the PPW (see Fig. 3.18(e)); a zoom image of it is shown in Fig. 3.18(f). Finally, the quarter part of the metal posts has been mirrored three times through the rest surface of the lens (see Fig. 3.18(g) and Fig. 3.18(h)) and the design has been completed.

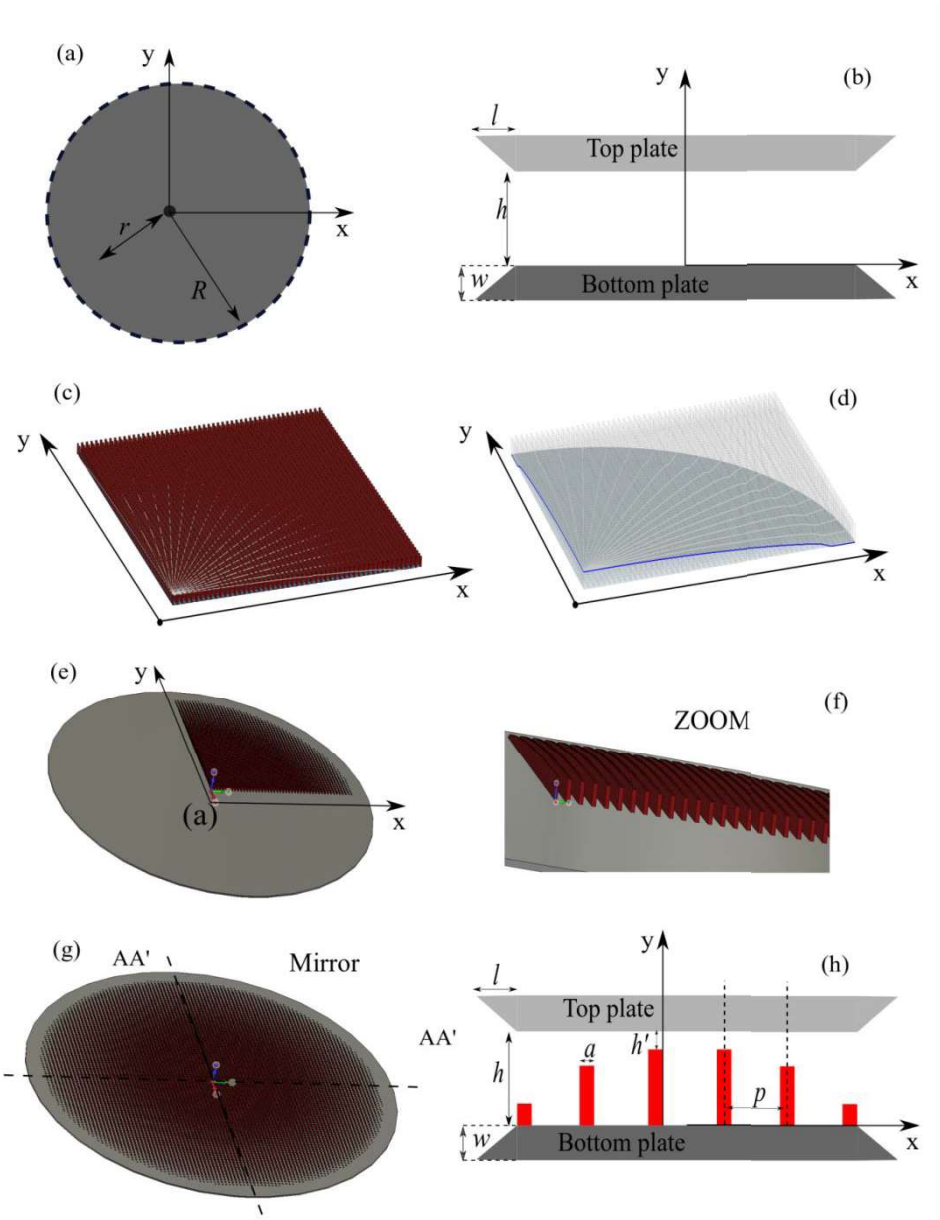

Figure 3.18: (a) Bottom PPW metal plate, (b) 2D view of PPW illustrating the bottom plate, (c) K×K matrix with equal heights, (d) spline representation imported to the K×K matrix, (e) modulated pins

placed on the quarter part of the bottom PPW, (f) zoom image, (g) modulated pins placed on the total surface of the bottom PPW, (h) 2D view.

To assimilate in depth the design methodology for the height calculation of the bottom metal posts we classify the steps adopted as follows:

- Compute the required index effective index of refraction distribution along the total surface of the Gutman lens with focal distance $f=R/2$.
- Compute the effective index of refraction of the proposed interleaved glide symmetry unit-cell and detect the maximum acceptance index value with low dispersion of the Gutman lens.
- Discretize the lens based on the periodicity of the selected unit-cell.
- Detect the positions inside the PPW of the unit-cells along the symmetric axis x of the Gutman lens based on the required index distribution of the lens.
- Map the positions of the unit-cell to the discretized values.
- Apply K (discretization) simulation to compute the effective index of refraction of the unit-cell for these K discretized positions.
- Calculate the bottom pin height along the symmetric axis x by extrapolating the required indices of the Gutman lens with the K computed indices of the unit-cell and its height.
- Design a 2D spline with the height of the bottom pins.
- Design a $K\times K$ matrix with rectangular metal post with equal heights (bottom posts) on CST Microwave Studio.
- Import to CST the 2D spline to modulate the metal posts.
- Mirror the modulated $K\times K$ matrix four times to complete the design of the modulated bottom metal posts.
- Apply the same methodology for the top metal posts.

3.3.2 Top metal posts height calculation

The technique that has been utilized for the height calculation of the top metal posts is identical to the methodology that has been presented in Subsection 3.3.1. However, slight differences are distinguished and they will be highlighted in this section.

The crucial factor that needs to be addressed is the computation of the 2D spline (see Fig. 3.19(a)) for the top metal posts. Based on the discretization values we need to form a 2D spline that is a vector of K=52 data points. From Subsection 3.3.1 we have distinguished two discretized ranges. The primary discretized range encloses the region $0\leq \text{range}_{(\text{gli sym cell})}\leq K_{42}$. At this range, the required values of the index of refraction are $1.48 \leq n_{eff} \leq 2.25$. In order to provide these high index values the glide symmetry unit-cell is in charge of it by varying only the bottom post of the cell. Since the top metal post of the glide symmetry unit-cell remains constant and equal to t=2.6 mm, we define the initial 42 data values of the spline vector to be equal to t (see Fig. 3.19(a, b)). For the range $K_{43}\leq \text{range}_{(\text{fakir cell})}\leq K_N$ we have proved that the fakir unit-cell will provide the required values of effective index of refraction which are $1 \leq n_{eff} \leq 1.48$. Finally, the heights of the top metal posts (fakir unit-cell) have been calculated by extrapolating the data of Fig. 3.13(a) which cover only the range $K_{43}\leq \text{range}_{(\text{fakir cell})}\leq K_N$ and the data of Fig. 3.14(b). Therefore, the last 10 values are added to the 2D spline vector and the final 2D spline has been formed and depicted in Fig. 3.19(b).

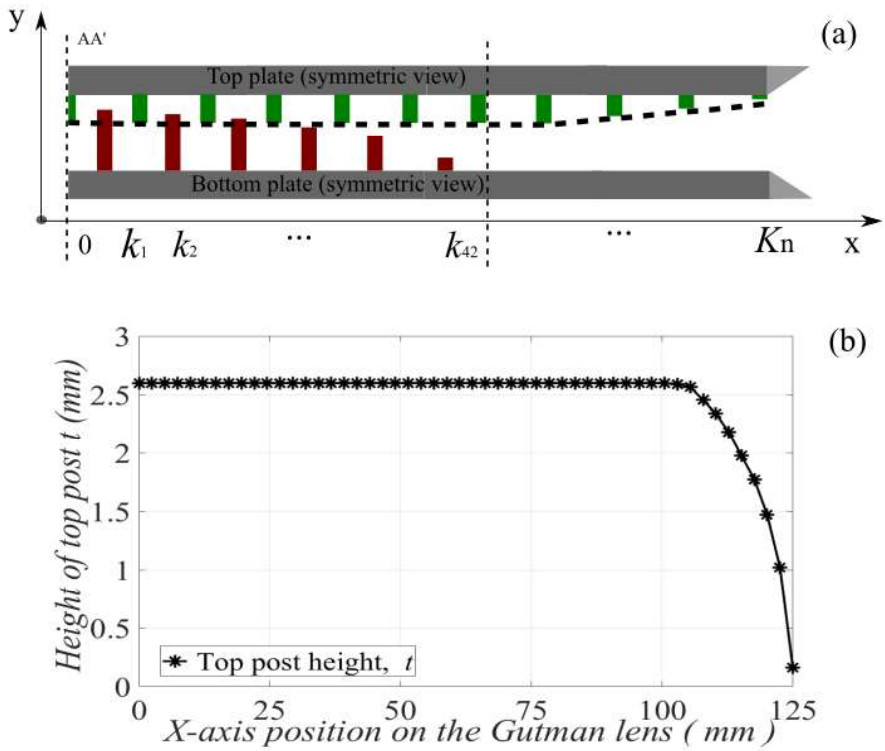

Figure 3.19: (a) Spline illustration that represent the height of the bottom plate posts. (b) Bottom metal post height *g* of the lens along axis x bottom plate.

3.4 Radiation Performance

3.4.1 Effect of cut surfaces on radiation patterns

The main advantage of the Gutman lens is the accommodation of the feeds inside the lens which leads to a more compact size lens. This is achieved by removing a part of the original lens. As larger part of the original lens is subtracted, more compact size and wider FOV is achieved. However, as larger parts are removed, the performance of the radiation patterns is degraded. This is next demonstrated by studying the radiation patterns as progressively part of lens is extracted. Three segregate electromagnetic simulations are actualized using CST Microwave Studio in order to test the broadside patterns at Ku-band while 3 disparate portions of surfaces are detached from the lens. In Fig. 3.20(a) a small portion of 7 % is subtracted with arc angle on the periphery of the lens equal to $a=\pi/10$. In Fig. 3.20(b) a larger portion of 12.4 % is subtracted with arc angle on the periphery of the lens equal to $a=\pi/4$ and in Fig. 3.20(c) the largest portion of 19 % is subtracted with arc angle on the periphery of the lens equal to $a=\pi/2.6$. In Fig. 3.21(a-c) the E-field is depicted for the broadside beam at center frequency f=12.5 GHz for these three distinguished cases.

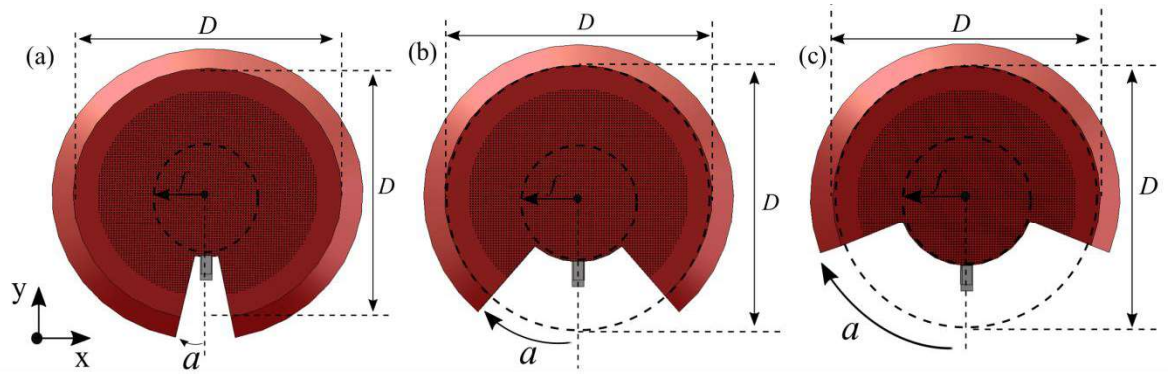

Figure 3.20: Broadside beam representation with focal angle (a) $a=\pi/\mathbf{10}$, (b) $a=\pi/\mathbf{4}$, (c) $a=\pi/\mathbf{2.6}$.

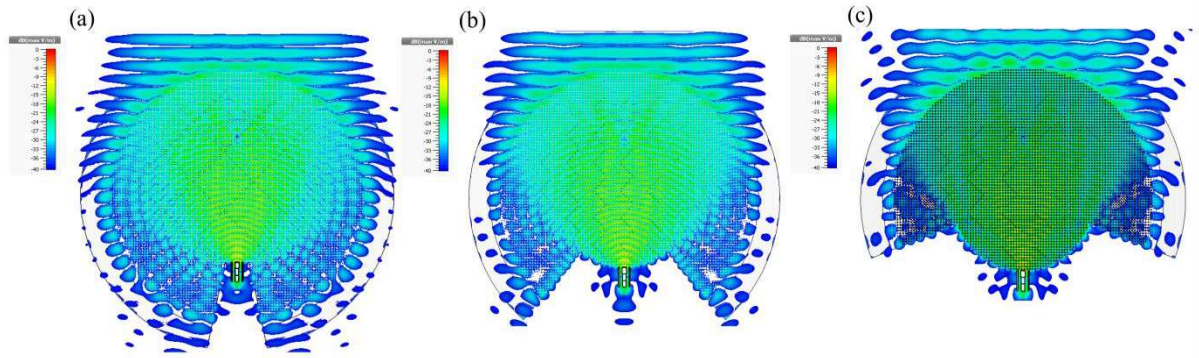

Figure 3.21: E-field at center frequency f=12.5 GHz for the broadside beam with focal angle (a) $a=\pi/\mathbf{10}$, (b) $a=\pi/4$, (c) $a=\pi/2.6$.

For $a=\pi/10$ and $a=\pi/4$ the spherical wave input of the excitation source has been auspiciously transformed into a plane wave which has a uniform distribution. For $a=\pi/2.6$ the plane wave has aberrations as long as the highest portion of the lens has been ejected. The corresponding radiation patterns are depicted in Fig. 3.22(a-c) for the broadside beam for these three cases and it is noticed that for $a=\pi/2.6$ the SLL increases. Considering the performance across the entire Ku-band, higher arc angles brings about higher SLL. However, for the broadside beam, the SLL level is under -15 dB for the edge frequency points, in addition to the center frequency which is an acceptable value.

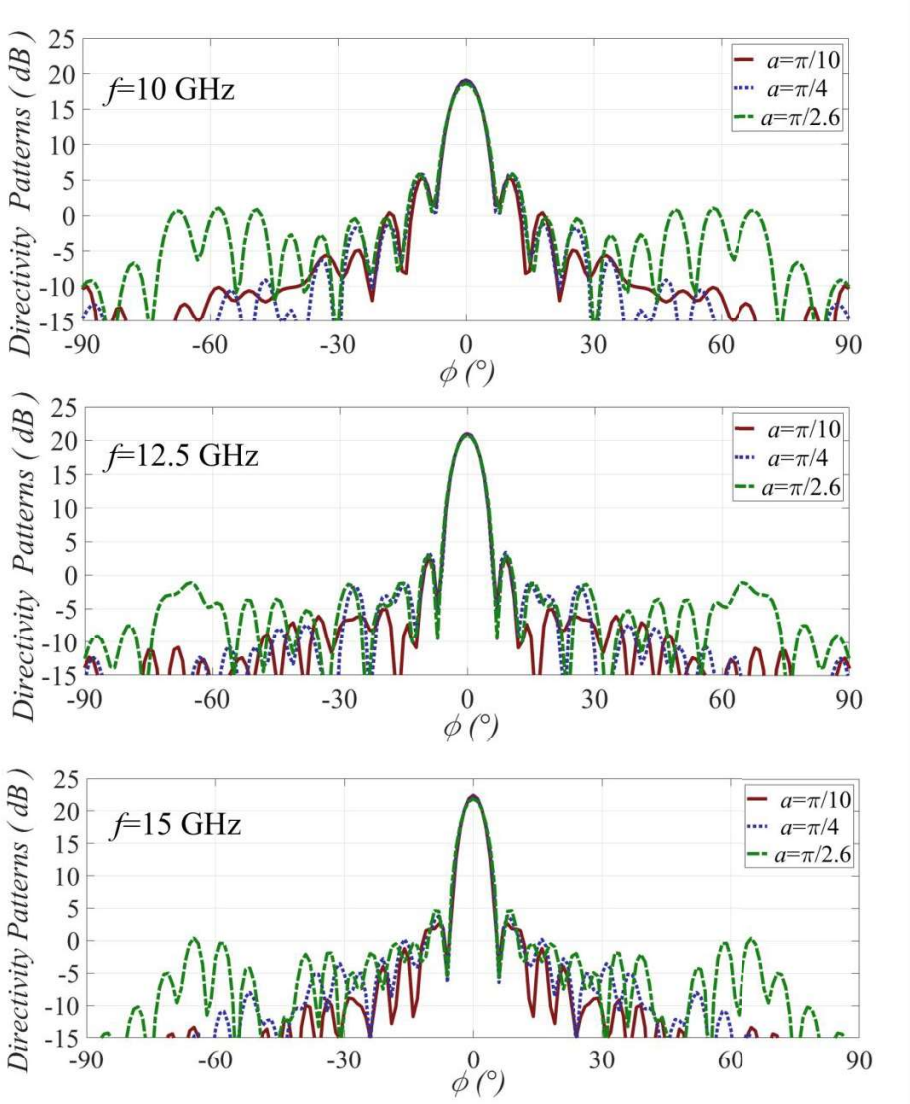

Figure 3.22: Radiation patterns for broadside beam of Fig. 3.20(a-c) in Ku-band (a) f=10 GHz (b) f =12.5 GHz (c) f=15 GHz.

The same simulation procedure has been followed to evaluate the leverage of the ejected surface of the lens on the patterns for one of the extreme offset beams at -58°. The feed is placed at -60° and three distinctive electromagnetic simulations are realized for $a=\pi/10$, $a=\pi/4$ and $a=\pi/2.6$ (see Fig. 3.23(a-c)). The most crucial scenario in these simulations is the case where the highest fragment of lens has been removed (see Fig. 3.23(c)). Since, the feed indicates to the pointing angle at -58° the exploitation of the lens surface is confined by virtue of the large extracted surface. The question that is emerged lies on the acceptable extracted lens surface that can be considered. It is unambiguous that extreme pointing angles demand for extreme feed settlement on the focal arc of the lens and consequently large fragment of lens. The impact of these extracted surface of the lens on the E-field of the lens is depicted in Fig. 3.24(a-c). We notice that larger extracted surface of the lens induce high level of SLL. This is evident on the radiation patterns that are depicted in Fig. 3.25(a-c) in selected frequencies at Ku-band. Furthermore, since less surface of the lens is exploited, directivity drops for high frequencies.

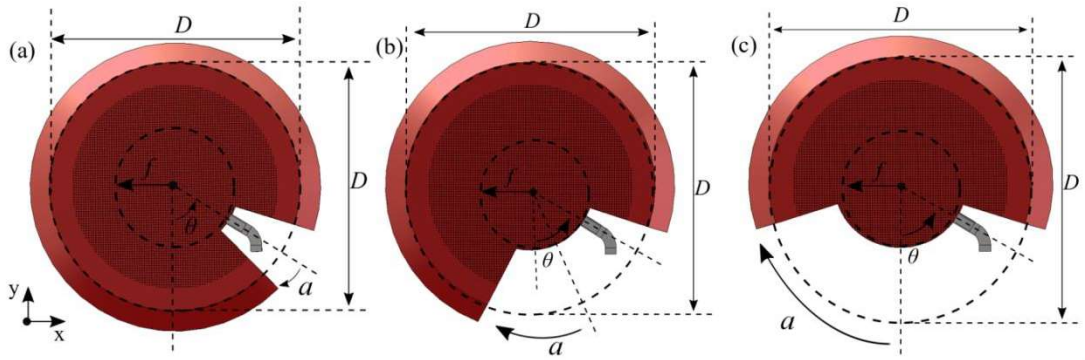

Figure 3.23: -58° scan beam representation with focal angle (a) $a=\pi/\mathbf{10}$, (b) $a=\pi/\mathbf{4}$, (c) $a=\pi/\mathbf{2.6}$.

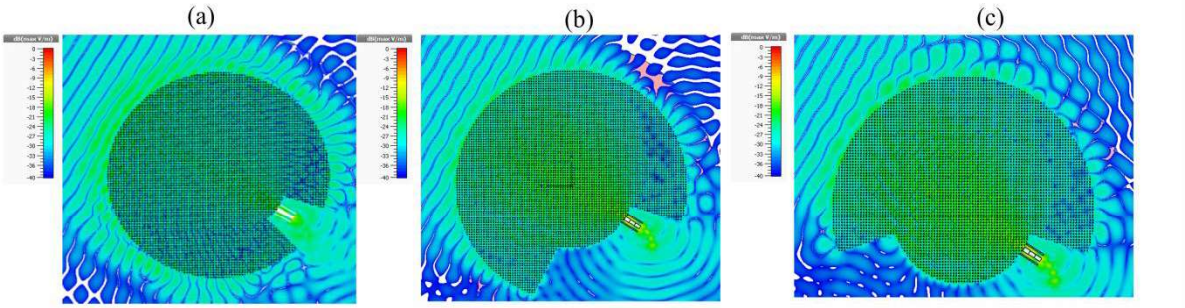

Figure 3.24: E-field at center frequency f=12.5 GHz for -58° scan beam with focal angle (a) $a=\pi/\mathbf{10}$, (b) $a=\pi/4$, (c) $a=\pi/\mathbf{2.6}$.

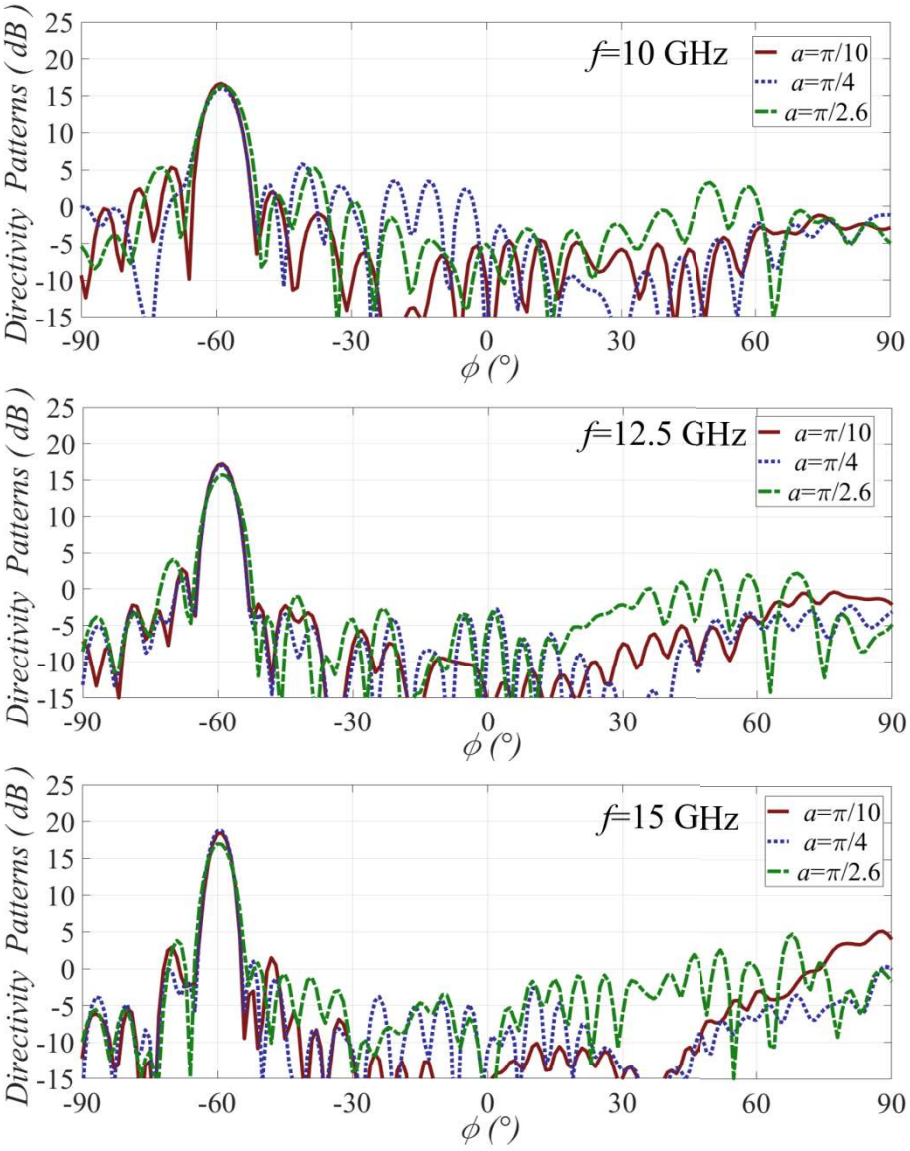

Figure 3.25: Radiation patterns for the -58° scan beam of Fig. 16(a) - Fig. 16(c) in Ku-band (a) *f*=10 GHz (b) *f*=12.5 GHz (c) *f*=15 GHz.

3.4.2 Lens radiation performance for individual scenarios

In this section we examine the radiation performance of the Gutman lens for three distinct scenarios. In the foremost case, the antenna is used as a single beam radiator (see Fig. 3.26(a)). In this scenario, only a tiny surface part of the lens has been removed to integrate the sole feed to excite the lens. This configuration embodies an ideal scheme since the excitation source exploits nearly the whole surface of the lens. The latter, renders the lens an excellent candidate for applications where merely a single beam is required.

The second scenario for the Gutman lens is the reconfigurable case and is depicted in Fig. 3.26(b). In this case the proposed excitation source is placed on the focal arc of the lens and it can be rotated using a proposed motor system. In this frame, a large surface of the lens has been extracted in order to allow the rotation of the feed into extreme pointing angles.

The last scenario is the fixed multi-beam configuration (see Fig. 3.26(c)) and is of great interest in the present thesis since the final demonstrator consists of multiple feeds along the focal arc of the lens. In this scenario, multiple feeds are settled in fixed positions and are excited separately.

A comparison between these three individual scenarios follows. The goal is to discern the impact of the extracted surface on the radiation performance of the Gutman lens when the sole feed is excited and points on the broadside direction.

(1) Broadside beam

We first begin placing the feed on the broadside orientation for both cases (see Fig. 3.26(a-c)) and in Fig. 3.27(a-c) the E-field is depicted. In Fig. 3.27(a) we notice that the output plane wave that has been formed on the periphery of the lens is uniform. Although, it is not the case for the reconfigurable example in Fig. 3.27(b) where the plane wave has aberrations by virtue of the broad extracted surface part of the lens. Once all feed placed along the focal arc of the lens (see Fig. 3.27(c)), the plane wave has slightly less aberrations compared to the configurable case. With respect to the radiation patterns that are depicted in Fig. 3.28(a-c) we observe nearly similar performance except for the reconfigurable scenario where the blank region of air around the focal arc of the lens induce a tiny increase level of SLL.

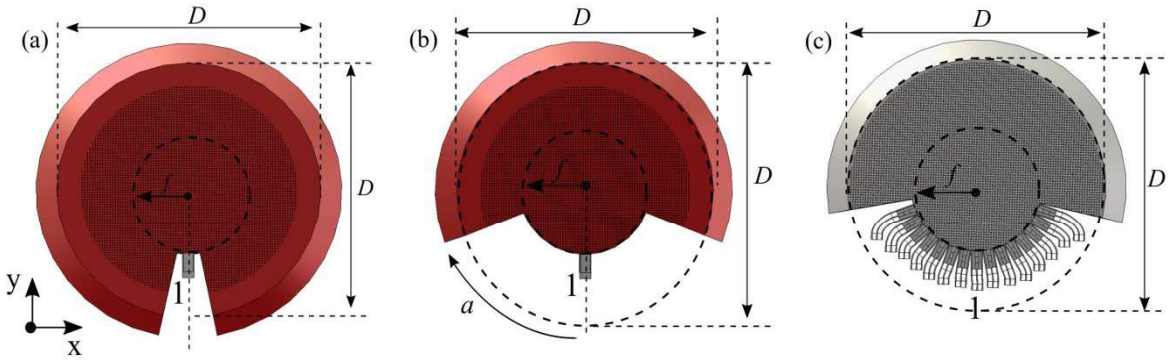

Figure 3.26: Single feed port 1 excitation (broadside beam) when (a) single feed is placed; lens surface with focal arc, $a=\pi/\mathbf{10}$ is extracted, (b) single feed is placed; lens surface with focal arc, $a=\pi/\mathbf{2.6}$ is extracted, (c) all feeds placed.

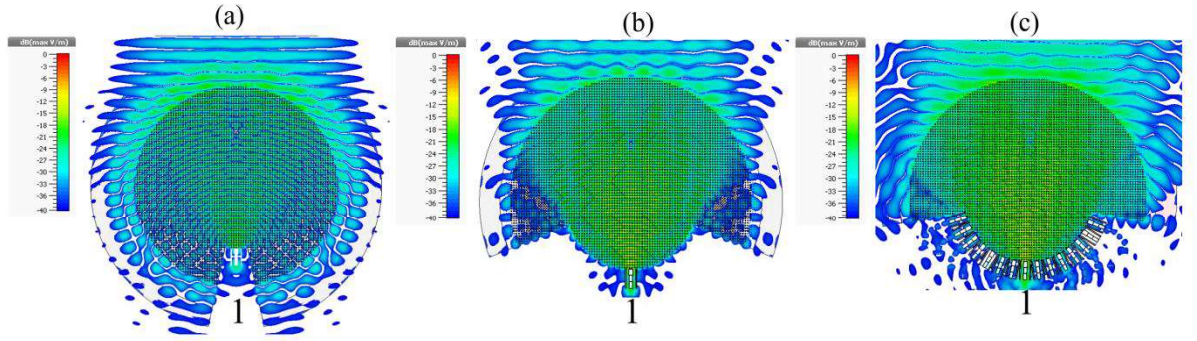

Figure 3.27: E-field illustration for the cases of Fig. 3.26 at center frequency f=12.5 GHz.

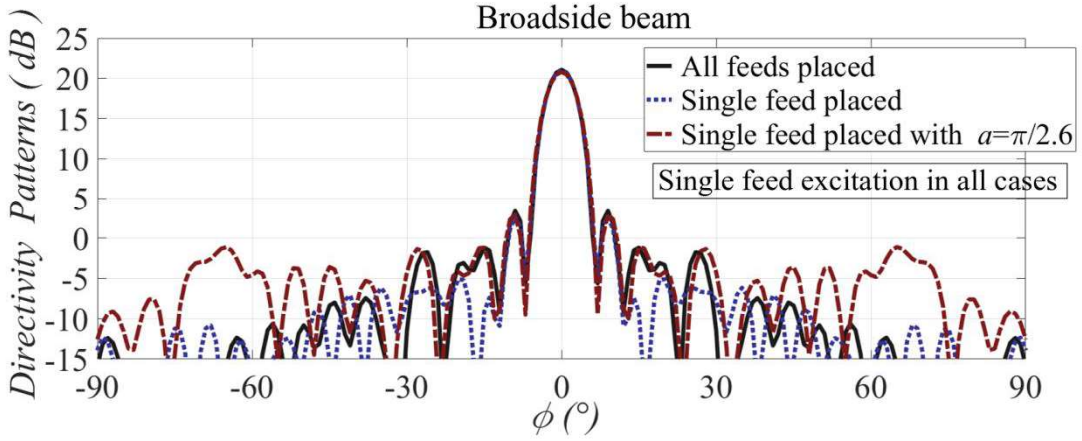

Figure 3.28: Directivity patterns comparison for the cases of Fig. 3.26 at center frequency f=12.5 GHz.

(2) Offset beam -37°

The next step is to designate the scan performance of the lens. In order to attain this objective we excite solely the feed port 2 which is oriented at -40°. Once again, we repeat three segregate electromagnetic simulations for the three individual scenarios that are examined, although the feed port 2 is excited (see Fig. 3.29(a-c)); the E-fields are depicted in Fig. 3.30(a-c). As denoted in Fig. 3.29(b), 12% of the lens has been subtracted and allows a scan range up to ±40°, since the extreme offset source is located at 40°. In Fig. 3.29(c) we likewise excite the feed port 2, although 19% of the lens has been extracted as long as we aim to evaluate the beam performance when all the rest feeds are placed along the focal arc of the lens. For the single beam radiation case, as well as the reconfigurable case, excellent performance has been accomplished (see Fig. 3.31(a, b)) with high directive beams and worst value of SLL at -15 dB. Concerning the multi-beam configuration we observe scant degradation to the directivity up to 1 dB along with meagre decrease on the SLL level on the region that is out of the main beam radiation range.

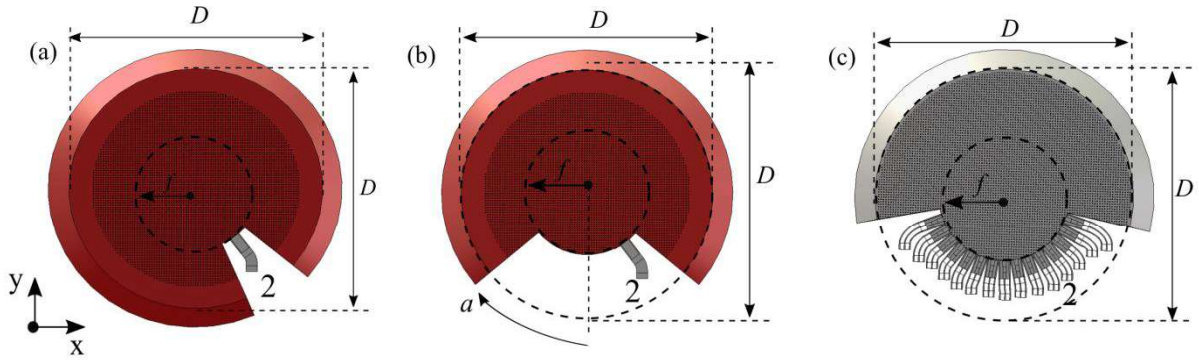

Figure 3.29: Single feed port 2 excitation (-37° offset beam) when (a) single feed is placed; lens surface with focal arc, $a=\pi/\mathbf{10}$ is extracted, (b) single feed is placed; lens surface with focal arc, $a=\pi/\mathbf{2.6}$ is extracted, (c) all feeds placed.

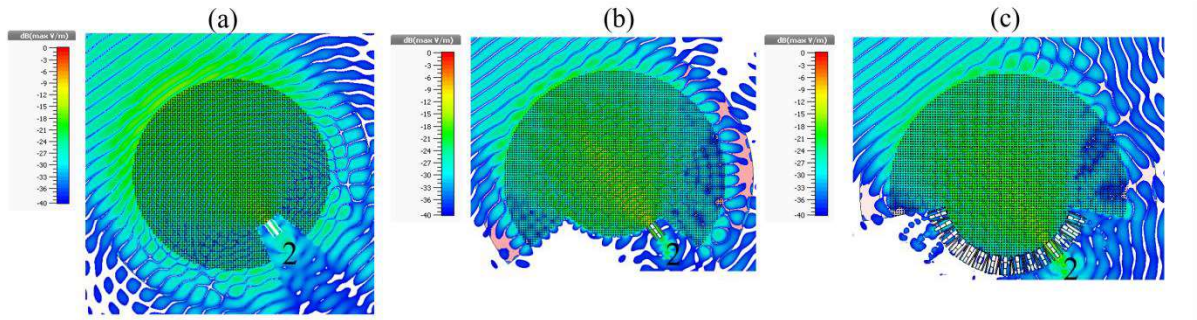

Figure 3.30: E-field illustration for the cases of Fig. 3.29 at center frequency f=12.5 GHz.

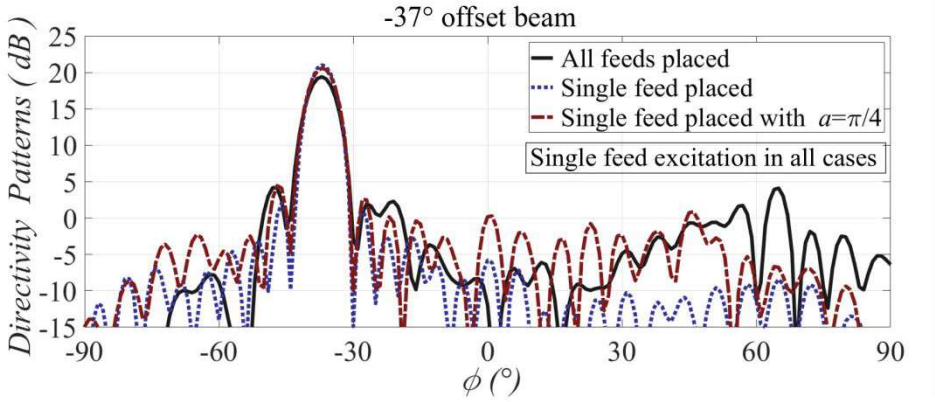

Figure 3.31: Directivity patterns comparison for the cases of Fig. 3.29 at center frequency f=12.5 GHz.

(3) Offset beam -60°

The last step is to clarify the FOV of the Gutman lens. In both three scenarios that we study 19% of the lens has been removed as depicted in Fig. 3.32(b, c) except for the case of the single beam radiator in Fig. 3.32(a). This amount of the extracted surface allows a maximum angle of the feed placement at 60°. It is apparent that this large extracted surface will redound the performance of the extreme radiated beam. The latter is evident in the illustration of the E-fields that are depicted in Fig. 3.33(a-c). It must be pointed out that the placement of all feed in the multi-beam scenario induce higher level of SLL compared to the configurable case, however their directivity values are similar (see Fig. 3.34).

To conclude, larger extracted surface of the lens induces higher SLL level, although the directivity remains constant. Additionally, the placement of all the feeds along the focal arc of the lens affect the SLL level but mainly reduce the directivity of the radiated beam.

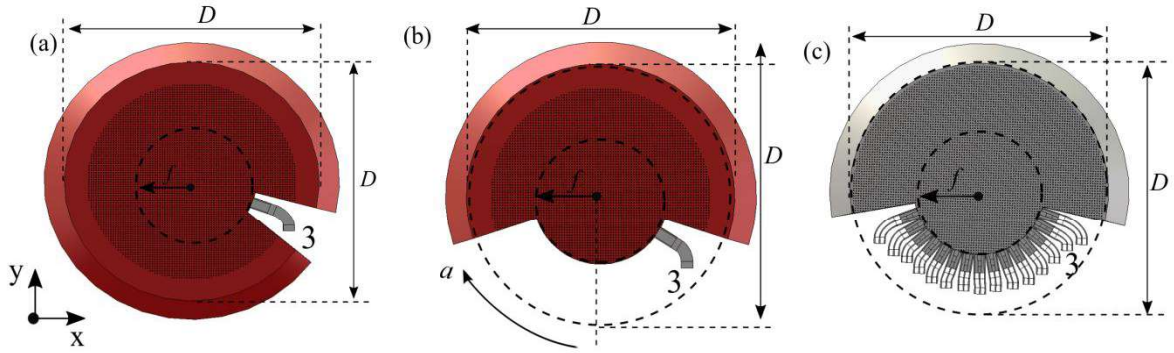

Figure 3.32: Single feed port 3 excitation (-58° offset beam) when (a) single feed is placed; lens surface with focal arc, $a=\pi/\mathbf{10}$ is extracted, (b) single feed is placed; lens surface with focal arc, $a=\pi/\mathbf{2.6}$ is extracted, (c) all feeds placed.

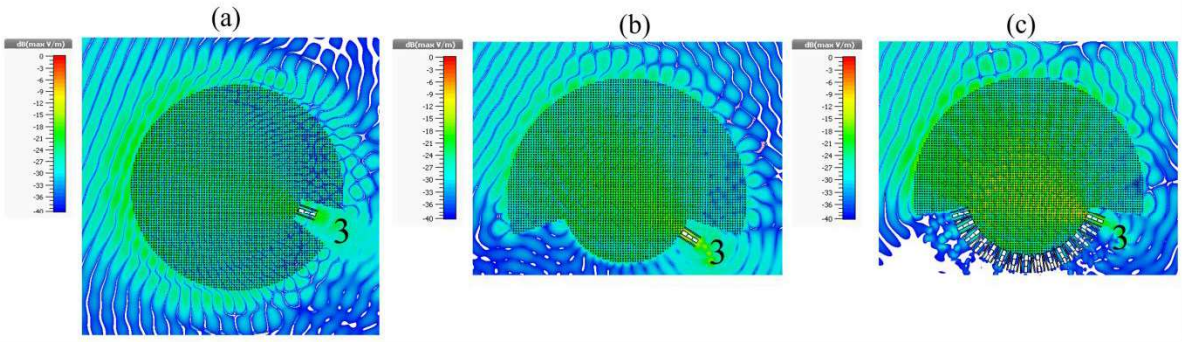

Figure 3.33: E-field illustration for the cases of Fig. 3.32 at center frequency f=12.5 GHz.

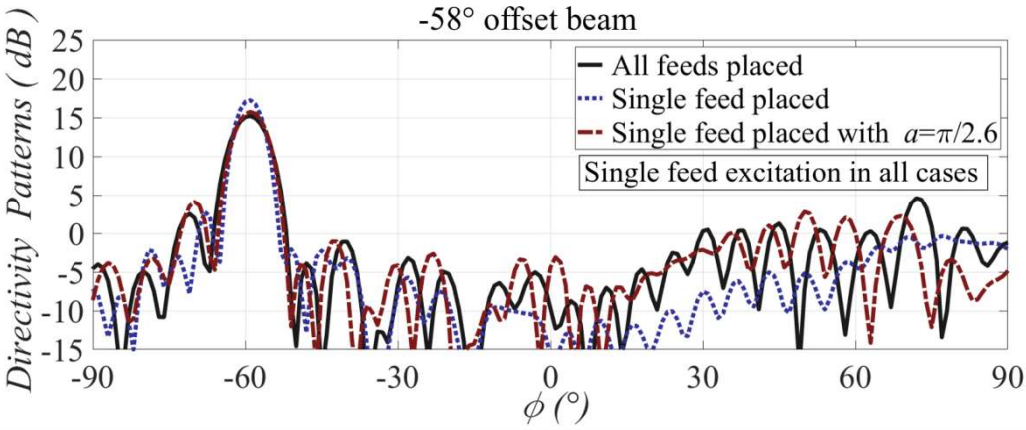

Figure 3.34: Directivity patterns comparison for the cases of Fig. 3.32 at center frequency f=12.5 GHz.

3.5 Compact feeds

The final purpose of this design is the implementation of a fixed multi-beam antenna system. High number of radiated beams, increases the capacity of the system and the available bandwidth can be re-used. However, as it has been mentioned in previous sections, the selection of smaller focal distance on the Gutman lens, leads to smaller focal arcs and the available space along the focal arc of the lens is restricted. Therefore, compact feeds in a

PPW technology that can be integrated along the small focal arc of the Gutman lens need to be examined. Common feeds used to excite a PPW all-metal lenses are traditional rectangular waveguides [79] or horn antennas [80]. However, the aperture of a WR75 standard waveguide at Ku-band is equal to 0.79λ and is very large. One of the goals of this study is to explore compact feeds with small apertures to integrate the maximum amount of them along the focal arc of the Gutman which is equal to 6.3λ.

The proposed solution, is the single ridge waveguide [85] that is depicted in Fig. 3.35(a, b). The compact size of the single ridge waveguide is based on the integration of a metal part inside a rectangular waveguide which drops the cut-off frequency of the fundamental propagating mode TE_{10}. The latter, leads on wider bandwidth and a more constant characteristic impedance. The single ridge waveguide has been used for impedance matching cascade networks [86] by tapering quarter wavelength ridges along the guide (see Fig. 3.35(c, b). It is named likewise as impedance transformer since it manages to match the discontinuities between the ridges. The latter, was a crucial fact in our study since a complex matching network has been designed to match the Gutman lens antenna.

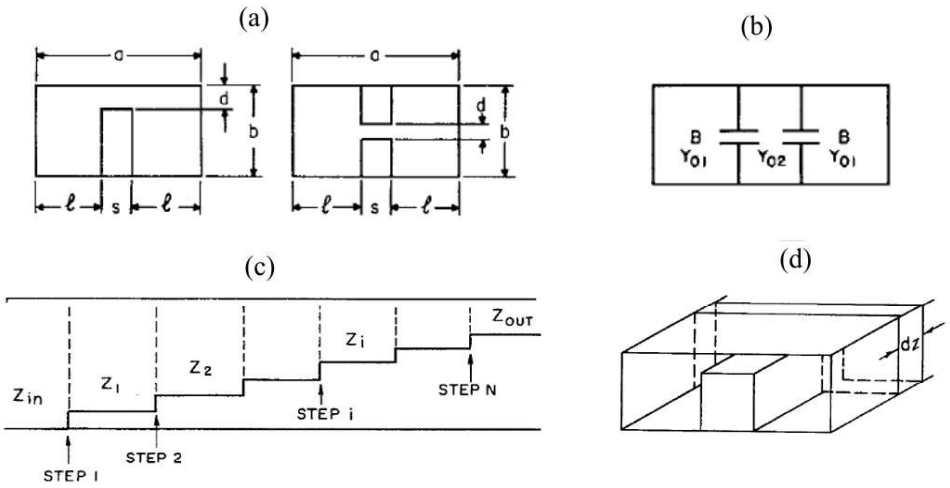

Figure 3.35: (a) Single and double ridge waveguide, [85], (b) equivalent admittances in the PPW region, (c) impedance transformer, (d) discontinuity representation of the single ridge.

3.5.1 Feed system

The single ridge waveguide has been selected to excite the Gutman lens. In order to measure the complete antenna configuration we need to excite the single ridge waveguide. A convenient choice can be the command of commercial adapters such as ridge to coaxial tranformers, [89], however these RF components are expensive. An alternative solution can be the design of a transition from the single ridge to a traditional commercial rectangular waveguide, [87] or the contactless waveguide to inline transition [88]. In that case, the large dimensions of the rectangular waveguide would enlarged the size of the whole system and thus increase its mass.

The transition from a single ridge waveguide to an SMA connector through a microstrip line is proposed here. This solution is low cost and the transition has a compact size (see Fig. 3.36(a)), [91] and is inspired by [90]. Since the impedance transformer (which consists of three quarter wavelengths stepped ridges is connected to the focal arc of the lens, a 50 ohm microstrip line has been designed and then the commercial SMA connector RS-170-6952 has

been connected to the line. To complete the total multi-beam antenna configuration, 15 identical transitions have been integrated along the focal arc of the lens (see Fig. 3.36(c)).

The 2D view layout of the total demonstrator is depicted in Fig. 3.36(b) and we observe that on the input of the antenna (focal arc of lens) the refractive index of refraction is not equal to unity. The latter, creates mismatches between the lens and the single ridge waveguide and thus the whole transition. In the following Subsection 3.5.2, a matching methodology is extensively analysed in order to match the lens to the SMA connector.

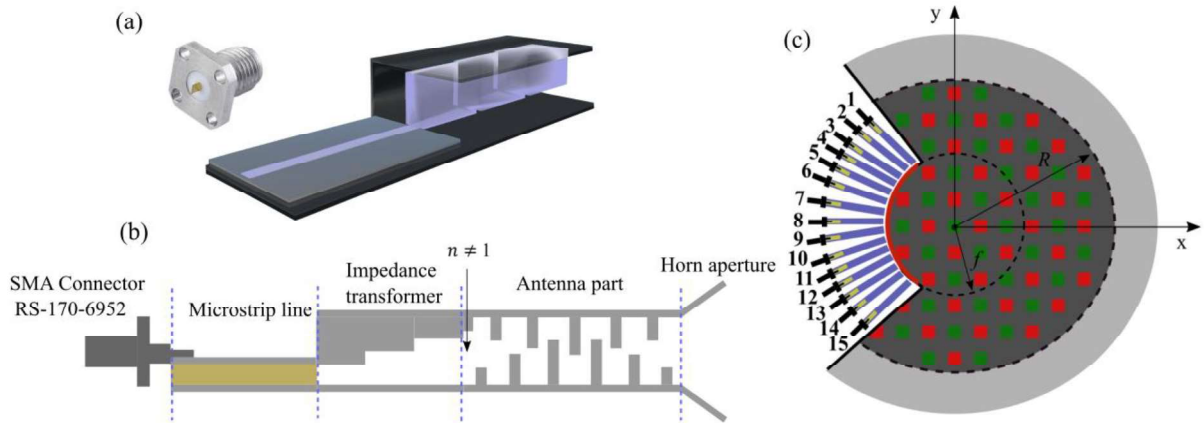

Figure 3.36: (a) Single ridge waveguide to microstrip line transition, (b) Gutman lens antenna with the proposed feed system integration, 2D view, (c) layout.

3.5.2 Impedance matching methodology

As it has been mentioned, the refractive index of the Gutman lens along its focal arc differs from unity and this can cause reflections to the input wave. Impedance transforming sections are thus needed in order to match the impedance in the input of the lens to the 50 ohm impedance of the SMA connector. For this purpose, an impedance matching methodology is proposed here and it is presented stage by stage.

-An overview of the steps adopted to match the lens follows as:

- Calculation of the characteristic impedance of the lens on its focal arc
- Calculation of the characteristic impedance of the single ridge waveguide
- Match the characteristic impedance of the lens to the characteristic impedance of the single ridge
- Match the characteristic impedance of the single ridge to the microstric line using an impedance transformer

(1) Lens to single ridge waveguide matching

The single ridge waveguide that is connected to the focal arc of the lens can be represented as a transmission line model terminated in a load impedance that is depicted in Fig. 3.37(a). Once, a transmission line is connected to a load impedance, the reflections between the line and the load can be defined by the voltage reflection coefficient, Γ, as it is shown in Eq. (3.2). In order to obtain zero reflections to the input wave towards the load the characteristic impedance, Z_o, of the line needs to be equal to the load impedance, Z_L, (Γ=0).

$$\Gamma = \frac{V_o^-}{V_o^+} = \frac{Z_L - Z_o}{Z_L + Z_o} \tag{3.2}$$

Concerning the single ridge waveguide and the lens interface, both depicted in Fig. 3.37(b), the characteristic impedance of the lens on its focal arc is considered to be the load impedance and the objective is match this to the characteristic impedance of the single ridge waveguide. This in turn will remove reflections between the single ridge waveguide and the lens, since according to Eq. (3.2) the voltage reflection coefficient will be zero. In order to achieve this first we proceed with the calculation of the characteristic impedance of the lens on its focal arc. Once this impedance is calculated, the dimensions of the single ridge waveguide are adjusted in order to end up on characteristic impedance equal to the impedance of the lens.

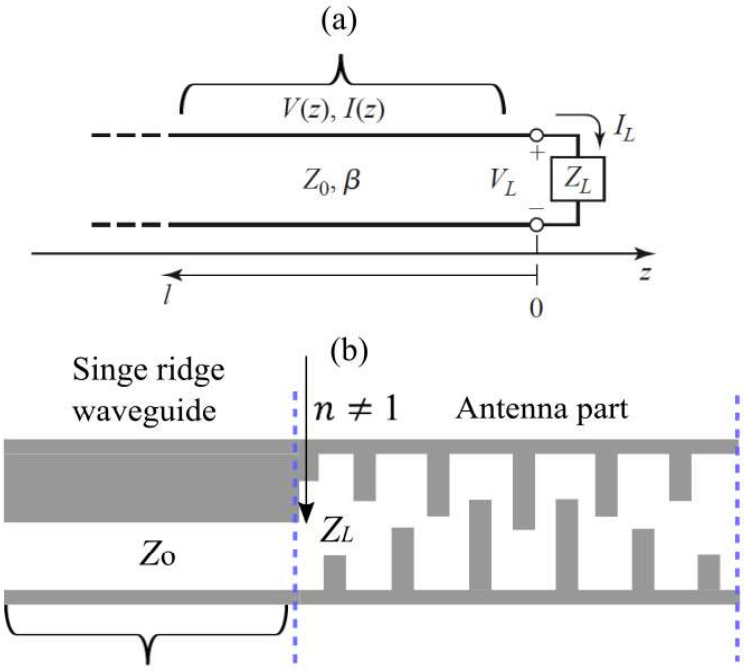

Figure 3.37: (a) Transmission line terminated in a load impedance, Z_L, ([83], Section 2.7) (b) single ridge waveguide integrated on the focal arc of the Gutman lens.

(2) Characteristic impedance calculation of the lens

The characteristic impedance of the lens is considered as the characteristic impedance of the a PPW waveguide which supports TEM propagation. Since the lens has been synthesized by modulated metasurfaces, the guided wave though the lens passes from regions with distinct values of effective index of refraction. Along the focal arc of the lens, the equivalent permittivity value equal to ε_r=4.038 based on the Eq. (3.1) of Section 3.1 and Fig. 3.13(a). Therefore, the PPW waveguide is considered to be filled with an artificial dielectric which provides a permittivity value ε_r=4.038. The characteristic impedance of a PPW filled with dielectric is defined by the following Eq. (3.3)

$$Z_o = \frac{\eta\, d}{W} \tag{3.3}$$

where, η, is the intrinsic impedance of the artificial dielectric that is filled inside the PPW, d is the PPW height and W the PPW width. The intrinsic impedance equal to $\eta=\eta_0\sqrt{\mu_r/\varepsilon_r}$, where η_0=377 ohm is the intrinsic impedance of the PPW filled with air and μ_r=1. Finally, for ε_r=4.038, η=188.5. The height, d is less than $\lambda_g/2$ to avoid the excitation of higher order modes and is equal to d=4 mm. The PPW width, W is defined as the aperture width of the single ridge waveguide that is analysed on next stage and equal to W=9 mm. It should be mentioned that this definition of the PPW width, W, is an approximation since the single ridge waveguide has closed metallic walls on the edges.

Once the parameters of the characteristic impedance of a PPW filled with the artificial dielectric on the focal arc of the lens have been specified we calculate the characteristic impedance of the lens, Z_{Lens}=Z_0=83.7 ohm.

(3) Characteristic impedance calculation of the single ridge waveguide

The next step is the calculation of the characteristic impedance of the single ridge waveguide on the focal arc of the Gutman lens. The objective here is to define properly the dimensions of the single ridge waveguide in order to end up on a characteristic impedance equal to the characteristic impedance of the lens that has been calculated formerly and equal to Z_{Lens}=83.7 ohm. The latter prevents reflections and leads to zero voltage reflection coefficient.

Based on Eq. (3.4), [84], [85], the characteristic impedance, Z_c of the single ridge is equal to

$$Z_c=\frac{Z_{0_x}}{1-\left(f_{c(ridge)}/f_0\right)} \tag{3.4}$$

where $f_{c(ridge)}$ is the cut-off frequency of the single ridge and is computed as

$$f_{c(ridge)}=\frac{1}{\pi\sqrt{\varepsilon\,\mu_0}\sqrt{\left(\frac{a_2}{b_2}+\frac{2C_d}{\varepsilon}\right)+(a_1-a_2)b_1}} \tag{3.5}$$

where, C_d is the capacitance that exists between the ridge and the ground and a_1, a_2, b_1, b_2, the dimensions of the single ridge (see Fig. 3.38(a, b)) and is calculated above

$$C_d=\frac{\varepsilon}{\pi}\left[\frac{x^2+1}{x}\cosh^{-1}\left(\frac{1+x^2}{1-x^2}\right)-2\ln\frac{4x}{1-x^2}\right] \tag{3.6}$$

where $x=b_2/b_1$.

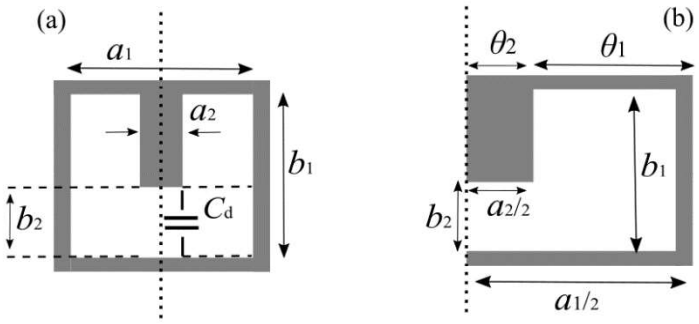

Figure 3.38: (a) Single ridge waveguide parameters, (b) half cut view of the single ridge waveguide representing the electrical length, $\boldsymbol{\theta_1}$, $\boldsymbol{\theta_2}$.

The calculation of the infinite impedance, Z_{c_∞}, is realized based on the above Eq. (3.7), where θ_1 and θ_2 are the electrical lengths of the single waveguide sections that are depicted in Fig. 3.38(b).

$$Z_{0_\infty}=\frac{\sqrt{\frac{\mu}{\varepsilon}}}{\frac{2C_d}{\varepsilon}cos\theta_2+\frac{1}{\pi}\frac{\lambda_{c(ridge)}}{b_2}\left(sin\theta_2+\frac{b_2}{b_1}cos\theta_2 tan\frac{\theta_1}{2}\right)} \tag{3.7}$$

A critical point in the calculation of the characteristic impedance is the need for the cut-off wavelength, $\lambda_{c(wg)}$, of the traditional waveguide and it is computed as

$$\lambda_{c(wg)}=2a_1 \tag{3.8}$$

Next, the cut-off wavelength of the single ridge waveguide is obtained by

$$\lambda_{c(ridge)}=\frac{1}{f_{c(ridge)}\sqrt{\varepsilon\mu_0}} \tag{3.9}$$

Thus, we are able to compute the electrical lengths θ_1 and θ_2.

$$\theta_1=\left(1-\frac{a_2}{a_1}\right)\frac{\lambda_{c(wg)}}{\lambda_{c(ridge)}}\frac{\pi}{2} \tag{3.10}$$

$$\theta_2=\frac{a_2}{a_1}\frac{\lambda_{c(wg)}}{\lambda_{c(ridge)}}\frac{\pi}{2} \tag{3.11}$$

Finally, the infinite impedance, Z_{c_∞} is computed. Once, the cut-off frequency of the ridge, $f_{c(ridge)}$and the infinite impedance, Z_{c_∞}, is known, the final characteristic impedance, Z_c for the desired center frequency, f_0, is evaluated.

Once all the design parameters have been specified, the objective is to attain a characteristic impedance value at center frequency, f_0=12.5 GHz, equal to Z_c=83.7 ohm. In order to achieve this goal the design variables, a_1, a_2, b_1, b_2, of the single ridge need to be tuned in order to reach the target value of the characteristic impedance, Z_c. The sole constraint though the tuning process, is the cut-off frequency, $f_{c(ridge)}$ of the single ridge to be less than 10 GHz, since we target to operate at Ku-band. Following the calculation of Eq. (3.2-3.11) the final

design parameters of the single ridge waveguide take the values, a_1=9 mm, a_2=4.1 mm, b_1=4 mm, b_2=0.9 mm.

The single ridge waveguide with the above dimensions has been integrated on the focal arc of the Gutman lens antenna oriented through the broadside as it is depicted in the below Fig. 3.39. We notice that the reflection coefficient $S_{1,1}$ takes very low values and the antenna has been matched over the whole Ku-band.

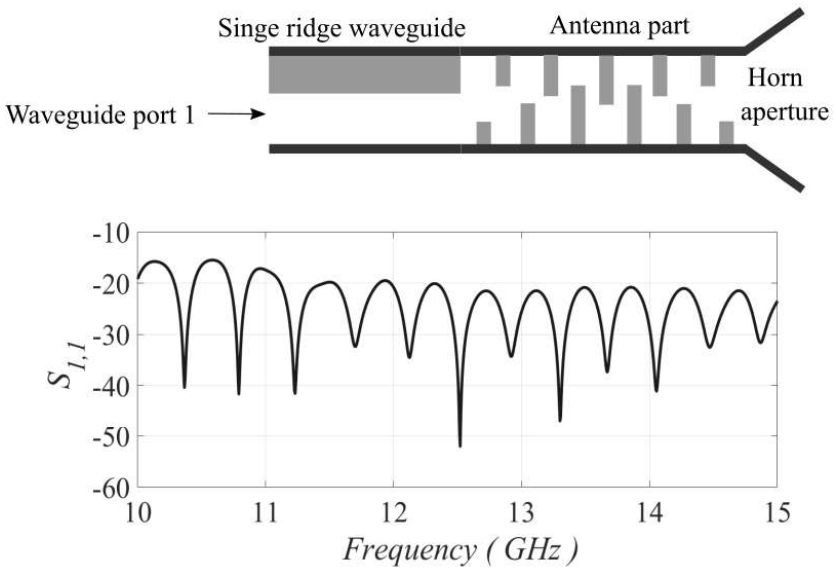

Figure 3.39: Reflection coefficient, $S_{1,1}$ of the Gutman lens antenna when it is excited by the single ridge waveguide.

(4) Impedance transformer

Once the dimensions of the single ridge waveguide on the focal arc of the lens have been defined, and the waveguide presents a characteristic impedance of Z_c=83.7 ohm, the next step is to match this impedance, Z_c to a microstrip line characteristic impedance Z_{line}=50 ohm. To match these 2 unequal characteristic impedances, a stepped transmission line impedance transformer which consists of a cascade network of stepped ridges with segregate widths and heights has been designed and dis designated in Fig. 3.40(a, b)). Three quarter wavelength (x_1=x_2=x_3=λ_g/4) ridges consist of the impedance transformer to gradually drop the impedance into the characteristic impedance 50 ohm of the microstrip line. The dimensions of the step 1 ridge have been previously specified. In order to calculate the dimensions of the rest ridge junctions a parametric study has been actualized to evaluate the impact of the design variables of the single ridge waveguide on its cut-off frequency, as well as, on its characteristic impedance and the bandwidth.

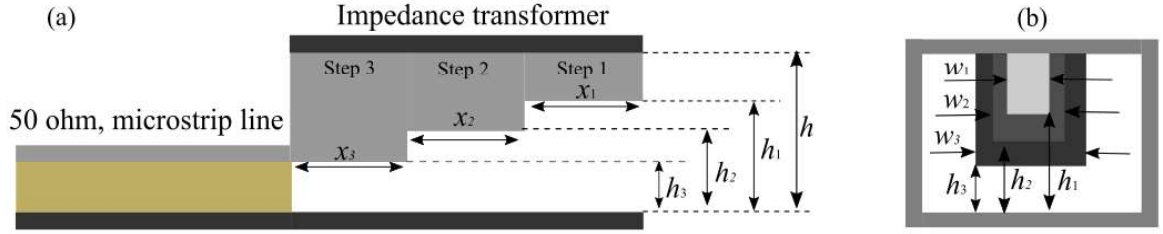

Figure 3.40: (a) Single ridge waveguide to microstrip line transition using an impedance transformer, (b) 2D cut view of the impedance transformer.

First, a parametric study has been realized in order to examine the effect of the design parameters on the cut-off frequency, $f_{c(ridge)}$ of its fundamental propagating mode TE_{10} of the single ridge. Since, a constant value has been defined for the width, a_1 and the height, b_1 of the single ridge waveguide, we vary the width, a_2 of the ridge to specify its cut-off frequency (see Fig. (3.41)). We repeat this process for separate heights, b_2 of the ridge; the height, b_2 is the distance between the ridge and the ground plane. We observe that for low values of b_2 the the cut-off frequency drops by virtue of the high capacitance, C_d that exists between the ridge and the ground plane. For higher values of b_2 the single ridge waveguide start to behave as the traditional waveguide, since the cut-off frequency increases. The latter, specifies the bandwidth difference between the single ridge and the traditional waveguide which is nearly 1.5 octaves.

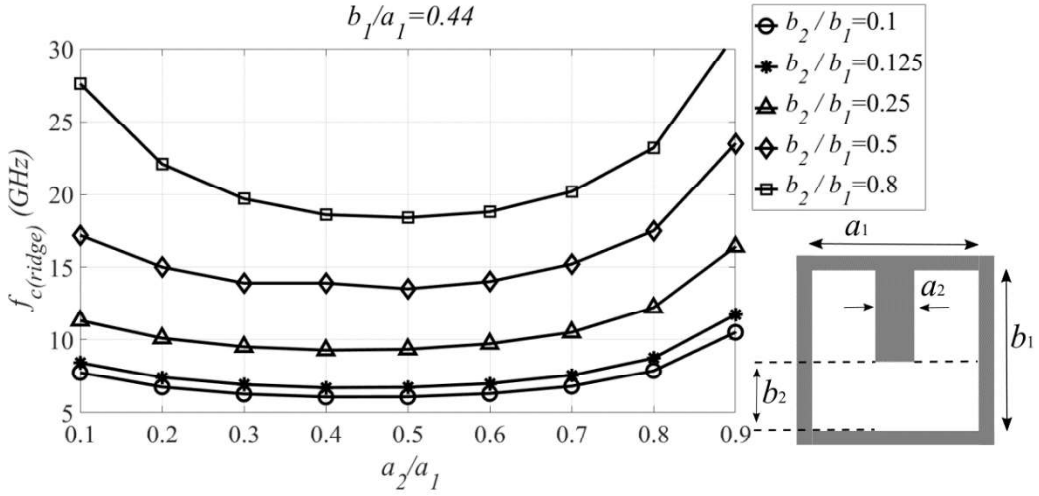

Figure 3.41: Parametric study for the design parameters of the single ridge waveguide to calculate its cut-off frequency, $f_{c(ridge)}$.

Going forward, we apply a parametric study on the design parameters of the single ridge waveguide to investigate their impact on the characteristic impedance, Z_c. On the primary parametric study that is depicted in Fig. (3.42), we notice that when the distance between the ridge and the ground plane decreases, the characteristic impedance takes lower values and likewise it is more stable over the frequency compared to high impedances. At this point, it should be marked that the single ridge waveguide presents lower and more stable characteristic impedance compared to the traditional waveguide.

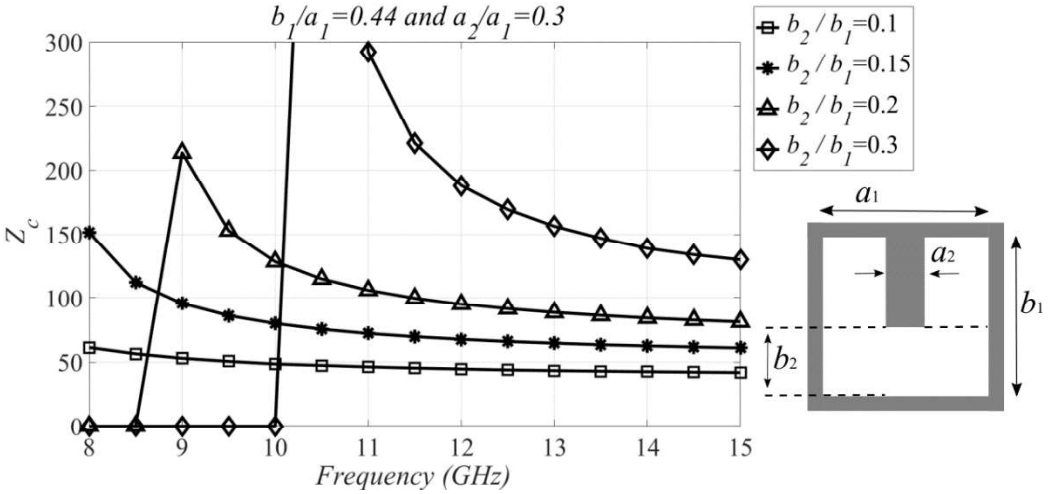

Figure 3.42: Parametric study of the characteristic impedance, Z_c of the single ridge waveguide for variable height, b_2.

The objective here is to achieve a characteristic impedance that is equal to 50 ohm for the ridge step 3 (see Fig. 3.40(a)), given that a 50 ohm microstrip line will be connected into it. From the above Fig. 3.42 low values of b_2, lead to low characteristic impedance. Therefore, an additional parametric study has been realized (see Fig. 3.43) where the width a_2 of the ridge varies. In this study, the ratio b_2/b_1 remains constant and has a low value, since we target to examine the influence of the width of the ridge for low characteristic impedances. We notice that for wider ridge width, the characteristic impedance drops.

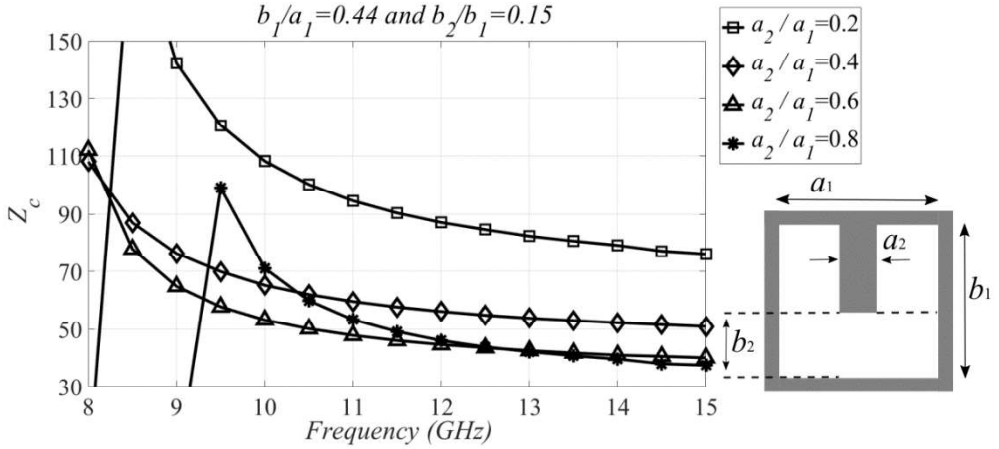

Figure 3.43: Parametric study of the characteristic impedance, Z_c of the single ridge waveguide for variable height, a_2.

Considering the parametric studies we conclude that wider width, as well as higher height of the ridge leads to lower and more stable characteristic impedance; the graphs have been calculated based on Eq. (3.2-3.11). Finally, the dimensions of the impedance transformer have been computed for the three ridge steps that are depicted in Fig. 3.40(a, b), h_1=0.9 mm, w_1=4.1 mm, h_2=0.7 mm, w_2=3.5 mm, h_3=0.4 mm, w_3=2.2 mm.

Transition simulation on CST Studio Suite

The proposed transformer with the dimensions that has been previously specified has been connected with a microstrip line which has a characteristic impedance equal to 50 ohm. The dielectric width is h=0.508 mm with permittivity ε_r=3.38 and the line width w=1.15 mm. The 50 ohm SMA connector that is connected to the microstrip line is the model 170-6952 from the company RS Radiospares. The transition that is depicted in Fig. 3.44(a, b) has been simulated in CST Microwave studio and shows low reflections and low losses (see Fig. 3.44(c)).

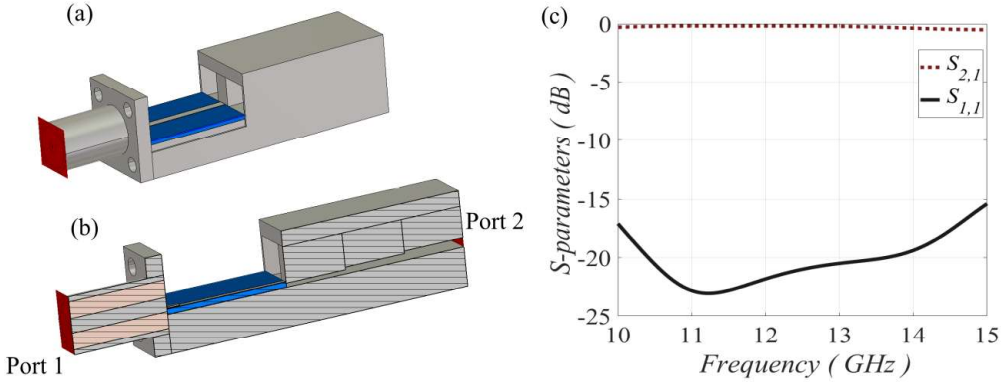

Figure 3.44: (a) CST model of the microstrip to single ridge waveguide, (b) 2D cut view, (c) reflection and transmission coefficients.

The above transition selected to excite the Gutman lens and it has been integrated on its focal arc oriented at broadside. A comparison is provided after four segregate electromagnetic simulations, to examine the evolution of the reflections of the lens (see Fig. 3.45(a-e)). The initial attempt to match the Gutman lens was the integration of the traditional waveguide that is depicted in Fig. 3.45(a). Since the effective index of refraction on the focal arc of the lens is unequal to unity strong reflections induced and are shown in Fig. 3.45(e). Afterwards, the single ridge waveguide has been matched with the lens and excellent performance achieved over the whole Ku-band as it is depicted in Fig. 3.45(e). Subsequently, the impedance transformer has been analysed to further investigate the characteristic impedance and design a stepped transmission line with three stepped ridges connected to the microstrip line. This transition that is depicted in Fig. 3.45(c) has been simulated and led to very low reflections. Finally, the proposed transition connected with a 50 ohm SMA connector has been integrated on the focal arc of the lens (see Fig. 3.45(d)) and low reflections are attained over the whole Ku- band.

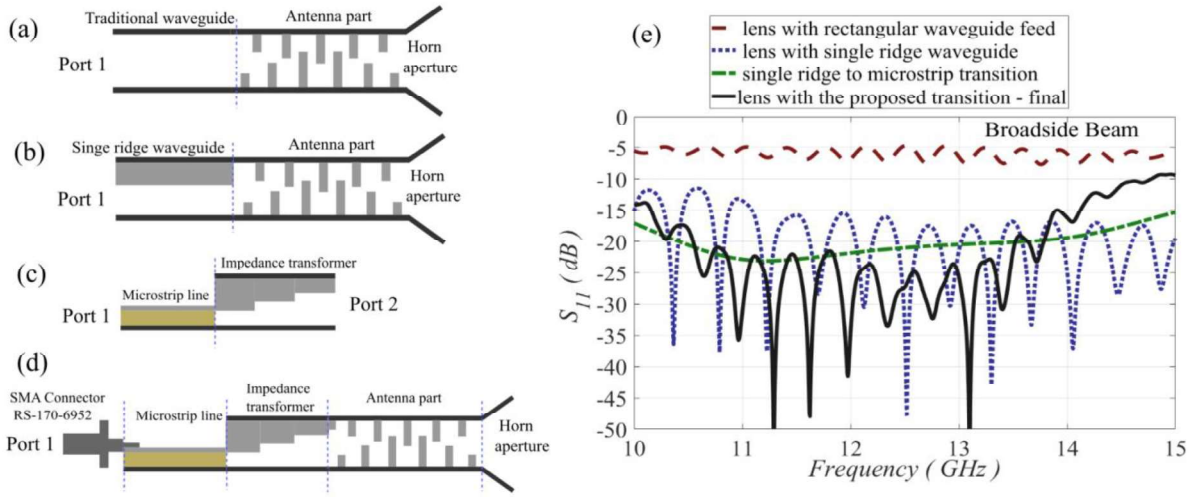

Figure 3.45: 2D view of (a) traditional waveguide integrated on the focal arc of the Gutman lens, (b) single ridge waveguide connected on the focal arc of the Gutman lens, (c) single ridge waveguide to microstrip line transition, (d) proposed transition connected to the focal arc of the lens.

3.6 Antenna simulation results

3.6.1 Geometry

The CST model of the proposed Gutman lens antenna demonstrator is depicted in Fig. 3.46(a-d). It is composed of two PPW metal plates. The top plate (see Fig. 3.46(a)), consists of the top metal posts of the interleaved unit cell. The impedance transformer which is composed of three stepped ridges is connected to the focal arc of the lens. On the periphery of the lens, a radiation horn flare has been attached to match the lens into the free space. The bottom plate (see Fig. 3.46(b)), consists of the bottom metal plates of the interleaved unit cell. The total number of metal posts is 14.000; 8.000 posts on the bottom plate and 6.000 posts on the top plate. The two metal plates are connected and screws have been integrated on the extended metal surfaces that are on the edge of the lens. Further details on the mechanical design of the lens will be presented on Chapter 4. The dielectric placed on the bottom plate in a distance, *d*, from the focal arc of the lens. This distance is the length of the impedance transformer which equal to 3 λ_g. The completed demonstrator is depicted in Fig. 3.46(c) and its 2D cut view in Fig. 3.46(d).

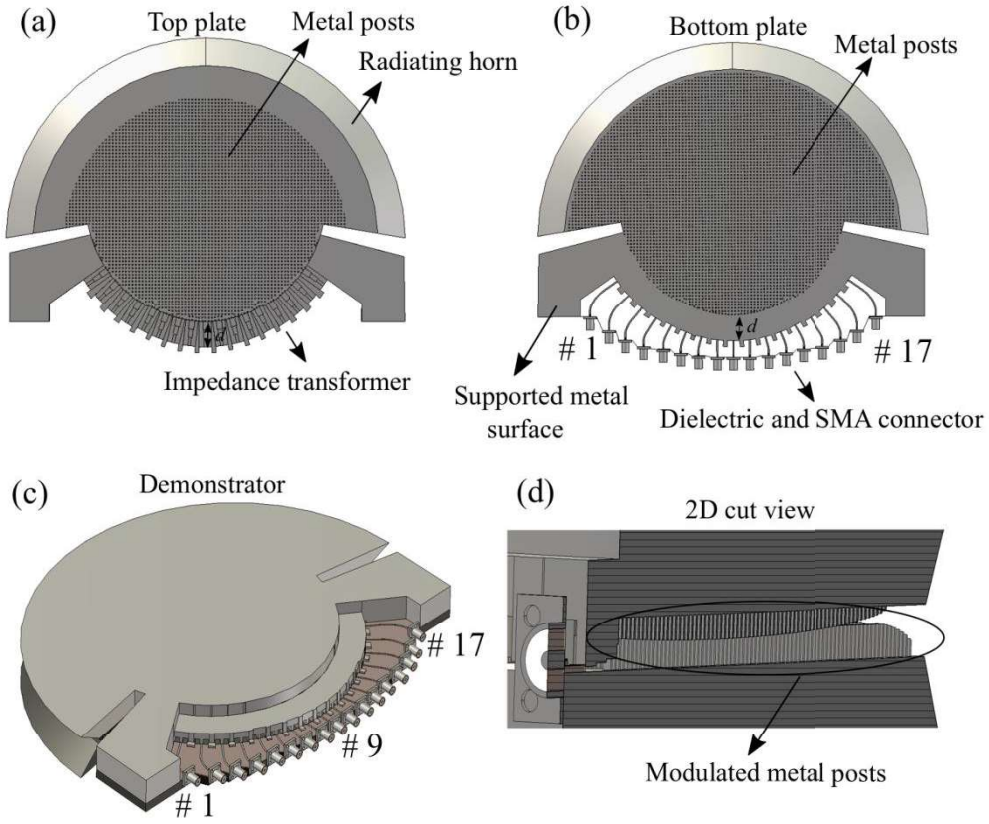

Figure 3.46: Final demonstrator, (a) top plate, (b) bottom plate, (c) perspective view of both plates, (d) 2D cut view for broadside orientation.

3.6.2 Computational resources

The time domain solver has been used to simulate the lens. The simulation complexity of this type of lens is its long simulation time. For a single beam simulation, 250 million mesh cells are needed. The large number of mesh cells calls for powerful computational resources. Large RAM memory is needed to apply the simulations. For instance, with a computer of RAM 100 GB, the EM simulation for a single beam lasts approximately 60 hours, although with a computer of RAM 240 GB, the simulation lasts 24 hours.

3.6.3 Radiation patterns

(1) Directivity Patterns

Electromagnetic simulations have been actualized on CST Microwave studio to evaluate the radiation patterns. Each feed of the lens has been separately excited. The directivity patterns on the H-plane are illustrated in Fig. 3.47(a-c)-Fig. 3.48(a, b). The antenna has circular symmetry and the pointing angle of the radiated beams are 0°, 9°, 19°, 28°, 37°, 48°, 58°, 68°, 78°. The antenna has been simulated for selected frequency points 10 GHz, 11 GHz, 12.5 GHz, 14 GHz and 15GHz over the Ku-band.

For all the selected frequencies we notice that the directivity of the patterns remains stable up to 37° and then it degrades. The losses are up to 3 dB for the entire FOV and emanate from the required extracted surface of the lens and the placement of all the feeds along the focal arc of the lens.

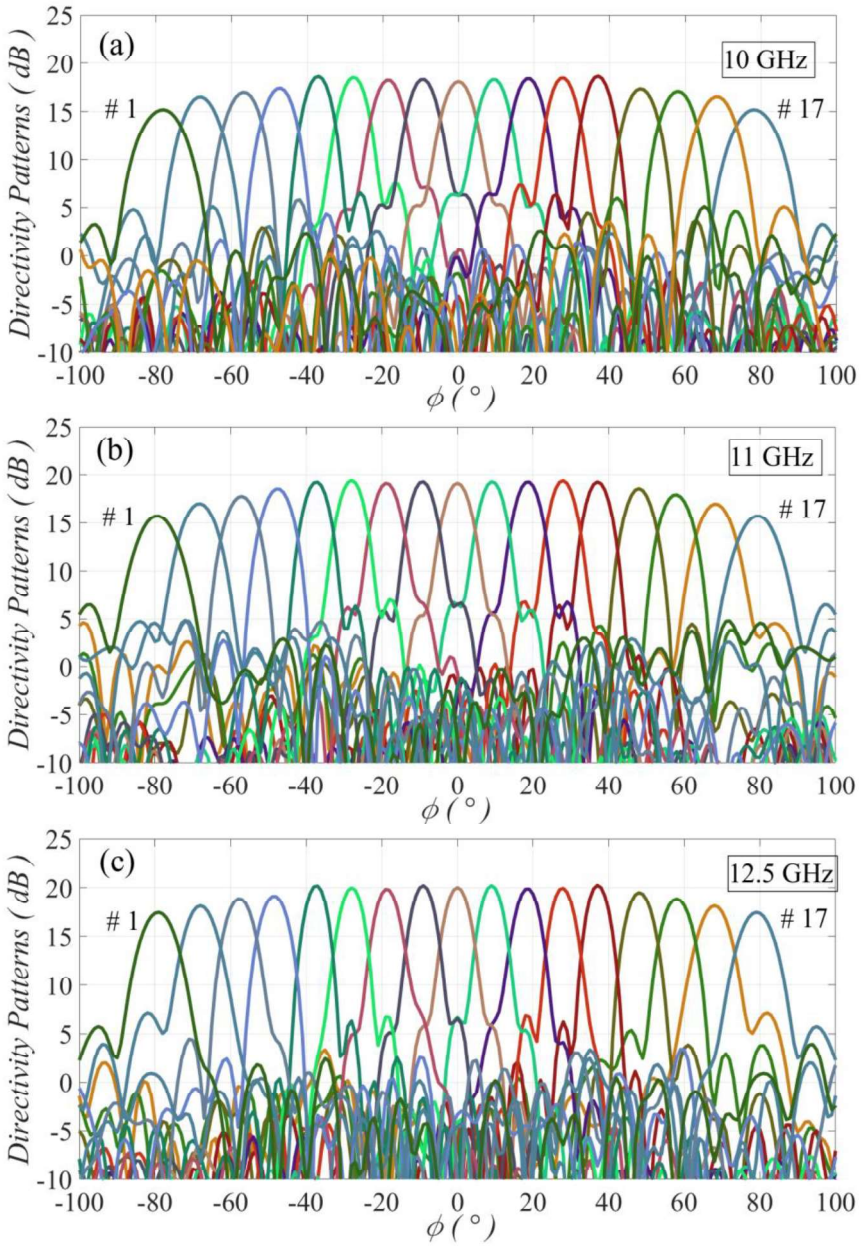

Figure 3.47: Directivity patterns of the Gutman lens demonstrator on H-plane for the frequencies (a) f=10 GHz, (b) f=11 GHz, (c) f=12.5 GHz.

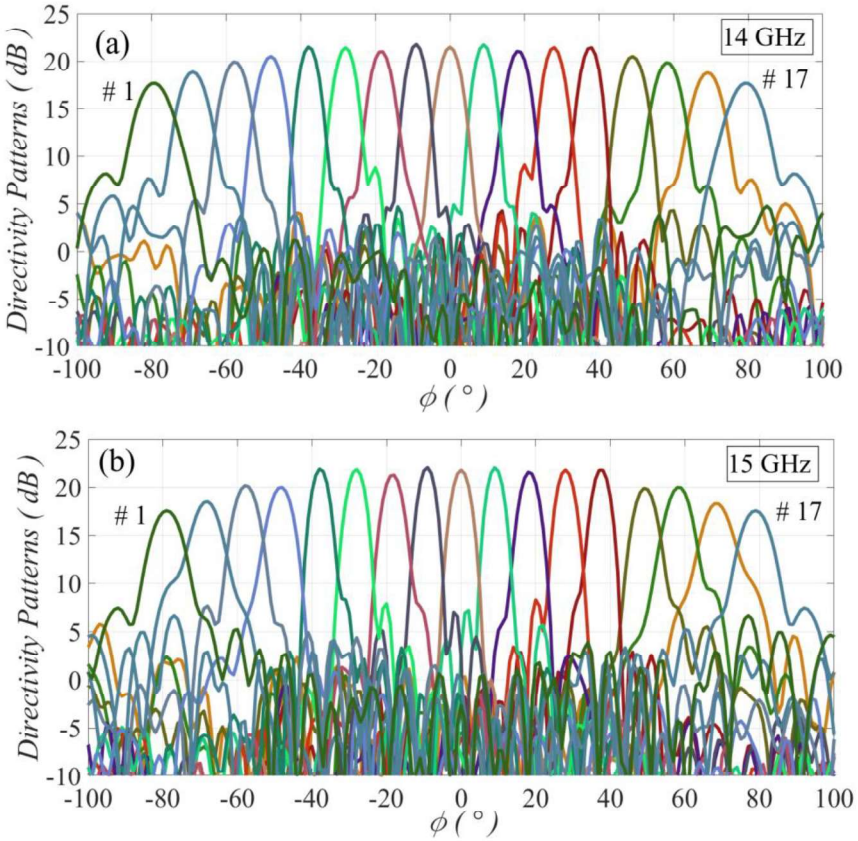

Figure 3.48: Directivity patterns of the Gutman lens demonstrator on H-plane for the frequencies (a) f=14 GHz, (b) f=15 GHz.

In Fig. 3.49 the performance of the directivity patterns for the selected frequencies over the Ku-band is presented. We notice that for the extreme offset beams #1-#4 the directivity value increases up to 14 GHz, however for the edge frequency, 15 GHz it remains stable and in some cases it drops. This is not the case for the beams #5-#9 where the directivity increases progressively over the whole Ku-band. Additionally, the beams #1-#4 present larger dB difference on their directivity values for nearly all the frequency points compared to the beams #5-#9 where their directivity difference is not significant. Moreover, the losses differ for segregate frequencies. For instance, for the center frequency f=12.5 GHz the losses between the broadside beam, #9 and the extreme beam #1 are 2.8 dB. At frequencies 10 GHz and 12 GHz the losses are 3.5 dB and 3.6 dB respectively. The maximum losses appear at highest frequencies 14 GHz and 15 GHz with 4.1 dB and 4.5 dB. This difference in the losses over the Ku-band is based on the dispersion of the interleaved unit-cell.

In Fig. 3.50 the overlapping between the radiating beams is illustrated. For higher frequencies the θ_{3dB} increases and thus the beams become more narrow. The latter, interpret the high cross over in high frequencies 14 GHz and 15 GHz. Since the directivity of the beams drops over wide angles, the θ_{3dB} decreases and thus the cross over progressively declines. Indeed, over the whole Ku-band the overlapping is improved, although it is valid for the extreme beams #1-#4. As it is mentioned above, the beams #5-#9 have similar directivity values and thus the overlapping between them is nearly stable.

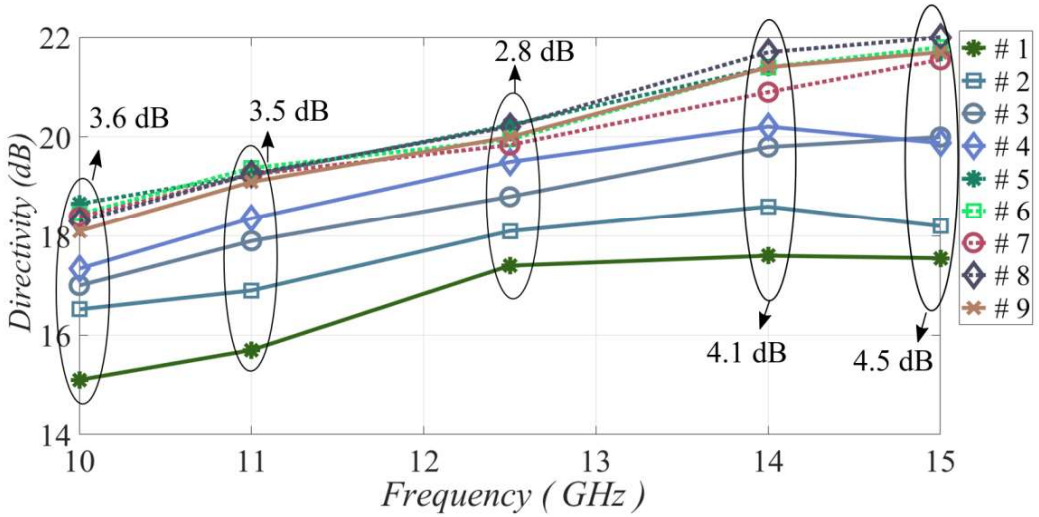

Figure 3.49: Directivity patterns on H-plane vs selected frequency points over the Ku-band.

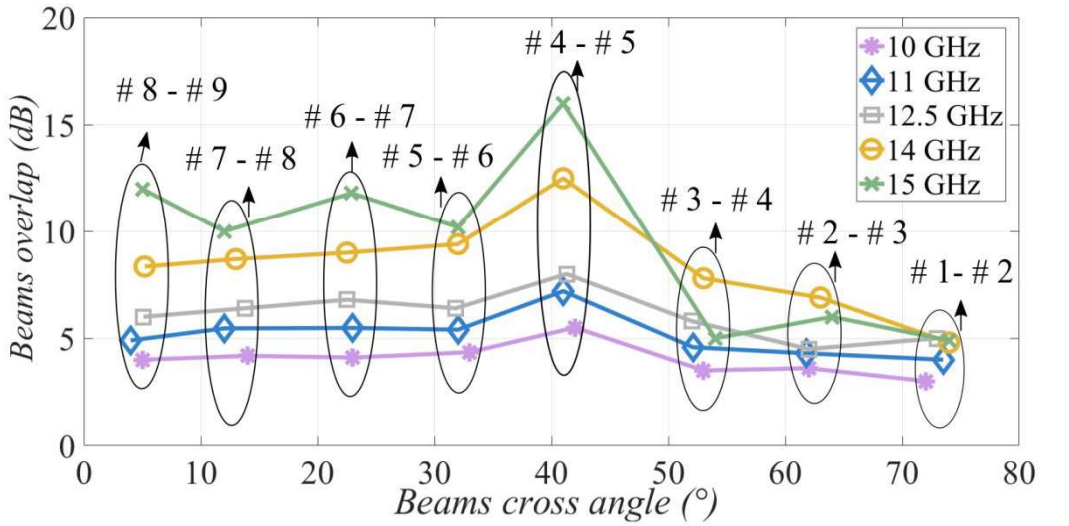

Figure 3.50: Overlapping between the radiating beams for selected frequencies over the Ku-band.

(2) Normalized directivity patterns

The normalized directivity patterns are illustrated in Fig. 3.51(a-c)-Fig. 3.52(a, b). We notice that for the extreme feed, #1 which points at 78° the SLL level takes values above -10 dB nearly through the whole Ku-band. However, for the rest offset beams, as well as the broadside, the SLL level is acceptable. Excellent values of SLL are -15 dB for space applications, because the high SLL level can induce interference between the beams. However, this interference can be treated with self-interference cancellation circuit in the RF domain.

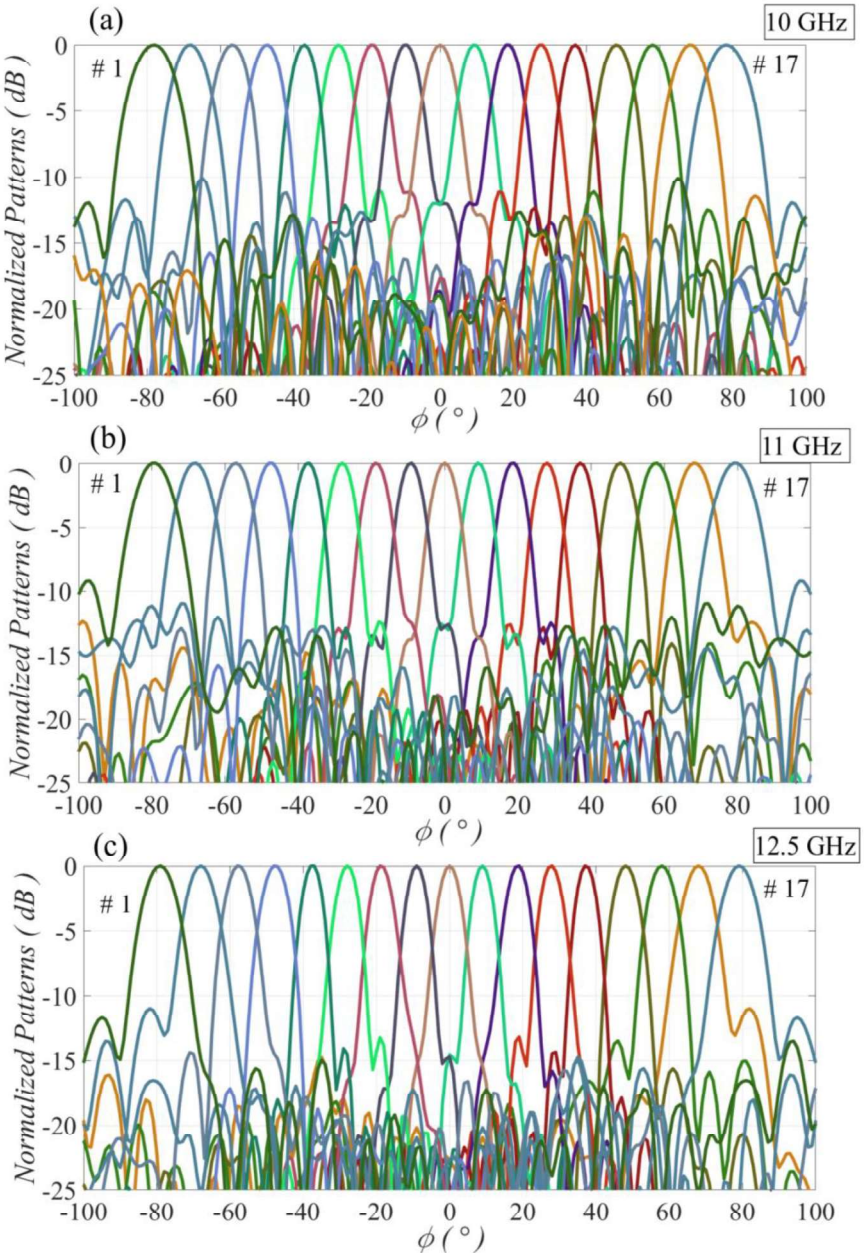

Figure 3.51: Normalized patterns of the Gutman lens demonstrator for the frequencies (a) f=10 GHz, (b) f=11 GHz, (c) f=12.5 GHz.

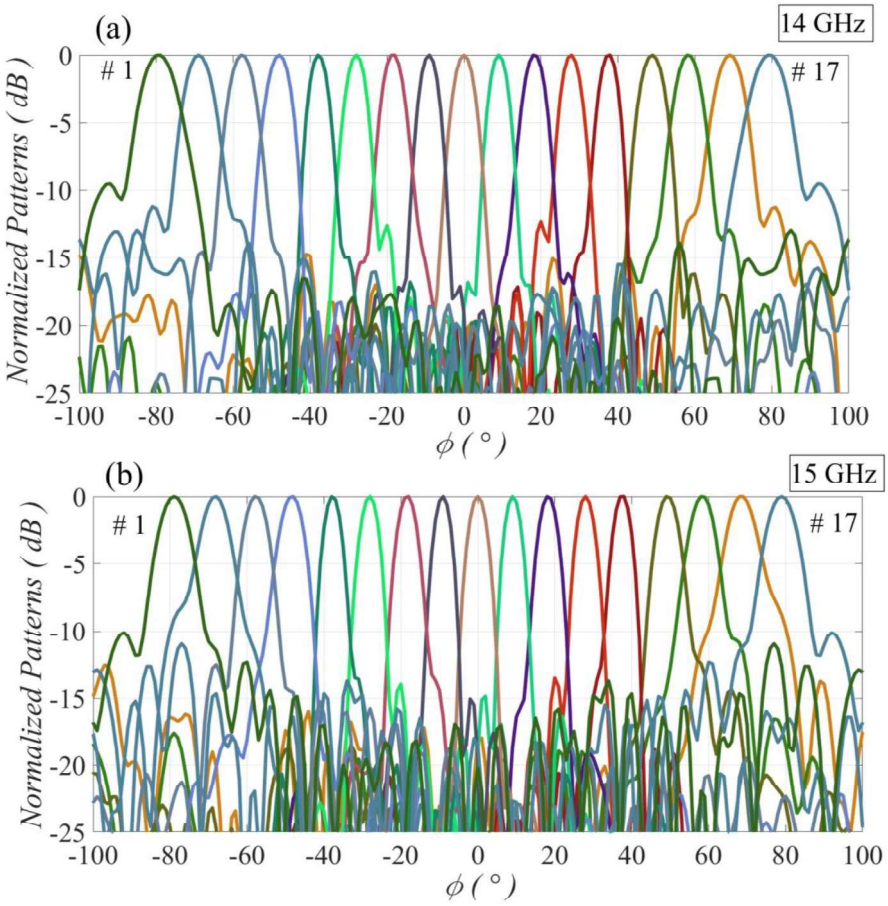

Figure 3.52: Normalized patterns of the Gutman lens demonstrator for the frequencies (a) f=14 GHz, (b) f=15 GHz.

In Fig. 3.53 we depict the SLL level of every beam over the pointing angles for the whole Ku-band. The bandwidth of the lens regarding to the SLL level is narrowband. For the frequencies 11 GHz, 12.5 GHz and 13 GHz the SLL level is less than -12 dB up to 60° FOV. For the edge frequencies, 10 GHz and 15 GHz we have a slight decrease up to 1 dB. Furthermore, in Fig. 3.54 the θ_{3dB} over the scan angle is shown. As expected, for higher frequencies, θ_{3dB} decreases and it is progressively increased as we scan over wider pointing angles by virtue of the decrease on directivity. As mentioned in previous sections, for wider scan angles the E-field of the excitation source doesn't explore the whole surface of the lens. The latter, results on wider beams for extreme orientations and thus larger values of θ_{3dB}.

In Fig. 3.55-Fig. 3.57 the E-plane radiation patterns are depicted for the broadside beam, the 37° offset beam and the 68° offset beam.

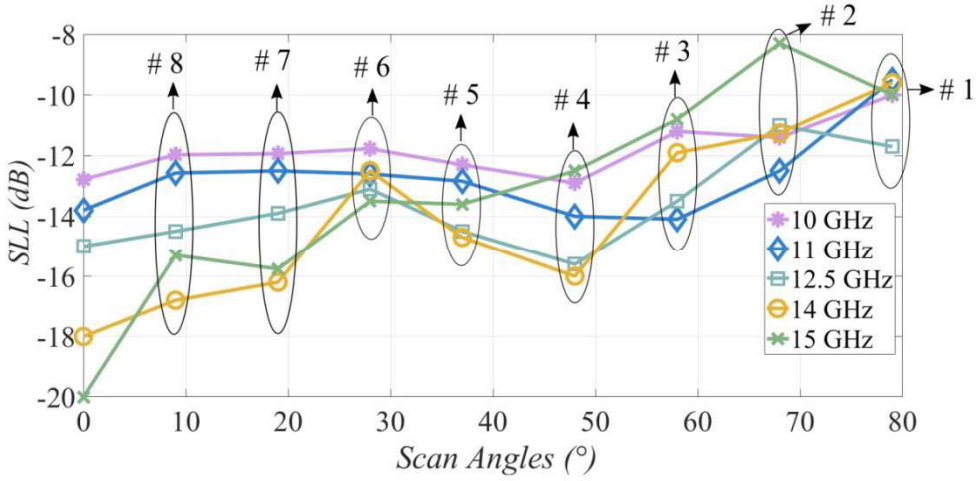

Figure 3.53: SLL level over scan angles for selected frequencies in Ku-band.

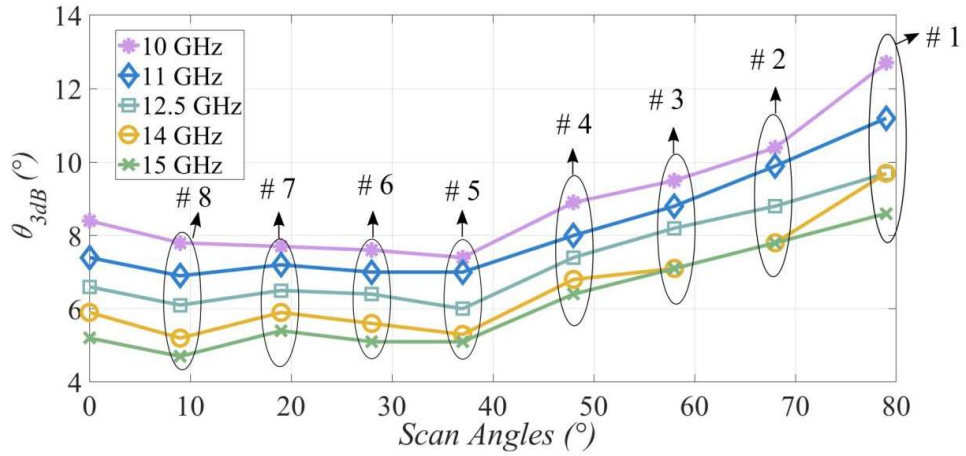

Figure 3.54: θ_{3dB} over scan angles for selected frequencies in Ku-band.

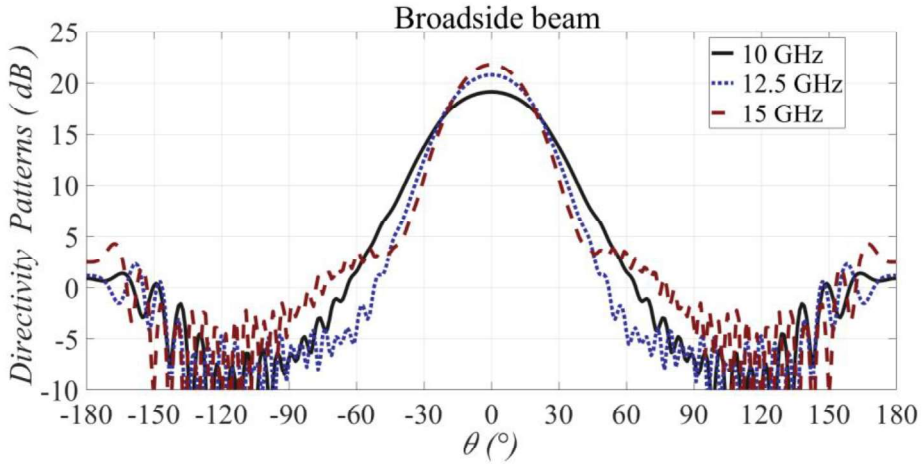

Figure 3.55: E-plane patterns for the broadside beam at frequencies f=10 GHz, f=12.5 GHz and f=15 GHz.

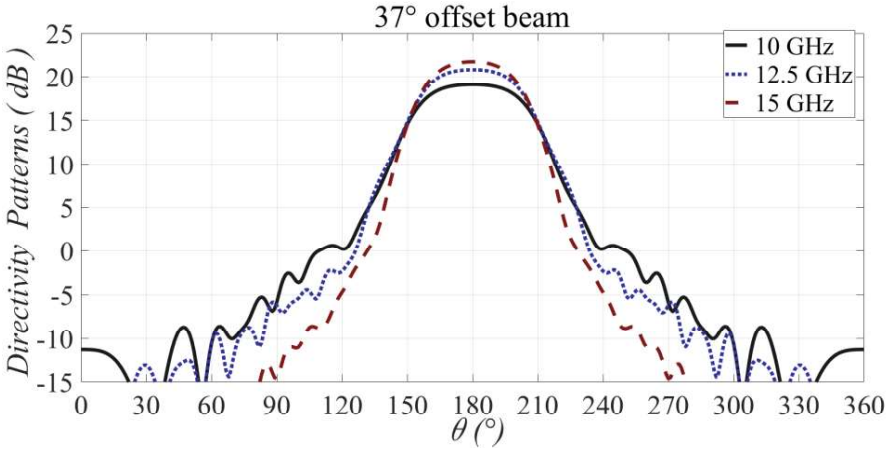

Figure 3.56: E-plane patterns for the 37° offset beam at frequencies f=10 GHz, f=12.5 GHz and f=15 GHz.

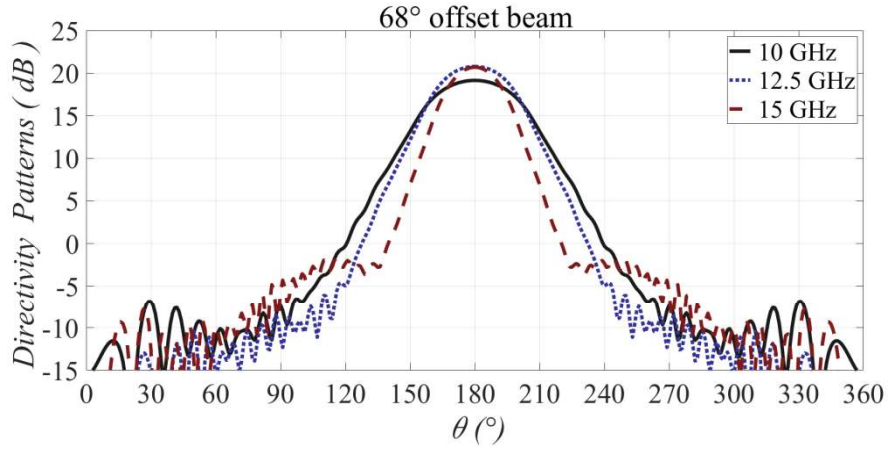

Figure 3.57: E-plane patterns for the 68° offset beam at frequencies f=10 GHz, f=12.5 GHz and f=15 GHz.

3.6.4 S-parameters

The Gutman lens antenna consists of 17 feeds. Therefore, a 17-by-17 matrix has been composed to represent the total S-parameters of the lens and it is shown in Table. 3.1. The S-parameters are divided into two groups. The first group is the reflection parameters and the second group the isolation parameters.

The reflection parameters are defined by the matrix elements, $S_{i,j}$ where $i \in \{1\text{-}17\}$ with $i = j$ and they are illustrated on the diagonal of the matrix in Table. 3.1. The antenna has a circular symmetry and the elements, $S_{i,j}$, for $i \in \{1\text{-}8\}$ are symmetric with the elements, $S_{i,j}$ for $i \in \{10\text{-}17\}$. The element $S_{9,9}$ represent the reflection coefficient of the feed that is placed on the broadside direction.

The isolation parameters are defined by the matrix elements, $S_{i,j}$ where $i \in \{1\text{-}17\}$ with $i \neq j$ and they are illustrated on the top and bottom triangular matrix in Table. 3.1.

Table 3.1: 17-by-17 matrix with all the S-parameters of the Gutman lens demonstrator

Ports	#1	#2	#3	#4	#5	#6	#7	#8	#9	#10	#11	#12	#13	#14	#15	#16	#17
#1	$S_{1,1}$	$S_{1,2}$	$S_{1,3}$	$S_{1,4}$	$S_{1,5}$	$S_{1,6}$	$S_{1,7}$	$S_{1,8}$	$S_{1,9}$	$S_{1,10}$	$S_{1,11}$	$S_{1,12}$	$S_{1,13}$	$S_{1,14}$	$S_{1,15}$	$S_{1,16}$	$S_{1,17}$
#2	$S_{2,1}$	$S_{2,2}$	$S_{2,3}$	$S_{2,4}$	$S_{2,5}$	$S_{2,6}$	$S_{2,7}$	$S_{2,8}$	$S_{2,9}$	$S_{2,10}$	$S_{2,11}$	$S_{2,12}$	$S_{2,13}$	$S_{2,14}$	$S_{2,15}$	$S_{2,16}$	$S_{2,17}$
#3	$S_{3,1}$	$S_{3,2}$	$S_{3,3}$	$S_{3,4}$	$S_{3,5}$	$S_{3,6}$	$S_{3,7}$	$S_{3,8}$	$S_{3,9}$	$S_{3,10}$	$S_{3,11}$	$S_{3,12}$	$S_{3,13}$	$S_{3,14}$	$S_{3,15}$	$S_{3,16}$	$S_{3,17}$
#4	$S_{4,1}$	$S_{4,2}$	$S_{4,3}$	$S_{4,4}$	$S_{4,5}$	$S_{4,6}$	$S_{4,7}$	$S_{4,8}$	$S_{4,9}$	$S_{4,10}$	$S_{4,11}$	$S_{4,12}$	$S_{4,13}$	$S_{4,14}$	$S_{4,15}$	$S_{4,16}$	$S_{4,17}$
#5	$S_{5,1}$	$S_{5,2}$	$S_{5,3}$	$S_{5,4}$	$S_{5,5}$	$S_{5,6}$	$S_{5,7}$	$S_{5,8}$	$S_{5,9}$	$S_{5,10}$	$S_{5,11}$	$S_{5,12}$	$S_{5,13}$	$S_{5,14}$	$S_{5,15}$	$S_{5,16}$	$S_{5,17}$
#6	$S_{6,1}$	$S_{6,2}$	$S_{6,3}$	$S_{6,4}$	$S_{6,5}$	$S_{6,6}$	$S_{6,7}$	$S_{6,8}$	$S_{6,9}$	$S_{6,10}$	$S_{6,11}$	$S_{6,12}$	$S_{6,13}$	$S_{6,14}$	$S_{6,15}$	$S_{6,16}$	$S_{6,17}$
#7	$S_{7,1}$	$S_{7,2}$	$S_{7,3}$	$S_{7,4}$	$S_{7,5}$	$S_{7,6}$	$S_{7,7}$	$S_{7,8}$	$S_{7,9}$	$S_{7,10}$	$S_{7,11}$	$S_{7,12}$	$S_{7,13}$	$S_{7,14}$	$S_{7,15}$	$S_{7,16}$	$S_{7,17}$
#8	$S_{8,1}$	$S_{8,2}$	$S_{8,3}$	$S_{8,4}$	$S_{8,5}$	$S_{8,6}$	$S_{8,7}$	$S_{8,8}$	$S_{8,9}$	$S_{8,10}$	$S_{8,11}$	$S_{8,12}$	$S_{8,13}$	$S_{8,14}$	$S_{8,15}$	$S_{8,16}$	$S_{8,17}$
#9	$S_{9,1}$	$S_{9,2}$	$S_{9,3}$	$S_{9,4}$	$S_{9,5}$	$S_{9,6}$	$S_{9,7}$	$S_{9,8}$	$S_{9,9}$	$S_{9,10}$	$S_{9,11}$	$S_{9,12}$	$S_{9,13}$	$S_{9,14}$	$S_{9,15}$	$S_{9,16}$	$S_{9,17}$
#10	$S_{10,1}$	$S_{10,2}$	$S_{10,3}$	$S_{10,4}$	$S_{10,5}$	$S_{10,6}$	$S_{10,7}$	$S_{10,8}$	$S_{10,9}$	$S_{10,10}$	$S_{10,11}$	$S_{10,12}$	$S_{10,13}$	$S_{10,14}$	$S_{10,15}$	$S_{10,16}$	$S_{10,17}$
#11	$S_{11,1}$	$S_{11,2}$	$S_{11,3}$	$S_{11,4}$	$S_{10,5}$	$S_{11,6}$	$S_{11,7}$	$S_{11,8}$	$S_{11,9}$	$S_{11,10}$	$S_{11,11}$	$S_{11,12}$	$S_{11,13}$	$S_{11,14}$	$S_{11,15}$	$S_{11,16}$	$S_{11,17}$
#12	$S_{12,1}$	$S_{12,2}$	$S_{12,3}$	$S_{12,4}$	$S_{12,5}$	$S_{12,6}$	$S_{12,7}$	$S_{12,8}$	$S_{12,9}$	$S_{12,10}$	$S_{12,11}$	$S_{12,12}$	$S_{12,13}$	$S_{12,14}$	$S_{12,15}$	$S_{12,16}$	$S_{12,17}$
#13	$S_{13,1}$	$S_{13,2}$	$S_{13,3}$	$S_{13,4}$	$S_{13,5}$	$S_{13,6}$	$S_{13,7}$	$S_{13,8}$	$S_{13,9}$	$S_{13,10}$	$S_{13,11}$	$S_{13,12}$	$S_{13,13}$	$S_{13,14}$	$S_{13,15}$	$S_{13,16}$	$S_{13,17}$
#14	$S_{14,1}$	$S_{14,2}$	$S_{14,3}$	$S_{14,4}$	$S_{14,5}$	$S_{14,6}$	$S_{14,7}$	$S_{14,8}$	$S_{14,9}$	$S_{14,10}$	$S_{14,11}$	$S_{14,12}$	$S_{14,13}$	$S_{14,14}$	$S_{14,15}$	$S_{14,16}$	$S_{14,17}$
#15	$S_{15,1}$	$S_{15,2}$	$S_{15,3}$	$S_{15,4}$	$S_{15,5}$	$S_{15,6}$	$S_{15,7}$	$S_{15,8}$	$S_{15,9}$	$S_{15,10}$	$S_{15,11}$	$S_{15,12}$	$S_{15,13}$	$S_{15,14}$	$S_{15,15}$	$S_{15,16}$	$S_{15,17}$
#16	$S_{16,1}$	$S_{16,2}$	$S_{16,3}$	$S_{16,4}$	$S_{16,5}$	$S_{16,6}$	$S_{16,7}$	$S_{16,8}$	$S_{16,9}$	$S_{16,10}$	$S_{16,11}$	$S_{16,12}$	$S_{16,13}$	$S_{16,14}$	$S_{16,15}$	$S_{16,16}$	$S_{16,17}$
#17	$S_{17,1}$	$S_{17,2}$	$S_{17,3}$	$S_{17,4}$	$S_{17,5}$	$S_{17,6}$	$S_{17,7}$	$S_{17,8}$	$S_{17,9}$	$S_{17,10}$	$S_{17,11}$	$S_{17,12}$	$S_{17,13}$	$S_{17,14}$	$S_{17,15}$	$S_{17,16}$	$S_{17,17}$

(1) Reflection coefficients

The reflection coefficients for the symmetric feeds of the lens are depicted in Fig. 3.58-Fig. 3.60. The worst value is appeared on the extreme beam at pointing angle 78° which is the port #1 and we notice in Fig. 3.58(a) that the value of $S_{1,1}$ is above the accepted value of -10 dB. The rest reflection coefficients $S_{i,j}$ for $i \in \{1\text{-}8\}$ have been matched and take values less than -10 dB over the whole Ku-band.

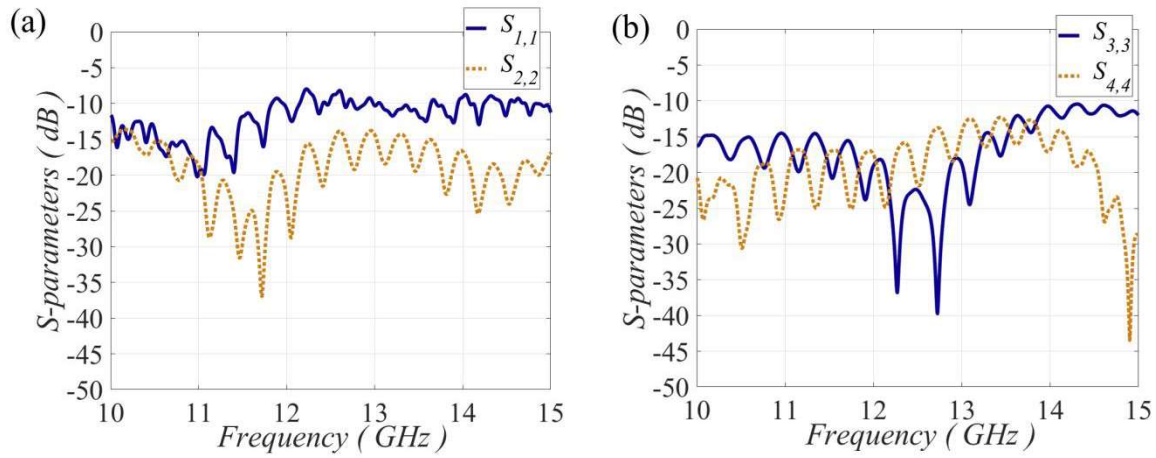

Figure 3.58: Reflection coefficients when (a) feed port #1 and #2 are separately excited, (b) feed port #3 and #4 are separately excited.

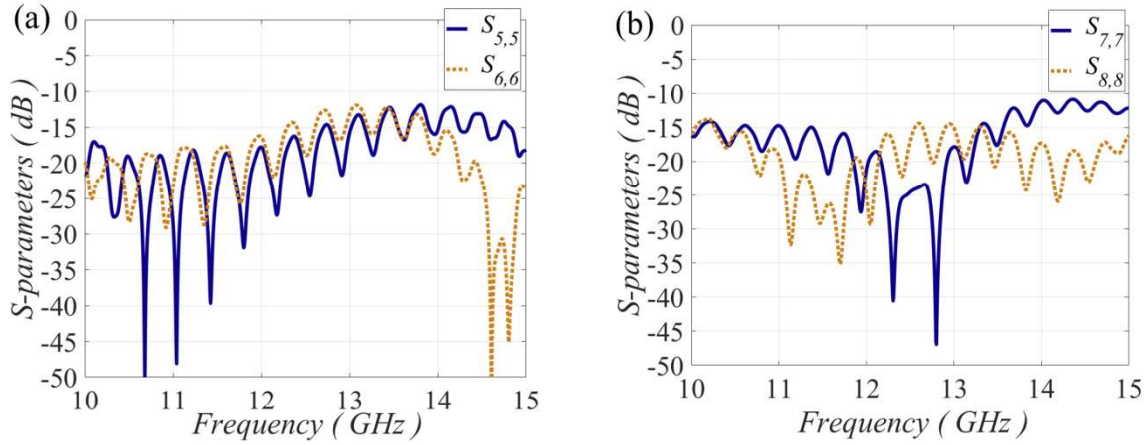

Figure 3.59: Reflection coefficients when (a) feed port #5 and #6 are separately excited, (b) feed port #7 and #8 are separately excited.

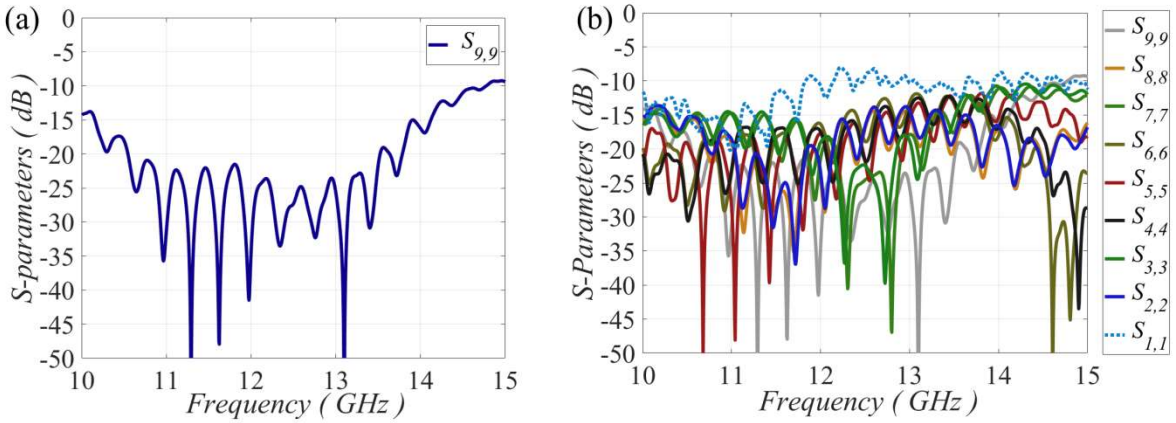

Figure 3.60: Reflection coefficients (a) of the feed port #9 which is placed on broadside direction, (b) of all the feeds of the Gutman lens.

(2) Coupling coefficients

The coupling coefficients are defined when a single feed is excited and the rests have a 50 ohm load. Therefore, when the feed port #1 is excited the isolation parameters are specified. The worst cases for the coupling parameters are presented in Fig. 3.61(a-d). The first case is the excitation of the extreme feed port #1. In this case the worst isolation parameters are the adjacent feed port #2 as well as the extreme opposite feed port #17. Besides, the isolation for the broadside feed port #8 is illustrated. According to Fig. 3.61(a), energy is transmitted into the extreme opposite feed #17 when the port #1 is excited. However, it is not significant. For the rest cases the coupling coefficients take values above -20 dB over the total Ku-band.

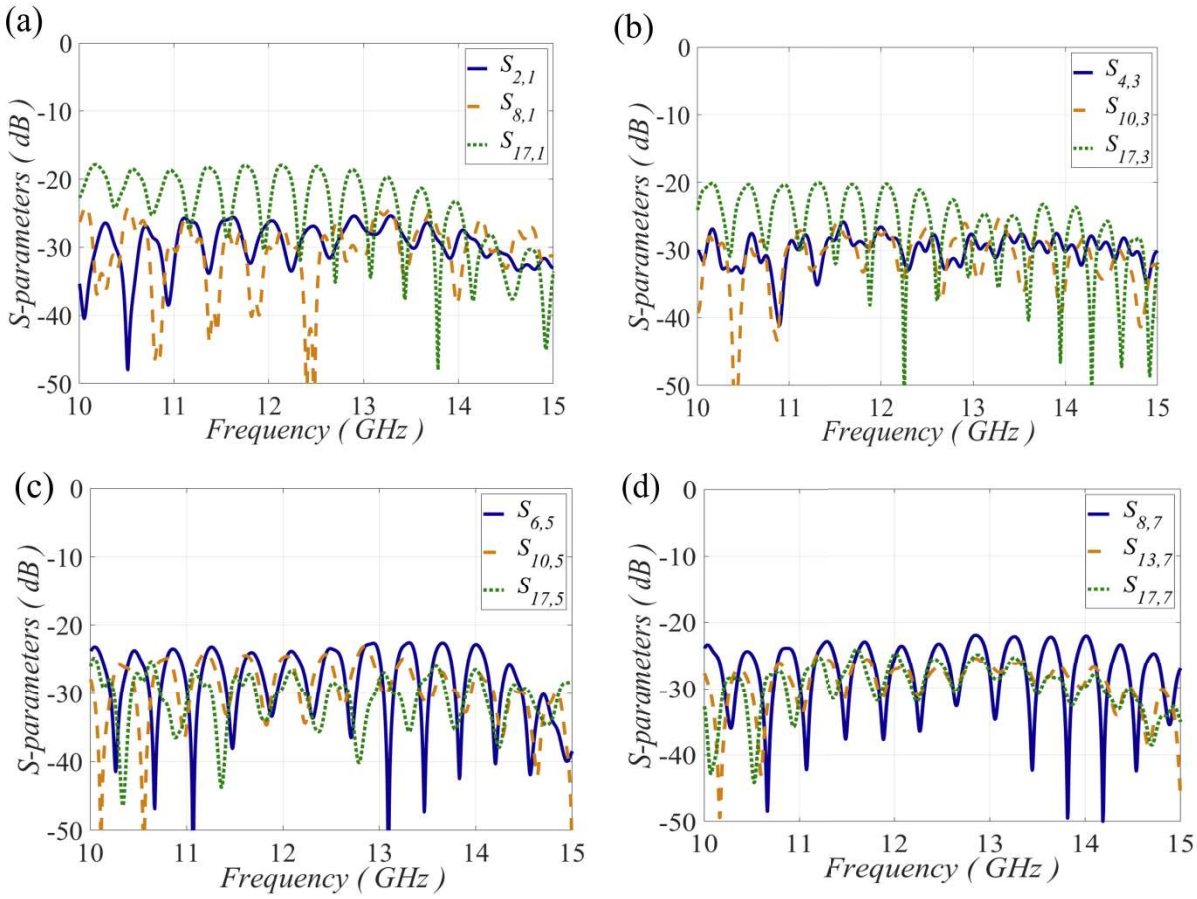

Figure 3.61: Coupling parameters when we excite the feed port (a) #1, (b) #2, (c) #5, (d) #7.

3.7 Conclusions

In this Chapter the Gutman lens antenna with focal point $f=R/2$ has been presented. The interleaved glide index unit-cell introduced and has been further investigated. It has been proved that interleaved glide symmetry periodic structures lead to high effective index of refraction with low dispersion.

A design methodology has been analysed to synthesize the lens. It is a simple and practical method which can be applied in every metasurface lens which has circular symmetry. The radiation performance of the lens examined for three identical scenarios. First, the lens as a single beam radiator. Afterwards, the lens as a reconfigurable radiator and finally the lens as a multi-beam antenna. The latter is the proposed demonstrator of this Chapter.

The single ridge waveguide has been selected to excite the lens along its focal arc. The compact size of that feed resulted on the integration of 17 feeds. A parametric study on the design parameters of the single ridge realized to evaluate its characteristic impedance. A matching methodology has been presented to match the characteristic impedance of the lens into the characteristic impedance of the single ridge waveguide. A single ridge waveguide to microstrip transition has been proposed to excite the proposed demonstrator. Finally, the simulation results on the radiation of the lens as well as on the reflection and the isolation parameters have been illustrated.

Chapter 4 All-Metal Graded Index Gutman Lens Antenna with focal point *f=R*/2 in a PPW technology – Prototyping and experimental tests

Contents

4.1 Mechanical antenna design

The mechanical design of the Gutman lens antenna is the subsequent step in order to manufacture the demonstrator. The ultimate scheme is depicted in Fig. 4.1(a, b).

-Multiple constraints need to be fulfilled:

- First, stiff connexion between the two PPW metal plates has to be secured through *z* axis.
- Second, the dielectric has to be manually connected on the bottom metal PPW plate.
- Soldering is necessary between the inner conductor of the coaxial probe and the microstrip line printed on the dielectric to provide good electrical contact. Misalignments have to be prevented.
- Furthermore, soldering is required to link the microstrip line with the single ridge waveguide.
- Finally, a mechanical support must be designed and attached to the lens to properly mount the antenna prototype on the receiving mast of the anechoic chamber.

The screws and the dowels that have been placed on the edge metal part of the antenna, as well as on the focal arc region of the lens, are visible in Fig. 4.1 (a,b). Furthermore, screws have been placed on the center of the top and bottom part of the lens to connect the mechanical support. Aluminium material has been selected for the metal plates of the lens.

Segregate parts of copper bricks have been manufactured and are connected to the aluminium top PPW plate. The integration of the copper bricks makes doable the soldering between the brick and the microstrip line, since both consist of copper material. The base of the mechanical structure has been strategically defined d=220 mm, since absorbers will be placed between the SMA connectors and the measurement mast. Precise details for every mechanical part of the lens are provided in the next Subsection 4.1.1.

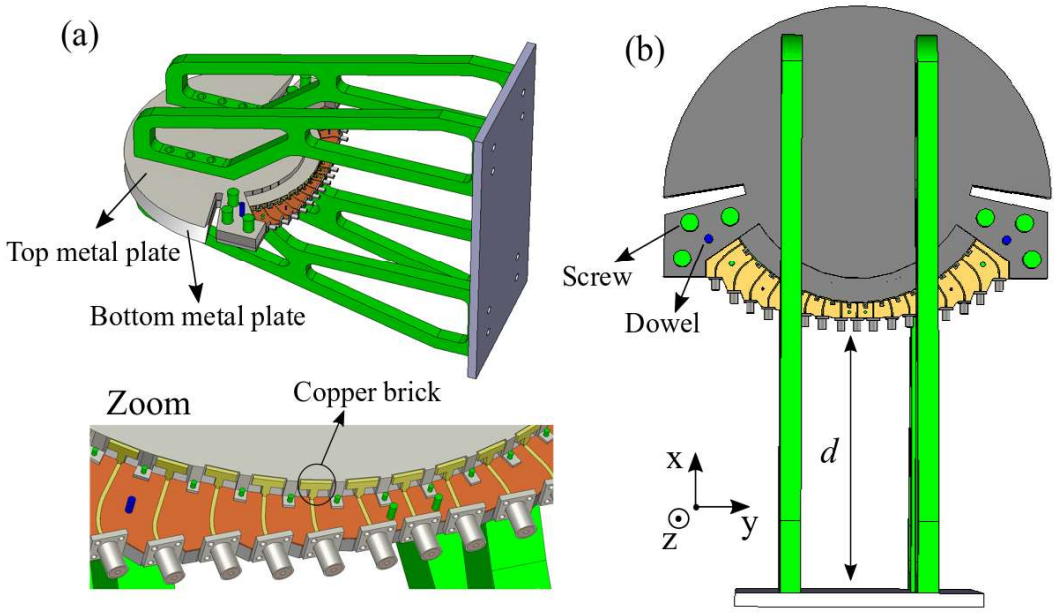

Figure 4.1: (a) Perspective view of the mechanical model of the Gutman lens antenna, (b) 2D view.

4.1.1 Stability of both PPW plates

The firm connection of the two PPW metal plates of the antenna is a major factor to avoid misalignments and air gaps. Both metal plates are heavy components and have to be stabilized and tightly fixed. For that purpose, extended metal surfaces have been designed on the lens to generate a supplementary metal face in order to incorporate screws between the top and the bottom metal plate.

The primary metal region that has been designed is depicted in Fig. 4.2(a). It consists of both top and bottom metal part of the lens which they have been stacked. In that area which lies close to the edge of the lens, 3 screws have been on each side placed between the top and bottom metal plates to guarantee steady connexion along z axis. In order to establish a further stability and avoid misalignments along x and y axes, a dowel has been additionally integrated. Therefore, misalignments along x, y and z axes have been prevented with the installation of both screws and dowels.

A sensitive factor of this mechanical design originates from the composition of the single-ridge waveguide. Possible misalignments on the connection of both metals plates may lead to additional loss in the transition. In order to avoid these mismatches, screws have been placed on the extended metal region between the stepped ridge transformer (see Fig. 4.2(b, c)).

Fig. 4.2(d) shows the copper brick that has been manufactured separately and attached to the top metal plate. This brick has been added in order to solder the microstrip line with the single-ridge waveguide part. The latter is vital considering that the line is composed of

copper material and electrical connexion is not feasible with the top metal plate made in aluminium.

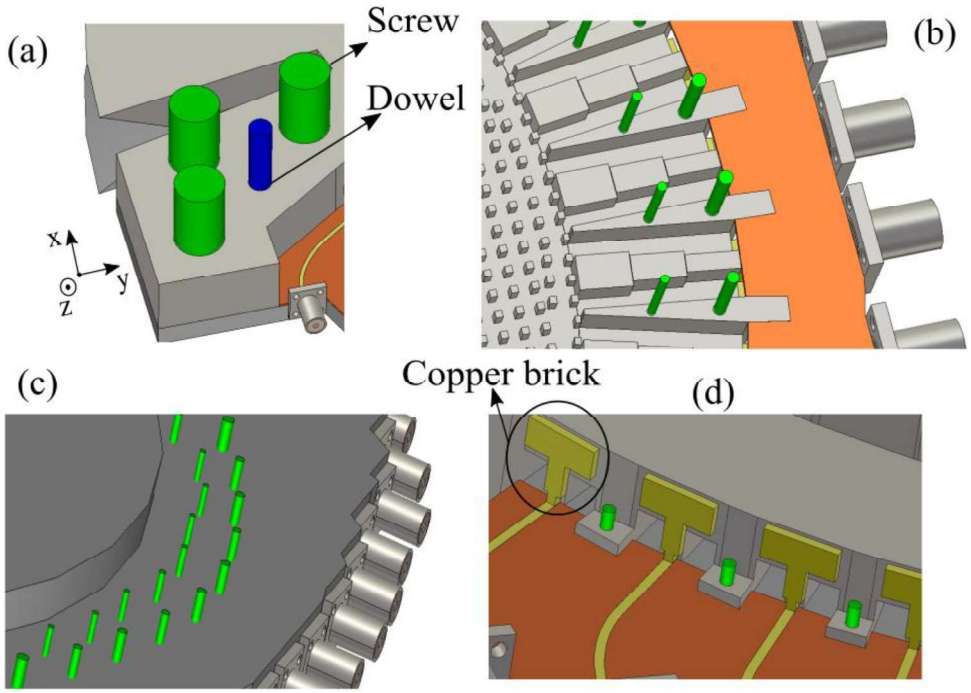

Figure 4.2: (a) Screws and dowel are placed on the edge metal part of the antenna, (b) screws placed between the waveguides, (c) side view of the screws between the waveguides, (d) screws placed on the extended metal part at the end of the microstrip line.

4.2 Design of the mechanical transition

The proposed mechanical design of the transition is depicted in Fig. 4.3(a), and its 2D cut view is represented in Fig. 4.3(b). The dielectric is dual side grounded, since its bottom part is bonded with the bottom metal plate and electrical connexion has to be assured. Soldering has been realised to attach the microstrip line with the inner conductor of the SMA coaxial probe.

The challenge in the transition here is to solder the microstrip line with the single ridge section. The single ridge face is made in aluminium material, and soldering is not feasible with the microstrip line in copper. Furthermore, the dielectric slab has been manufactured separately. As it is connected with the single ridge part, stability needs to be addressed, since the whole antenna volume is heavy.

The solution proposed here consists in introducing a metal brick (in copper), as represented in Fig. 4.3(c). The brick provides two significant contributions. First, it stabilizes the dielectric, since the brick is attached to the microstrip line. Additionally, soldering is now doable between the microstrip line and the brick, since they are both made in copper.

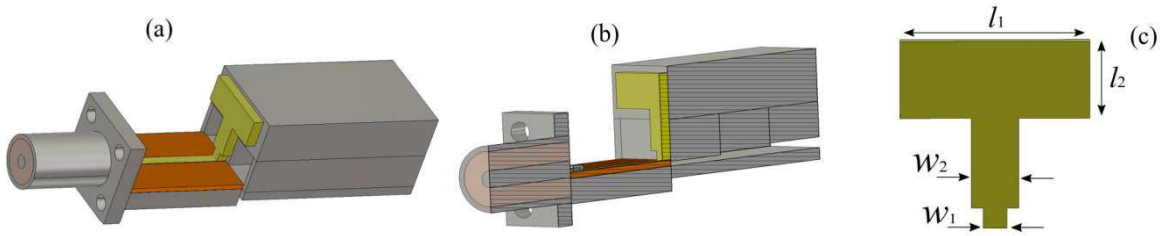

Figure 4.3: Mechanical design model of the transition (a) perspective view, (b) 2D view, (c) copper brick with dimensions, $\boldsymbol{w_1}$=1, $\boldsymbol{w_2}$=2, $\boldsymbol{l_1}$=8, $\boldsymbol{l_2}$=3, all in mm.

Initial design transition vs mechanical model transition

The integration of the copper brick on the transition ensured the consistent connexion of the dielectric slab on the whole antenna. It has further improved the reflection performance of the transition. Fig. 4.4 shows a comparison between the initial transition and the mechanical design. The transition with the integrated copper brick leads to lower reflections in comparison with the transition with the absence of the brick.

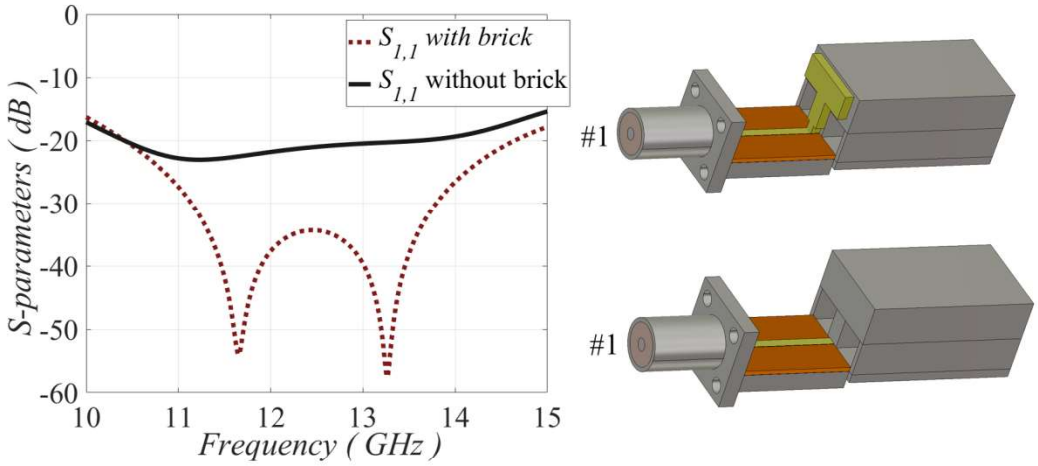

Figure 4.4: Comparison of the transition with the copper brick and without it.

4.2.1 Sensitivity test

The dual metalized dielectric slab has been separately manufactured and then manually attached to the bottom PPW metal plate. During this manual operation, possible slight misalignments are expected and need to be addressed. Therefore, sensitivity tests have been applied through numerical simulations to evaluate the performance of the mechanical transition model for segregate scenarios.

The foremost hypothesis that is considered here is a small air gap between the dielectric and the single ridge. This air gap is represented by the distance *x* in Fig. 4.5. The tiny piece of metal that is attached to the microstrip line and the copper brick mimics the soldering. It is observed that the level of the reflection increases when the air gap is large, although the bandwidth is slightly increased. Hence, wide air gaps induce additional reflections; however in all cases the reflection coefficient remains below -20 dB.

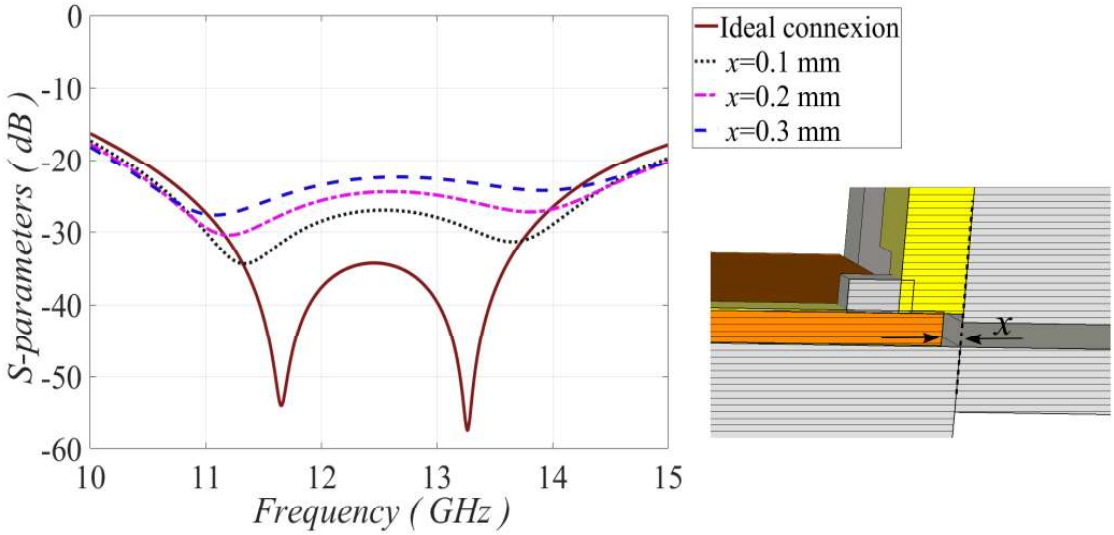

Figure 4.5: Misalignment sensitivity test when the distance, *x*, varies.

The second hypothesis that is considered is the air gap between the copper brick and the dielectric (see Fig. 4.6). This air gap, represented by distance *z*, varies from 0 to 0.5 mm. For these numerical tests, the distance *x* remains constant (*x*= 0.2 mm). The numerical results are provided in Fig. 4.6. In this figure, we observe that large air gap values lead to significant mismatch. However, the present scenario is the extreme hypothesis where air gap exists between the dielectric and both copper brick and single ridge.

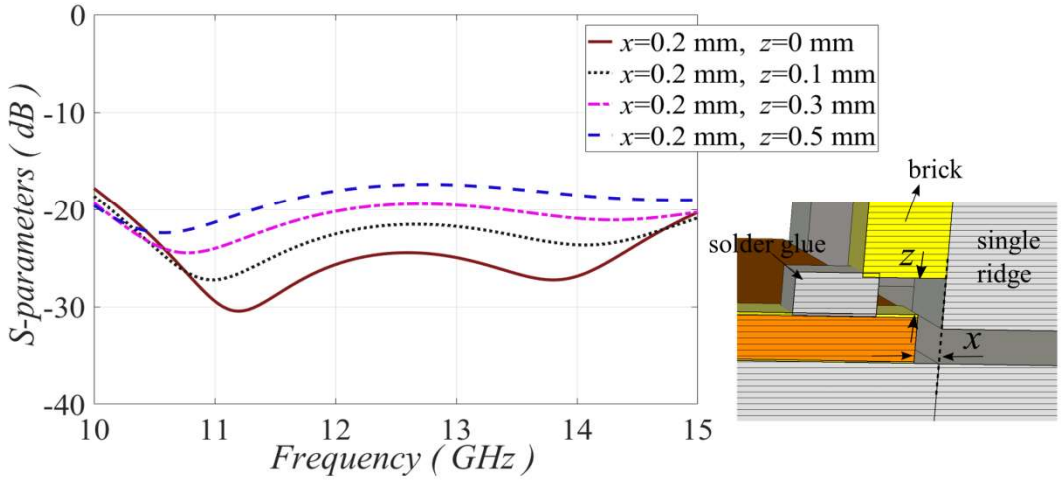

Figure 4.6: Misalignment sensitivity test when the distance, *z*, varies and the distance, *x* is constant.

4.3 Mechanical design process

-The mechanical parts of the antenna are divided into two structures:

- The first part is the bottom metal plate with the modulated periodic structures,
- The second one is the top metal plate with the modulated metal posts and all the integrated feed.

The material that has been used for both metal plates is aluminium. Both parts have been manufactured using the traditional milling technology. Eventually, the machine used to fabricate the proposed demonstrator was a Computer Numeral Control (CNC) 5 axis milling center (DECKEL MAHO) available at IDONIAL, partner of the REVOLVE project. The manufacturing procedure is comparable for both metal plates despite slight differences; it is descripted in the following Subsection 4.3.1 and Subsection 4.3.2

4.3.1 Mechanical design procedure of the bottom metal plate

Sketch the height of the metal posts

The objective here is to propose a mechanical design that is low cost and effective. Thousands metal posts need to be manufactured, and the milling machine needs to be programed in the most efficient way in order to reduce the manufacturing time as much as possible (the most important cost of the prototype is the working hours of the CNC machine). Therefore, the incentive here is to program the CNC to perform the smartest milling path to form all the modulated metal posts. It follows the mechanical parts of the bottom metal plate that have been progressively manufactured by the CNC machine; this procedure leads to a low cost design.

-An outline of all the design steps of the CNC is presented below:

- Form a rectangular aluminium plate
- Sketch the profile of the post heights
- Outline the focal arc of the lens
- Sketch the shape of the rectangular aluminium to place the dielectric

-The above steps are thoroughly explained below.

The foremost step that has been addressed is a rectangular aluminium metal plate that is illustrated in Fig. 4.7(a, b). This is the maximal metal volume; the CNC starts to subtract progressively metal surfaces in different phases to form the demonstrator.

The initial path of the cutting tool of the spindle of the CNC has been programed to form a metal surface which corresponds to the height of the bottom metal plate posts. For that purpose, a step file with the 3D surface is imported to the CNC which starts to mill over the whole surface of the rectangular aluminium plate. This 3D surface has been designed in the previous Chapter 3 and it has been explicitly analysed in Subsection 3.3.1. Since, the 3D step file has been imported to the CNC, the cutting tool creates a cymbal shape metal surface which is defined in Fig. 4.7(c). The cymbal shape represents the height of the metal posts along z axis.The next step of the CNC is to sketch the outline of the focal arc of the Gutman lens (Fig. 4.7(d)).

The final process is the formulation of the outline of the dielectric that is placed on the aluminium (Fig. 4.7 (e)). It needs to be mentioned that the distance, d, represents the length of the dielectric that is placed on the bottom aluminium plate, plus the length of the stepped single ridges. The ridges have been integrated on the focal arc of the top aluminium plate and are presented in the next subsection. The dielectric that has been settled on the bottom aluminium plate is shown in Fig. 4.7(f).

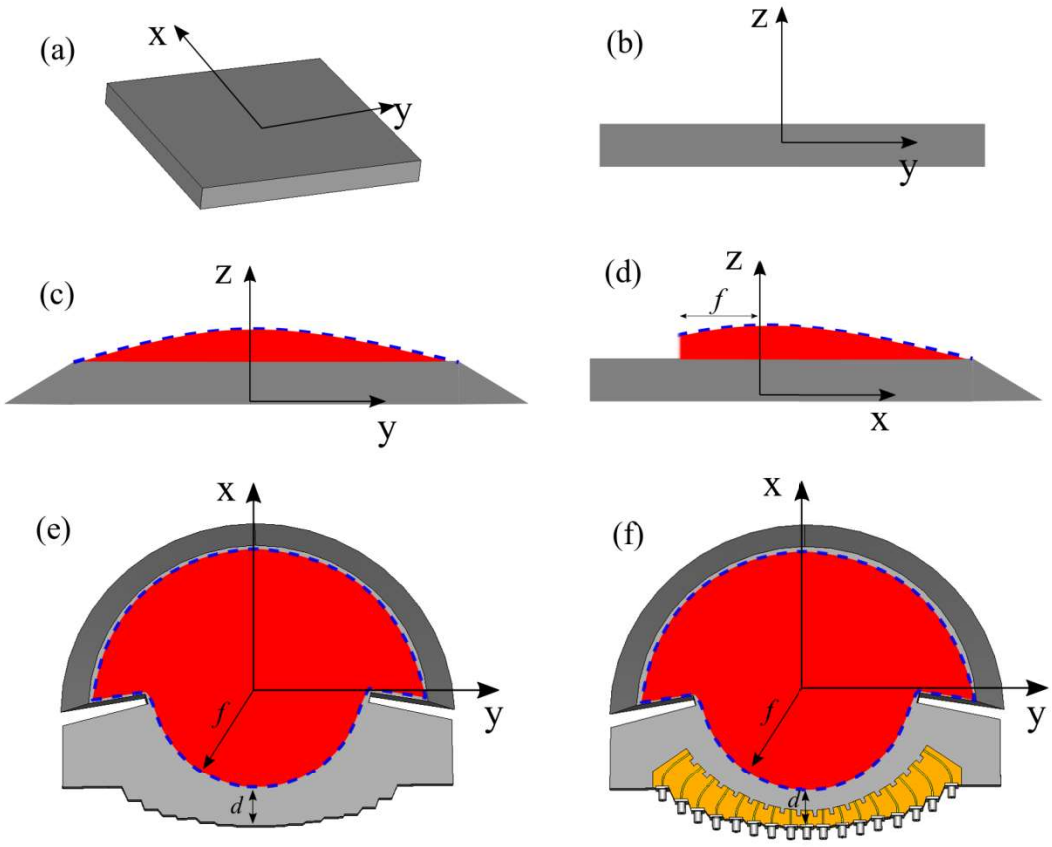

Figure 4.7: (a) Perspective view of aluminium rectangular plate, (b) 2D cut view of the rectangular aluminium plate (c) cymbal shape metal surface, (d) focal arc outline of the Gutman lens, (e) outline of the dielectric, (f) dielectric placement on the completed bottom plate.

Fabrication of the bottom metal posts

The ultimate stage of the mechanical design is the fabrication of the metal pins. From the previous mechanical procedure that has been presented, the CNC has manufactured a metal surface in a shape of a cymbal which mimics the height of all metal posts. In order to fabricate the pins, the milling paths through the whole cymbal shape surface need to be programed appropriately in the CNC machine. At this stage the cutting tool has been moved only through the *xy* plane.

The most efficient and quickest path has been defined and imported along the computer station of the CNC. The proposed solution here is the design of a $2K \times 2K$ matrix that is illustrated in Fig. 4.8(a). The parameter K is the discretized value which is equal to $K=52$ and has been described in Section 3.3. The 3D matrix consists of $2K$ vertical metal slabs and $2K$ horizontal metal slabs. All of them have equal height along z axis ($z=3.6$ mm). This height value is the maximum height of the metal post that is placed on the center of the lens. It needs to be mentioned that this matrix is only the guidance of the CNC in order to detect the paths that the cutting tool is going to pass. With the help of that matrix the cutting tool is now aware of the paths which are divided in two parts. First, the cutting tool subtracts the metal through the horizontal, y axis as it is shown in Fig. 4.8(b). Then, it passes through the vertical, x axis removing the rest metal surfaces. As a result, the modulated metal pins have

been manufactured (see Fig. 4.8(b)). In order to assimilate the operation of the matrix, 2D views are illustrated. In Fig. 4.8(c) shows the vertical metal slabs of the matrix integrated into the cymbal shape metal surface in *yz* plane. The horizontal metal slabs of the matrix integrated into the cymbal shape metal surface in *xz* plane are shown in Fig. 4.8(d). Since, the cutting tool has passed through both vertical and horizontal directions, the cross-section views of the fabricated modulated metal posts are represented in Fig. 4.8(e) and Fig. 4.8(f).

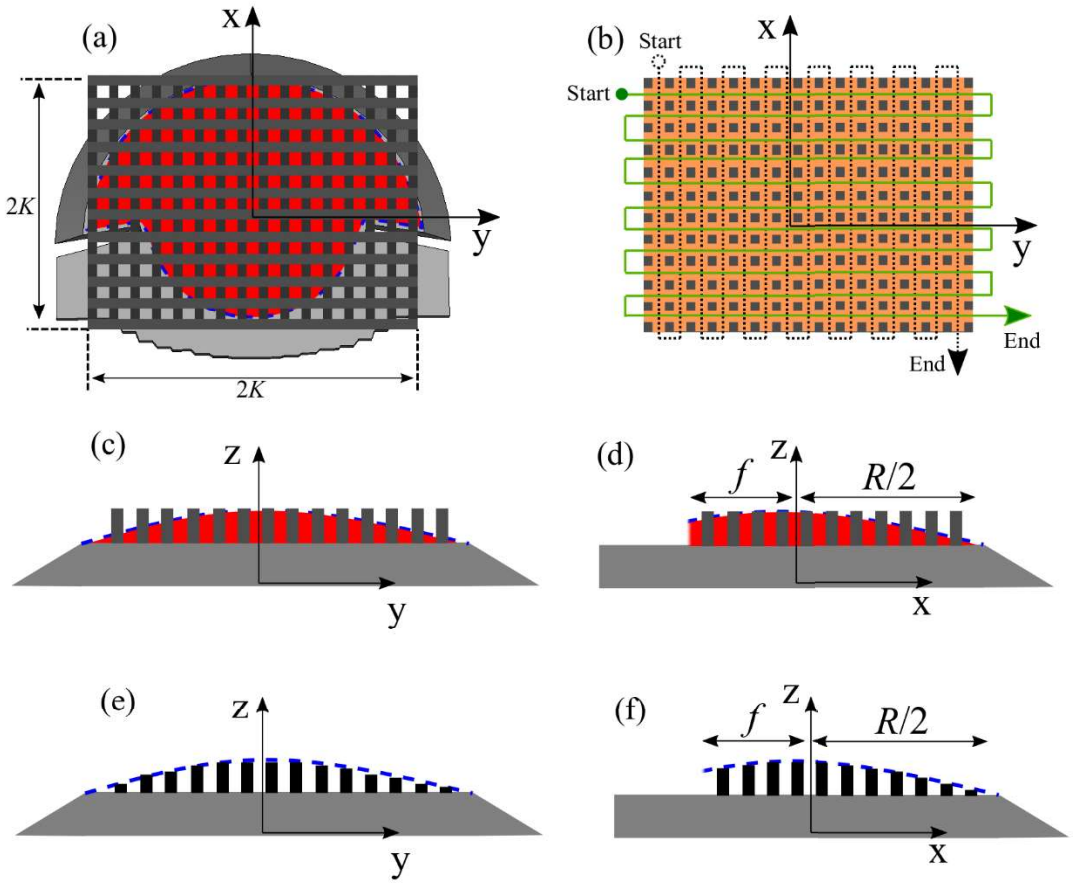

Figure 4.8: (a) $2K \times 2K$ matrix on the bottom metal plate, (b) paths of the cutting tool through the matrix (c) 2D view of the vertical slaps of the matrix on the cymbal surface, *zy* plane (d) 2D view of the horizontal slaps of the matrix on the cymbal surface, *zx* plane (e) modulated bottom plate pins, *zy* plane, (f) modulated bottom plate pins, *zx* plane.

4.3.2 Mechanical design procedure of the top metal plane

We describe here the stages implemented to manufacture the top PPW plate of the demonstrator. The procedure is similar to the bottom plate that has been presented in the above Subsection 4.3.1. The differences are highlighted.

Sketch the outline height of the metal posts and the feeds

The foremost step is to insert a rectangular aluminium metal (see Fig. 4.9(a, b)) to the CNC machine to begin the milling process. The cutting tool formulates a cymbal shape metal surface and its 2D view on *yz* plane is shown in Fig. 4.9(c). This surface has been manufactured using a 3D spline which represents the height of the top plate metal posts. Consequently, the tool mills the metal surfaces that are required to create the Gutman lens profile. For instance, Fig. 4.9(d) represents a 2D view in the *zy* plane. The difference in this

scenario compared to the bottom plate of the previous subsection lies on the integration of the stepped ridges. The cutting tool sketches the lens profile and the outline of the stepped ridges that are attached on the cymbal shape surface (see Fig. 4.9(d)). A top view of the layout of the top aluminium plate is illustrated in Fig. 4.9(e) where it is noticed that the cymbal shape surface is connected to all the integrated feeds.

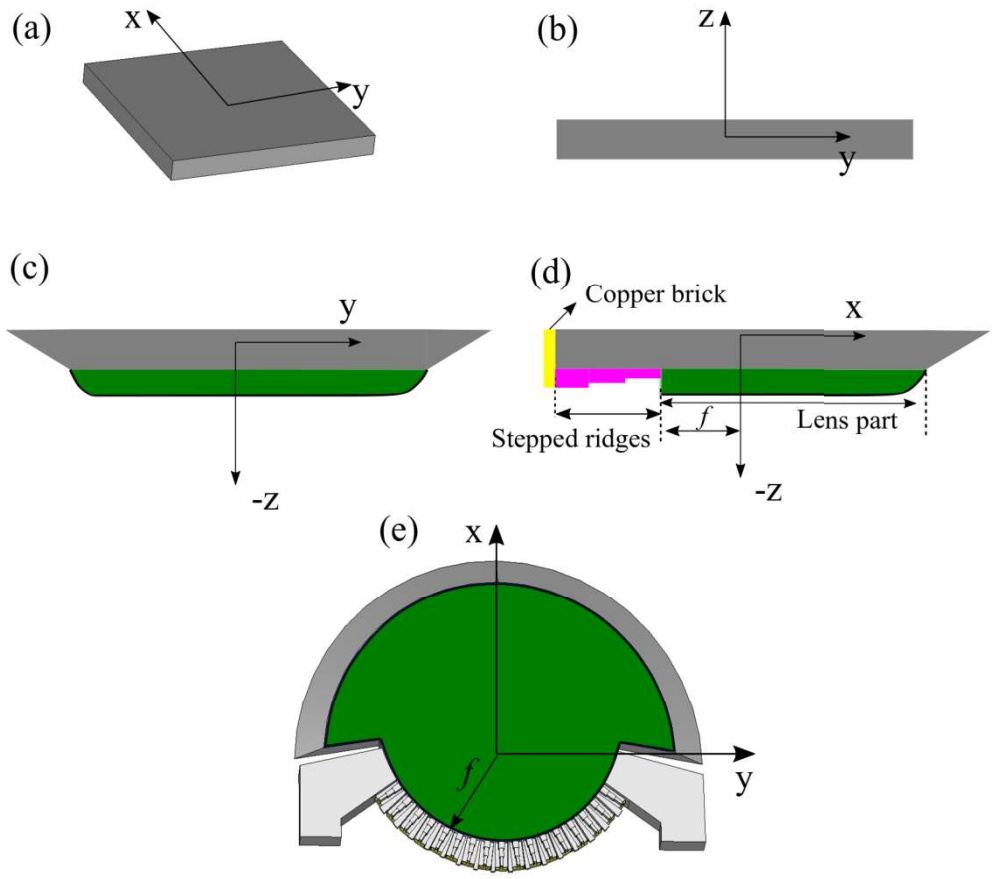

Figure 4.9: (a) Perspective view of aluminium rectangular plate, (b) 2D cut view of the rectangular aluminium plate (c) sketch of the height of the metal posts, (d) focal arc, stepped ridges and copper brick outline of the Gutman lens, (e) front view layout of the top plate.

Form the top metal posts

Since the cymbal shape surface with the integrated stepped ridges have been completed, the cutting tool proceeds to the composition of the pins. The $2K \times 2K$ matrix is imported to the CNC program and is depicted in Fig. 4.10(a). The tool follows the milling path depicted in Fig. 4.11(b); the procedure is similar to the one descripted in Subsection 4.3.1 for the bottom plate. The distinction here is the manufacturing of the stepped ridges which are attached to the metal pins on the focal arc of the Gutman lens (see Fig. 4.10(d)). The final scheme of the bottom plate is illustrated in Fig. 4.10(e) and Fig. 4.10(d) in the *yz* and *xz* planes, respectively.

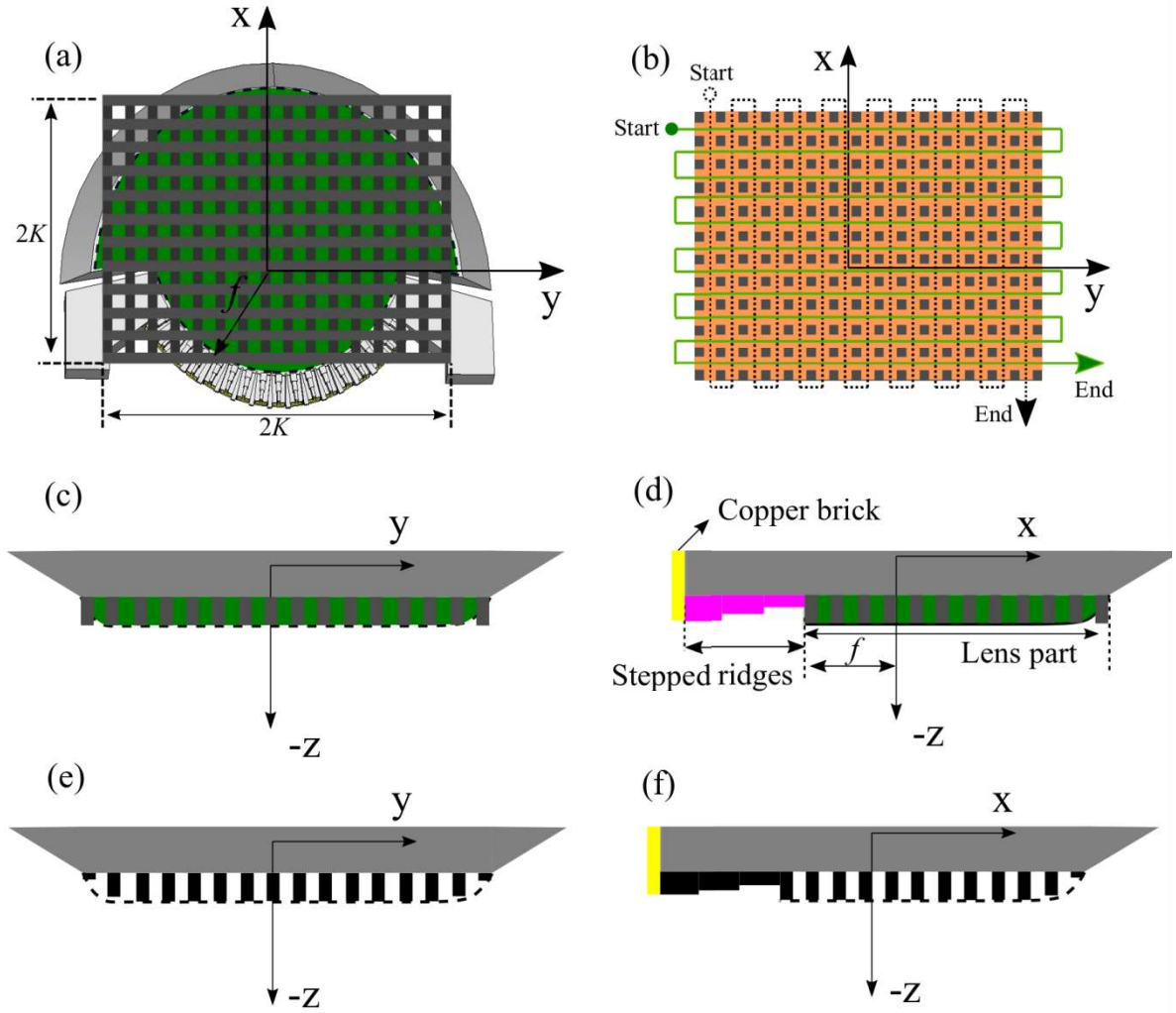

Figure 4.10: (a) $2K \times 2K$ matrix on the top metal plate, (b) paths of the cutting tool through the matrix (c) 2D view of the vertical slaps of the matrix on the cymbal surface, *zy* plane (d) 2D view of the horizontal slaps of the matrix on the cymbal surface with the integrated stepped ridges, *zx* plane (e) modulated top plate pins, *zy* plane, (f) completed top plate, 2D view on *xz* plane.

4.3.3 Connexion of the two metal plates

The ultimate step is the connexion of the bottom and top aluminium plates. The assembly principle is depicted in Fig. 4.11. Since the 2 plates have been connected, the dual metalized dielectric has been attached to the bottom plate and stabilized through screws and dowels that are placed along *x* axis. The cooper metal brick has been separately manufactured and then manually connected through screws on the top metal plate. To complete the assembly of the prototype, soldering has been realized to provide electrical connexion between the SMA connector and the microstrip line, as well as between the copper brick and the microstrip line.

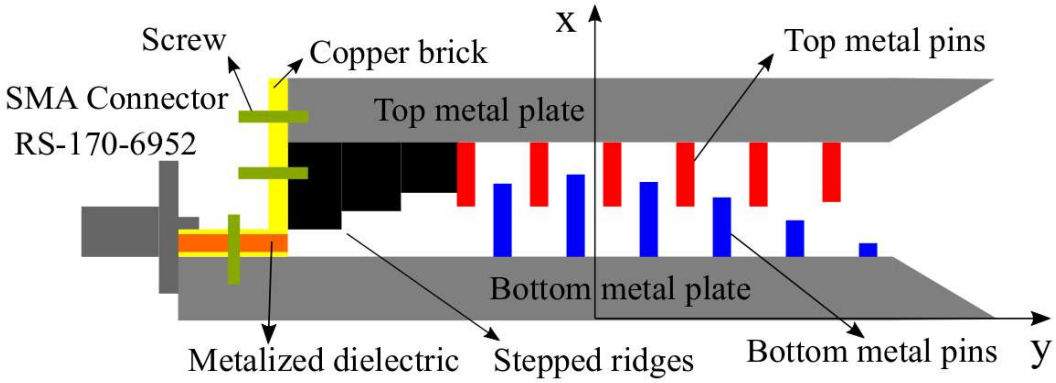

Figure 4.11: Final 2D view of the Gutman lens with the two metal plates connected.

4.4 Prototype

In Fig. 4.12(a) the demonstrator is illustrated. On the edges of the antenna we can observe the three screws and the one dowel that are attached to stuck properly the two metal plates. The connector is attached to the bottom plate by two screws and soldering has been realised between the inner conductor of the SMA connector and the microstrip line. Soldering has been manually realised likewise between the microstrip line and the copper brick. The top and the bottom part of the antenna are illustrated in Fig. 4.12(c) and in Fig. 4.12(d) respectively. The tiny hole of the dielectric represents the screw that will be placed in later stage, the larger hole represents the dowel. Finally, the demonstrator has been connected with the mechanical support (see Fig. 4.12(b)) and is prepared to be mounted on the base of the anechoic chamber for the experimental tests.

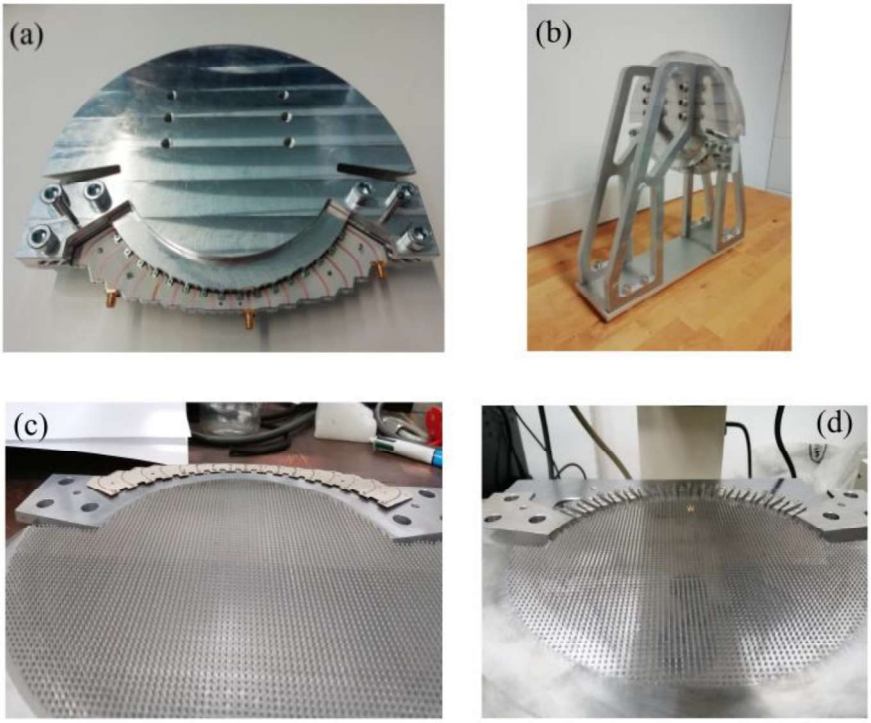

Figure 4.12: (a) Prototype, (b) perspective view of the antenna connected to the mechanical support, (c) bottom plate, (d) top plate.

4.4.1 Measurement setup

Measured Radiation Patterns

Fig. 4.13(a, b) shows the far field pattern measurement setup of the Gutman lens antenna prototype in the IETR centimetric anechoic chamber. The antenna under test (AUT) can rotate around two axis for measurements in the H-plane or in the E-plane. The azimuthal rotation enable the H-plane measurements of the AUT, and the elevation rotation the E-plane measurements. A standard horn antenna which is placed inside the anechoic chamber holds a fix position and operates as a receive antenna. It does not move and measure the power transmitted by the AUT. From this power, the AUT directivity is derived. Solely, the symmetric ports #1-#9 have been measured, due to the high cost of the measurement campaign. Each port has been measured separately, when 50 ohm loads have been connected to the rest ports to avoid interferences. The antenna is operated at Ku-band, although measured patterns will be shown merely from f=12 GHz to f=13 GHz, since the campaign of the experimental test has not yet completed. The rest frequency points will be presented on the presentation of the Ph. D thesis.

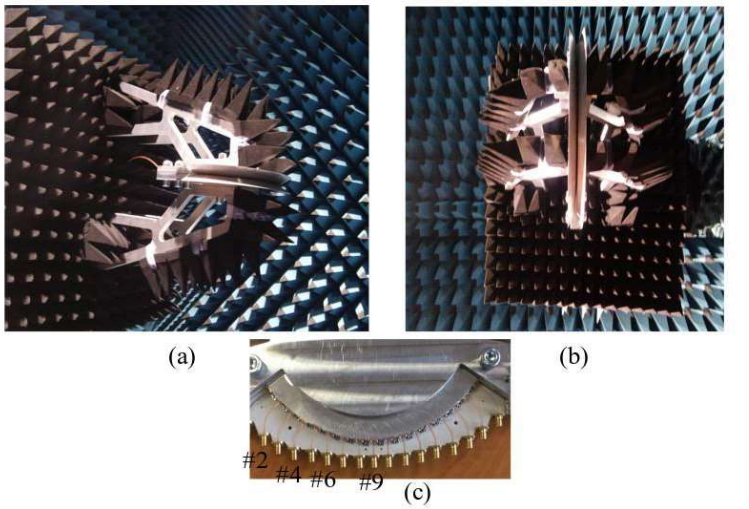

Figure 4.13: Prototype mounted on the anechoic chamber, (a) perspective view, (b) top view.

We notice high level of side lobes for mostly all the radiation patterns. Besides, some deformation of the patterns are ended up for the radiating beams of the ports #2 and #4 at frequency f=13GHz. Manufacturing errors can explain this poor performance in terms or radiation. Some metal pins of the bottom part of the antenna (see Fig. 4.18(a)) have been connected. This leads to a distortion of the electric field inside the Gutman lens antenna and causes distortion of the radiation patterns. Apart from that, there are reflections inside the antenna part which induces side lobes. The bottom part of the antenna is planned to be manufactured again to correct these errors and disconnect the metal pins.

Manufacturing errors in the dielectric are shown in Fig. 4.18(b) and ended up in strong misalignments in the placement of the dielectric onto the bottom part of the prototype. However, these errors influence mainly the matching of the antenna which it is presented in the next subsection.

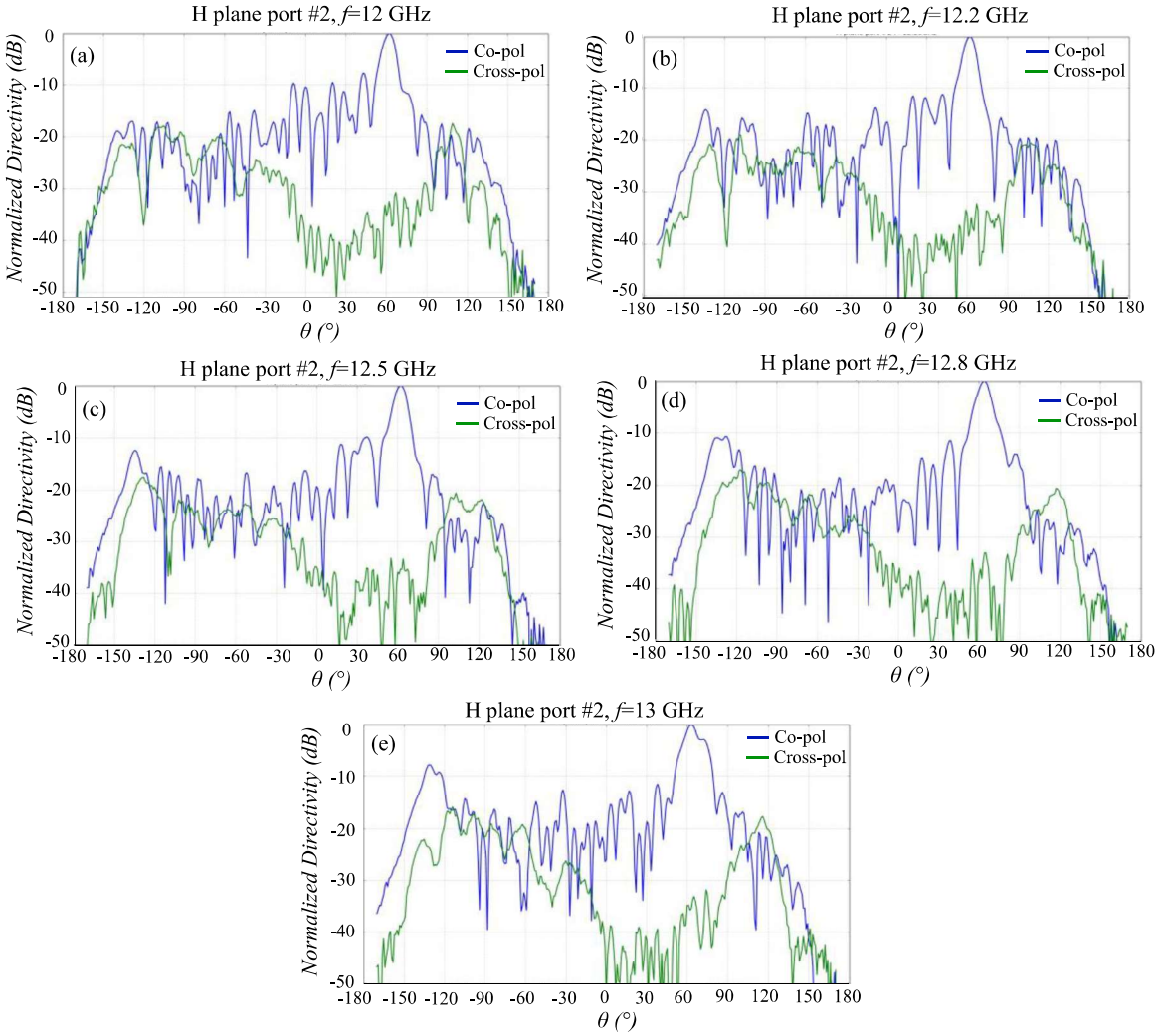

Figure 4.14: Normalized directivity patterns excited the feed port #2.

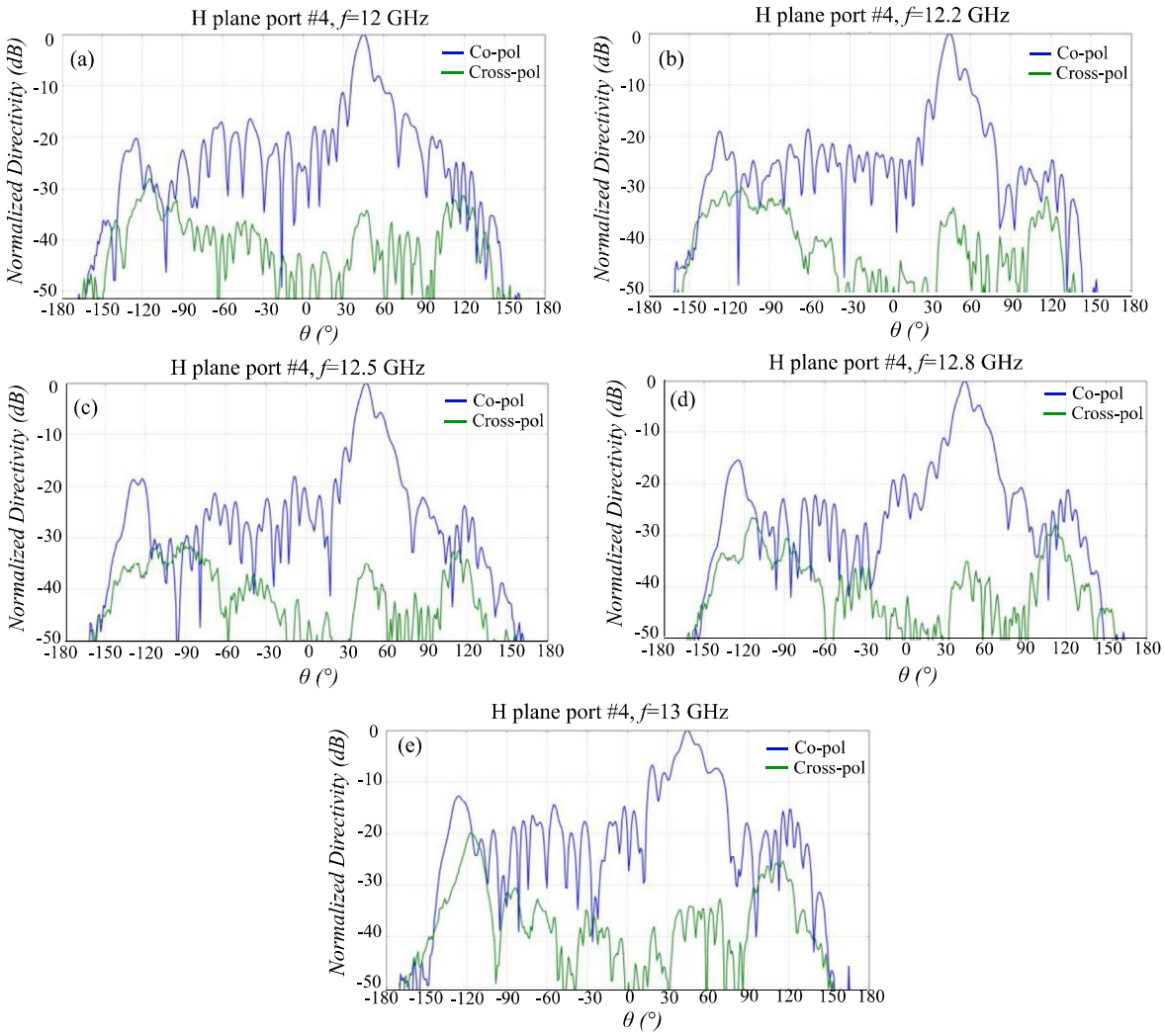

Figure 4.15: Normalized directivity patterns excited the feed port #4.

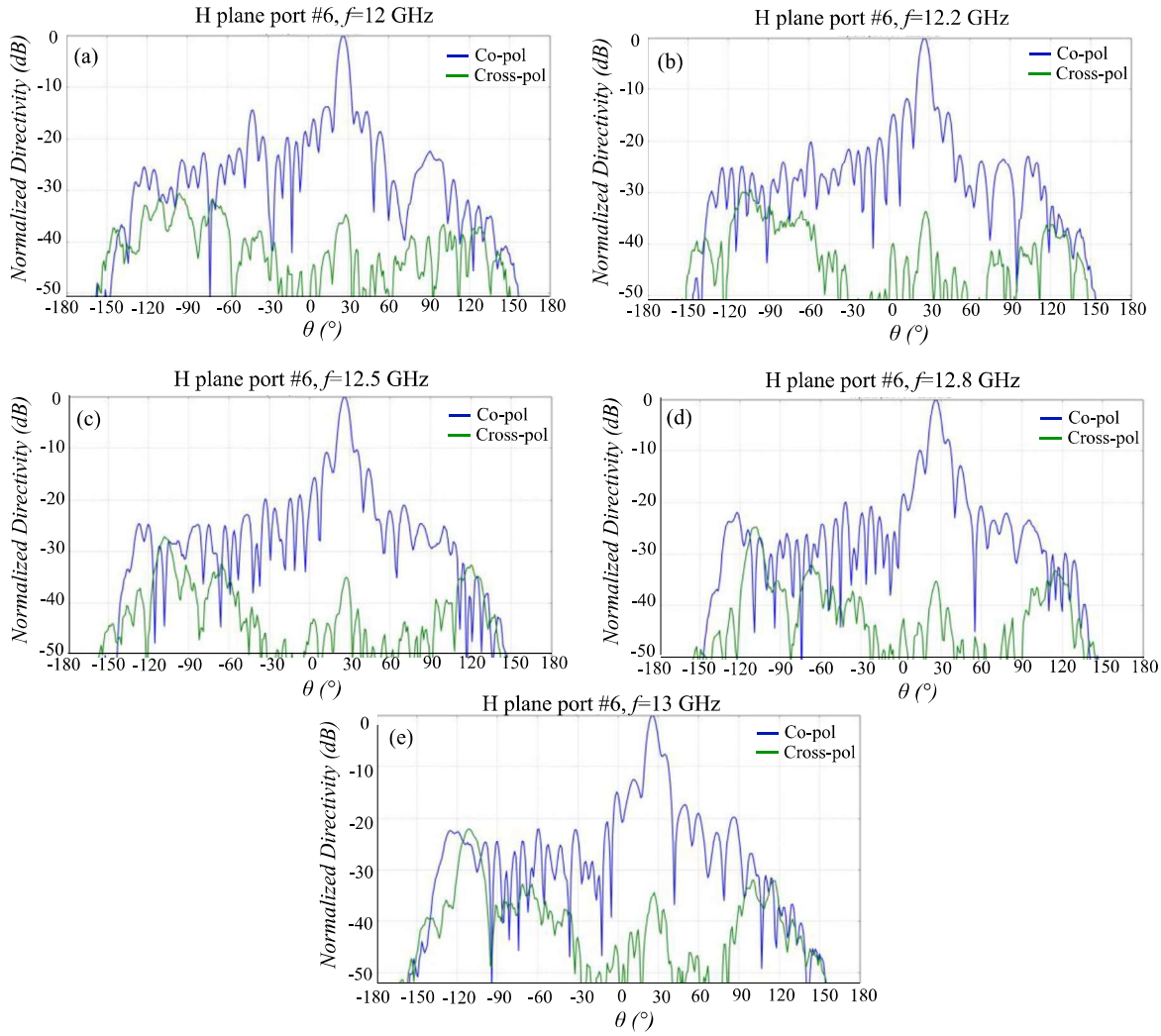

Figure 4.16: Normalized directivity patterns excited the feed port #6.

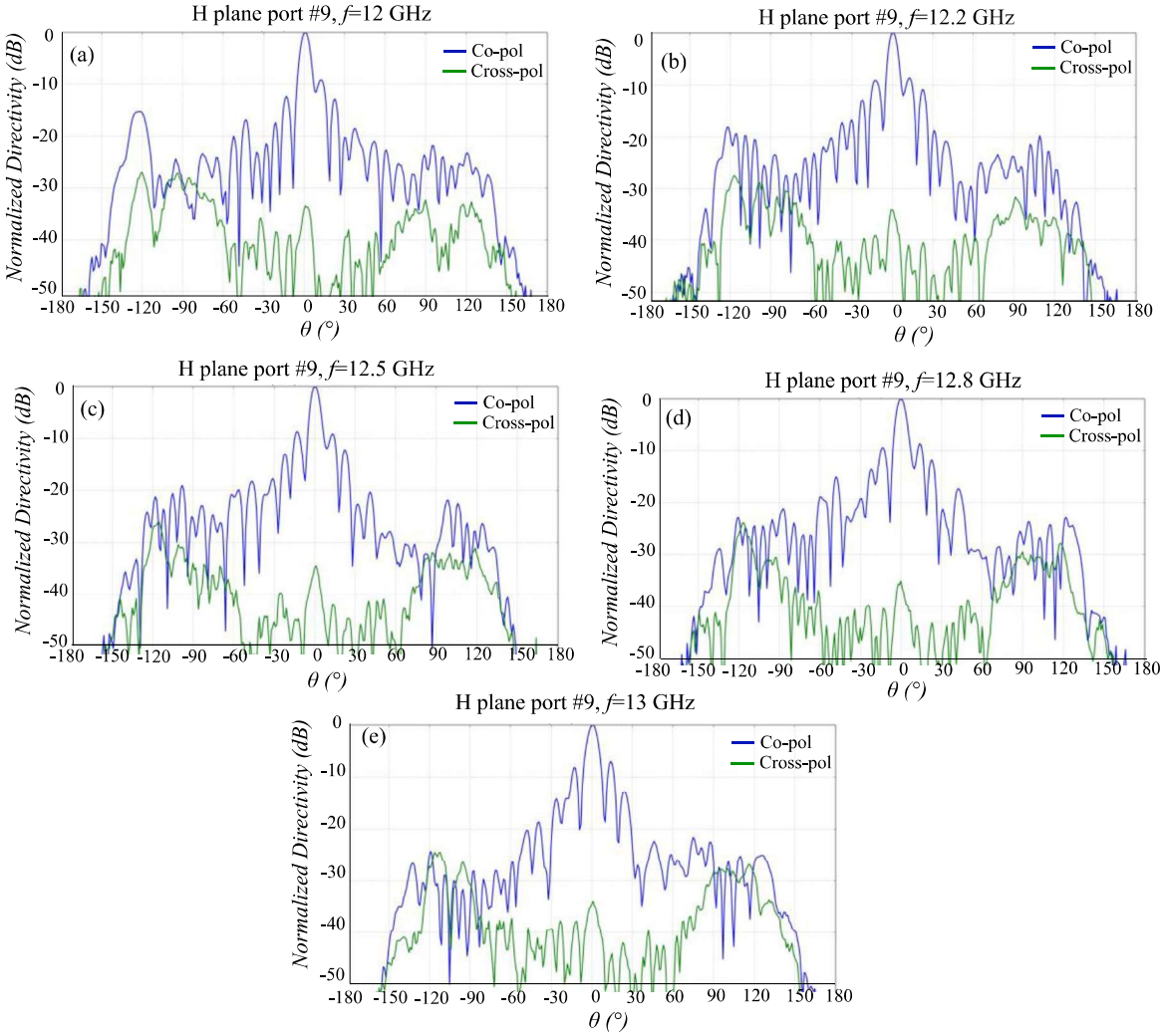

Figure 4.17: Normalized directivity patterns for the broadside beam.

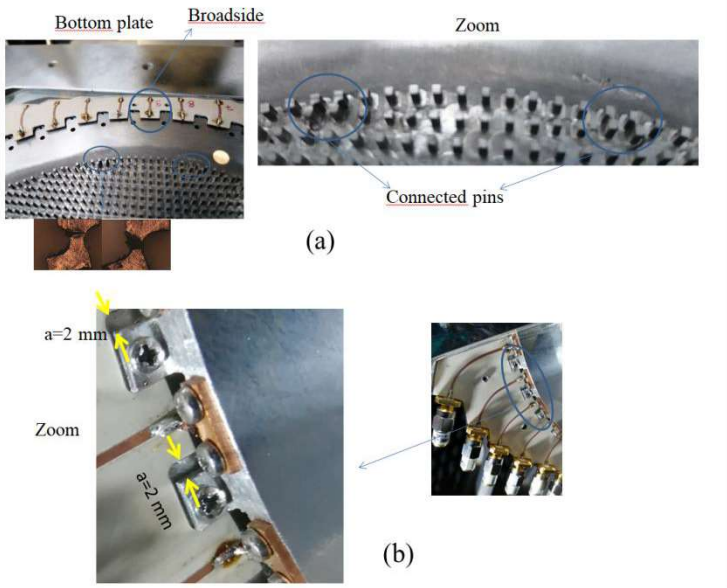

Figure 4.18: (a) Connected pins in the bottom plate of the antenna, (b) strong misalignment of the dielectric.

Measured S-Parameters

The measurements of the S-parameters of the Gutman lens prototype have been realised using a 2-port vector network analyser (VNA), as well as, a 8-port VNA to facilitate the total measurements. The VNA is provided by Keysight and operates from 10 MHz to 26.5 GHz.

First, the VNA has been calibrated using a Short-Open-Load-Thru (SOLT) calibration method. To calibrate the 2-port VNA, each cable has been connected with a coaxial short, a coaxial open and a coaxial load. Then, the a through has been connected to the 2 cables. After the calibration of the VNA, the cables have been connected to each port of the antenna prototype while the rest ports have been connected to 50 ohm loads. An illustration of the prototype connected to the VNA is shown in Fig. 4.19(a, b).

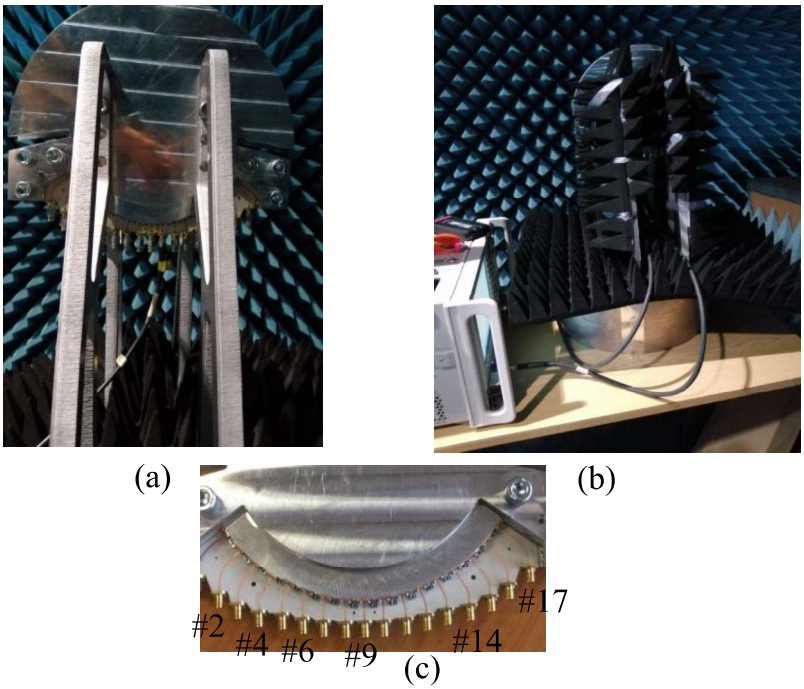

Figure 4.19: (a) Gutman lens antenna prototype inside the anechoic chamber connected to the VNA, (b) Gutman lens antenna prototype protected with absorbers, (c) demonstration of the ports of the prototype.

The measured reflection coefficients of every port of the Gutman lens antenna prototype is shown in Fig. 4.20(a-e). Strong reflections have been caused in mainly the ports that are placed close to the broadside port #9 and the antenna presents narrowband performance. The strong reflections are explained by the misalignments of the dielectric that has been placed on the bottom aluminium part of the antenna. Besides, the dowels and the screws have not been connected before the measurements and resulted in internal losses inside the antenna. Moreover, the metal pins that have been connected in the bottom part of the antenna (see Fig. 4.18(a)) are placed in the focal arc of the lens and cause further reflections to the input RF signal. The dielectric is planned to be fabricated again and properly connected to the antenna lens and then specify on advance the campaign of the experimental tests.

The measured coupling coefficients of the antenna prototype are shown in Fig. 4.21-Fig. 4. 24. The selected ports #1, #8, #9, #10, are shown. Low coupling has ended up between the ports of the antenna.

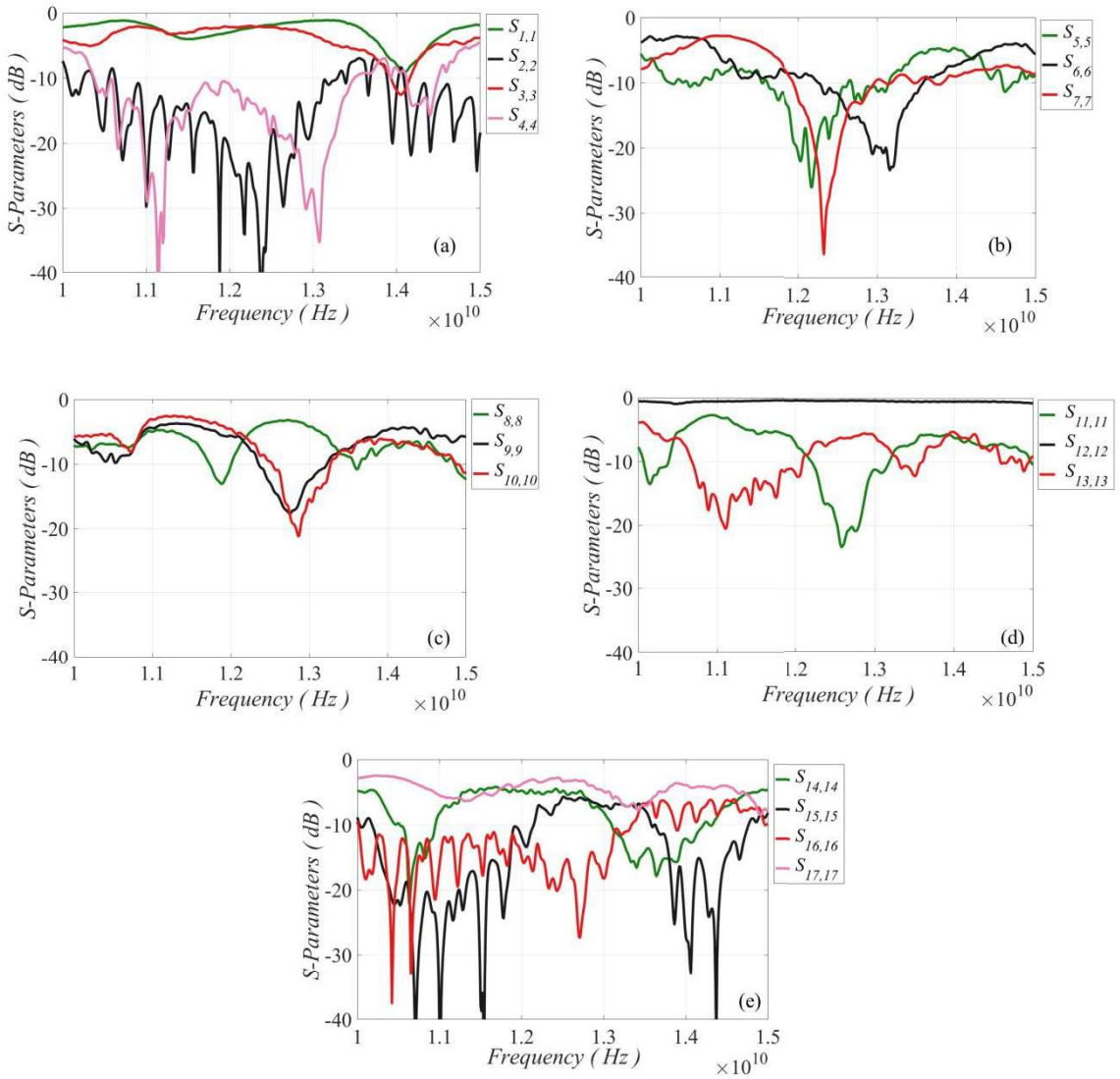

Figure 4.20: Measured reflection coefficients for the ports, (a) #1, #2, #3, #4, (b) #5, #6, #7, (c) #8, #9, #10, (d) #11, #12, #13, (e) #14, #15, #16, #17.

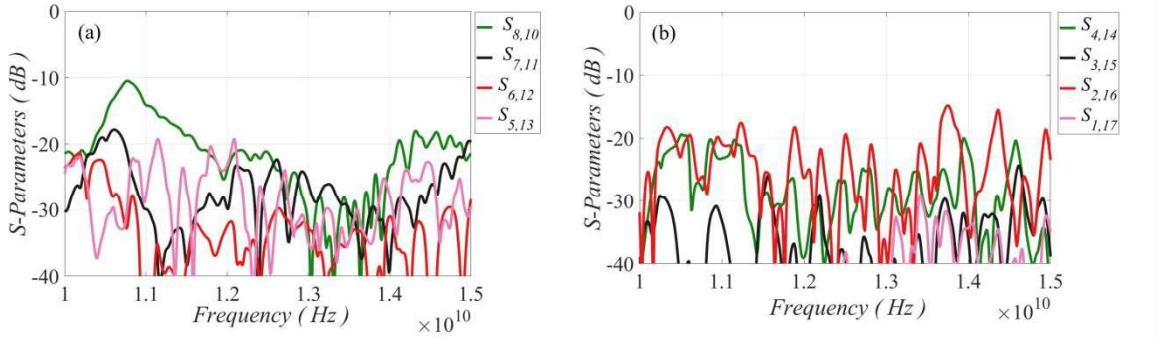

Figure 4.21: Measured coupling coefficients for the symmetric ports, (a) #8-#10, 7#-#11, #6-#12, #5-#13, (b) #4-#14, #3-#15, #2-#16, #1-#17.

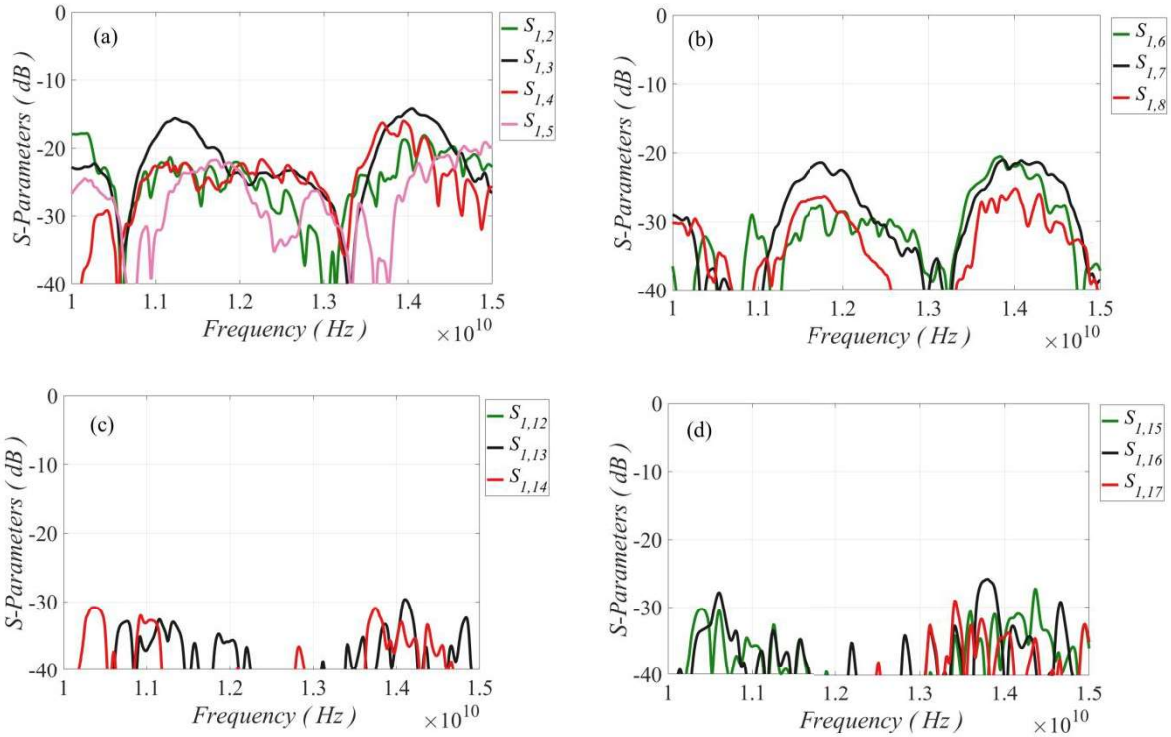

Figure 4.22: Selected coupling coefficients of port #1.

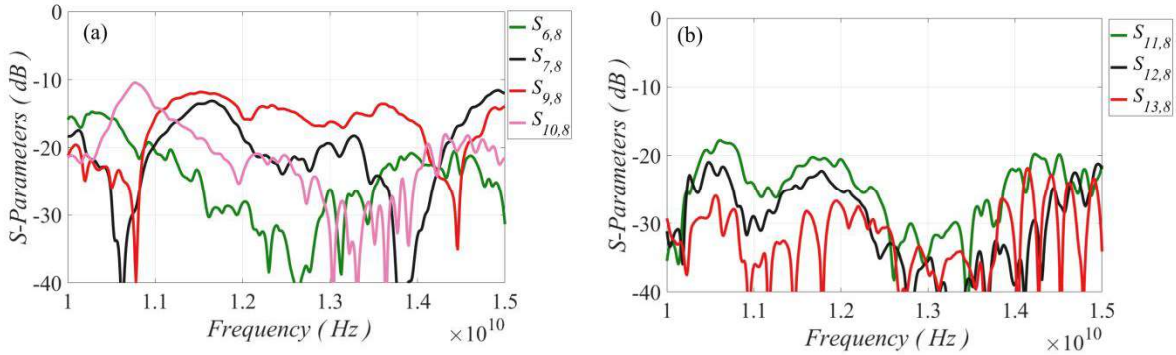

Figure 4.23: Selected coupling coefficients of port #8.

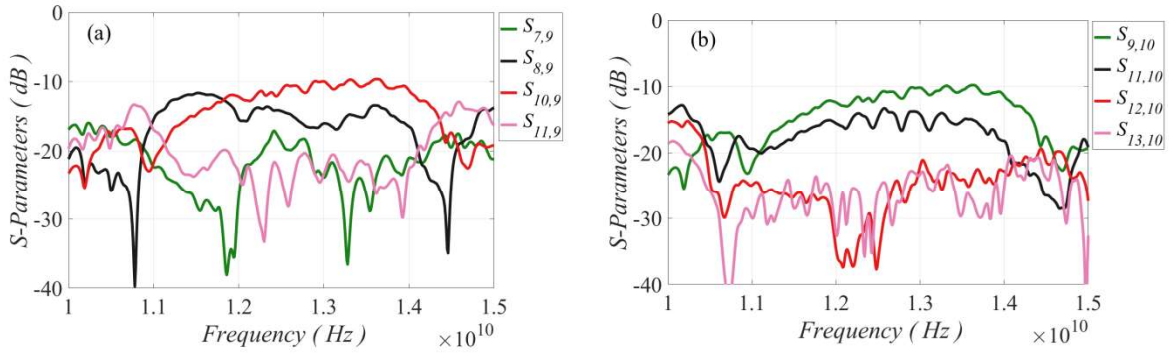

Figure 4.24: Selected coupling coefficients of port #9 and #10.

4.5 Conclusions

In this chapter the Gutman lens antenna prototype together with the mechanical steps to program the CNC machine have been presented. The experimental tests of the antenna have been likewise shown. It has been demonstrated the placement of the screws and the dowels on strategical regions of the prototype in order to stabilize the two metal plates. The design procedure of both plates has been presented in order to import the proper 3D step files into the CNC computer station. Furthermore, the regions that the soldering is needed have been highlighted. Based on the experimental tests, the antenna presents narrowband performance. The radiation patterns present high level of side lobes and are distorted due to the connection of the metal pins inside the lens antenna. High reflections are caused in the majority of ports of the antenna due to the strong misalignments of the dielectric that is placed in the bottom part of the prototype.

Chapter 5 Gutman Lens Antenna Vs Luneburg Lens Antenna. All-Metal Graded Index Gutman Lenses Vs Dielectric lenses

Contents

-The Chapter is divided in two sections as follows:

- In the first Section 5.1, a comparison between all-metal GRIN lenses is presented. In particular, this includes, a Gutman lens with focal point *f*=*R*/2, a Gutman lens with focal point *f*=*R*/2.85 and a Luneburg Lens. The design of the Gutman lens with focal point *f*=*R*/2 has been extensively analysed in Chapter 3, therefore only the design of the Gutman lens with focal point *f*=*R*/2.85 is illustrated. A brief design description is likewise presented for the all-metal GRIN Luneburg lens, although some of the data that are presented here have been extracted from [92].
- In the second Section 5.2, a comparison with the equivalent dielectric lenses is presented, where non-dispersive homogeneous dielectric layers have been used to synthesize the lenses. In conclusion, a comparison between all-metal and dielectric lenses is provided in order to evaluate their performance.

5.1 All-metal graded index lenses – Gutman Vs Luneburg lens

5.1.1 Effective index distribution comparison

The effective index distribution n_{eff} of the Luneburg lens along its surface is calculated by $n_{eff}=\sqrt{2-\left(r/R\right)^2}$ where, *r* is the spatial position from the center of the lens until its periphery and *R* its radius. According to this index variation the focal point, *F* of the lens is placed in any direction along the periphery of the lens and thus the focal distance is equal to *f*=*R*. The required index variation to formulate the Luneburg covers the range $1\leq n_{eff}\leq 1.4$. Since this

index distribution is synthesized along the whole surface of the lens, by placing any spherical wave source along its periphery a plane wave is formed on its opposite direction by virtue of the circular symmetry of the antenna.

Hamiltonian optic techniques have been applied to the Luneburg lens profile, [11] and a new transformed index variation is calculated along the surface of the new transformed lens which is given by the Eq. (3.1) in previous Chapter 3. The focal point, *F,* of the Gutman lens is placed inside the circular lens contour and closer to the center of the lens. The radius, *R* of the Gutman lens, is equal to the radius, *R* of the Luneburg lens. As the focal point is placed on focal arcs that are closer to the center of the lens, the maximum required effective index of refraction increases and the total index distribution along the surface of the lens is modified accordingly. The displacement of the focal points in focal arcs closer to the center of the lens results to more compact size; this is a key advantage of the Gutman lens compared to the Luneburg lens. However, synthesizing periodic structures with higher effective indices of refraction is a challenging topic, since these structures present higher dispersion and thereby more narrowband performance.

Three designs are compared here. The Luneburg lens (see Fig. 5.1(a)), the Gutman lens with focal distance, $f=R/2$ (see Fig. 5.1(b)) which has been analyzed in Chapter 3 and the Gutman lens with focal distance $f=R/2.85$ (see Fig. 5.1(c)). The index distribution for the Gutman with $f=R/2$, covers the index region $1\leq n_{eff}\leq 2.2$ and the index distribution for the Gutman with $f=R/2.85$, covers the region $1\leq n_{eff}\leq 3$. The comparison of the indices of both lenses are depicted in Fig. 5.1(d).

To formulate the required index values for the Luneburg lens, the fakir bed of nails unit-cell is used and properly modulated along the whole surface of the lens to mimic the index zone $1\leq n_{eff}\leq 1.4$. A top and a cut view of the Luneburg is depicted in Fig. 5.2(a) where the fakir cell is placed on the bottom metal plate of the PPW section. In Fig. 5.2(b, c), the top view of Gutman lenses with focal distances $f=R/2$ and $f=R/2.85$, respectively, is depicted. For the Gutman lens with $f=R/2$, the interleaved glide symmetry unit-cell is used to synthesize the lens and covers the index region $1\leq n_{eff}\leq 2.2$. For the Gutman lens with $f=R/2.85$ the interleaved glide symmetry unit-cell with higher effective index of refraction is used to synthesize the lens and covers the index range $1\leq n_{eff}\leq 3$.

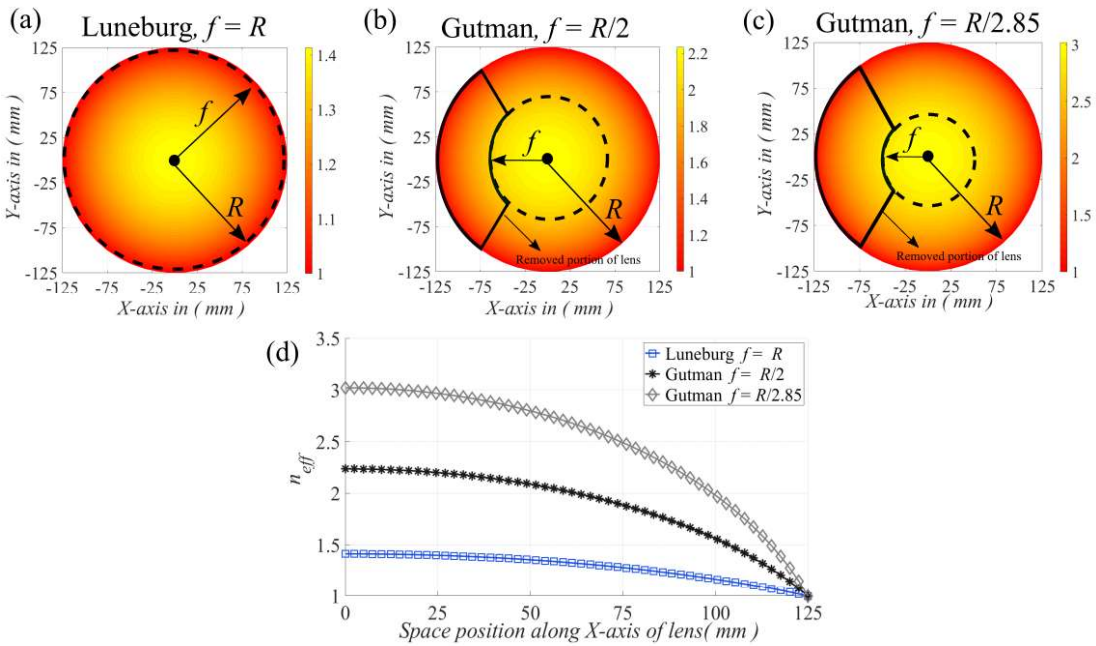

Figure 5.1: Index distribution along the total surface of the (a) Luneburg lens, (b) Gutman lens with focal distance f=R/2, (c) Gutman lens with focal distance f=R/2.85, (d) 2D effective index of refraction along x axis; comparison of both lenses.

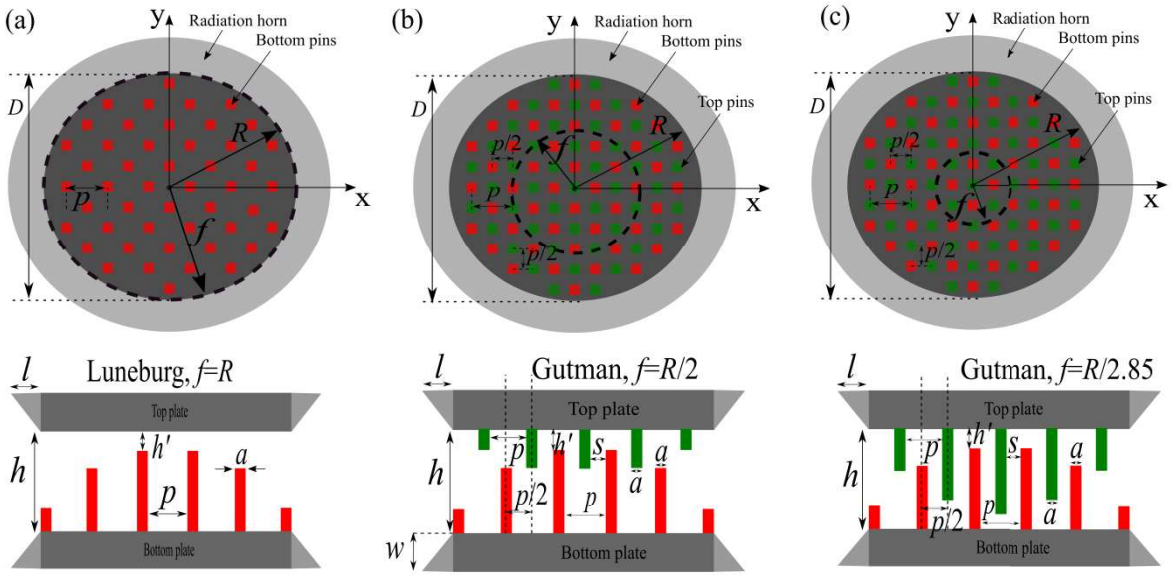

Figure 5.2: (a) Luneburg schematic top and cut view using the fakir cell (b) Gutman with f=R/2 and (c) f=R/2.85 schematic top and cut view using the interleaved glide symmetry cell.

5.1.2 Metasurface Luneburg lens design

(1) Unit-cell

The Luneburg lens that is described here, has been synthesized using the fakir bed of nails metallic unit-cell in a PPW technology (see Fig. 5.3(a)). The present lens has been extensively analysed in [92], however the critical design parameters are mentioned here in order to compare it with the Gutman lens. The maximum effective index of refraction that is

required is $n_{eff_{(max)}}$=1.4 (see Fig. 5.3(b)) and the fakir bed of nails unit-cell reaches that value. In that type of unit-cell, a sole rectangular metal part is attached on the top PPW metal plate and its width and height defines the dispersion characteristics. The width of the unit-cell specifies the operation frequency band of the lens. For instance, for wider widths the cell operates in low frequencies and for narrow widths, in high frequencies. In order to operate at Ku-band the width of the unit-cell has been defined as w=0.8 mm. The drawback of this cell is that for higher frequencies, its width is very narrow and thus manufacturing is more challenging. Despite this issue, for operation at Ku-band (and even at Ka-band), the maximum required value of effective index of refraction for a Luneburg lens can be achieved with manufacturable structures and still maintain low dispersion.

In order to calculate the effective index of refraction of the fakir unit-cell of Fig. 5.4(a), the eigenmode solver has been used in CST Studio Suite to compute the dispersion diagram for multiple design parameters of the unit-cell. A parametric simulation has been performed where the width of the cell remains constant and its height varies from t=0 mm to t=2.6 mm. Selected values of the effective index of refraction are shown in Fig. 5.4(b).

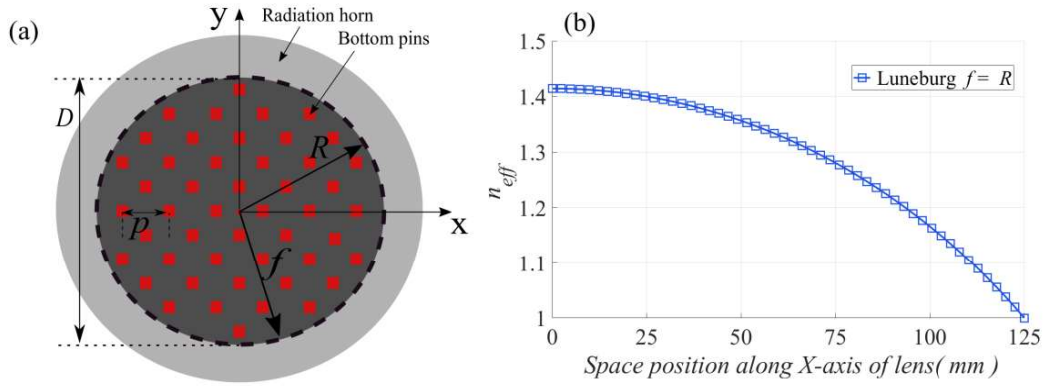

Figure 5.3: (a) Metasurface Luneburg lens antenna layout using the fakir bed of nails unit-cell, (b) required effective index of refraction along x axis of the lens.

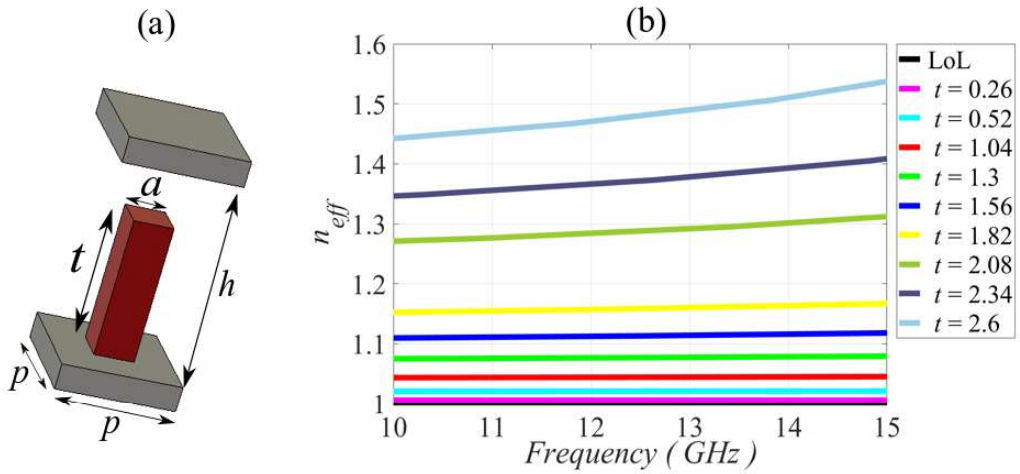

Figure 5.4: (a) Fakir bed of nails unit-cell, a=0.8 mm, h=4 mm, p=2.4 mm, (b) effective index of refraction for segregate heights of the pin.

(2) Feed Excitation

The effective index of refraction along the periphery of the Luneburg lens is equal to n_{eff}=1. This value, facilitates the matching of the feed into the lens since the PPW region with the absence of metal posts is purely matched into free space. Therefore, a traditional all-metal waveguide with the dimensions, h=4 mm, w=19.05 mm, has been integrated along the focal arc of the Luneburg lens.

The objective here is to present the design of the Luneburg lens in order to compare it with the Gutman lens in later sections. For that purpose, 15 waveguides have been placed along the periphery of the lens to provide 15 output radiated beams, (see Fig. 5.5(a)). Fig. 5.5(b) shows the 3D view of the waveguide and Fig. 5.5(c) the 2D cut view of the lens with the integrated waveguide on xz plane.

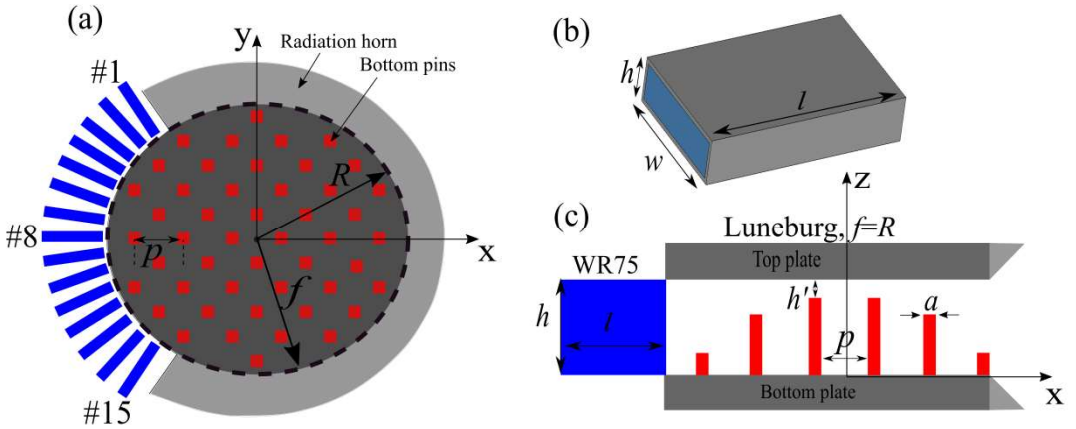

Figure 5.5: (a) 15 waveguides connected along the focal arc of the Luneburg lens, (b) 3D view of the waveguide, h=4 mm, w=19.05 mm (c) 2D cut view of the Luneburg lens with the integrated waveguide, #8.

5.1.3 Metasurface Gutman lens design with focal distance *f*=*R*/2.85

In present subsection, the all-metal Gutman lens antenna with focal distance, f=R/2.85 in a PPW technology is introduced. The lens has 6% more compact size compared to the Gutman lens with focal distance, f=R/2 that has been analyzed in Chapter 3 and 25% more compact size in comparison with the Luneburg lens that has been described in the previous Subsection 5.1.2. Aforementioned compactness of the lens derives from its small focal distance. The layout of the Gutman lens antenna with focal distance f=R/2.85 is depicted in Fig. 5.6(a). The antenna has circular symmetry and the distribution of the effective index of refraction along its symmetric x axis, is depicted in Fig. 5.6(b).

The major challenge that confronts this type of lens is the demand of high required effective index of refraction which is equal to n_{eff}=3. The solution that is proposed here to overcome this challenge is the selection of the interleaved glide symmetry unit-cell; its design distinguishes from the unit-cell that has been introduced in Subsection 3.2.1, since it presents higher interleaving between the top and bottom metal posts.

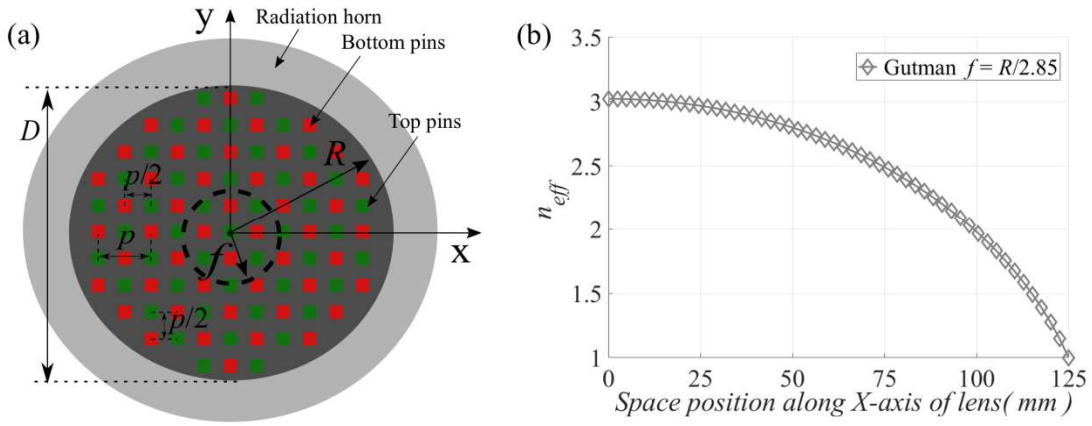

Figure 5.6: (a) Gutman lens antenna with focal distance f=R/2.85, layout, (b) required distribution of the effective index of refraction.

(1) Glide symmetry unit-cell with high interleaving

The interleaved glide symmetry unit-cell that has been used to design the lens is illustrated in Fig. 5.7(a). It consists of four bottom metal posts and a solitary top metal post. The height of the unit-cell has been defined, h=4 mm which is <λ/2 to avoid high order modes inside the PPW region. The objective here is to reach the required maximal effective index of refraction $n_{eff_{(max)}}$=3, with low dispersion.

-Hence, two parametric studies have been applied as follows:

- In the first parametric study, the height of the top metal post is constant and is equal to t=2.6 mm and the bottom metal post varies from g=0 mm to g=3.1 mm with step 0.4. Fig. 5.7(b) displays the effective index of refraction over frequency for segregate values of g; for high index values, the unit-cell is more dispersive. The latter influences the performance of the lens which needs to be evaluated. Ideally, the desirable case is to have constant values of effective index of refraction for every design variable, g which is not the case here.
- In the parametric study that is shown in Fig. 5.7(c), the height of both the bottom and top metal posts vary simultaneously from g=0 mm to g=3.1 mm where g=t. In this scenario, the dispersion of the unit-cell is less in comparison with the first parametric case. For instance, considering solely the maximal effective index of refraction of both parametric studies, it is apparent in Fig. 5.8 that the second parametric study provides lower dispersion compared to the first.

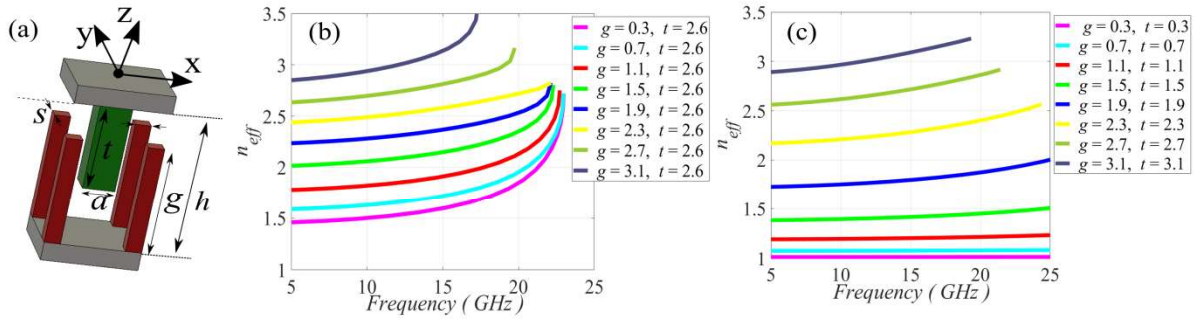

Figure 5.7: Effective index of refraction for (a) variation of g and constant, t (b) simultaneous variation of post heights g, t.

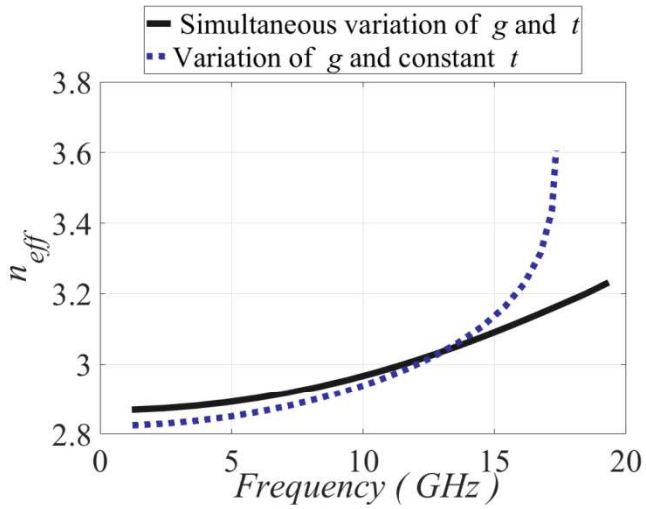

Figure 5.8: Dispersion comparison of the two parametric studies for the highest index value n_{eff}=3.

Dispersion associated with high effective index of refraction

The dispersion deviation is an inherit feature of the unit-cell and affects the performance of the antenna. Therefore, deviations for all the values of the effective index of refraction of the Gutman lens are presented here. First, the meaning and the method that this deviation has been calculated, is explained and then the accepted deviation of dispersion of the unit-cell is examined.

According to the parametric study that has been previously presented, the unit-cell with dimensions g=t=2.095 mm presents an equivalent effective index of refraction which is equal to n_{eff}=2.0021 at center frequency f=12.5 GHz (see Fig. 5.9(a)) when computed by calculating the mean value of the indices at the edge frequencies, f=10 GHz and f=15 GHz. In the remaining, and in order to quantify dispersion we define the dispersion value for the unit-cell associated with an effective refractive index of n_{eff}=2.0021 the difference of the values associated with the two edge frequencies. Consequently, the dispersion is defined to be dev=$n_{eff_{(fmax)}}$-$n_{eff_{(fmin)}}$=2.0338-1.9747=0.0591. This calculation has been performed for all the values of the effective index of refraction for both parametric studies and the results are shown in Fig. 5.9(b). For the parametric study where both top and bottom posts vary simultaneously, the deviation of the dispersion progressively increases for high values of effective index of refraction. The maximum value of deviation is 0.12 at the highest index $n_{eff_{(max)}}$=3. For the parametric study where only the height of the bottom metal posts varies and the top post remains constant, t=2.6 mm, we observe that the dispersion value remains stable up to n_{eff}=2.5 and then it abruptly increases. At this point, it has to be noted that this parametric study has been used to synthesize the Gutman lens with focal distance f=R/2 that has been analysed in Chapter 3 and it has ended up in satisfied performance in terms of radiation. Its maximal index of refraction is equal to $n_{eff_{(max)}}$=2.2.

To synthesize the Gutman lens with focal arc f=R/2.85, the parametric study where both top and bottom posts vary simultaneously has been used. The maximal deviation for the maximal effective index of refraction of the unit-cell, n_{eff}=3 is equal to 0.12. It follows the method to synthesize the lens using the interleaved glide index symmetry unit-cell where both top and bottom posts vary simultaneously.

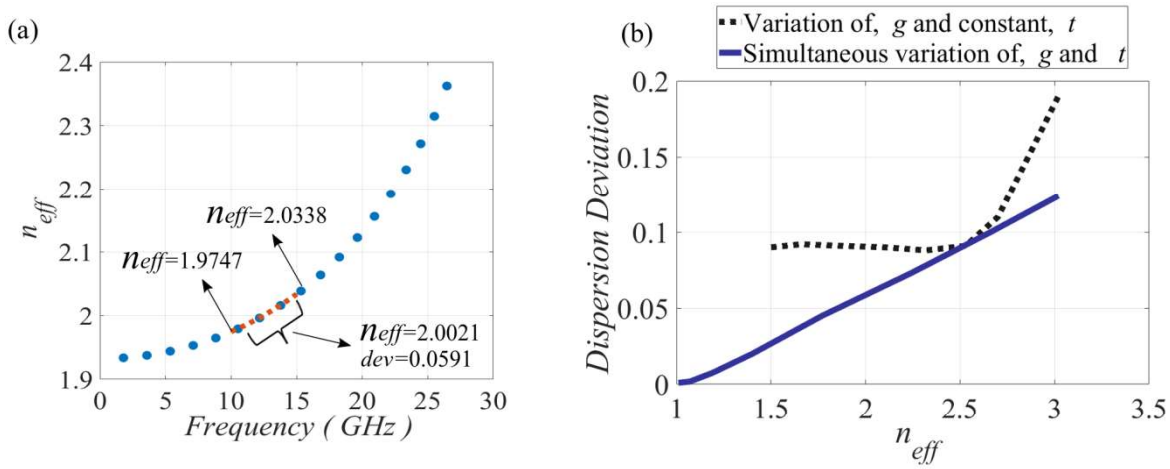

Figure 5.9: (a) Calculation of the dispersion deviation, (b) dispersion deviation for the two segregate parametric studies.

(2) Synthesizing the lens

The periodicity of the unit-cell is p=2.4 mm and therefore the lens has been discretized in unit cells of $K=R/p=52$. Every discretized value corresponds in an equivalent effective index of refraction which should be achieved by selecting unit-cell design parameters. Fig. 5.10 shows the evolution of the design parameters of the unit-cell along the symmetric, x axis. Considering the selected unit cell geometry, the height of the posts at the top and bottom metal plates suffice to match to an equivalent index of refraction.

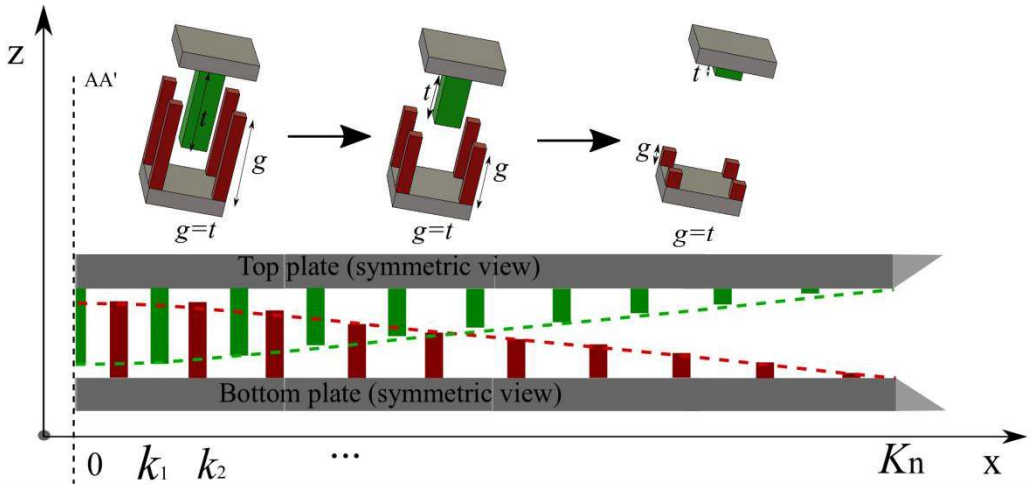

Figure 5.10: Top and bottom posts of the unit-cell along the symmetric, x axis of the Gutman lens with focal distance $f=R/2.85$.

Height calculation of the metal posts

Based on the K discretized values, K simulations have been realized on the CST Studio Suite in order to calculate K dispersion diagrams. The initial simulation has been performed for $t=g=0$ mm and the last simulation for $t=g=3.1$ mm with step $n_{max}/K=3/52=0.0576$. All K dispersion graphs have been calculated, the equivalent effective index of refraction for every K value has been computed and all the indices are depicted in Fig. 5.11(a) for the relevant

heights, *t*. Thereafter, the data of the graph in Fig. 5.11(a) have been extrapolated with the data of the graph in Fig. 5.6(b) and the height of all the bottom metal posts has been calculated along the symmetric, *x* axis of the lens and is depicted in Fig. 5.11(b). The data of the graph in Fig. 5.11(b) extracted to form a 2D spline which has been imported to CST Studio Suite to form the posts. Hence, the bottom metal posts have been modulated on the symmetric, *x* axis of the lens. Exploiting the circular geometry of the lens, the 2D spline has been rotated through *z* axis to modulate the rest posts of the lens. Thorough details of this design methodology have been analyzed in Subsection 3.3.1. The above steps have been likewise adopted for the modulation of the top metal posts to complete the design of the lens.

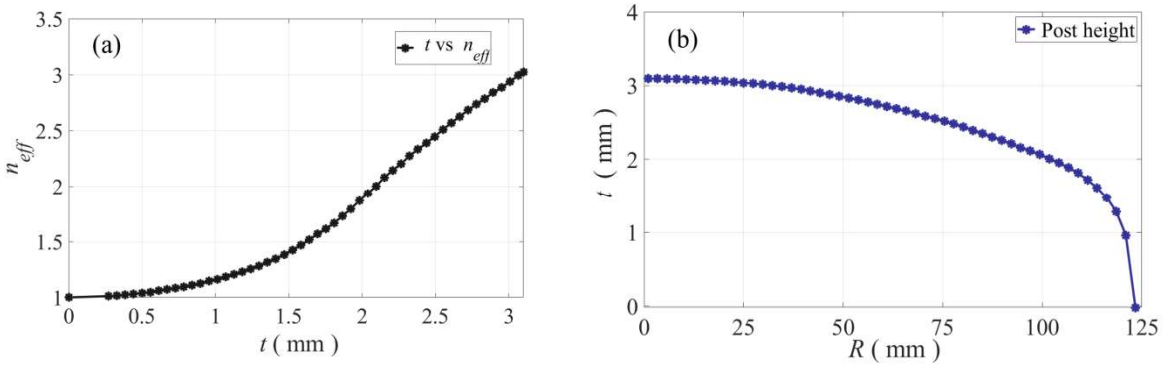

Figure 5.11: (a) Extracted index data from the dispersion of the interleaved glide symmetry unit-cell, (b) spline illustration that represents the height of the bottom plate posts.

(3) Feed Excitation

In order to integrate the feeds along the focal arc of the lens, a significant part of the lens has been subtracted. This removed part corresponds to the 25 % of the total surface of the lens. The feed system of the lens comprises the transition from single ridge waveguide to microstrip line that has been presented in Subsection 3.5.1 (see Fig. 5.12(a, b)). The target here is to compare the performance of lens with the Gutman lens with focal distance $f=R/2$. Therefore, the feeds have been oriented along the focal arc of the lens in order to point similar offset beams. The number of feeds are 11 which are less than the 17 feeds that have been placed on the Gutman lens with focal distance $f=R/2$; this is due to the smaller focal arc of the present lens. The matching of the antenna needs to be addressed since the equivalent index of refraction takes values $n_{eff}\neq 1$. However, the matching methodology that has been applied in the Gutman lens with focal distance $f=R/2$ can be used to match the lens.

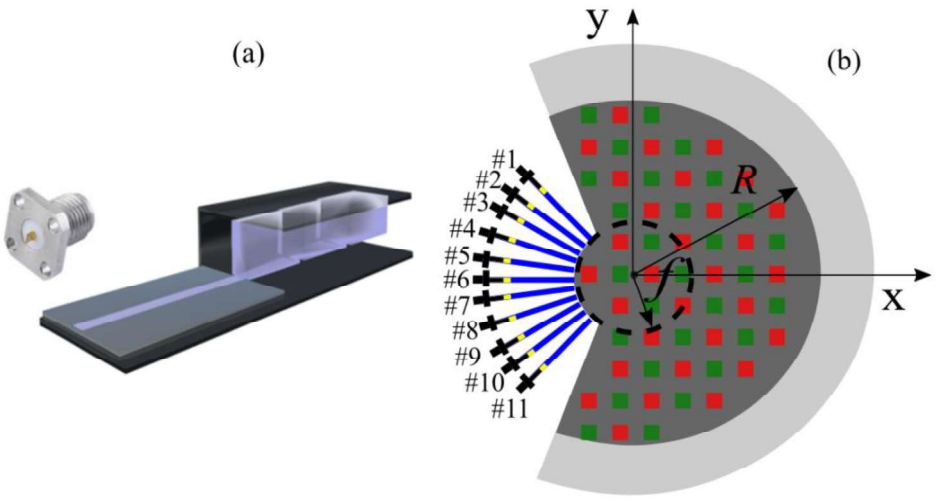

Figure 5.12: (a) Single ridge waveguide to microstrip line transition, (b) Gutman lens antenna with the transition integration, layout.

5.1.4 Radiation performance comparison

(1) Simulation results

CST antenna models

The CST antenna models for the Luneburg lens, the Gutman lens with focal distance $f=R/2$ and the Gutman lens with focal distance $f=R/2.85$ are shown in Fig. 5.13(a-c). Both lenses comprise 15 feeds along their focal arc excluding the Gutman lens with focal distance $f=R/2.85$ which consists of 11 feeds.

The objective here is to compare the radiation patterns of both lenses. Concerning the Luneburg lens, the excitation of the feeds, #1, #4, and #8 results on the offset beams at 70°, 40° and 0°, respectively. This is likewise, the case for the Gutman lens with focal distance $f=R/2$. Regarding to the Gutman lens with focal distance $f=R/2.85$, the excitation of the feeds, #1, #3, and #6 results on the offset beams at 70°, 40° and 0°, respectively. These are the theoretically anticipated cases and then we proceed to perform the comparison with full-wave simulations.

Electromagnetic simulations have been realized exciting the above mentioned feeds in both lenses on CST Studio Suite. The E-Field comparison of the directivity patterns at Ku-band frequencies points, 10 GHz, 12.5 GHz and 15 GHz is presented below.

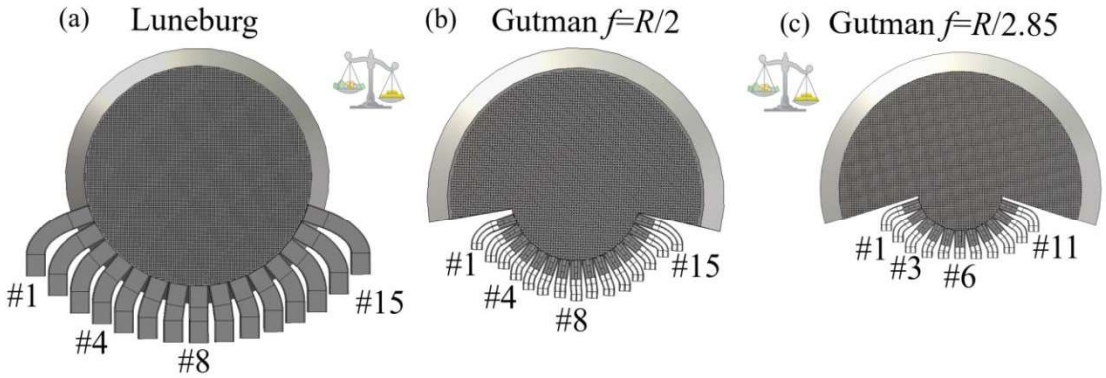

Figure 5.13: Design models from CST Studio Suite of the (a) Luneburg lens, (b) Gutman lens with focal distance $f=R/2$, (c) Gutman lens with focal distance $f=R/2.85$.

E-Field distribution

The E-field distribution of both lenses at the center frequency f=12.5 GHz for the broadside, the offset beam at 40° and the offset beam at 70° is illustrated in Fig. 5.14. Considering the broadside beam, we observe that the radiated field aperture on the periphery of the Luneburg lens is more confined compared to both Gutman lenses by virtue of the larger aperture of the excitation feed of the Luneburg lens. The feeds that have been placed along the focal arc of the Luneburg lens are WR75 waveguides with an aperture of w=19.5 mm. The feeds that have been placed along the focal arcs of both Gutman lenses are single ridge waveguides with aperture w=9 mm. The output radiated field of feeds that have small apertures is large and exploits larger surface of the lens. The latter, leads to more directive beams on the periphery of the lens.

Regarding the offset beam at 40°, we observe that the E-field has been smoothly transformed in a plane wave for the Luneburg lens and the Gutman lens with focal distance $f=R/2$. For the Gutman lens with focal distance $f=R/2.85$, side lobes on the opposite direction of the pointing angle are observed. The latter, is explained by virtue of the large subtracted area of the lens. Concerning the offset beam at 70°, for both lenses we observe side lobes on the opposite direction of the pointing angle. These side lobes are justified by the subtracted surface which is likewise the case for the Gutman lenses.

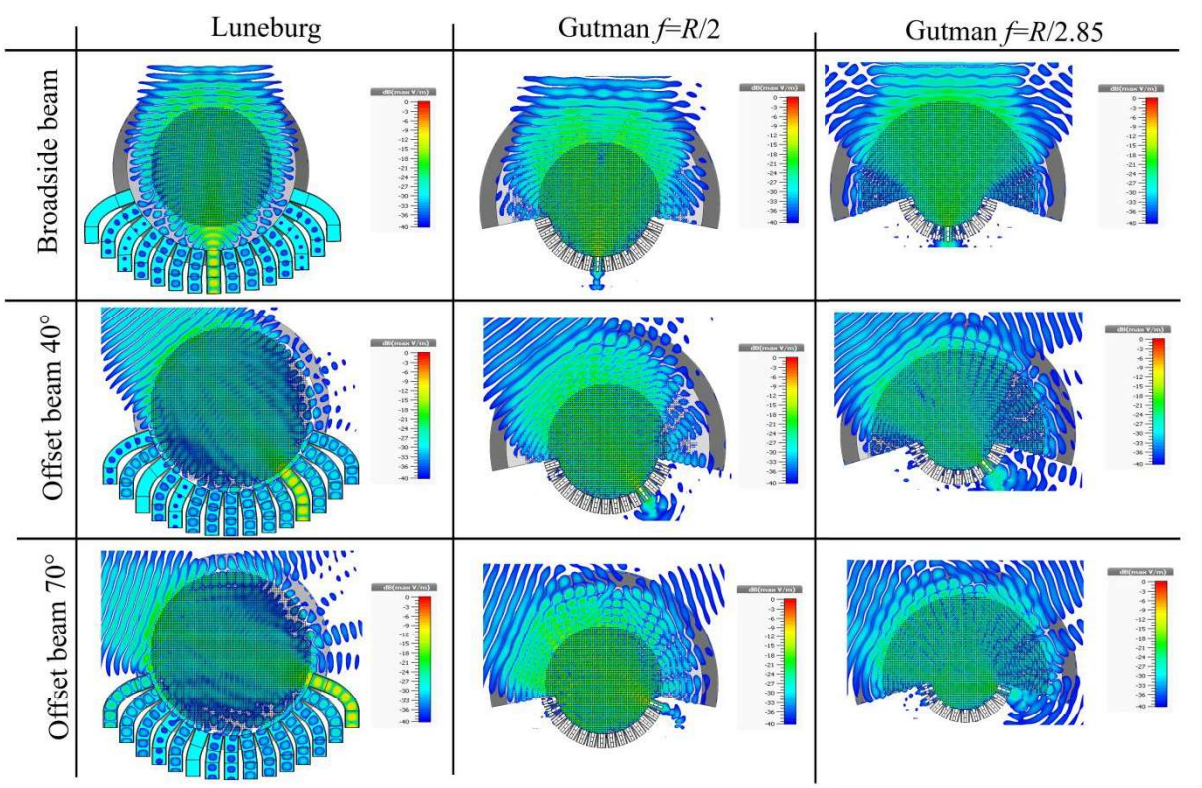

Figure 5.14: E-field distribution at center frequency, f=12.5 GHz for Luneburg lens, Gutman lens with focal distance $f=R/2$ and Gutman lens with focal distance, $f=R/2.85$, oriented at broadside, 40° and 70°.

Directivity patterns comparison – Broadside beam

The directivity patterns of the Luneburg lens, the Gutman lens with focal distance $f=R/2$ and Gutman lens with focal distance $f=R/2.85$ at frequencies f=10 GHz, f=12.5 GHz, f=15 GHz are depicted in Fig. 5.15(a-c). Regarding the Luneburg lens, high directivity has been achieved with very low SLL, barring the beam at the edge frequency f=15 GHz. At this frequency the SLL increases due to the high dispersion of the fakir bed of nails unit-cell at higher frequencies; at this frequency the distribution of the effective index of refraction is thus not following the required distribution.

Regarding to the Gutman lens with focal distance $f=R/2$ we observe that the directivity increases for higher frequencies, although at lower values compared to the Luneburg lens. The reason is the extracted surface of the lens where the feed fails to exploit the total surface of the lens resulting on a decreased directivity of the output radiated beam. Finally, the SLL progressively ameliorates with the frequency.

Concerning the Gutman lens with focal distance, $f=R/2.85$, excellent performance has been achieved for all the Ku-band. The directivity of the patterns is equal to the directivity of the patterns of the Gutman lens with focal distance $f=R/2$.

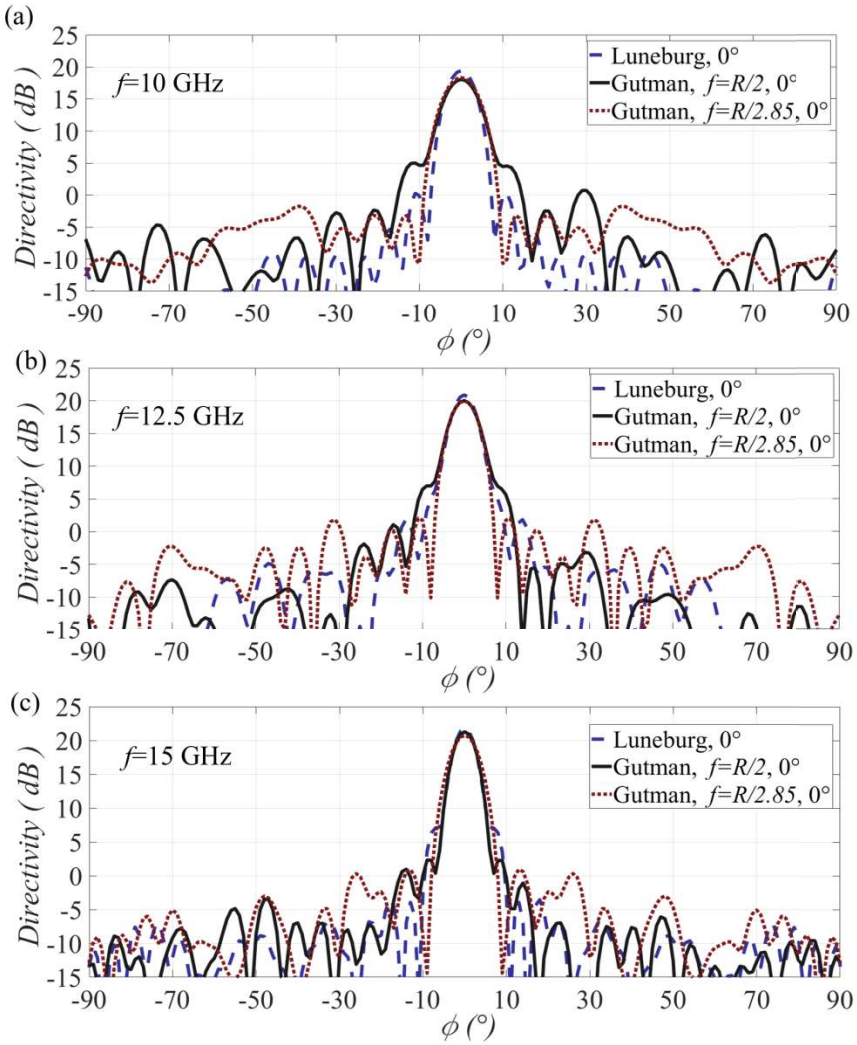

Figure 5.15: Directivity patterns on H-plane for the for Luneburg lens, Gutman lens with focal distance $f=R/2$ and Gutman lens with focal distance $f=R/2.85$ at broadside.

Directivity patterns comparison – Offset beam 40°

The directivity patterns of the Luneburg lens, the Gutman lens with focal distance $f=R/2$ and Gutman lens with focal distance $f=R/2.85$ at frequencies f=10 GHz, f=12.5 GHz, f=15 GHz for the offset beam at 40°, are depicted in Fig. 5.16(a-c).

The directivity of the patterns for the Luneburg lens is progressively increased, although at f=15 GHz, it takes the same value as at f=12.5 GHz. Also, the θ_{3dB} beam width is larger than the θ_{3dB} beam width at f=12.5 GHz and f=10 GHz. This is explained by the high dispersion of the bed of nails unit-cell at frequency f=15 GHz which distorts the effective refractive index distribution. Besides, the aperture feed of the Luneburg is larger compared to the aperture feed of the Gutman lenses and illuminates narrower aperture. Therefore a beam with larger beamwidth on the periphery of the Luneburg lens is expected.

For both Gutman lenses a slight mismatch on the pointing angle is observed. This is clarified first, by the required extracted surface of the lens and second, by the dispersion of the interleaved glide symmetry unit-cell. Moreover, the Gutman lens with focal distance $f=R/2.85$ has narrowband performance, since the beam at limit f=15 GHz has been distorted by virtue of the high dispersion deviation of the unit-cell (see Fig. 5.9(b)).

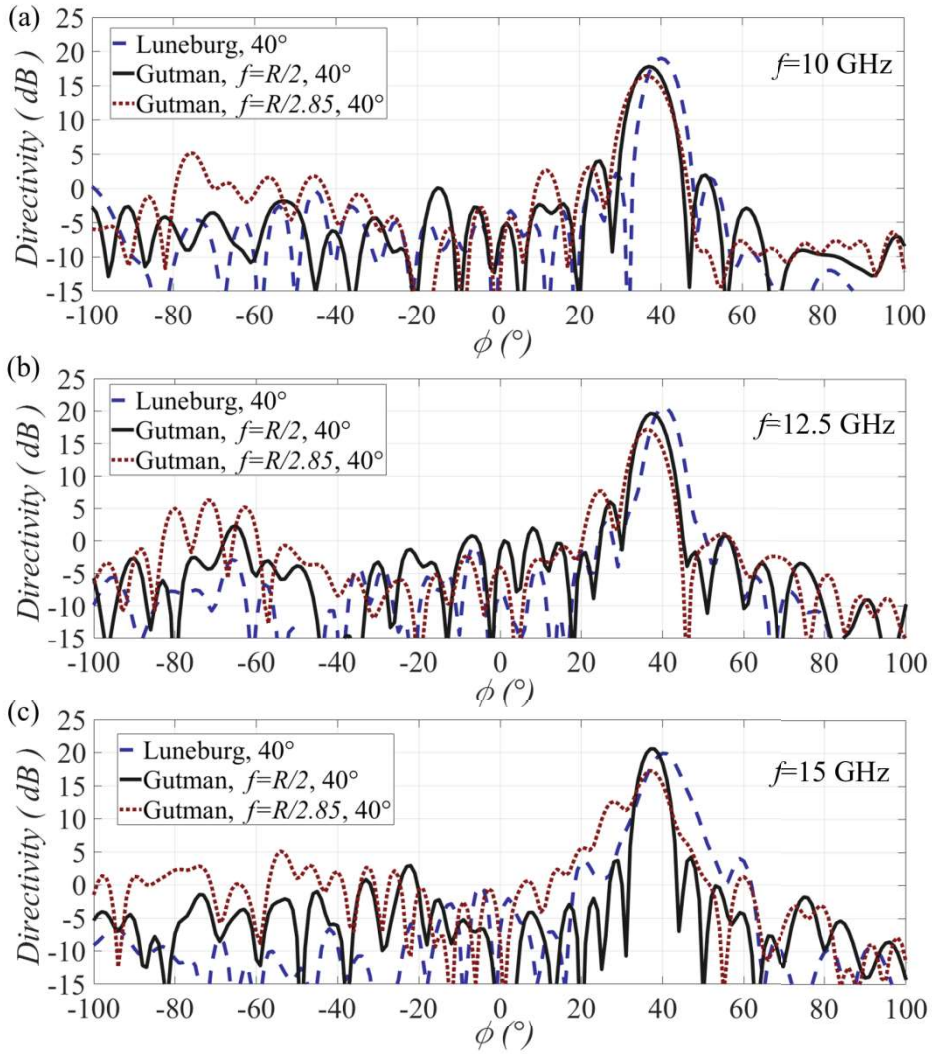

Figure 5.16: Directivity patterns on H-plane for the for Luneburg lens, Gutman lens with focal distance $f=R/2$ and Gutman lens with focal distance $f=R/2.85$ at 40°.

Directivity patterns comparison – Offset beam 70°

The directivity patterns of the three lenses at frequencies f=10 GHz, f=12.5 GHz, f=15 GHz for the offset beam at 70°, are visible in Fig. 5.16(a-c). We observe that the directivity of the beams of the Gutman lenses at all the selected frequencies is lower compared to the directivity of the Luneburg lens. This is attributed by the extracted lens' surfaces of the Gutman lenses. Once again, the Gutman lens with focal distance $f=R/2.85$ presents narrowband performance, since the beam at limit f=15 GHz has been distorted. The directivity data values over the frequency for both lenses are depicted in Fig. 5.18 and the SLL over the scan angles in Fig. 5.19.

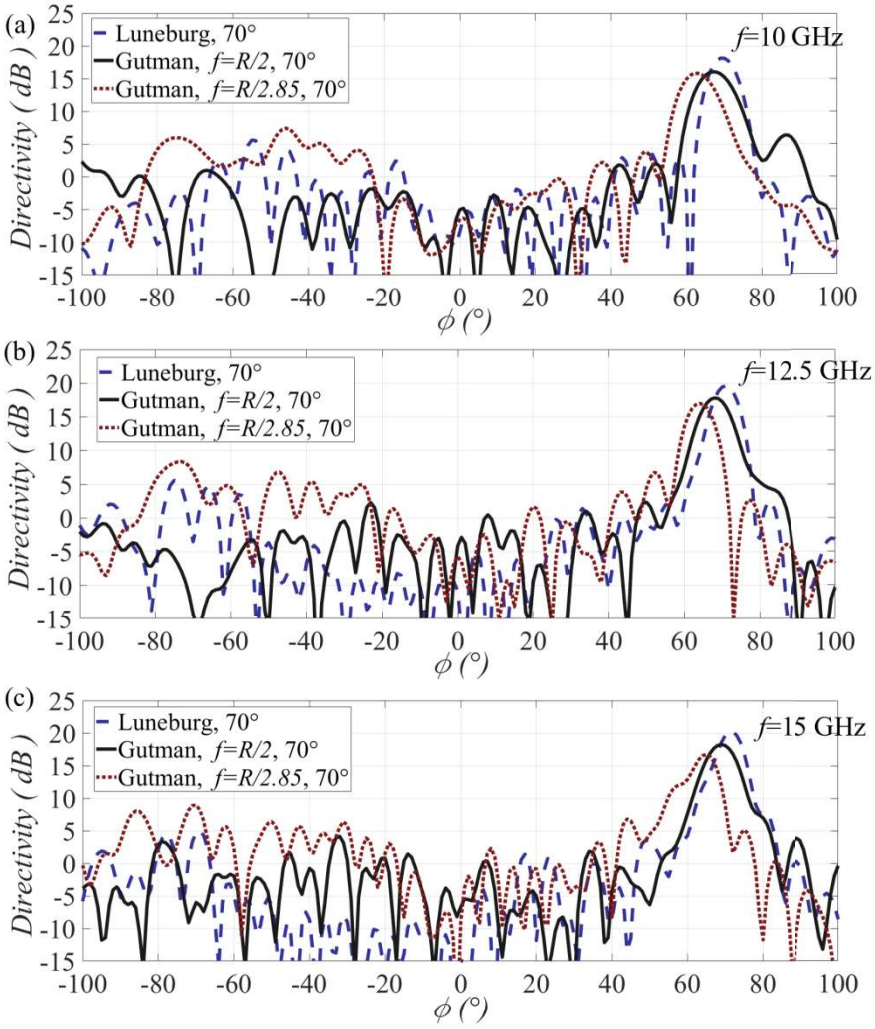

Figure 5.17: Directivity patterns on H-plane for the for Luneburg lens, Gutman lens with focal distance $f=R/2$ and Gutman lens with focal distance $f=R/2.85$ at 70°.

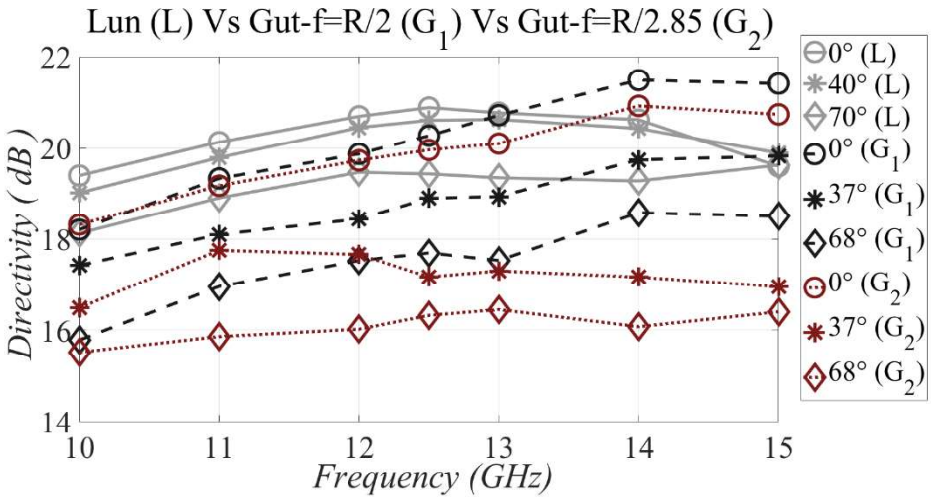

Figure 5.18: Directivity patterns on H-plane vs selected frequency points over the Ku-band for the Luneburg lens, the Gutman lens with focal distance $f=R/2$ and Gutman lens with focal distance $f=R/2.85$ for broadside, offset beam 40° and offset beam 70°.

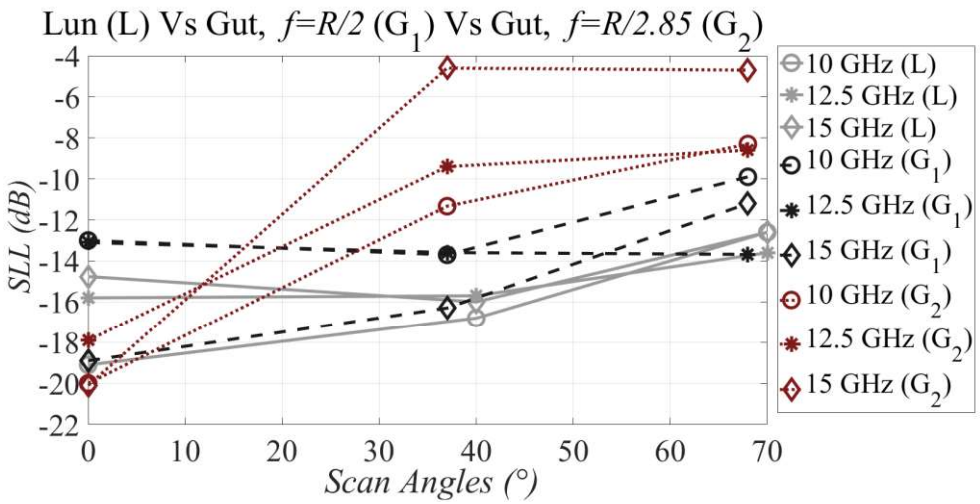

Figure 5.19: SLL level over scan angles for frequency in Ku-band for the Luneburg lens, the Gutman lens with focal distance $f=R/2$ and Gutman lens with focal distance $f=R/2.85$ for broadside, offset beam 40° and offset beam 70°.

S- Parameters

The reflection coefficients of the Luneburg lens and the Gutman lens with focal distance $f=R/2$ are depicted in Fig. 5.20. The feeds that have been excited separately in both cases are #1, #4, #8. For both lenses, the level of the reflection coefficient is above -10 dB. It is noted that in terms of complexity, the Luneburg lens can be easily matched since along its focal arc presents an equivalent effective index of refraction which is equal to n_{eff}=1. However, the Gutman lens presents and effective index of refraction along its focal arc which is $n_{eff} \neq 1$ and therefore the matching is more intricate.

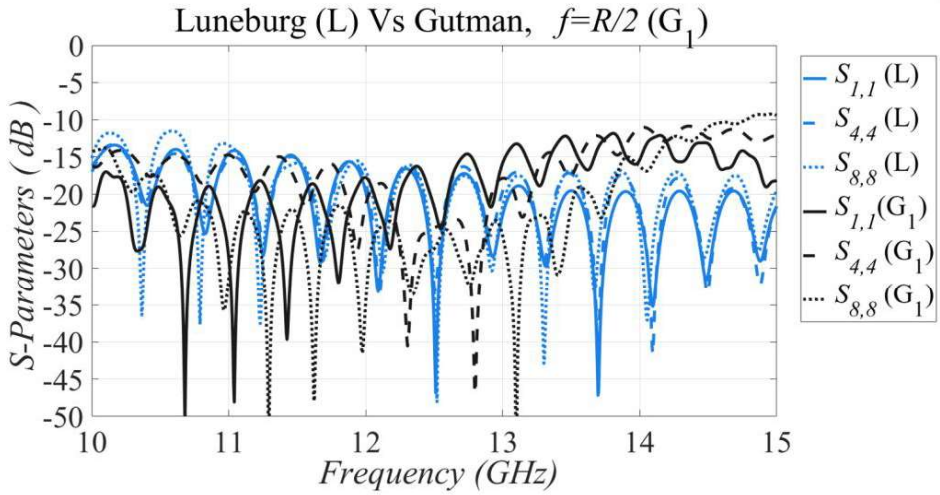

Figure 5.20: Reflection coefficients for the Luneburg lens, the Gutman lens with focal distance $f=R/2$ and Gutman lens with focal distance $f=R/2.85$ for broadside, offset beam 40° and offset beam 70°.

The coupling coefficient between the extreme feed and other ports for the Luneburg lens and the Gutman lens with focal distance $f=R/2$, are depicted in Fig. 5.21. The coupling coefficient associated with the extreme feed, #1 of the lenses represents a worst case scenario.

It is observed that for the Luneburg lens, the extreme opposite feed #15 induces reflections to the excited feed, #1; this is likewise the case for the Gutman lens.

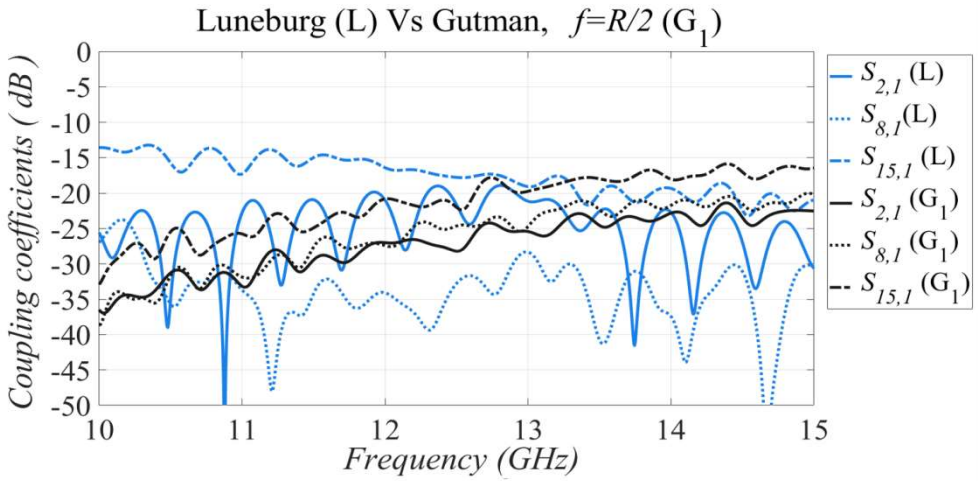

Figure 5.21: Coupling coefficients for the Luneburg lens, the Gutman lens with focal distance $f=R/2$ and Gutman lens with focal distance $f=R/2.85$ for broadside, offset beam 40° and offset beam 70°.

5.1.5 Conclusion

In this subsection, the all-metal GRIN Gutman lens antenna with focal distance $f=R/2.85$ has been introduced. The interleaved glide symmetry unit-cell has been used to synthesize the lens and presents a maximal effective index of refraction equal to n_{eff}=3. Furthermore, the all-metal GRIN Luneburg lens has been described. The fakir bed of nails has been used to design the lens. Both lenses have been compared to the all-metal GRIN Gutman lens antenna with focal distance $f=R/2$ that has been presented in Chapter 3.

The interleaved glide symmetry unit-cell presents higher index of effective index of refraction compared to the fakir bed of nails unit-cell. In addition, it reduces the dispersion deviation for lower effective indices of refraction. The Luneburg lens can be synthesized using the interleaved glide symmetry unit-cell and this will lead on more efficient performance. The prime advantage of the Gutman lens is its compact size. In addition, it achieves similar FOV as the Luneburg lens, although it has worst values of SLL and directivity.

5.2 Dielectric lenses – Luneburg lens Vs Gutman lens

In this section, the design of the Luneburg lens, the Gutman lens with focal distance $f=R/2$ and Gutman lens with focal distance $f=R/2.85$ using non-dispersive dielectric layers is presented. Both lenses have identical dimensions with the all-metal lenses presented in Chapter 3 and in the Section 5.1. They operate at Ku-band and have been designed in a PPW housing. This consists of two metal PPW metal plates filled with dielectric layers that comprise the required distribution of the effective index of refraction. 26 dielectric slabs fill inside the PPW region of every lens to approximate the required index distribution for each lens. The goal of the present designs is to compare the performance of the lenses that have been synthesized by all-metal dispersive artificial dielectric to the lenses that have been synthesized by homogeneous non-dispersive dielectric materials.

5.2.1 Dielectric Luneburg lens

(1) CST antenna model

The dielectric Luneburg lens antenna has been designed in CST Studio Suite and is shown in Fig. 5.22(a, b). It comprises 26 homogeneous non-dispersive dielectric layers in cylindrical form. Every layer consists of an identical permittivity value ε, and the permittivity that corresponds to each layer is depicted in Fig. 5.22(c).

In order to provide a fair comparison between the lenses, in the present design of the dielectric Luneburg lens, ideally the number of dielectric layers to synthesize the lens should be equal to the discretized value, K=52. However, a high number of dielectric cylinders appends complexity in the manufacturing process. Therefore, a realistic design scenario is considered here and the numbers of dielectric cylinders is defined as $K/2$=26. The width of every cylinder is twice the periodicity, p=2.4 mm of the unit-cell that has been used in the all-metal case of the Luneburg lens. All the widths of the cylinders are equal and takes the value, w=4.8 mm. The radius of the lens is equal to $R=f$=5.21 λ =125 mm.

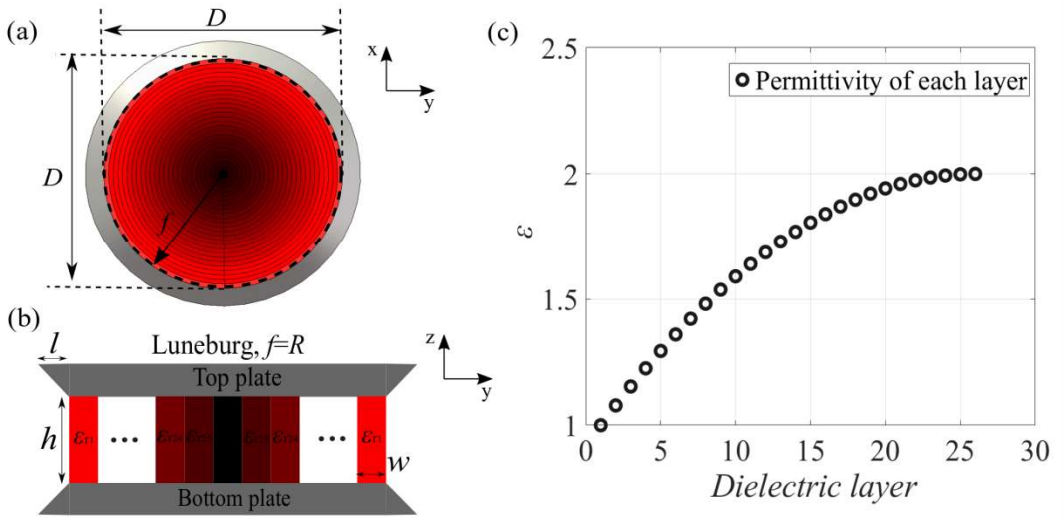

Figure 5.22: (a) Luneburg antenna model on CST Studio Suite, with 26 dielectric layers, (b) 2D cut view of the lens, (c) permittivity values for each dielectric layer.

(2) Feed excitation

The feed that has been selected to excite the Luneburg lens along its focal arc is the vacuum filled rectangular waveguide. The waveguide has identical dimensions with the one that has been used to the all-metal Luneburg lens. The aperture of the feed that excites the lens influences the radiation properties of the lens; therefore using feed with identical aperture a direct comparison between the dielectric lens and the all-metal GRIN lens can be made. 15 waveguides have been placed along the focal arc of the lens (see Fig. 5.23(a)) and the 2D cut view on the zx plane is depicted in Fig. 5.23(b) where it is evident that the waveguide is attached to the dielectric cylinder layer on the periphery of the lens.

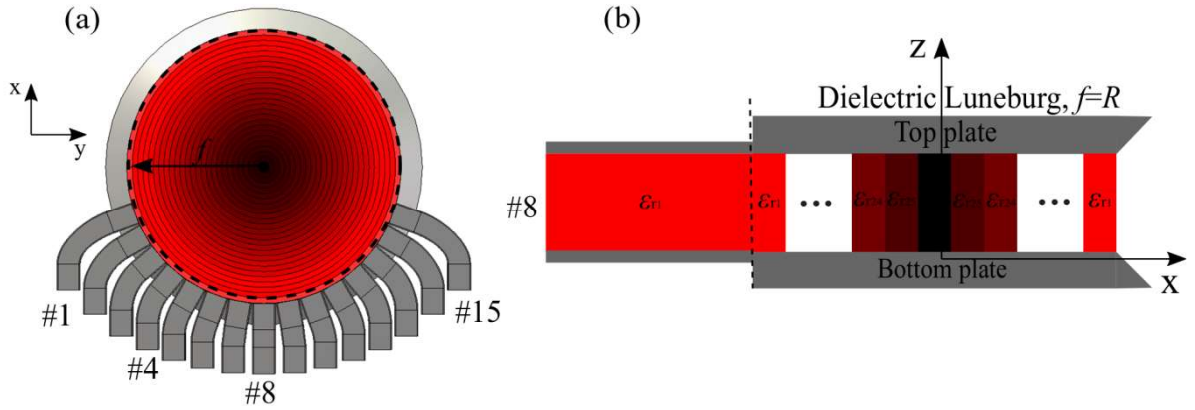

Figure 5.23: (a) 15 waveguides connected along the focal arc of the Luneburg lens, (b) 2D cut view of the Luneburg lens with the waveguide.

(3) Dielectric Luneburg lens Vs all-metal GRIN Luneburg lens – Radiation performance comparison

In the present subsection, the radiation performance of the dielectric Luneburg lens antenna with 26 non-dispersive homogenous dielectric layers is compared with the all-metal Luneburg GRIN lens that has been presented in Subsection 5.1.2. Both lenses operate at Ku-band and comparison of radiation patterns at the selected frequencies, f=10 GHz, f=12.5 GHz, f=15 GHz, for the broadside beam, the offset beam at 40° and the offset beam at 70° is provided.

The broadside beam for both lenses at frequencies, f=10 GHz, f=12.5 GHz, f=15 GHz is depicted in Fig. 5.24(a-c). We observe very good agreement in the radiation patterns. The directivity value for both lenses is identical for all frequencies and likewise the SLL.

Fig. 5.25(a-c) shows the offset beam, 40° for both lenses at frequencies, f=10 GHz, f=12.5 GHz, f=15 GHz. We notice very good agreement in the radiation patterns in terms of the directivity value at frequencies, f=10 GHz, f=12.5 GHz. The SLL value and far side lobes are slightly increased for the all-metal lens. At f=15 GHz, a mismatch on the patterns is observed; this is due to the beam of the all-metal GRIN lens being distorted as a consequence of the higher dispersion of the fakir bed of nails unit-cell.

Fig. 5.26(a-c) shows the offset beam, 70° for both lenses at frequencies, f=10 GHz, f=12.5 GHz, f=15 GHz. We observe very good agreement in the radiation patterns in terms of the directivity value and SLL at frequencies, f=10 GHz, f=12.5 GHz. However, at f=15 GHz, a mismatch on the patterns is observed similar to the offset beam, 40°.

To conclude, in lower frequencies very good agreement has been attained between the lenses. On the other hand, the radiation pattern for the all-metal GRIN Luneburg lens is distorted for the scan angles 40° and 70° at the edge frequency f=15 GHz compared to the dielectric Luneburg lens by virtue of the dispersion of the unit-cell. The latter, allows a significant reduce in the time simulation of the lens, since we can first design and simulate lenses using non-dispersive dielectric layers to take approximate results on the performance of the lens. It needs to be recalled that the simulation time for a sole excitation feed of the dielectric lens lasts 30 minutes compared to the all-metal lens which lasts 24 hours.

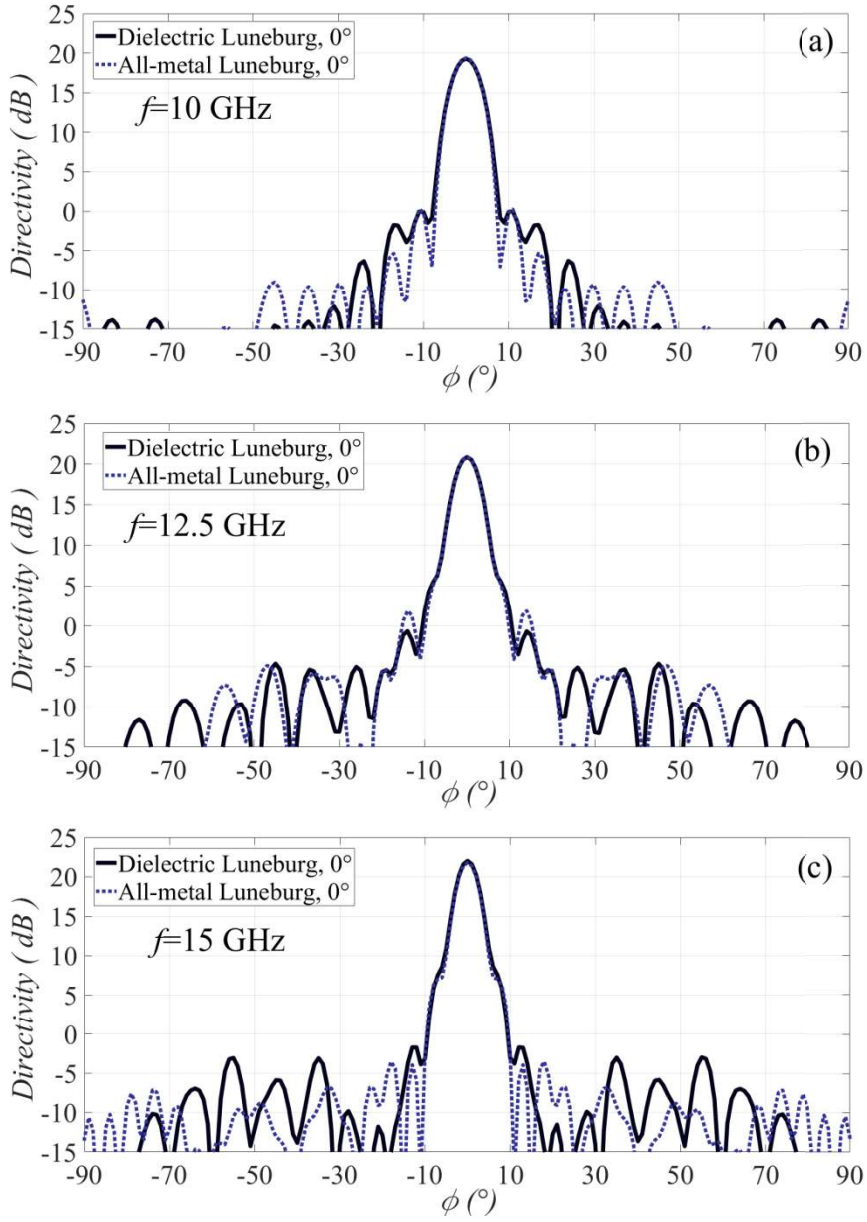

Figure 5.24: Comparison of the dielectric Luneburg lens with 26 non-dispersive layers with the all-metal Luneburg GRIN lens, for the broadside beam at frequencies, f=10 GHz, f=12.5 GHz, f=15 GHz.

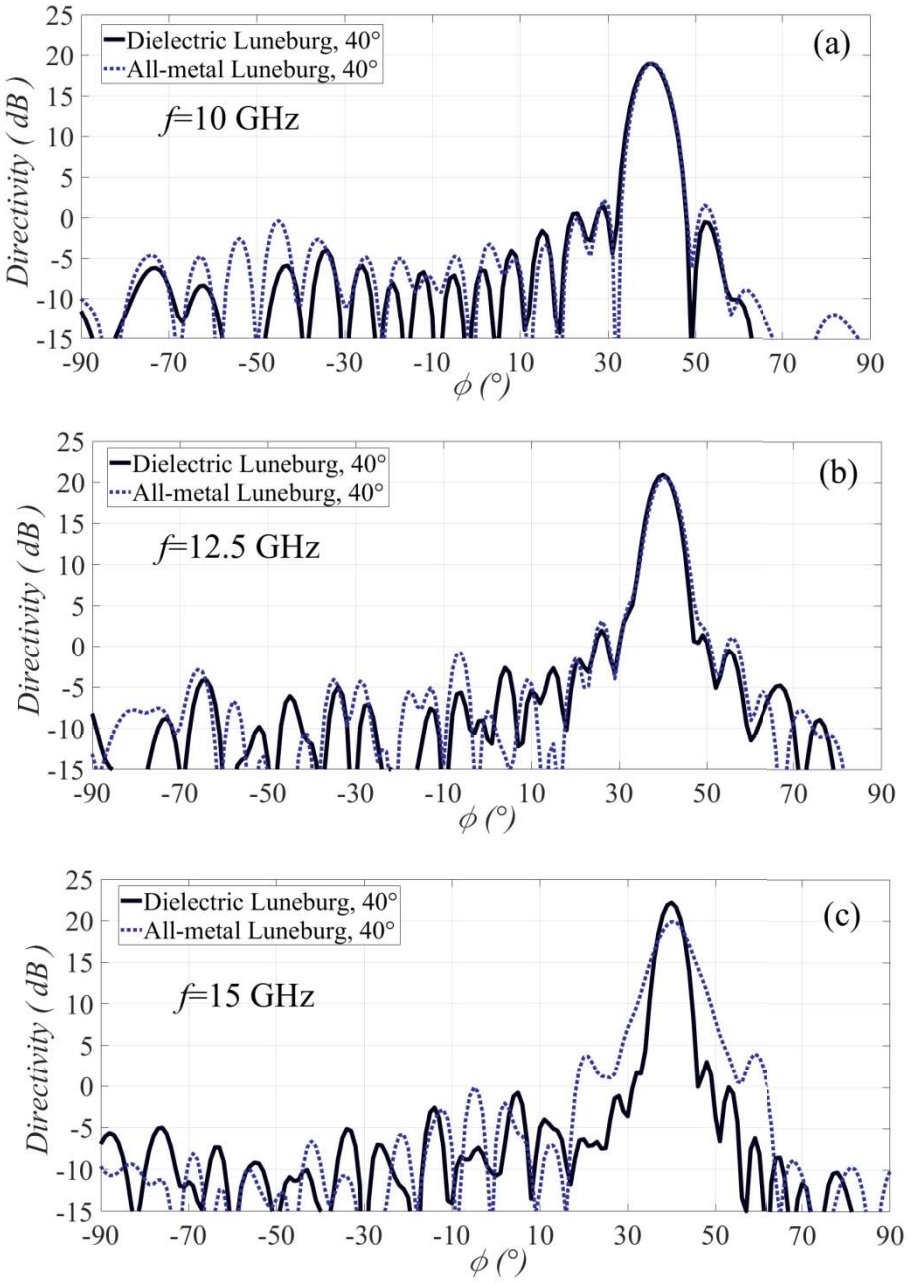

Figure 5.25: Comparison of the dielectric Luneburg lens with 26 non-dispersive layers with the all-metal Luneburg GRIN lens, for the 40° offset beam at frequencies, f=10 GHz, f=12.5 GHz, f=15 GHz.

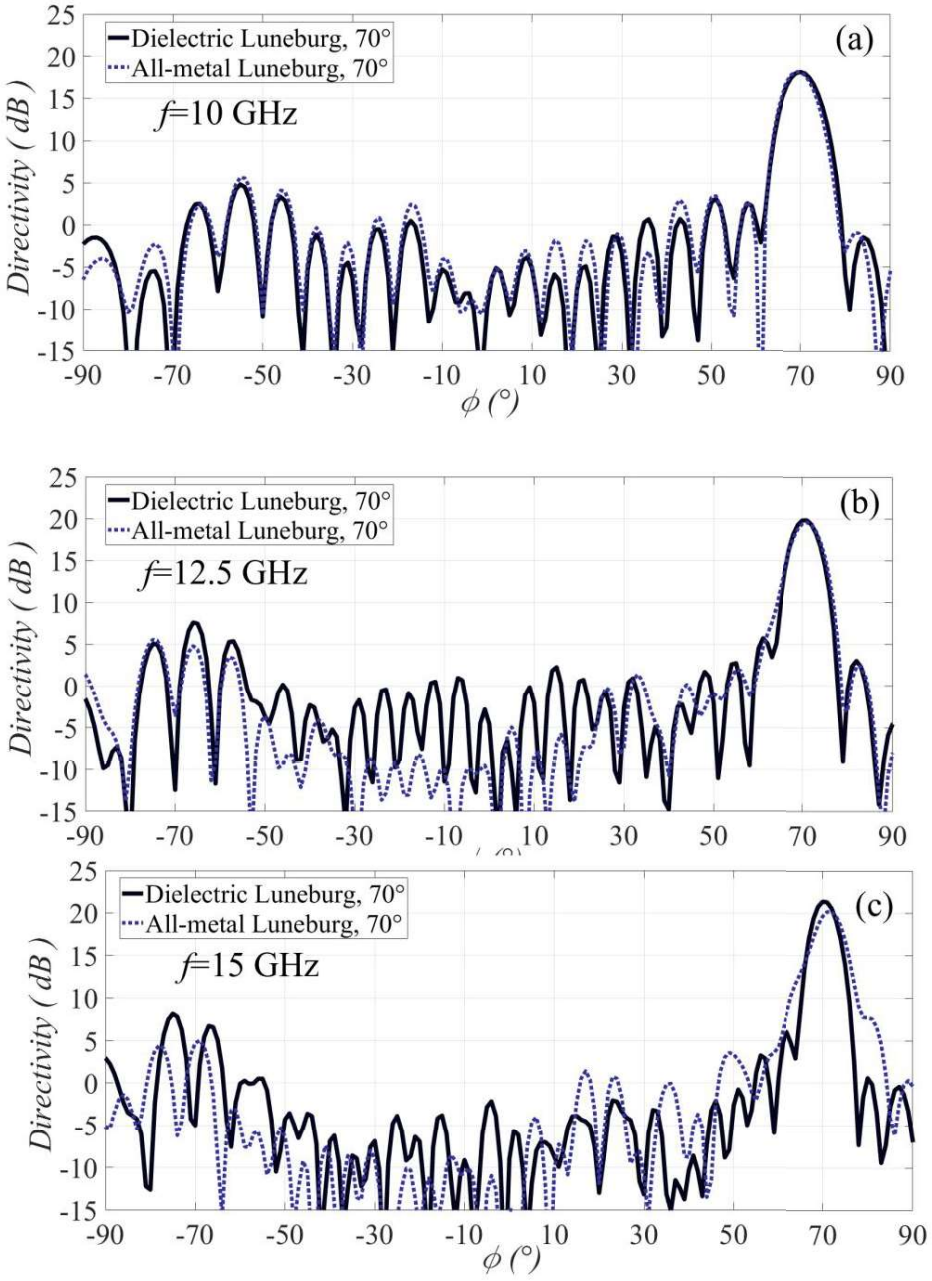

Figure 5.26: Comparison of the dielectric Luneburg lens with 26 non-dispersive layers with the all-metal Luneburg GRIN lens, for the 70° offset beam at frequencies, f=10 GHz, f=12.5 GHz, f=15 GHz.

(4) S-Parameters

The comparison of the reflection coefficients of both lenses when the broadside feed, #8 and the extreme feed, #1 are separately excited, is illustrated in Fig. 5.27(a, b). For both feeds, the dielectric lens presents slightly better performance compared to the all-metal lens. The antennas have been matched and the worst value of reflection coefficient is -11 dB. The reflection coefficient for the rest 13 feeds is not presented since the extreme feed, #1, is the worst case of all feeds and the broadside feed, #8 is the best case.

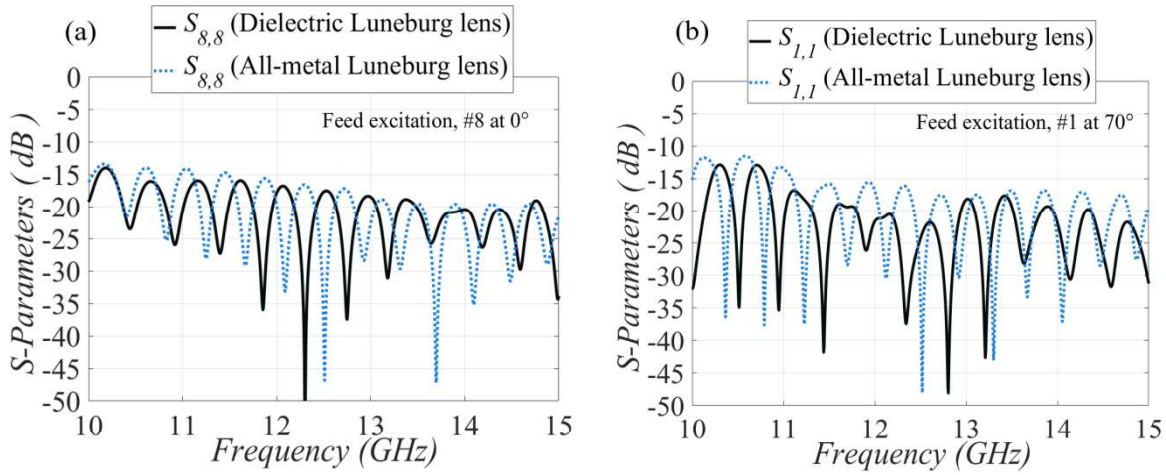

Figure 5.27: Reflection coefficient comparison between the dielectric Luneburg lens and the all-metal Luneburg lens when (a) broadside feed, #8 is excited, (b) extreme feed, #1 is excited.

Regarding to the comparison of the coupling coefficients between the ports of the lenses, we present the worst case which is the excitation of the extreme feed #1, of the lens. The results are depicted in Fig. 5.28(a, b) where similar performance has been ended up for both lenses. We notice that the extreme opposite feed #15 causes higher reflection to the excited feed #1 compared to the adjacent feed #2.

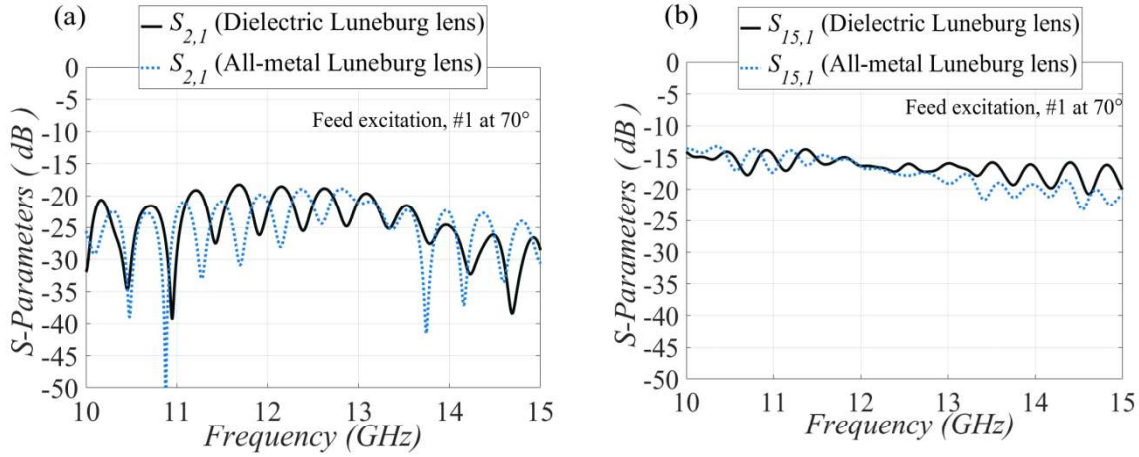

Figure 5.28: Comparison between the dielectric Luneburg lens and the all-metal Luneburg lens when the extreme feed, #1 is excited for the coupling coefficients (a) $S_{2,1}$ and (b) $S_{15,1}$.

5.2.2 Dielectric Gutman Lens antenna with focal distance *f*=*R*/2

(1) Antenna design model

The Gutman lens antenna with focal distance *f*=*R*/2 has been designed in CST Studio Suite and is illustrated in Fig. 5.29(a, b). It consists of 26 homogeneous non-dispersive dielectric layers in a cylindrical form. Every layer consists of an identical permittivity value ε, and the permittivity that corresponds to each layer is depicted in Fig. 5.29(c). The permittivity distribution has been computed based on Eq. (3.1). The lens has identical dimensions with the all-metal Gutman lens with focal distance *f*=*R*/2 that has been presented in Chapter 3.

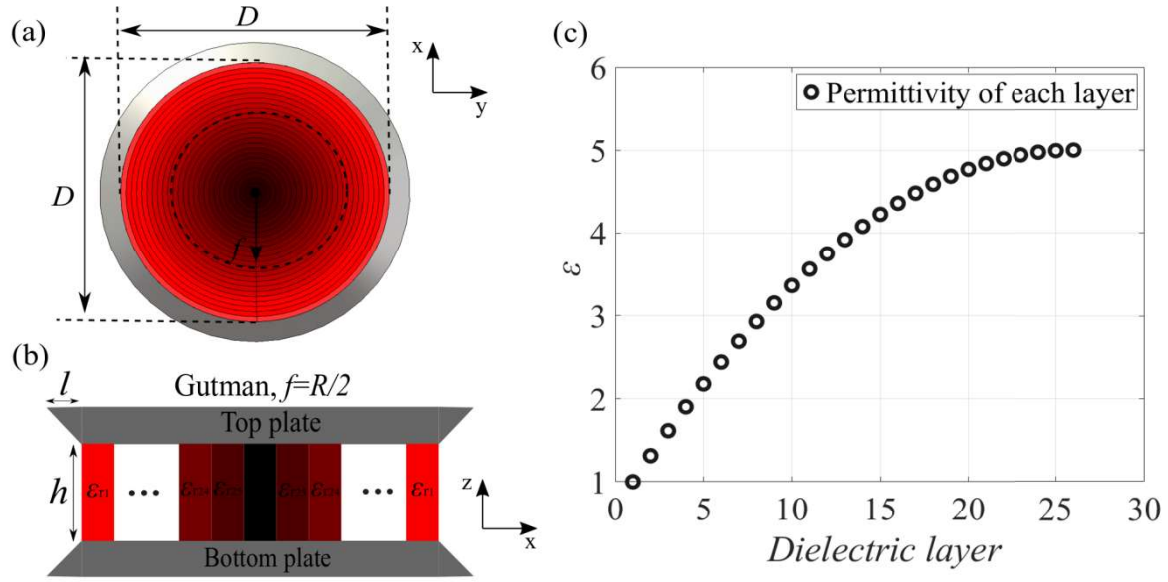

Figure 5.29: (a) Gutman lens with focal point $f=R/2$, antenna model on CST Studio Suite, with 26 dielectric layers, (b) 2D cut view of the lens, (c) permittivity values for each dielectric layer.

(2) Feed system

In order to excite the dielectric Gutman lens, a waveguide filled with dielectric is selected. The dielectric waveguide has been selected because it is easy to be designed and integrated into the focal arc of the lens.

-In order to provide a valid comparison between the present dielectric Gutman lens and the equivalent all-metal GRIN Gutman lens, 2 constraints need to be fulfilled:

- First, the waveguide needs to be filled with dielectric which has the same permittivity value as the required permittivity of the Gutman lens along its focal arc.
- Second, the number of waveguides along the focal arc of the dielectric Gutman lens has to be equal with the number of the waveguides that have been placed along the focal arc of the all-metal GRIN Gutman lens.

A significant part of the circular lens has been removed in order to accommodate 15 waveguides filled with dielectric (see Fig. 5.30(a)). The waveguide aperture is w=9 mm and its height, h=4 mm which is the height of the PPW. The permittivity of the dielectric that has been filled inside the waveguide is equal to ε=3.4. In Fig. 5.30(c), it is apparent that permittivity value of the dielectric of the waveguide is equal to the permittivity value of the dielectric cylinder #13. The cylinder, #13 is placed along the focal arc of the lens.

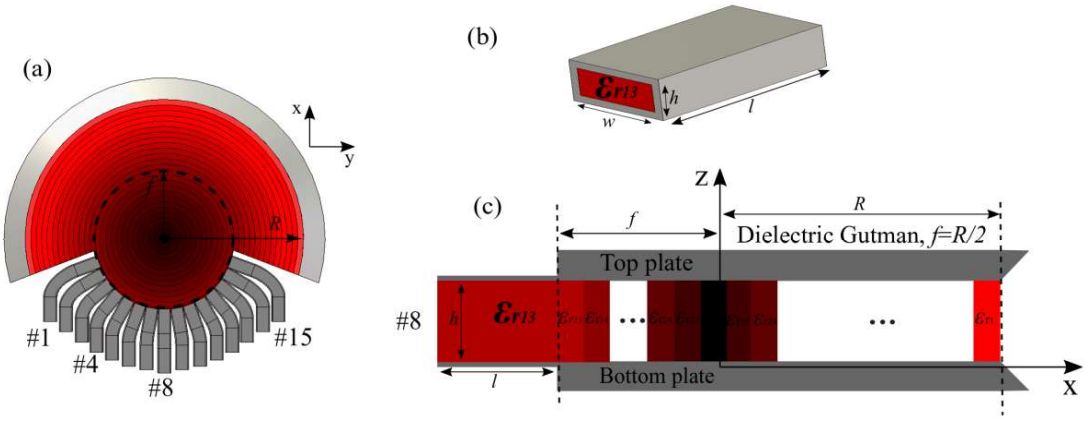

Figure 5.30: (a) 15 waveguides connected along the focal arc of the Gutman lens, (b) 3D view of the waveguide, (c) 2D cut view of the lens with the integrated waveguide.

(3) Dielectric Gutman lens Vs all-metal Gutman lens – Radiation performance comparison

In the present subsection the radiation performance of the dielectric Gutman lens antenna with 26 non-dispersive homogenous dielectric layers with the all-metal Gutman GRIN lens that is presented in Chapter 3, is compared. Both lenses operate in Ku-band and comparison of radiation patterns at the selected frequencies, f=10 GHz, f=12.5 GHz, f=15 GHz, for the broadside beam, the offset beam at 40° and the offset beam at 70° is provided. Electromagnetic simulations have been realized in CST Studio Suite using the time domain solver. Every feed, #1, #4, #8 of both lenses has been separately excited and corresponds to the pointing angles, 0°, 40° and 70° respectively.

The broadside beam for both lenses at frequencies, f=10 GHz, f=12.5 GHz, f=15 GHz is depicted in Fig. 5.31(a-c). We observe that the directivity value for the dielectric Gutman is decreased at all selected frequencies compared to the directivity of the all-metal Gutman. The reason for that is the use of the single ridge waveguide in the all-metal case. The single ridge gives a different field distribution for the propagating mode compared to the dielectric waveguide. Hence, it influences the radiation pattern. In terms of the SLL, similar performance is attained in both lenses expect the center frequency, f=12.5 GHz where the all-metal lens has higher SLL.

The offset beam, 40° for both lenses at frequencies, f=10 GHz, f=12.5 GHz, f=15 GHz is depicted in Fig. 5.32(a-c). Similar to the broadside case we notice that the directivity value for the dielectric Gutman is decreased at all selected frequencies compared to the directivity of the all-metal Gutman. Besides, the pointing angle of the all-metal antenna is slightly shifted by virtue of the dispersion of the interleaved glide symmetry unit-cell.
The offset beam, 70° for both lenses at frequencies, f=10 GHz, f=12.5 GHz, f=15 GHz is depicted in Fig. 5.26(a-c). Once again, the directivity in the all-metal lens is decreased and the beam is slightly shifted from the ideal pointing angle 70°.

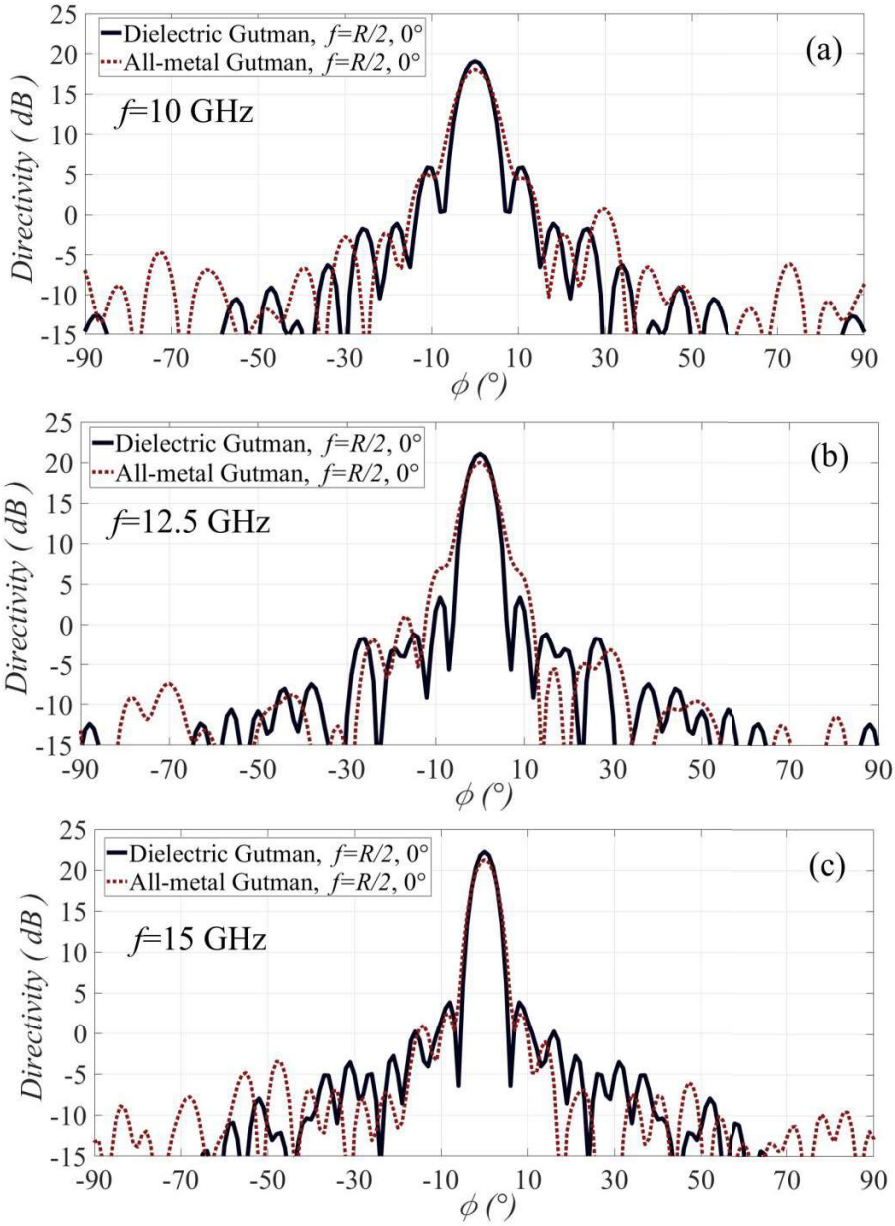

Figure 5.31: Comparison of the dielectric Gutman lens with 26 non-dispersive layers with the all-metal Gutman GRIN lens, for the broadside beam at frequencies, f=10 GHz, f=12.5 GHz, f=15 GHz.

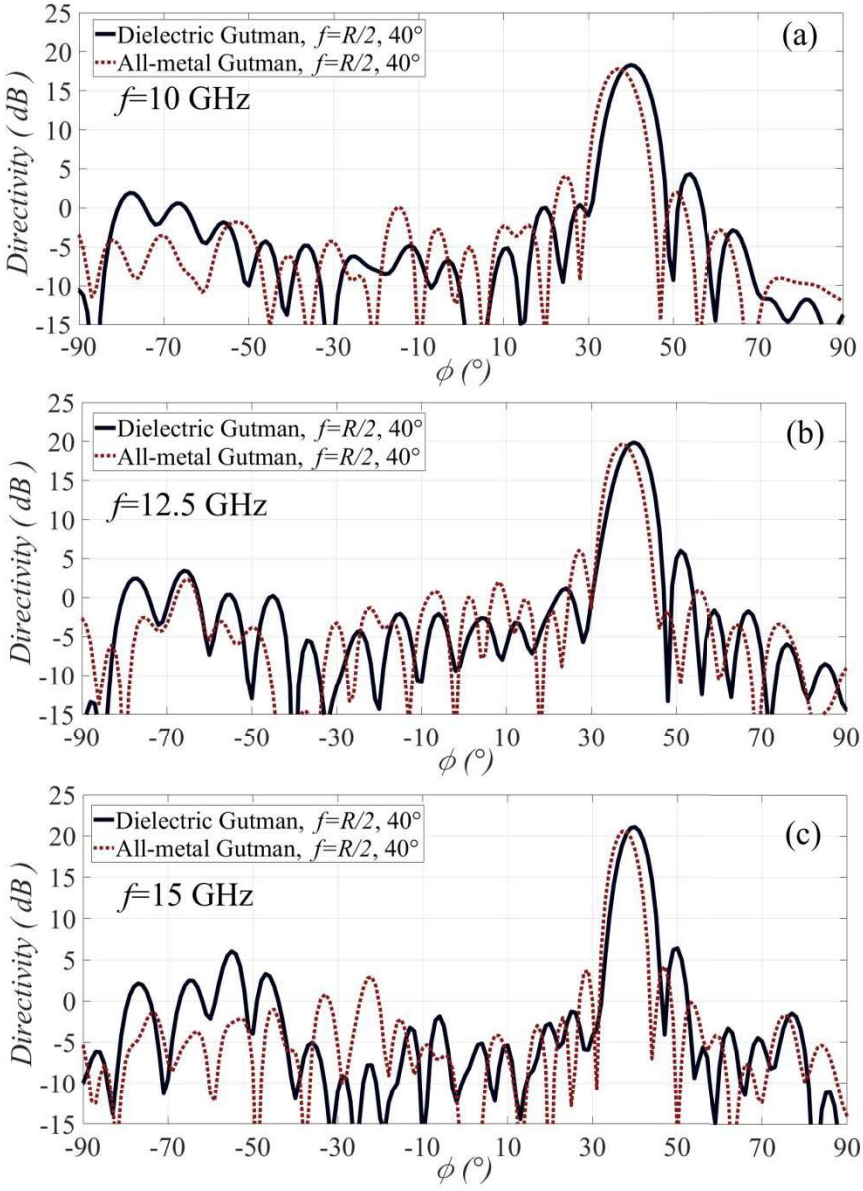

Figure 5.32: Comparison of the dielectric Gutman lens with 26 non-dispersive layers with the all-metal Gutman GRIN lens, for the 40° offset beam at frequencies, f=10 GHz, f=12.5 GHz, f=15 GHz.

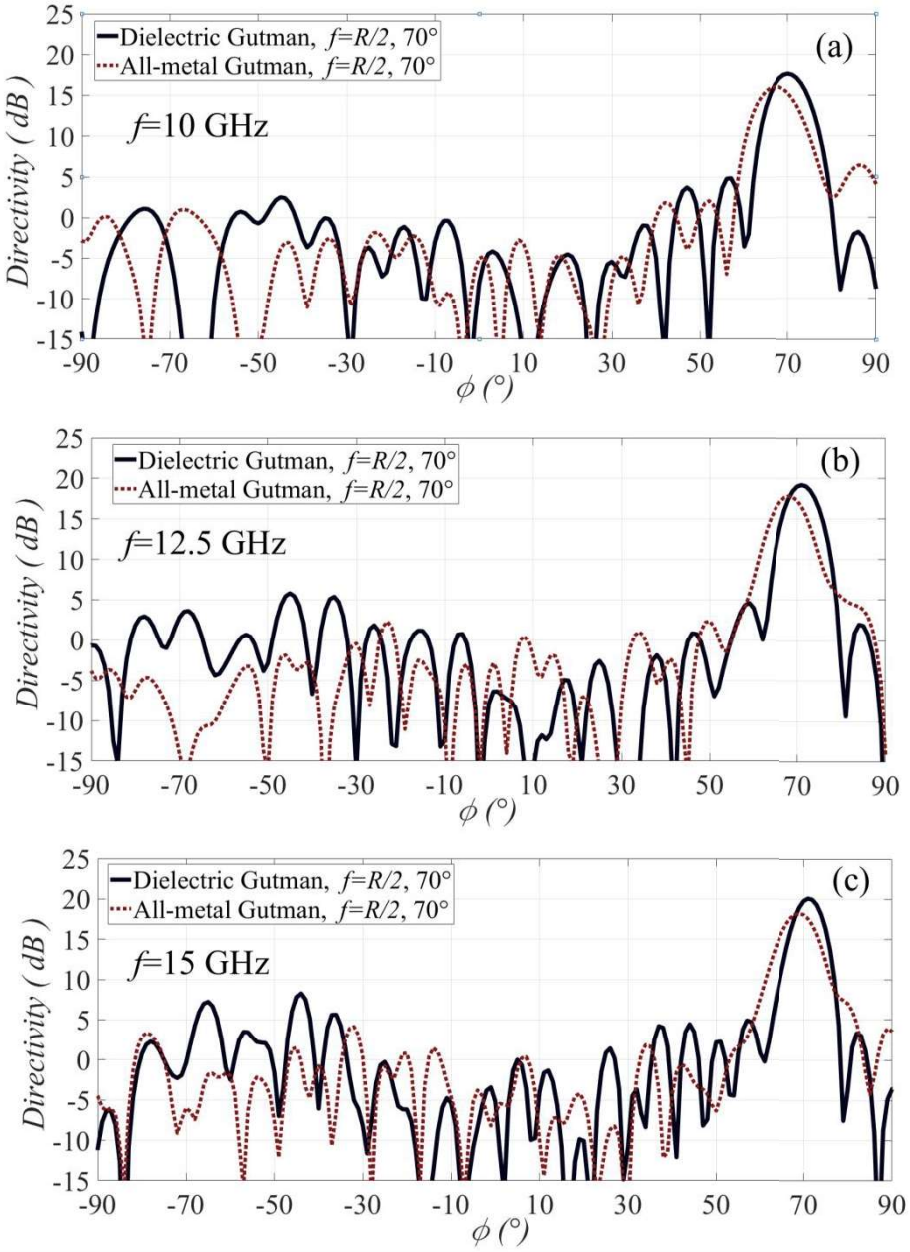

Figure 5.33: Comparison of the dielectric Gutman lens with 26 non-dispersive layers with the all-metal Gutman GRIN lens, for the 70° offset beam at frequencies, f=10 GHz, f=12.5 GHz, f=15 GHz.

(4) S-Parameters

The comparison of the reflection coefficients of both lenses when the broadside feed, #8 and the extreme feed, #1 are separately excited, is illustrated in Fig. 5.34(a, b). The worst case and the best case is presented here. The worst case, is the excitation of the extreme feed, #1 where the dielectric lens has more wideband performance. The best case is the excitation of the broadside feed, #8 where both lenses have similar performance.

Regarding to the comparison of the coupling coefficients of the lenses we present merely the worst case which is the excitation of the extreme feed #1, of the lens. The ports that have the highest impact on the excited port feed #1, are the adjacent port #2 (see Fig. 5.35(a)) and the

extreme opposite port #15 (see Fig. 5.35(b)). We observe that both coupling coefficients $S_{2,1}$ and $S_{15,1}$ are improved for the dielectric Gutman lens.

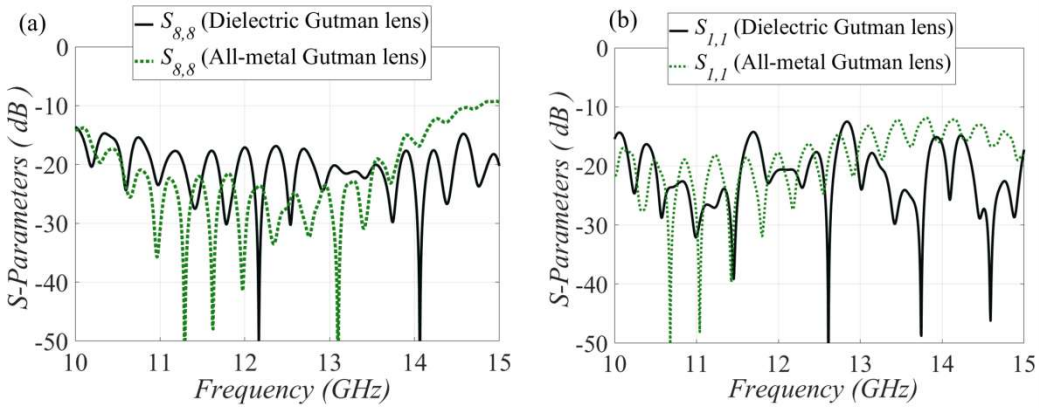

Figure 5.34: Reflection coefficient comparison between the dielectric Gutman lens and the all-metal Gutman lens when (a) broadside feed, #8 is excited, (b) extreme feed, #1 is excited.

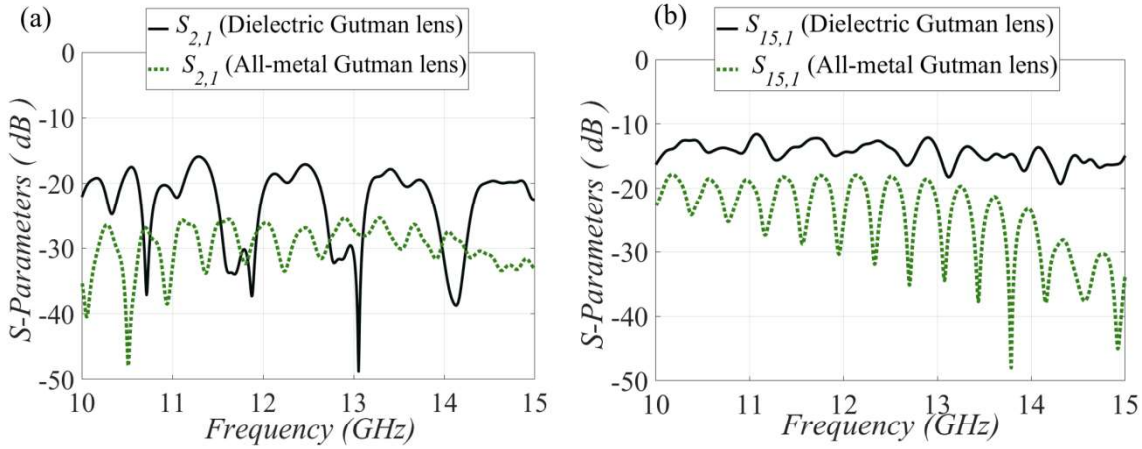

Figure 5.35: Comparison between the dielectric Gutman lens and the all-metal Gutman lens when the extreme feed, #1 is excited for the coupling coefficients (a) $S_{2,1}$ and (b) $S_{15,1}$.

5.2.3 Dielectric Gutman Lens antenna with focal distance *f*=*R*/2.85

(1) Antenna design model

The dielectric Gutman lens with focal distance, $f=R/2.85$ has been designed in CST Studio Suite and is shown in Fig. 5.36(a, b). The present lens comprises of 26 non-dispersive dielectric layers with segregate permittivity values. The distribution of permittivity for every dielectric layer is designated in Fig. 5.36(c).

The width of every cylinder is twice the periodicity, p=2.4 mm of the unit-cell that has been used in the all-metal case of the Gutman lens. All the widths of the cylinders are equal and takes the value, w=4.8 mm. The radius of the lens is equal to $R=f=5.21\,\lambda$ =125 mm. It needs to be mentioned that the width, w, of the dielectric layers is equal for both lenses, Luneburg, Gutman lens with focal distance $f=R/2$ and the present Gutman lens with focal distance $f=R/2.85$. It has been selected based on the similar discretization of the all-metal lenses which is likewise identical.

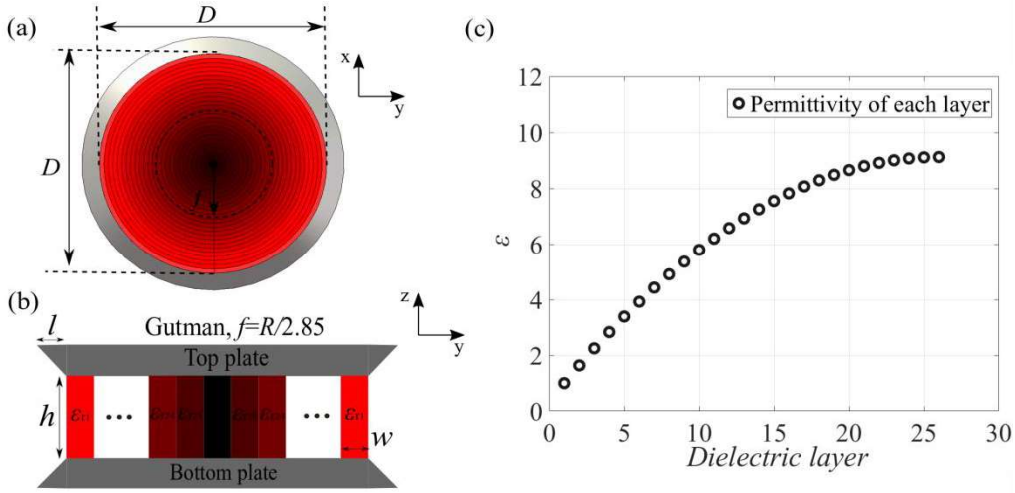

Figure 5.36: (a) Gutman lens with focal point f=R/2.85, antenna model on CST Studio Suite, with 26 dielectric layers, (b) 2D cut view of the lens, (c) permittivity values for each dielectric layer.

(2) Feed system

In order to excite the lens, the rectangular waveguide filled with dielectric is used. The permittivity of the dielectric of the waveguide is equal to the equivalent permittivity along the focal arc of the lens. The aperture of the waveguides is equal to the aperture of the waveguide of the feed that has been used in the all-metal Gutman lens in order to provide a valid comparison regarding to the radiation patterns of both lenses. The latter, has ended up on the use of 11 waveguides and have been integrated along the focal arc of the lens (see Fig. 5.37(a)). The permittivity of the dielectric that is filled inside the waveguide is equal to ε_{19}=4.91 and is depicted in Fig. 5.37(b, c). The feed ports, #1, #3, #6 have been separately excited and the comparison of the radiation patterns between the dielectric Gutman lens and the all-metal GRIN Gutman lens of the Subsection 5.1.1 is shown in the following subsection.

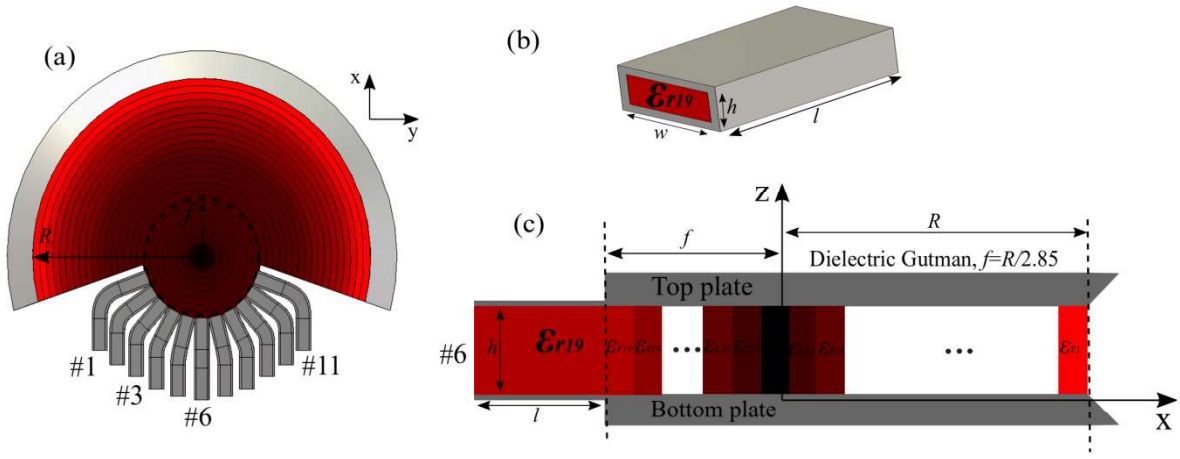

Figure 5.37: (a) 15 waveguides connected along the focal arc of the Gutman lens, (b) 3D view of the waveguide, (c) 2D cut view of the lens with the integrated waveguide.

(3) Dielectric Gutman lens Vs all-metal Gutman lens – Radiation performance comparison

The radiation performance of the dielectric Gutman lens antenna with the all-metal Gutman lens that is presented in Subsection 5.1.1, is compared. Both lenses operate in Ku-band and comparison of radiation patterns in the selected frequencies, f=10 GHz, f=12.5 GHz, f=15 GHz, for the broadside beam, the offset beam at 40° and the offset beam at 70° is provided.

In Fig. 5.38(a-c) the comparison of the broadside beams is depicted. The all-metal GRIN Gutman with focal distance $f=R/2.85$ has more efficient performance in terms of the SLL compared to the equivalent dielectric lens. The directivity values are similar for both lenses. In particular, the beam at the edge frequency, f=15 GHz for the dielectric lens has been distorted which proves that the Gutman lens with smaller focal circles is narrowband.

Fig. 5.39(a-c) shows the comparison of the offset beams, 40°. We observe that for all frequency points the directivity of the dielectric lens is decreased. It needs to be remarked that this fact is likewise observed for the previous comparisons between dielectric and all-metal lenses. Fig. 5.39(c) shows the beam at the limit frequency, f=15 GHz which has been deformed for the all-metal Gutman lens and not for the dielectric one, as it was the case for the broadside beam. The latter, is attributed to the high dispersion of the interleaved glide symmetry unit-cell at high frequencies. Similar observation are noted in the Fig. 5.40(a-c) for the extreme offset beam 70°.

To conclude, both all-metal GRIN Gutman lens with focal distance $f=R/2.85$ and the equivalent dielectric lens have narrowband performance by virtue of the high dispersion of the unit-cell and the large extracted surface of the lens.

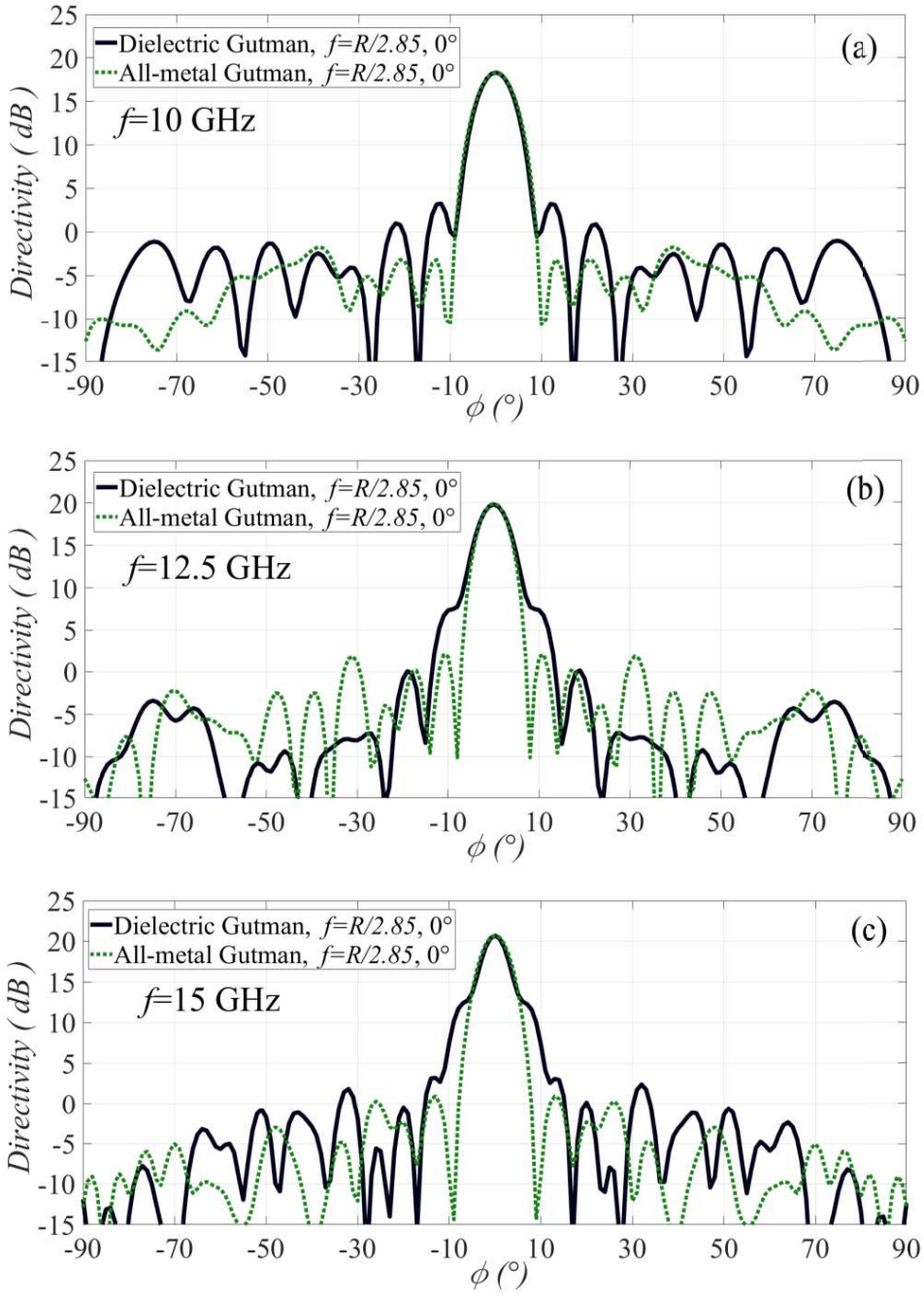

Figure 5.38: Comparison of the dielectric Gutman lens with 26 non-dispersive layers with the all-metal Gutman GRIN lens, for the broadside beam at frequencies, f=10 GHz, f=12.5 GHz, f=15 GHz.

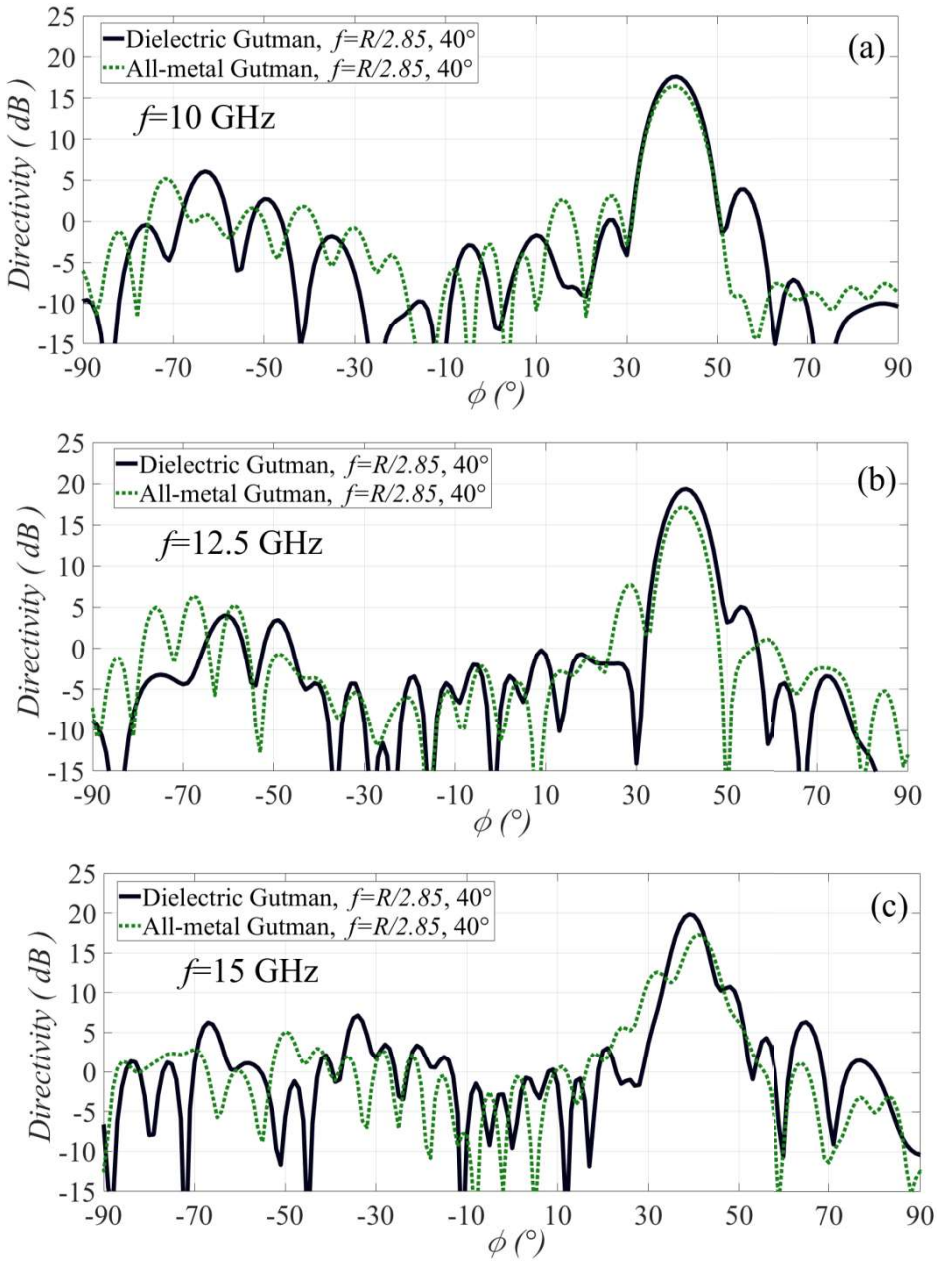

Figure 5.39: Comparison of the dielectric Gutman lens with 26 non-dispersive layers with the all-metal Gutman GRIN lens, for the 40° offset beam at frequencies, f=10 GHz, f=12.5 GHz, f=15 GHz.

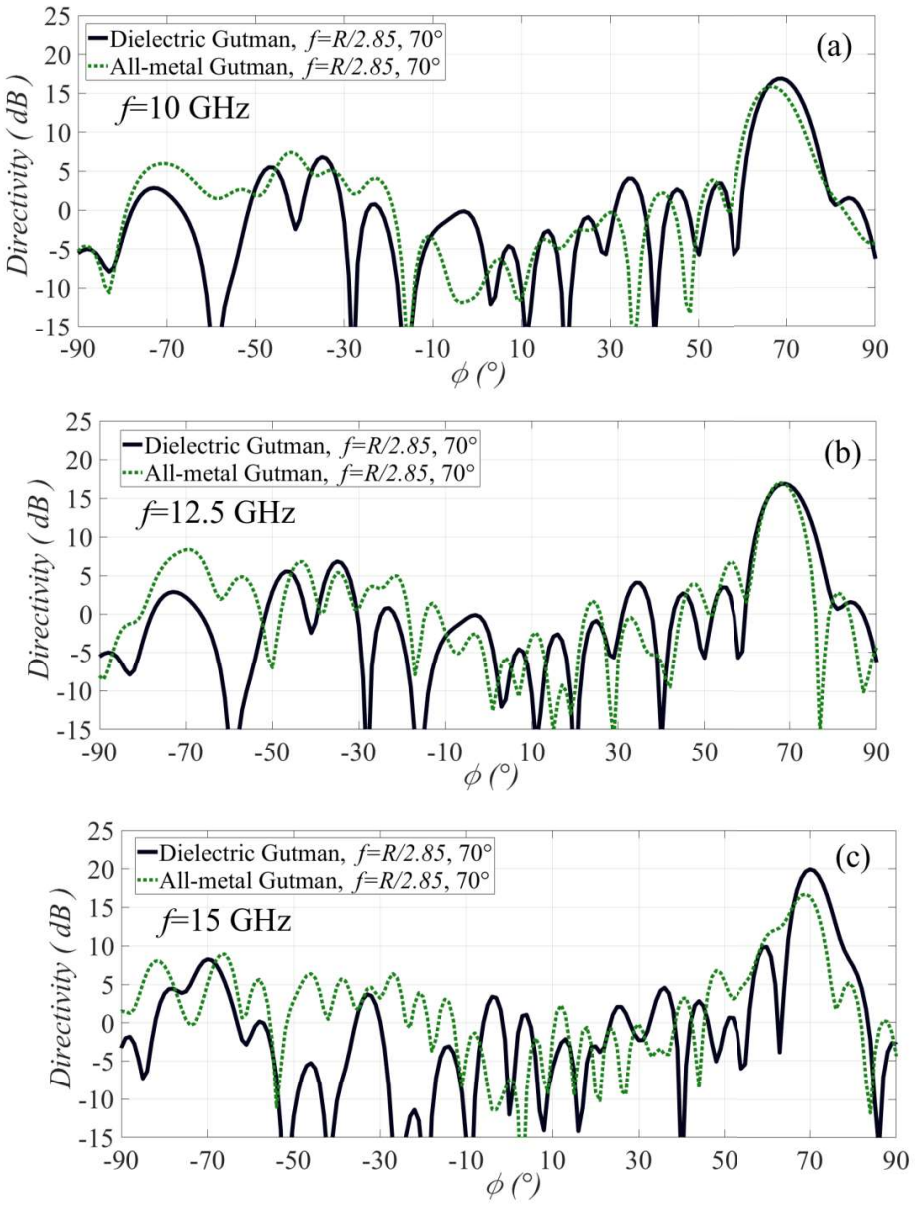

Figure 5.40: Comparison of the dielectric Gutman lens with 26 non-dispersive layers with the all-metal Gutman GRIN lens, for the 70° offset beam at frequencies, f=10 GHz, f=12.5 GHz, f=15 GHz.

(4) S-parameters

The reflection coefficients of the lenses are depicted in Fig. 5.41(a, b). It is shown that the all-metal lens is not well matched compared to the dielectric lens. The reason is the high required value of the effective index of refraction along the focal arc of the lens which calls for smaller feed apertures. However, exploiting the matching methodology that has been analysed in Subsection 3.5.2, the reflection can be drastically improved. The coupling coefficients of the lenses are depicted in Fig. 5.42(a, b) where similar performance in both lenses is observed.

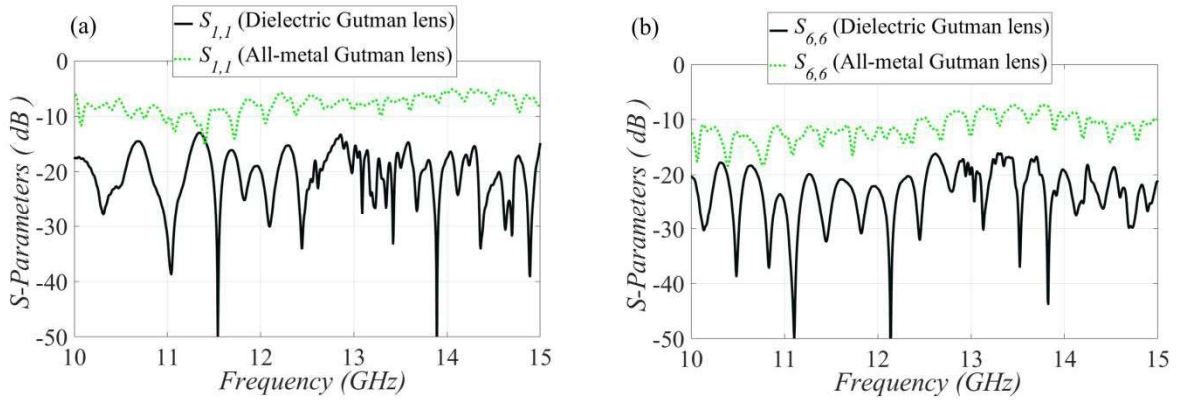

Figure 5.41: Reflection coefficient comparison between the dielectric Gutman lens and the all-metal Gutman lens when (a) broadside feed, #6 is excited, (b) extreme feed, #1 is excited.

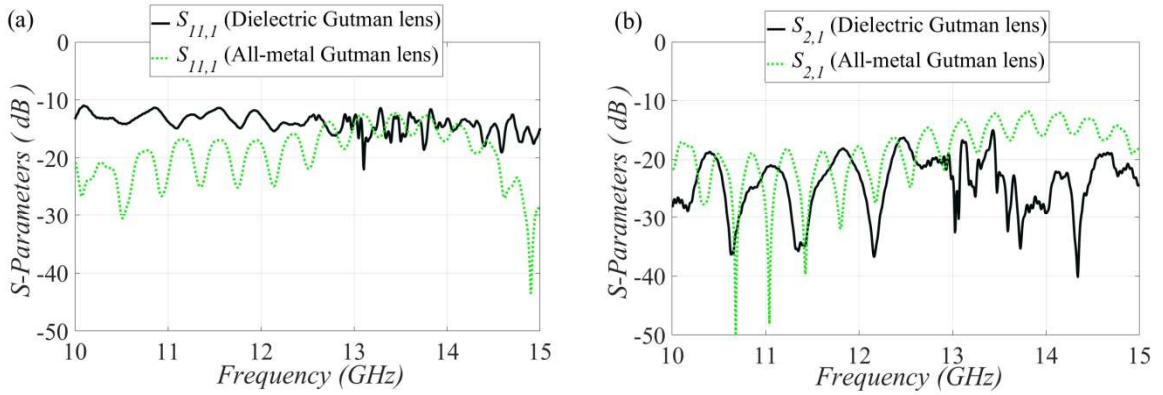

Figure 5.42: Comparison between the dielectric Gutman lens and the all-metal Gutman lens when the extreme feed, #1 is excited for the coupling coefficients (a) $S_{2,1}$ and (b) $S_{11,1}$.

5.3 Conclusions

In this Chapter the all-metal Gutman lens with focal distance f=R/2.85 together with the all-metal Luneburg lens have been presented. The radiation performance, in addition to the S-parameters, have been compared to the all-metal Gutman lens with focal distance f=R/2 of the Chapter 3. It is concluded that the Gutman lens has similar FOV with the Luneburg lens, although it has higher level of side lobes and higher scan losses. In terms of the reflections of both lenses, the Luneburg lens shows slightly better performance. Furthermore, the matching of the Gutman lens is more complicated since compact feeds have to be designed. However, the design of the single ridge waveguide eliminated the reflections of the Gutman lens.

The equivalent dielectric lenses, Gutman lens with focal distance f=R/2, Gutman lens with focal distance f=R/2.85 and Luneburg lens have been designed. Both have been compared to the all metal designs. It has been concluded that the dielectric lenses show slightly higher directivity compared to the metal lenses and they are easy to be matched.

Chapter 6 An Optimized Continuous Delay Line Lens Antenna with Isoflux Envelope Mask Performance

Contents

6.1 Introduction

6.1.1 Objectives

The need of isoflux performance in the radiation patterns of the multi-beam antenna is emerging for the mega-constellation missions. At low orbits, the path loss of the signal of the user that is at the edge coverage of the earth is larger compared to the signal of users that are in the nadir of the earths' coverage. Hence, a multi-beam antenna needs to compensate this high path losses at extreme pointing angles. However, this is in contrast with the traditional theory of the antennas arrays where scan losses exist as we steer the titled beam in wider scan angles.

The objective of this part of the thesis is to design a multi-beam all-metal lens antenna in order to steer the radiated titled beam and progressively increase the directivity of the offset beams. Fig. 6.1 shows an approximate scheme to clarify the concept and the specifications of

the lens in terms of radiation performance. In this example graph, it is apparent that the directivity of the offset beams is progressively increased and all the beams create an envelope mask which has the form of an isoflux graph. Exploiting the frequency hopping spread spectrum (FHSP), the transmitting signals of the antennas are switched among several frequency channels and the interference between the adjacent beams is decreased by virtue of the low values of the carrier to interference (C/I).

The scan range that we target is ±52° and the directivity of the extreme offset beam needs to be higher compared to the directivity of the broadside beam; the ideal dB difference between them should be 6.2 dB. The lens should operate at Ka-band and the required directivity for the extreme offset beam at 52° is 26.2 dB and for the broadside beam, 20 dB. Additionally, low values of, C/I are required to avoid the interference between the beams. An C/I > 16 dB at 95% of the beam coverage is considered acceptable. The cross over value between consecutive beams should be in the level of 6 dB.

Considering the above mentioned specifications, the topology of the antenna that has been selected to be examined is the continuous delay line lens on a PPW technology that has been introduced in [12].

This type of lens antenna has been preferred compared to the GRIN Gutman lens and Luneburg lens due to the following advantages:

- The periodic structures inside the PPW of the Gutman lens have very small size at Ka band and the high vibrations during the launcher can impact the geometry of the unit cells. Hence, the continuous delay line lens is preferred.
- A single EM simulation of the continuous delay line lens for a single radiating beam using transient or frequency solvers lasts approximately 30 minutes using a computer of 96 G RAM. However, the same EM simulation of the GRIN Gutman lens lasts approximately 2.000 minutes due to the high amount of periodic the periodic structures.
- An in-house optimizer is available which is capable to optimize the profile of the continuous delay line lens and define targets for the desirable radiating patterns of the antenna. This optimizer facilitates our work to achieve the targeting radiation patterns.

The objective here is to optimize the lens in order to produce titled beams that all of them comprise an isoflux envelope mask. A geometrical optics (GO) tool which has been introduced in [93] and the optimizer that has been presented in [94] has been used to design the profile of the lens and then optimize it. A preliminary modified design of the continuous delay line lens has been implemented based on [74] and then optimization techniques have been be utilized to achieve our targets.

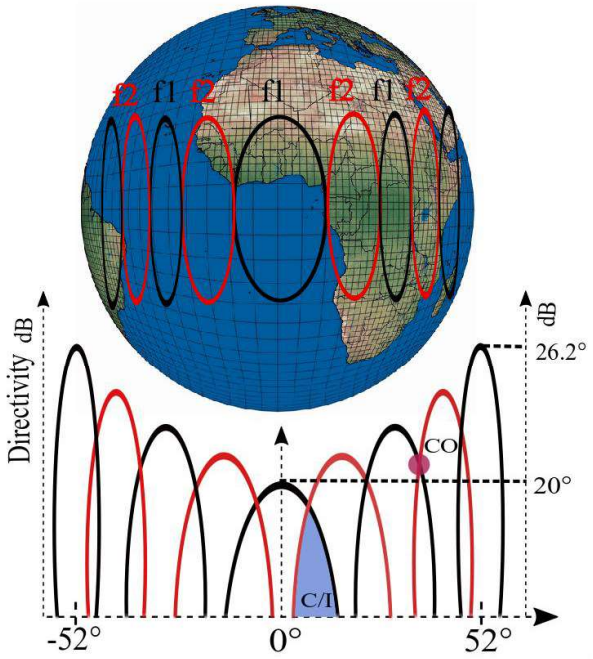

Figure 6.1: Specifications of the isoflux envelope multi-beam patterns representation.

6.2 Antenna architecture

6.2.1 Antenna topology model

The antenna technology that has been selected to be investigated is the continuous PPW delay line lens which has been introduced in [12] and is depicted in Fig. 6.2(a). The lens transforms the cylindrical waves that are launched in the PPW section into plane waves along its periphery. This transformation is realised by a PPW region in the lens which is composed of a transversal ridge (see Fig. 6.2(b)). The lens achieves excellent performance in terms of radiation and reflections, although it has limited FOV up to ±30° on the H-plane (see Fig 6.3(a, b)). In [93], a Geometrical Optics (GO) tool has been developed based on ray tracing which predicts accurately the normalized radiation patterns of the antenna. The GO tool characterizes the wave front in the PPW section of the travelling wave of the excitation source before the lens' region and also in the PPW section of the transversal ridge (see Fig. 6.2(a)) to predict the performance of the antenna in terms of radiation patterns in all the predefined pointing angles. The time delay of the signal inside the transversal ridge is controlled by the shape and the height of the ridge which forms the required phase distribution in order to focus the beam.

In the present lens model, the constrained delay-lens is approximated as a bifocal lens model. The approximation has been adopted by virtue of the bifocal lens theory model [95] which consists of two identical focal points which lead on two offset beams that point on opposite directions. Ideally, these beams should provide the maximum directivity for an offset feed that is oriented in wide scan pointing angles. Therefore, the focal points of the lens are (F_1, F_2) where $F_1 = F_2$.

The present antenna is a constrained based lens approach and it avoids the discretization for the phase values. The use of the transversal ridge leads to better performance in terms of

bandwidth and complexity, in comparison with the traditional constrained lenses with discrete profiles [49].

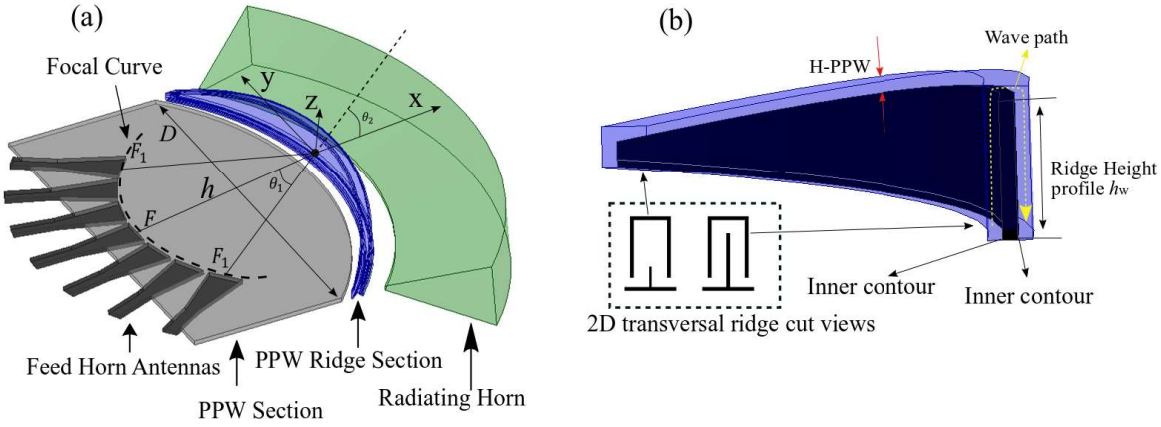

Figure 6.2: (a) 3D model of the PPW continuous delay line lens, (b) 3D model of the PPW ridge.

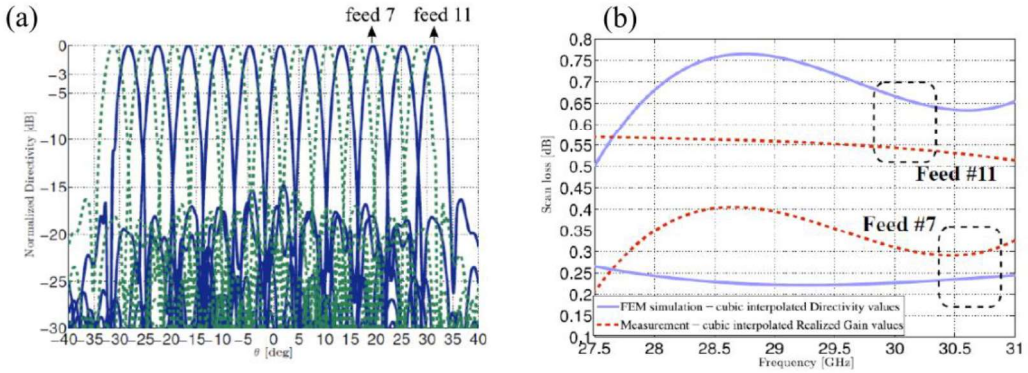

Figure 6.3: (a) Normalized patterns of the reference design and (b) scan losses for the offset beams [96].

-The working plan that has been adopted here follows as:

- First, the GO model tool that has been used to design the lens is described.
- Second, a preliminary design of the transversal ridge is presented using the GO model tool. The aperture of the lens has been designed in order to maximize the directivity of the extreme offset beam and on parallel to minimize the directivity of the broadside beam.
- Then, an optimization technique has been endorsed to optimize the transversal ridge and the aperture of the excitation feeds of the lens in order to progressively increase the directivity of the offset beam.
- Finally, a design demonstrator is presented which achieves an isoflux envelope mask with wide FOV up to ±48°.

6.2.2 GO model tool

A brief description of the GO model tool is presented here. The design of the continuous delay line lens on the GO tool in matlab is depicted in Fig. 6.4. The inner profile of the lens is noted with the green curve and the outer profile with the red one. The blue curves represent both the inner and the outer profile of the ridge. It needs to be mentioned that the colors of every curve will be the same for every following design, as well as in the optimization process that is presented in later subsection. The metal thickness of the ridge is the distance between the red and the green curves. The focal distance, h_0 is determined from the center point of the outer profile of the lens (center of the *xyz* coordinate system) till the point source. The point source represents the phase center of the feed horn antenna that will be used in the later full-wave simulations to verify the results of the GO tool. The titled beam of the lens radiates along *x* axis.

The profiles of the inner and outer contours of the lens, as well as the inner and the outer contour of the transversal ridge are elliptical. The definition of the profiles are based on the Eq. (6.1-6.3). Eq. (6.1) specifies the inner contour of the lens; Eq (6.2) the outer contour of the lens and Eq. (6.3) the profile of the ridge. The design parameters, a_{inner}, a_{outer}, a_{ridge} define the elliptical profile and value, d the diameter of the lens where $d = D/f$. All the variables in Eq. (6.1-6.3) are normalized by the focal distance, f.

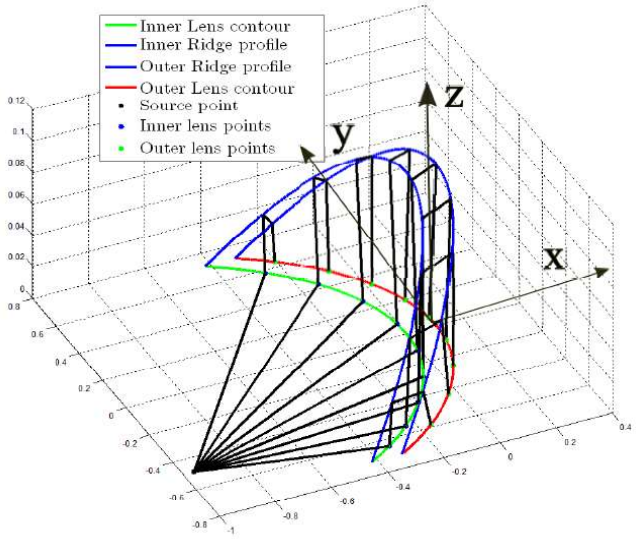

Figure 6.4: 3D continuous lens-design model of the GO tool in Matlab.

$$x_{inner}=a_{inner}\left(\sqrt{(1-y^2)}-1\right) \tag{6.1}$$

$$x_{outer}=a_{outer}\left(\sqrt{(1-y^2)}-1\right) \tag{6.2}$$

$$x_{ridge}=a_{ridge}\left(\sqrt{(1-y^2)}-\sqrt{\left(1-\left(d/2\right)^2\right)}\right) \tag{6.3}$$

6.3 Design methodology

To achieve the isoflux envelope radiation performance on the continuous delay line lens, a design methodology has been adopted based on numerical and full wave simulations. First, using the GO modelling tool, we have designed the elliptical profile of the lens. The inverse axis technique has been implemented to the profile of the lens targeting the isoflux envelope patterns and it will be extensively presented in Subsection 6.3.1. Then, in order to have some preliminary results, the design parameters of the profile of the lens have been tuned together with its focal distance and the aperture of the waveguide feeds. Since we have noticed that the θ_{3dB} of an extreme beam is more narrow to the θ_{3dB} of the broadside beam we have proceed with the development of an optimization technique using an in-house optimizer to improve and specify precisely the performance of the radiation patterns. The design parameters of the lens, its focal distance and the aperture of the feeds have been optimized and the goal was to achieve more narrow θ_{3dB} beam width for the extreme radiation beam compared to the θ_{3dB} beam width of the broadside radiation beam. Then, the best agents of the optimizer have been imported to the GO model tool where we have evaluated the normalized directivity patterns. Finally, the antenna has been designed and simulated in HFSS using the best agents of the optimizer to apply full wave simulations. A brief description of the steps that have been adopted is illustrated in the Table 6.1.

Table 6.1: A brief analysis of the steps that have been followed to design and optimize the continuous delay line lens.

Design steps of the continuous delay line lens	
Step 1	Design the elliptical profile of the lens based on the inverse axis technique using the GO model tool.
Step 2	Tune the profile of the lens, its focal distance and the aperture of the waveguide and verify the normalized radiation patterns for the broadside beam and for the extreme beam. The goal is to verify that the θ_{3dB} beam width of the extreme beam is more narrow compared to the broadside one.
Step 3	Optimize the elliptical profile of the lens, as well as, its focal distance and the apertures of the waveguide feeds using the in-house optimizer.
Step 4	Verify the normalized directivity patterns in the GO tool importing the best agents of the optimizer.
Step 5	Validate the directivity patterns utilizing full wave simulations in HFSS.

6.3.1 Aperture design with isoflux mask envelope distribution

The first step in the design process, before optimizations, is the design of an elliptical profile lens to retrieve some preliminary results. In Fig. 6.5(a) the profile of the lens of the reference design, [93] is depicted where the inner contour of the lens is equal to the outer contour of the lens. It is evident that the minor axis is defined by the B radius and the major axis by the A radius. In our proposed design which is depicted in Fig. 6.5(b), we invert these two axis A, B by modifying the contour of the lens; the inner contour remains equal to the outer contour. Thoroughly, in our design, the minor axis is defined by the A' radius and the major axis by the B' radius. Utilizing this ellipse axis inversion, the extreme feed illuminates larger effective aperture profile of the lens compared to the broadside feed (see Fig. 6.5(c)). As a result, the plane wave that is formed on the periphery of the contour profile of the lens is

larger and results on more narrow θ_{3dB} compared to the θ_{3dB} on the broadside oriented feed. The contour of the ridge is likewise elliptical and its profile is identical to the profile in [95]. Thus, using the GO tool we tuned only the values, a_{inner} and a_{outer}, where a_{inner}= a_{outer}. To achieve the elliptical axis inversion as it is shown in Fig. 6.5(b) we should have always a_{inner} > 1.

The design variables a_{inner}= a_{outer} has been tuned for a_{inner}=1, 1.5, 2, 2.5, 3 (all the values should be > to 1 in order to verify the elliptical axis inversion where B' is the major axis of the ellipse and A' is the minor axis of the ellipse). The variable, a_{ridge} represents the height of the ridge and is constant and equal to a_{ridge} = 0.3 as in [94]. The next two variables that have been tuned are the width aperture, w and the focal distance, h. The feed horns have been placed in a circular arc as designated in Fig. 6.5(d) and point the center of the coordinate system. Applying these values to the GO tool, normalized directivity patterns have been verified for the broadside beam and the extreme offset beam, 43° (see Fig. 6.6(a)). It is apparent that the θ_{3dB} of the broadside beam is wider compared to the extreme beam at 43°. Fig. 6.6(b) shows the normalized field aperture on the periphery of the lens for both beams. It is clearly shown that the amplitude of the electric field for the extreme beam is wider compared to the field of the broadside beam.

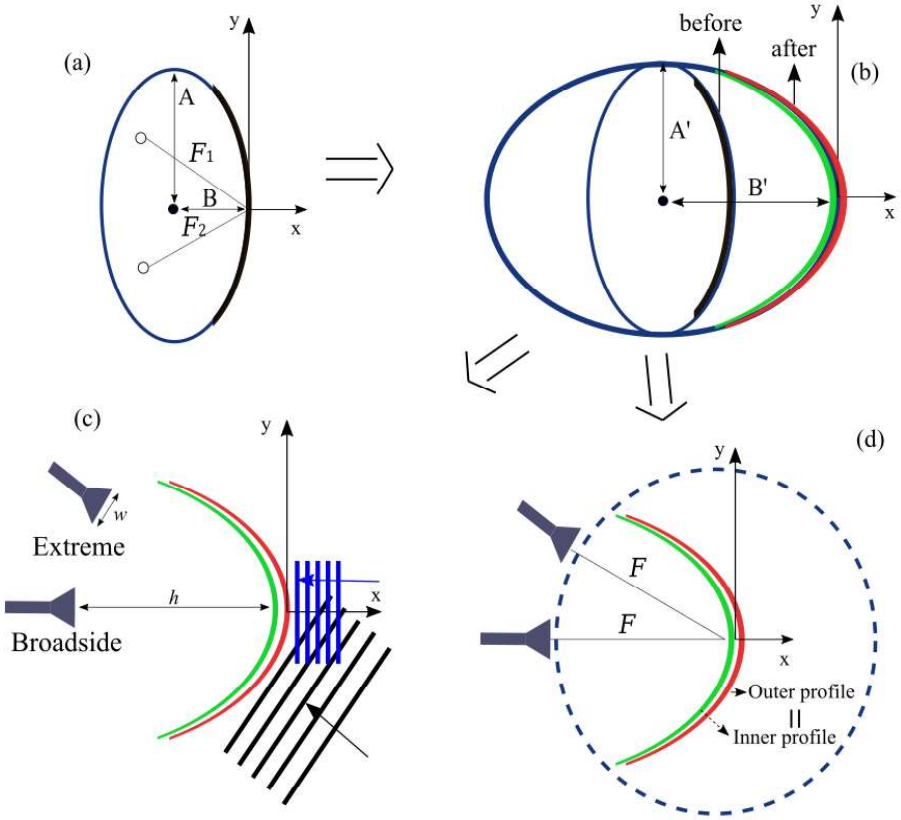

Figure 6.5: (a) Aperture of the reference design, (b) Proposed aperture based on the ellipse axis inversion (c) effective apertures for the broadside and the extreme beams, (d) feeds placed on a circular arc.

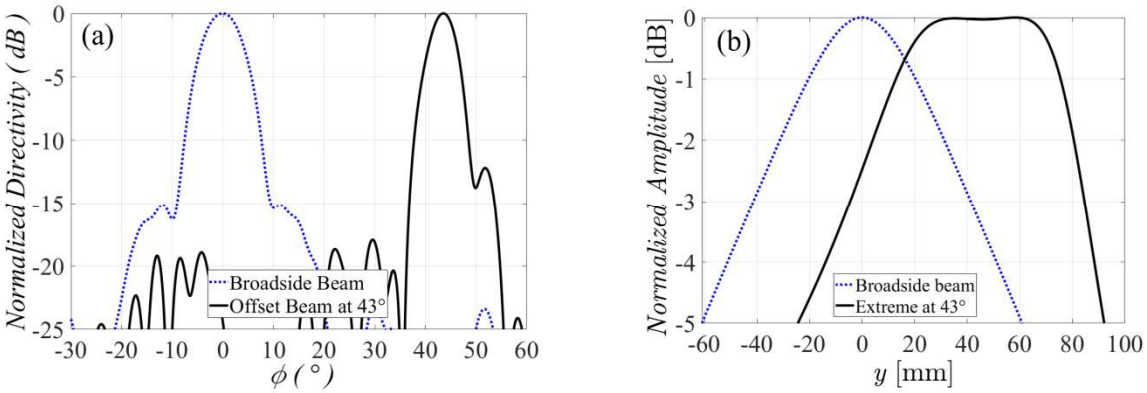

Figure 6.6: (a) Normalized directivity patterns for the broadside beam and the extreme offset beam, 43°, (b) normalized amplitude comparison of the electrical field along the periphery of the lens.

Since the extreme beam has more narrow θ_{3dB} beam width compared to the θ_{3dB} beam width of the broadside beam, the next step is to verify the progressive decrease of the θ_{3dB} for the rest offset beam in order to attain an isoflux distribution. Hence a parametric sweep has been realized in the GO tool for the selected scan angles, 18°, 32°, 43°, as shown in Fig. 6.7(a-d); all feeds have identical aperture. We notice that θ_{3dB} of the broadside radiating beam is wider than the θ_{3dB} of the offset beam at 18° and a progressive decrease of θ_{3dB} has been attained for the rest offset beams 32° and 43° (see Fig. 6.8(a-d)). The extracted data of the θ_{3dB} over the selected scan pointing angles are depicted in Fig. 6.9 where θ_{3dB}= 9°-broadside beam, θ_{3dB}= 8.2°-offset beam 18°, θ_{3dB}= 7.8°-offset beam 32°, θ_{3dB}= 5.9°-extreme beam 43°.

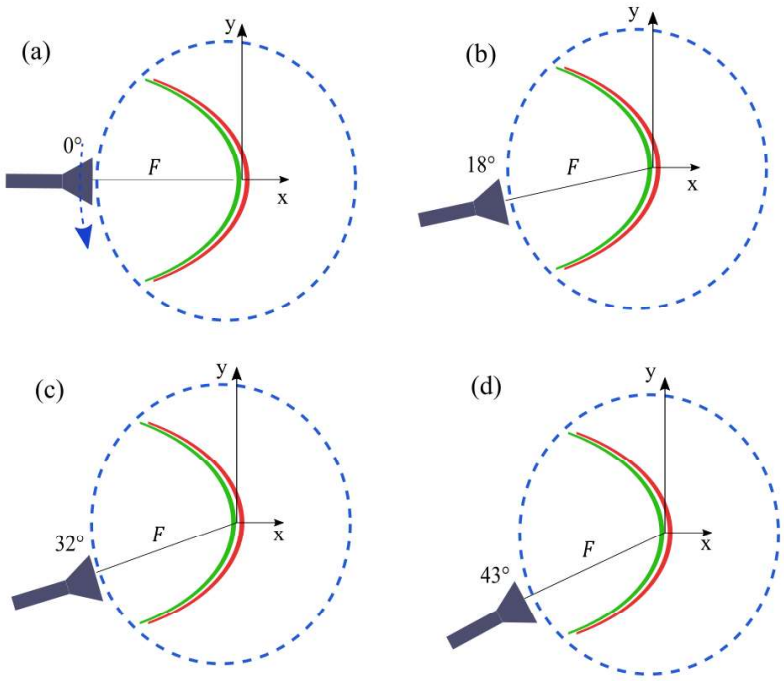

Figure 6.7: Parametric sweep for the (a) broadside beam, (b) offset beam at 18°, (c) offset beam at 32°, (d) and the offset beam at 43°.

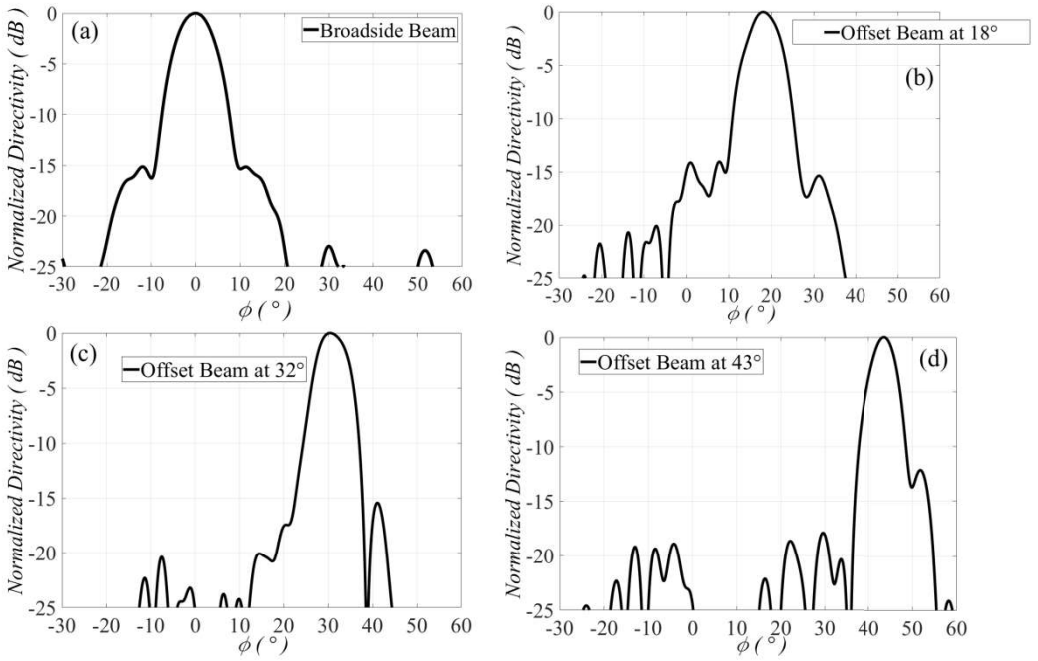

Figure 6.8: Normalized directivity patterns for (a) broadside beam, (b) offset beam at 18° (c) offset beam at 32°, (d) offset beam at 43°.

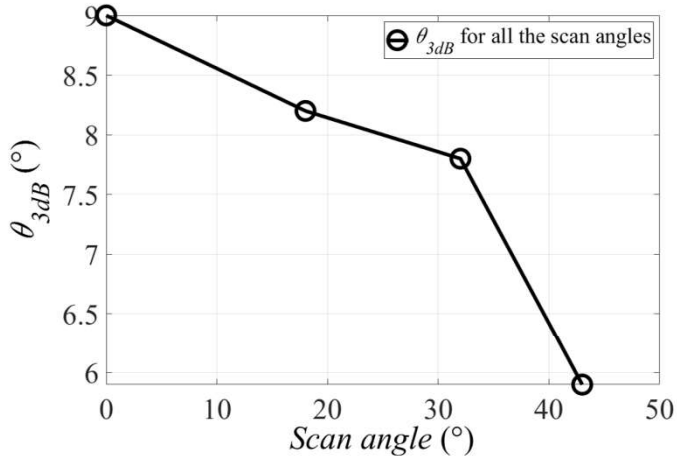

Figure 6.9: θ_{3dB} vs scanning.

-The conclusions after the completion of the preliminary design of the lens follow as:

- A progressive decrease of the θ_{3dB} beam width has been achieved compared to the θ_{3dB} beam width of the broadside beam of directivity using the inverse axis technique on the outer contour of the lens, although the width aperture of the feeds is very large and there is significant physical overlapping between the consecutive feed horns.
- The beam widths are very wide and we have high overlapping values. However, the lens can be used for a reconfigurable case scenario. In this scenario, a single waveguide with very large aperture can be placed on the focal arc of the lens antenna and can be steered mechanically.

In order to confront the above challenges, an optimization technique has been endorsed and is presented in the following Section 6.4.

6.4 Optimization technique

The parametric study that has been presented in the previous Subsection 6.3.1, motivated our task to proceed with optimizations of the profile of the lens antenna, as well as, the aperture of its excitation feeds and its focal distance.

In this section, the optimization methodology that has been adopted to achieve our goals is presented. The optimizer that is developed in [96] has been used to apply our specifications.

-The optimization process is divided in 3 stages.

- In the first stage, the power mask definition is described.
- In the second part, we specify the DoFs that have been used to optimize the inner and the outer profile of the lens, as well as the single ridge profile. Multi-objective optimizations have been utilized where two power mask patterns have been specified to achieve distinct targets, concurrently.
- In the third section, we optimize merely a single DoF which is the feed width aperture, *w,* to avoid the overlapping between consecutive feeds and further improve the performance of the patterns. In this case we specify solely one power mask pattern and we optimize the feed width aperture for all the scan angles separately.

6.4.1 Power Mask Pattern-Stage 1

The first step is to define the power mask pattern and specify our targets in terms of the desired pointing angle and the beam width of the patterns. The mask pattern for the broadside beam is computed with respect to [96] as

$$Mask=\text{sinc}\left[\left({}^{50.76}/_{\theta_{3dB}}\right)\cdot\sin\ \ \left(\theta-\theta_{target}\right)\right] \tag{6.4}$$

and is shown in Fig. 6.10. The desired targets that are defined are the θ_{3dB} of the normalized far field, the θ_{target} which is the desired target pointing scan angle and the desired *SLL*. For the SLL value which is designated in the left side of the target beam, we compute the limit M_u

$$M_u=\max(Mask)=SLL_{targetlevel} \tag{6.5}$$

which is the maximum value of the region from −90° till the first zero of the left side of the main target beam, $-\pi/2<\theta<\theta_{target}-\theta_{1N}$, where $\theta_{1N}=\arcsin\ (\theta_{3dB}/50.76)$. For the SLL value that is in the right side of the main target beam we re-use the limit, M_u to detect the maximum value, although in the opposite region $\theta_{target}+\theta_{1N}<\theta<\pi/2$.
To compute the desired θ_{3dB} we specify the region from $\theta_{target}-\theta_{3dB}$ to $\theta_{target}+\theta_{3dB}$ as it is shown in Fig. (6.10) and we compute the integral of the mask pattern as

$$M_L=\int_{\theta_{target}-\theta_{3dB}}^{\theta_{target}+\theta_{3dB}} Mask^2\left(\theta_{target,}\theta_{3dB}\right)\mathrm{d}\theta \tag{6.6}$$

The same region from θ_{target}-θ_{3dB} to θ_{target}+θ_{3dB} is computed once more

$$M_{GO}=\int_{\theta_{target}-\theta_{3dB}}^{\theta_{target}+\theta_{3dB}} P_{GO}{}^{2}\left(\theta_{target,}\theta_{3dB}\right)\mathrm{d}\theta \tag{6.7}$$

where, P_{GO} is the normalized far field that is imported from the GO model tool.

Hence, we define the minimum square error function (*MSE*) as

$$MSE=M_{GO}-M_{L} \tag{6.8}$$

which is the subtraction of the two areas, M_{GO} and M_L which must be minimized to achieve our desired targets regarding to θ_{3dB}. Thereafter, for the SLL level, we define a penalty which is the difference between the maximal value of the normalized far field of the GO tool, P_{GO} and the M_u as follows

$$Penalty=\max\left(P_{GO}(\theta)\right)-M_{u} \tag{6.9}$$

Finally, the cost function is defined as

$$CostFuction=MSE+Penalty \tag{6.10}$$

where both *MSE* and *Penalty* need to be minimized to reach our targets.

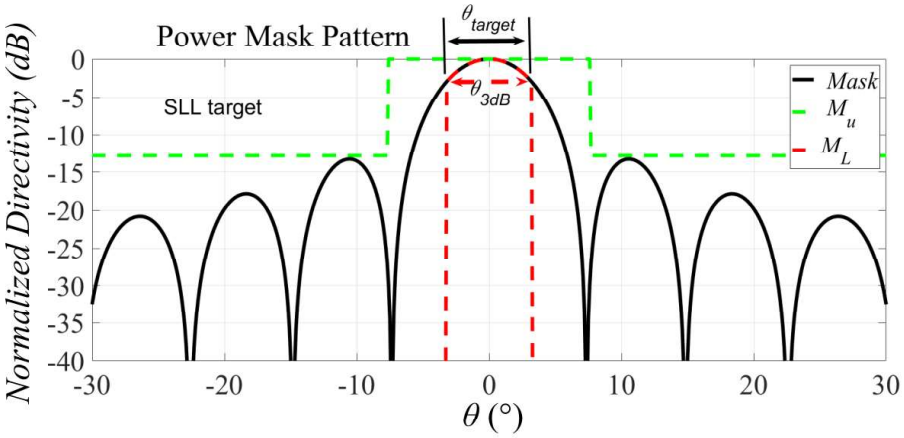

Figure 6.10: Power mask pattern for the broadside beam.

The definition and calculation of the cost function has been defined. However, the optimizer needs to be programmed in order to apply 2 distinct mask patterns simultaneously; one for the broadside beam and a second for the desired extreme offset beam. Therefore, the cost function has to consider 2 mask patterns simultanuously. Hence, the final multi-objective cost function is defined as

$$CostFunction_{(n)}=\sum_{n\text{-}1}^{n}\left(MSE_{(n)}+Penalty_{(n)}\right) \tag{6.11}$$

where the variable, n represents the number of mask power patterns in segregate pointing angles with separate θ_{3dB} values. For instance, through a single optimization run, for n=2 we define 2 power mask patterns. Thereafter, we specify the constraint, $\theta_{3dB_{(broadside)}} > \theta_{3dB_{(extreme)}}$ in order to attain higher directivity for the extreme beam. Fig. 6.11 shows an example of 2

power mask patterns. The final targets for the broadside beam that have been specified, are $\theta_{3dB} = 6°$, $\theta_{target} = 0°$ and SLL = −15 dB. For the extreme beam $\theta_{3dB} = 4°$, $\theta_{target} = 30°$ and SLL = −15 dB.

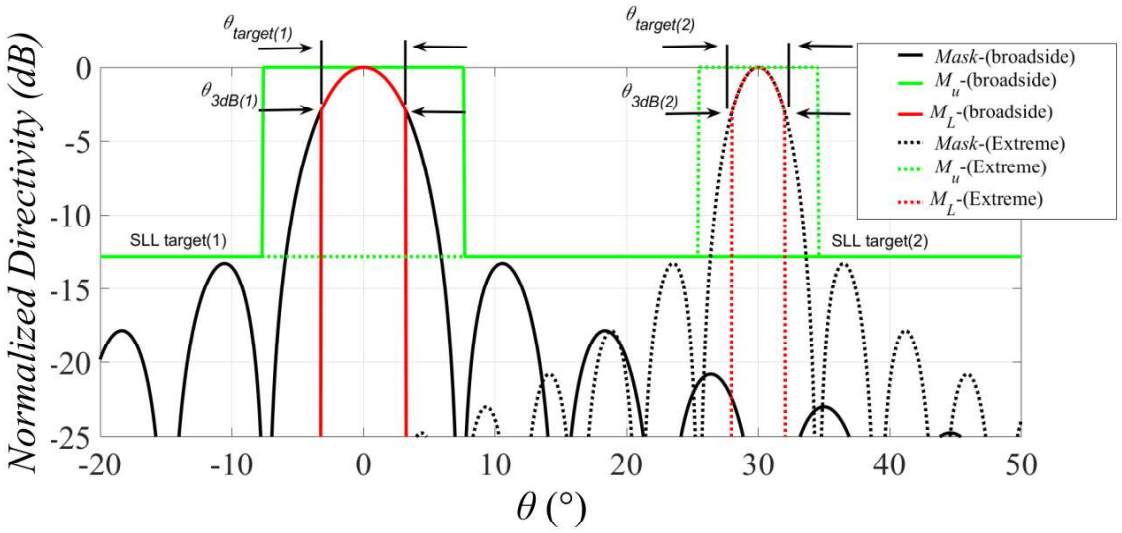

Figure 6.11: Final power mask patterns with cost function in (6.11) for n=2.

To conclude, the definition and calculation of the power mask patterns has been presented and allows the insertion of the specifications of the desired targets of the optimizer in terms of θ_{3dB}, θ_{target} and SLL.

6.4.2 Degrees of Freedom (DoF)-Stage 2

In this second stage of the optimization process, DoFs have been used to achieve the targets that have been specified and are illustrated in Fig. 6.12(a). It follows the description of every DoF that has been used in the optimization. Once more, it needs to be mentioned that both inner and outer profiles of the lens together with the ridge height are based on elliptical profiles that have been defined in Eq. (6.1)-(6.3). All the values of the design variables have been normalized to the focal distance $F = 0.7 \cdot D$, where D is the diameter of the lens.

Fig. 6.12(b) shows the distinct profiles of the lens for n number of iterations of the focal distance, h_0 and the outer contour, a_{outer}. Regarding to the outer profile, as it has been mentioned in previous Subsection 6.3.1, in the optimization process, the major axis needs always to be the B' axis and the minor axis, the A' axis in order to apply the ellipse axis inversion. For that purpose, the design parameter of the outer profile of the lens needs to be greater than unity, $a_{outer} > 1$ in every iteration; for $a_{outer} = 1$, A'=B' and the profile is circular. Hence, the range of the optimizer has been specified as $1 < a_{outer} \leq 5$. Precisely, the increase of the design parameter, a_{outer} leads to the increase of the major B' axis of the lens when the minor axis A' remains constant. Fig. 6.12(b) designates selected sample curves of the iteration of the optimizer trying to select the best agent of every iteration. The profiles of the curves of every iteration have been derived from the optimization of the design variable $a_{outer_{(1)}}$, $a_{outer_{(2)}}$, ... , $a_{outer_{(n)}}$ where n = 100 with minimal value, $a_{outer_{(1)}} = 1$ and maximal value, $a_{outer_{(100)}} = 5$. Finally, the best agent from the last iteration of the optimizer ended up to a_{outer} =

1.40. Regarding to the focal distance, h_0, the limits of that value in the optimizer is set from 0.6 to 1.5 and the best agent has ended up to h_0 = 1.05.

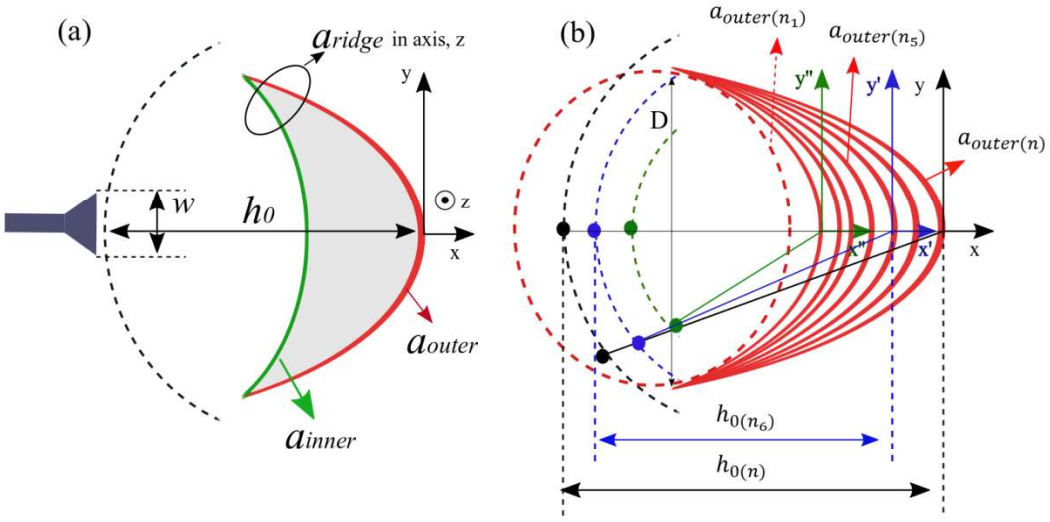

Figure 6.12: (a) 5 DoFs, (b) representation of the outer profiles of *n* iterations (red curves) and also the focal distances h_{0_n}.

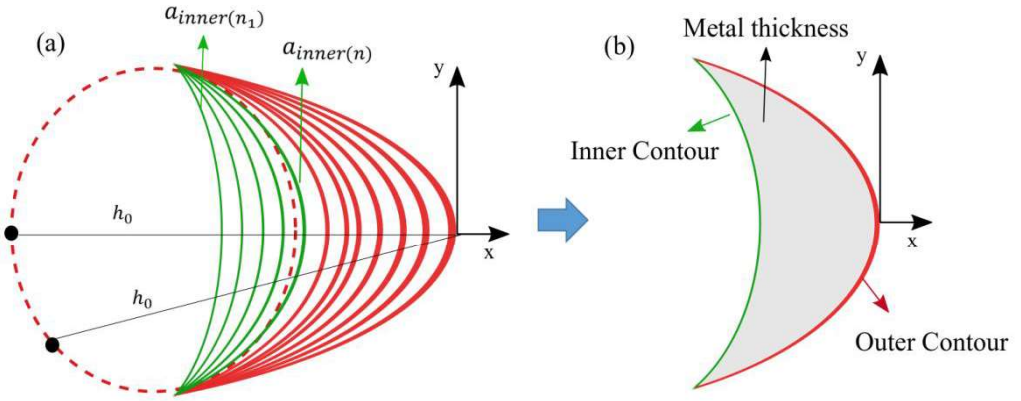

Figure 6.13: (a) Representation of the inner profiles of *n* iterations (green curves) and (b) final inner and outer optimized profiles.

The profiles of every iteration of the inner contour of the lens are likewise depicted in Fig. 6.13(a) (green curves). In this case we don't apply any axis conversion because the inner profile of the lens doesn't affect drastically the radiation performance compared to the outer profile. Thus, the design variable, a_{inner} has been optimized between the range $0.2 \leq a_{inner} \leq 3$. The variable profiles from the iterations are shown in Fig. 6.13(a) (green curves) where $a_{inner_{(1)}}$, ... , $a_{inner_{(n)}}$ for n = 100. Finally, the optimized inner and outer contour of the lens are illustrated in Fig. 6.13(b).

The same principle has been adopted for the optimization of the elliptical profile of the transversal ridge. The shapes of the transversal ridge along *z* axis for *n* iterations are depicted in Fig. 6.14(a, b) where the design variable, a_{ridge} has been optimized inside the range, $0.05 \leq a_{ridge} \leq 1$.

The last DoF is the feed width apertures of both broadside and extreme beam where w_1=w_2 = w as shown in Fig. 6.15. The range that has been selected for both widths is, 10 mm ≤w≤ 19 mm. The maximal value, w=19 mm has been selected strategically taking into account the minimum focal distance, h_0, to avoid the overlapping between the feed horn antennas.

The best agents of this second part of the optimization process with five DoFs are a_{outer}=1.40, a_{inner}=0.81, a_{ridge}=0.36, h_0 = 1.05, w=19 mm, all normalized to the focal distance, F.

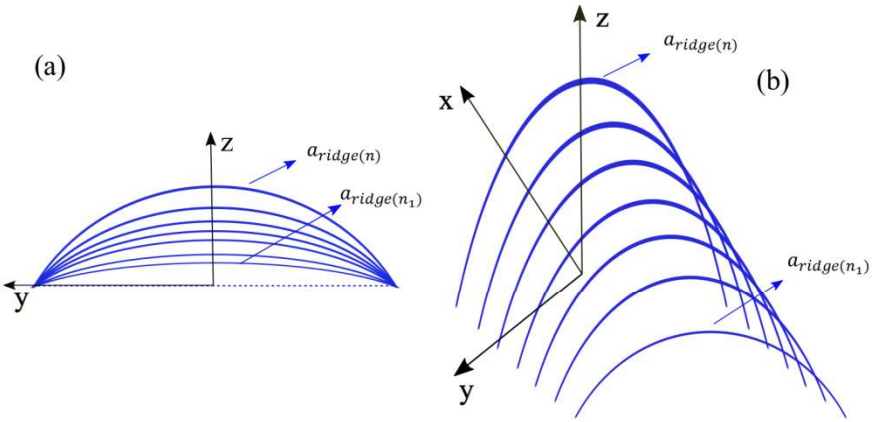

Figure 6.14: (a) 2D and (b) 3D view of the ridge profile.

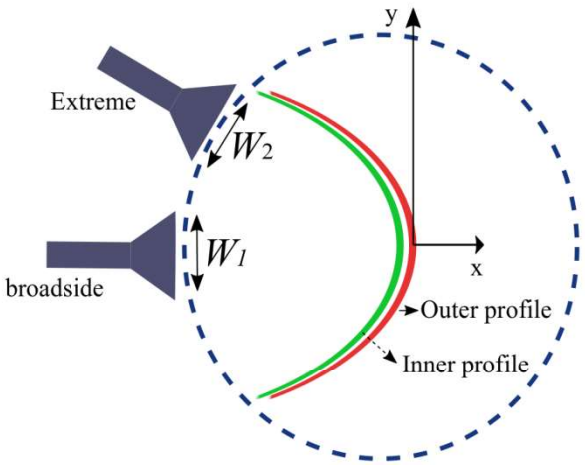

Figure 6.15: Feed width aperture representation for the DoFs, $\boldsymbol{w_1 = w_2 = w}$.

Since the best agents of the optimization have been extracted, the optimized values a_{inner}, a_{outer}, a_{ridge}, h_0 and w, have been imported to the HFSS design model (see Fig. 6.16) to apply full-wave simulations and verify the directivity of the patterns. The antenna is purely symmetric and merely the H-plane patterns in one symmetry plane are shown at the center frequency of the receiving Ka-band, f=30 GHz. The feed horns #1, #2, #3, #4, #5 have been separately excited in order to produce the offset beams pointing at 0°, 8.4°, 16.7°, 24.8°, 33°.

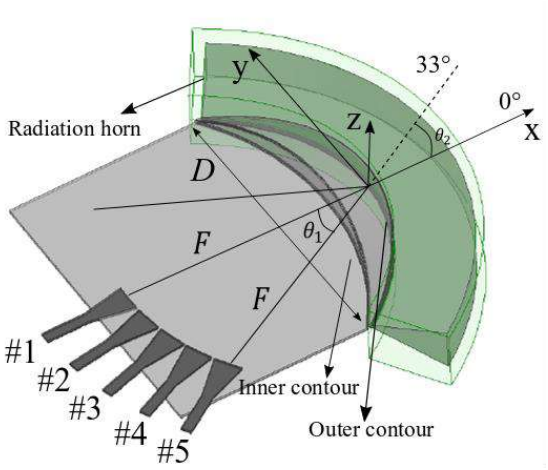

Figure 6.16: 3D HFSS delay line lens model with the symmetric beams.

In Fig. 6.17(a) we present the final patterns (from HFSS simulations). We notice that the directivity is progressively increased as we scan up to 33° and 1.3 dB difference has been achieved between the broadside and the extreme beam. The data values concerning the directivity are illustrated in Fig. 6.17(b).

In Fig. 6.18(a) the normalized patterns are depicted to verify the evolution of θ_{3dB}, and the SLL level of the patterns. In Fig. 6.18(b) we notice that θ_{3dB} is decreased as we scan which is the reason that we have higher directivity in the offset beams. In Fig. 6.19(a) we notice that first, the level of cross over is high and second, this level is not stable. As we scan and θ_{3dB} is more narrow and therefore the cross over level deteriorates progressively. In Fig. 6.19(b) the SLL values improves progressively as we scan, excluding the extreme offset beam.

To conclude, 1.3 dB difference has been attained between the broadside and the extreme beam and the directivity is smoothly increased. However, the target here is to increase that difference up to 5 dB. Drawback is the high level of cross over (varies from -8 to -17 dB) and must be improved. Therefore, the third optimization stage has been adopted in the next subsection which targets to improve the cross over level and increase the dB difference between the broadside beam and the extreme offset beam.

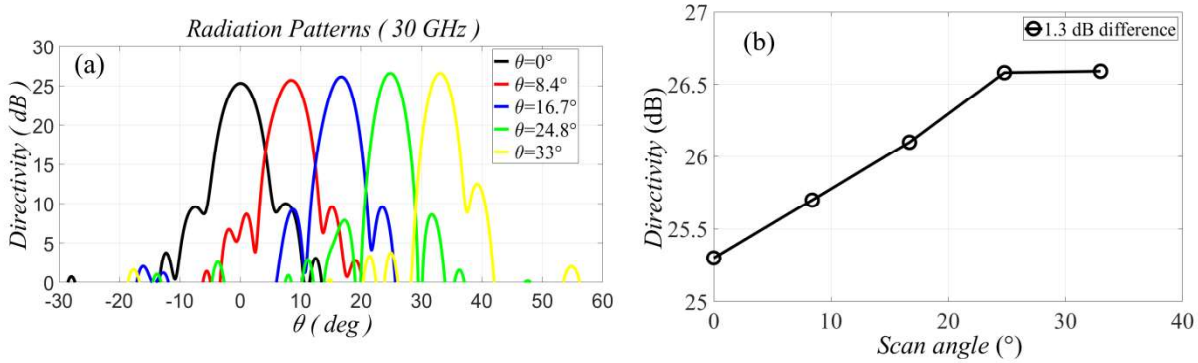

Figure 6.17: (a) Directivity patterns and (b) directivity data values over scan angle. Optimized design parameters: a_{outer}=1.40, a_{inner}=0.81, a_{ridge}=0.36, $\boldsymbol{h_0}$ = 1.05, w=19 mm.

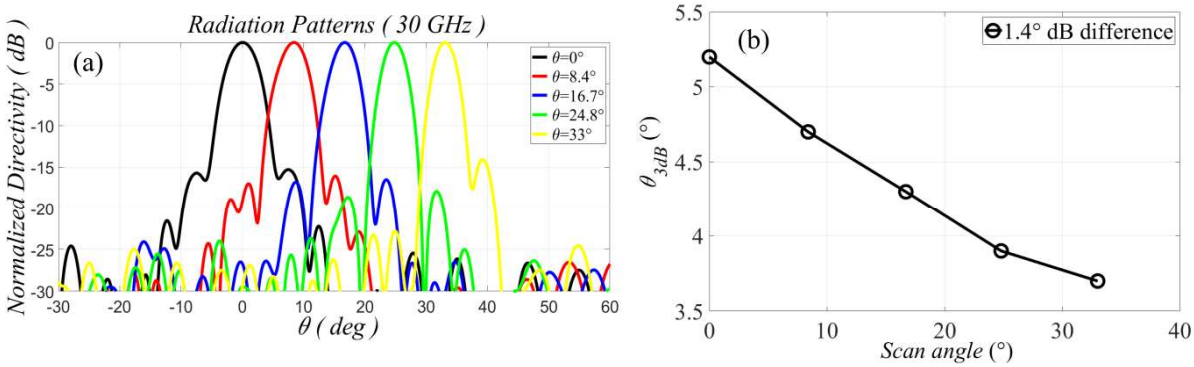

Figure 6.18: (a) Normalized directivity of patterns #1-#5 and (b) θ_{3dB} values.

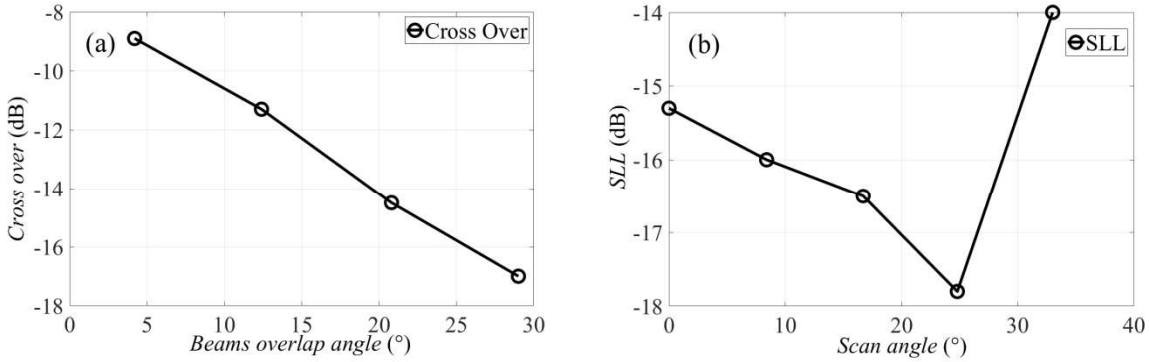

Figure 6.19: (a) Cross over values for consecutive beams, (b) SLL for the symmetric beams #1-#5.

6.4.3 Aperture feed-Stage 3

To overcome the high cross over values of the previous optimized patterns, a third optimization process has been endorsed using the in-house optimizer. In this optimization stage, we optimize merely the aperture of the feed horn of the lens, while its profile is constant having the best agents of the optimization stage 2. Thoroughly, in this stage we optimize separately the feed width aperture of every scan angle horn utilizing solely a single segregate power mask pattern for each one. Thus, in this case, the cost function in Eq. (6.10) has been used; each cost function has different targets regarding to the θ_{3dB} of the power masks. The sole variable that has been optimized in the present optimization stage, is the feed width aperture, *w* of each horn.

The initial step is to optimize only the feed horn aperture of the broadside beam. The mask pattern for that beam is shown in Fig. 6.20(a) where θ_{3dB} is defined at 6.5° and the SLL level at -15 dB. The best agent that has ended up from the optimization is equal to *w*=17 mm. Therefore, the horn that has been placed on the broadside direction has aperture width, *w*=17 mm.

Afterwards, we define a segregate mask pattern for the offset beam at 8.4° (see Fig. 6.20(b)) where θ_{3dB} has been defined as θ_{3dB}=5° and the SLL level at -15.5 dB. It needs to be highlighted that the SLL level has been strategically defined to have improved value compared to the SLL of the power mask pattern of the broadside beam. The reason is that we desire to attain a pattern which has higher directivity and therefore we expect to have better SLL level.

The major objective of this optimization process is to define more narrow θ_{3dB} values progressively on the power mask patterns of the consecutive offset beams and also to improve the SLL. The same procedure has been implemented for the rest three offset beams at 16.7°, 24.8° and 33° where progressively more narrow θ_{3dB} has been specified and likewise progressively improved SLL levels; the mask patterns are depicted in Fig. 6.20(c-e). Finally, five distinct feed width apertures for the five scan angle positions consist the best agents of the five separate optimizations. The exact targets that have been defined in the five separate mask patterns concerning, θ_{3dB}, SLL and the best agents of the widths, *w,* are shown in Table. 6.2.

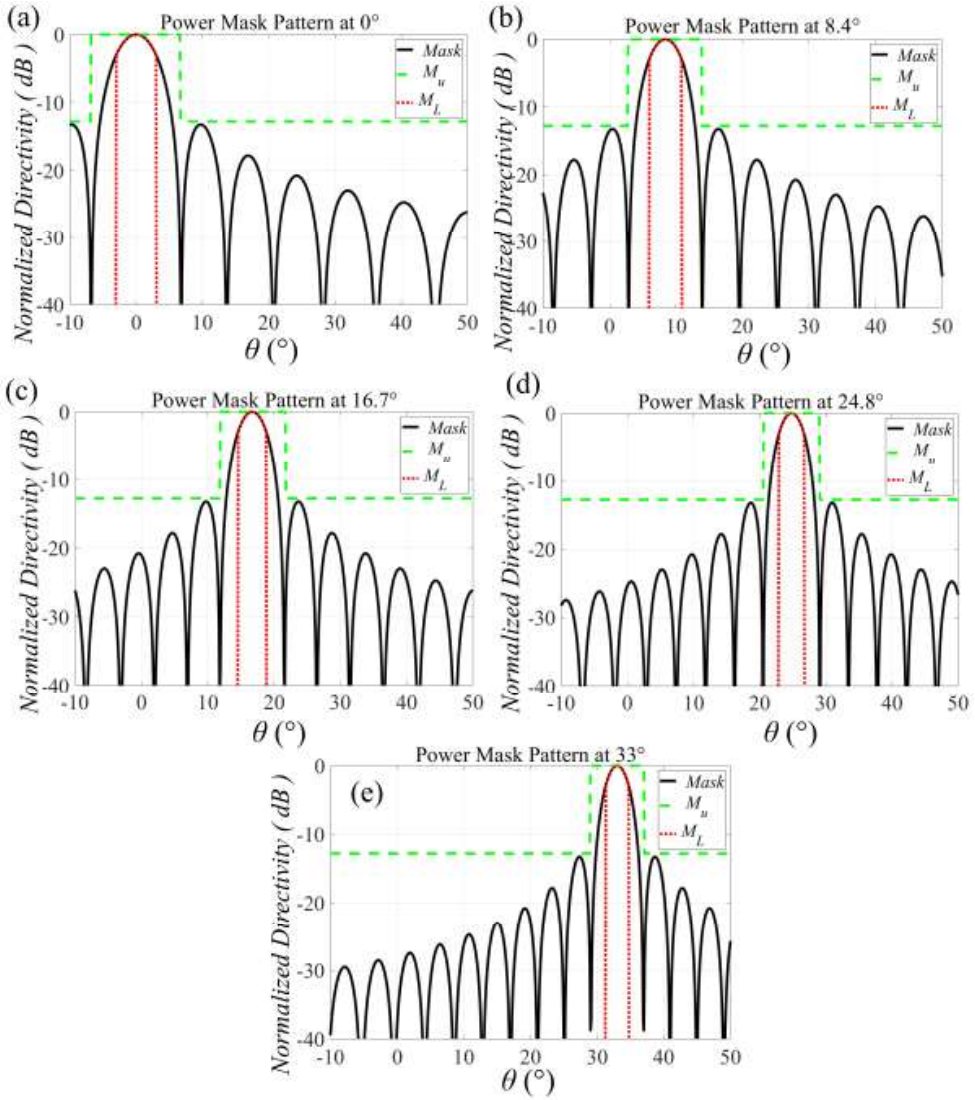

Figure 6.20: Mask patterns at (a) broadside with θ_{3dB} = 6.5°, (b) 8.4° with θ_{3dB}= 5°, (c) 16.7° with θ_{3dB}= 4.5°, (d) 24.8° with θ_{3dB}= 4°, (e) 33° with θ_{3dB}= 3.5°.

Table. 6.2: Targets for all the separate power mask patterns.

Mask patterns	Scan angles	0°	8.4°	16.7°	24.8°	33°	Best agent (w)
Mask 1	θ_{3dB}	6.5	-	-	-	-	17 mm
	SLL	-15	-	-	-	-	
Mask 2	θ_{3dB}	-	5	-	-	-	17 mm
	SLL	-	-15.5	-	-	-	
Mask 3	θ_{3dB}	-	-	4.5	-	-	16.5 mm
	SLL	-	-	15.8	-	-	
Mask 4	θ_{3dB}	-	-	-	4	-	15.7 mm
	SLL	-	-	-	-16	-	
Mask 5	θ_{3dB}	-	-	-	-	3.5	15 mm
	SLL	-	-	-	-	-16.5	

Simulation results on HFSS

All the optimized feed width apertures for every feed that are shown in Table. 6.2 have been imported in the HFSS model to apply full wave simulations. The design of the antenna model in HFSS is identical to the model of Fig. 6.16. The sole distinction is the feed apertures which are not identical; the aperture of the feeds #1-#5 is equal to the best agents that ended up the third optimization process and are depicted in Table. 6.2.

The directivity patterns of the lens with non-identical feed apertures are illustrated in Fig. 6.21(a). We observe that the directivity of the patterns is progressively increased over the scan angles. Fig. 6.21(b) shows the comparison of the lens with identical feed apertures that comprises the best agents of the second optimization stage with the present lens that has been excited by feeds with non-identical apertures. The dB difference between the extreme offset beam and the broadside beam has been increased compared to the lens with identical feed apertures. However, we observe a slight decrease in the FOV of the lens. Fig. 6.22(a, b) shows the normalized patterns and the comparison of the lenses in terms of θ_{3dB}. We notice that the θ_{3dB} is abruptly decreased for the lens with segregate feed apertures compared to the lens with identical feed apertures.

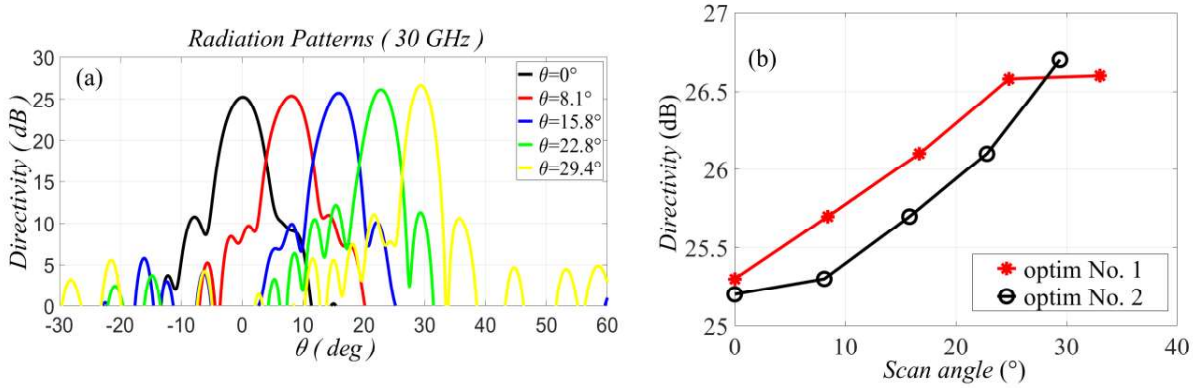

Figure 6.21: (a) Directivity patterns for the optimization of stage No. 3 (b) directivity values comparison between the optimized stages No. 2 and No. 3.

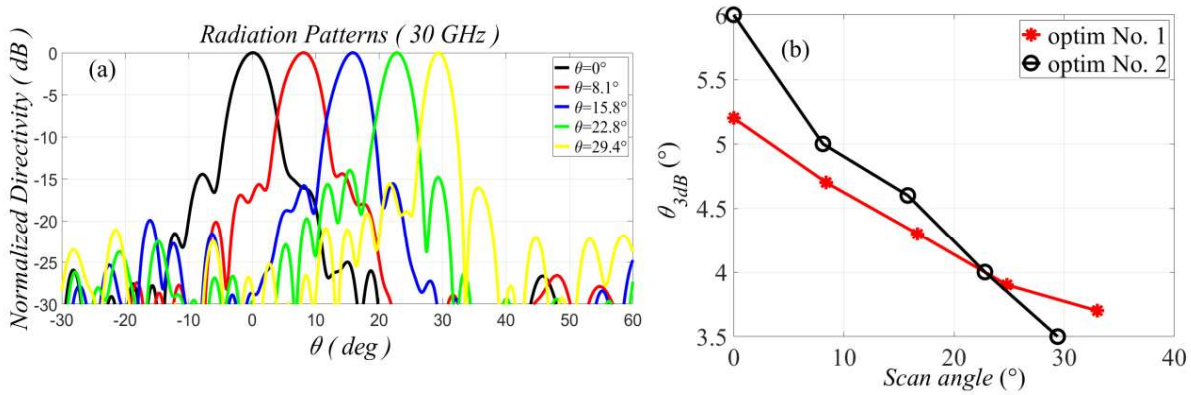

Figure 6.22: (a) Normalized patterns for the optimization of stage No. 3 and (b) θ_{3dB} values comparison between the optimized stages No. 2 and No. 3.

In Fig. 6.23(a) the comparison of the lenses in terms of the beam overlapping between consecutive beams is illustrated. We observe that the lens with segregate feed apertures has improved values of cross over compared to the lens with identical feed apertures and this is the major contribution of the third stage of the optimization. Besides, an improvement on the SLL is likewise observed in Fig. 6.23(b).

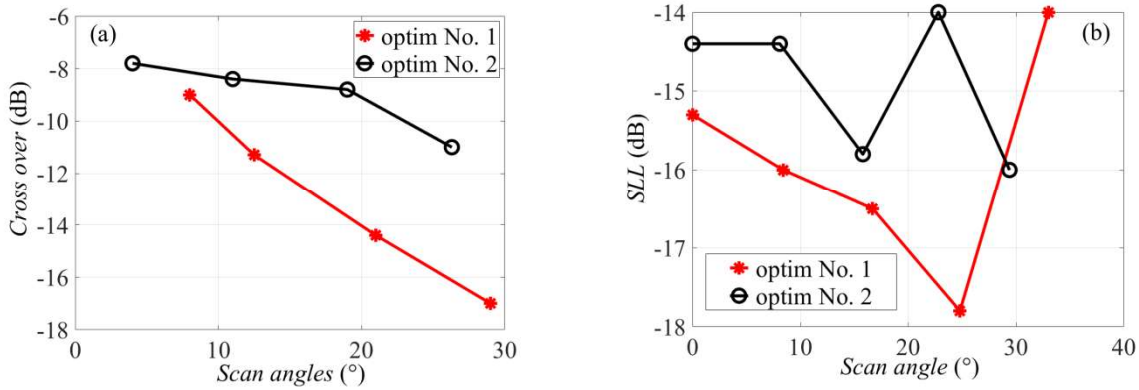

Figure 6.23: (a) Cross over values comparison between the optimized stages No. 2 and No. 3 and (b) SLL values comparison between the optimized stages No. 2 and No. 3.

To conclude, in the second optimization stage we have used five DoFs which are the inner contour and the outer contour of the lens, the ridge profile, the feed width aperture and the focal distance. The cost function in Eq. (6.11) has been used with two mask patterns simultaneously to achieve our targets. Promising results have been achieved with 1.3 dB difference between the broadside and the extreme beam and worst value of SLL at -14 dB. However, we had high level of cross over with worst value at -17 dB. In the third stage of the optimization, merely the feed width aperture has been optimized for all the scan angles separately using the cost function in Eq. (6.10). An improvement in cross over level has been achieved where the worst value is at -11 dB and also a slightly higher dB difference at 1.6 dB.

6.4.4 Wide field of view

The same optimization process of the previous sections has been adopted here, although the objective here is to maximize the FOV of the lens and the dB difference between the broadside and the extreme beam. In this optimization circle, the target of the pointing angle of the extreme offset beam has been defined at 48°. Then, in the initial optimization runs we have defined two power mask patterns with maximal dB difference of 5 dB between the offset extreme beam at 48° and the broadside beam. Since, the new targets have been specified, we optimize the five DoFs, a_{outer}, a_{inner}, a_{ridge}, h_0, and w using the cost function in Eq. (6.11). However, the cost function finds barriers to be minimized. In order to accomplish the targets that have been defined in the optimizer, the cost function needs to take zero value after the completion of all the iterations. Therefore, the targets of the optimizer have been mitigated in order to minimize the cost function. The target for the dB difference of the patterns has been defined to take smaller value and equal to 4 dB. Once again, the cost function has not been minimized. Concerning the challenging targets, we have mitigated even further the dB difference to be equal to 2 dB and as a result the cost function has been minimized. The best agents of the optimizer are a_{outer}=1.409, a_{inner}=0.802, a_{ridge}=0.362, h_0 = 0.887, w_1=23.81 mm, w_2=24.09 mm, w_3=24.04 mm, w_4=21.05 mm, w_5=19.52 mm, where w_1 is the aperture of the broadside horn and w_5 the aperture of the extreme offset feed horn at 48°.

6.5 Antenna demonstrator

6.5.1 Radiation patterns

The best agents of the optimizer have been imported to the HFSS antenna model to apply full-wave simulations. The antenna model is illustrated in Fig. 6.24(a) where 9 feed horns have been placed along the circular focal arc of the lens. The antenna is purely symmetry and thus the aperture of the feeds, #1-#4 is equal to the aperture of the feeds #6-#9.

Every feed port has been separately excited for the selected frequencies, *f*=27 GHz, *f*=29 GHz, *f*=27 GHz at Ka-band and the directivity patterns are illustrated in Fig. 6.24(b-d). We observe that for all frequencies the directivity patterns form an isoflux mask envelope. The directivity data values of the symmetric patterns are shown in Fig. 6.25(a) where we notice that the directivity is progressively increased over the scan angles up to 48°. Fig. 6.25(b) shows the SLL values of the patterns where it is increased for high frequencies. The E-field distribution for the symmetric beams #1-#5 is illustrated in Fig. 6.26(a-f).

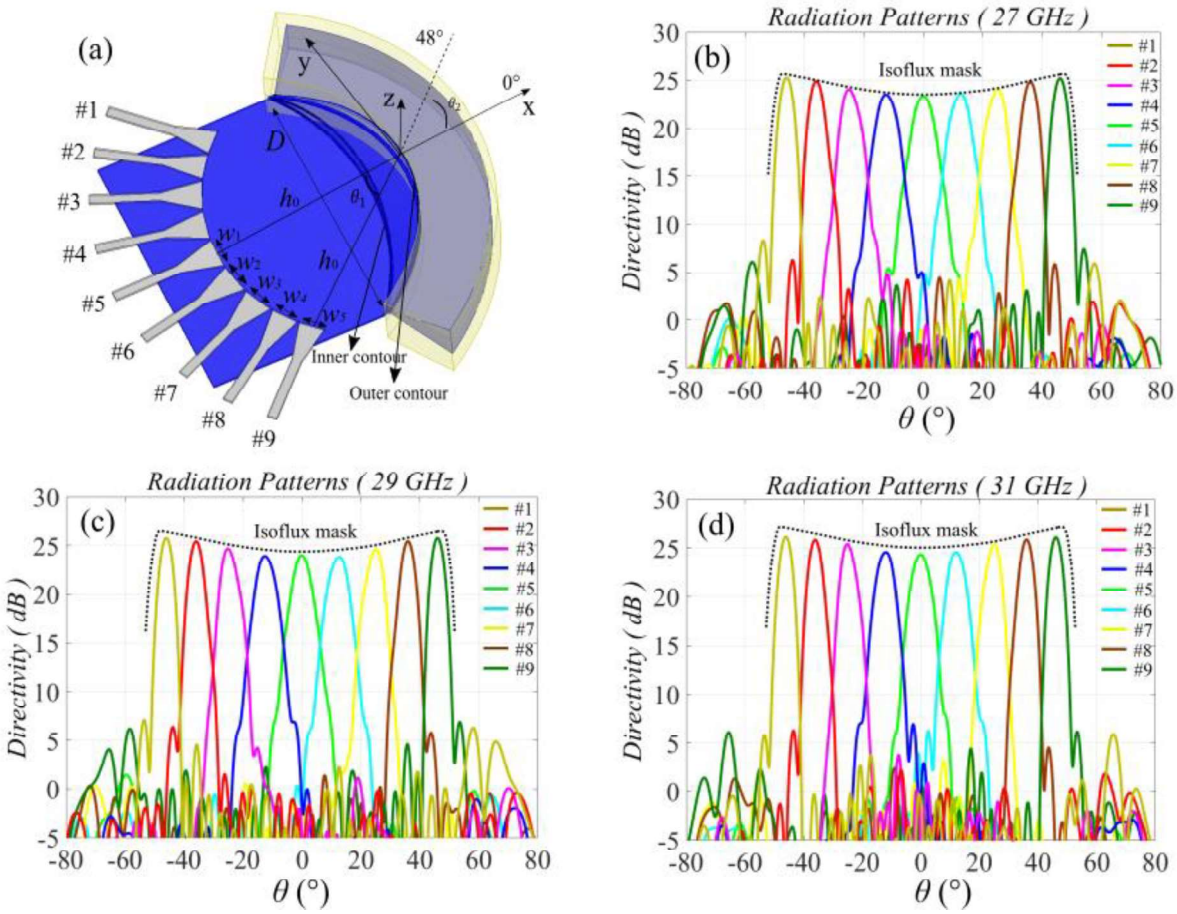

Figure 6.24: (a) 3D antenna model in HFSS. (b) Directivity patterns for all the beams of the final antenna at 27 GHz, (c) directivity patterns for all the beams of the final antenna at 29 GHz, (d) directivity patterns for all the beams of the final antenna at 31 GHz.

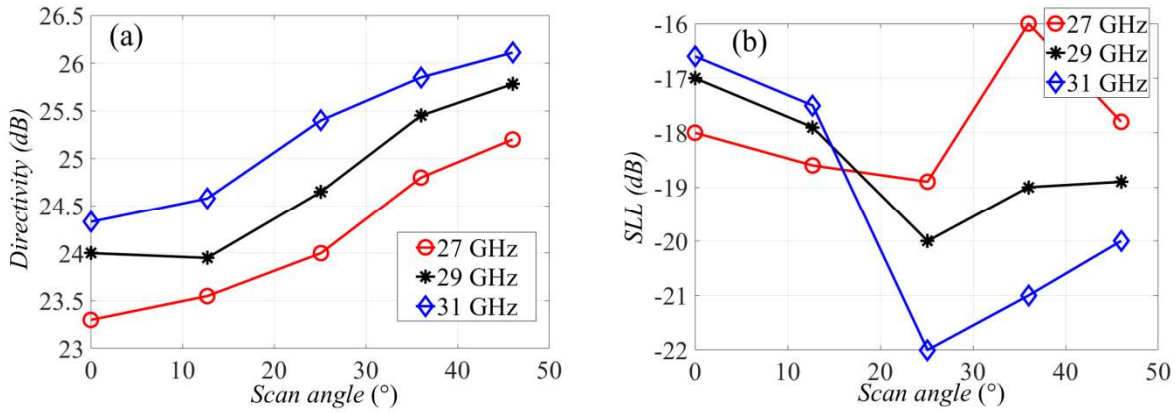

Figure 6.25: (a) Exact values of directivity for all the scan angles up to 46° in Ka band of the final demonstrator (the antenna is purely symmetric thus it is shown only the symmetric beams), (b) exact values of SLL for all the scan angles up to 46° in Ka-band.
Ka band.

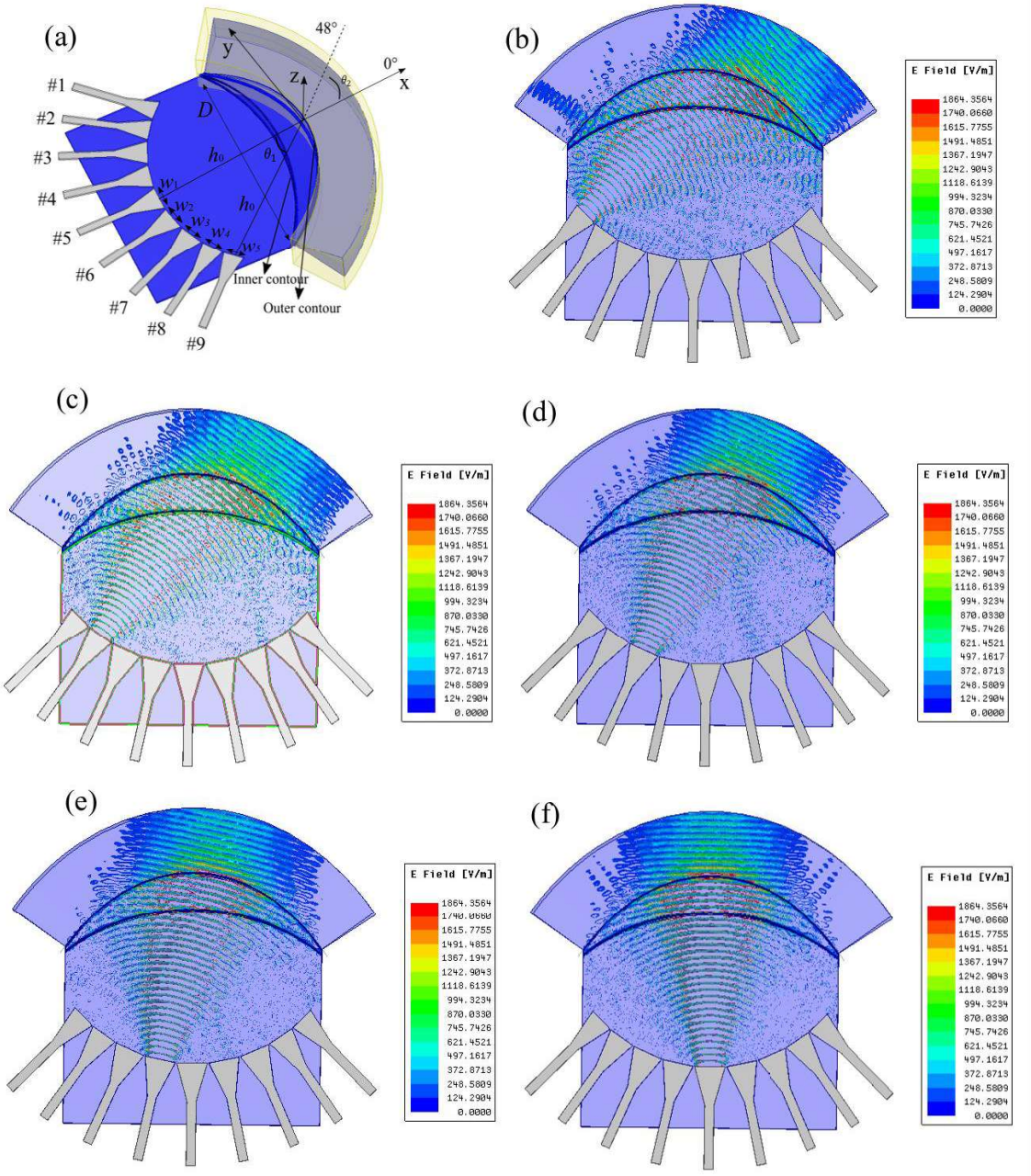

Figure 6.26: E – field distribution of the symmetric patterns #1-#5.

6.5.2 S-parameters

In Fig. 6.27 the reflection coefficients of the symmetric feed ports #1-#5 of the lens are depicted. We notice that low reflections have been attained and the highest level is shown at the extreme offset feed #1. The coupling coefficients of the lens when the symmetric feed ports, #1-#5 are excited separately are shown in Fig. 6.28(a-d) where is shown that the lens has very good isolation between its excitation feeds.

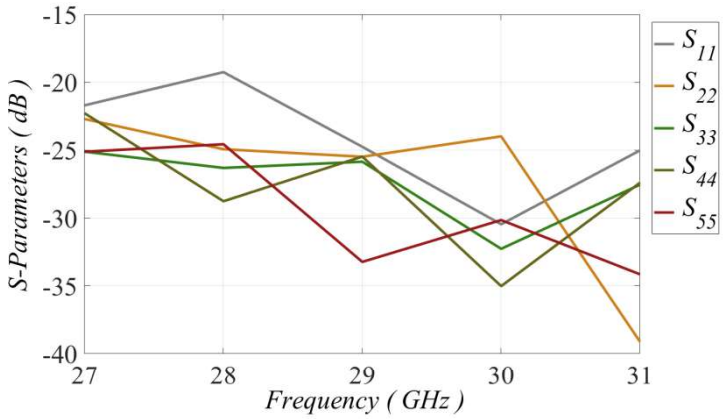

Figure 6.27: Reflection coefficients of the symmetric feeds #1-#5 of the antenna.

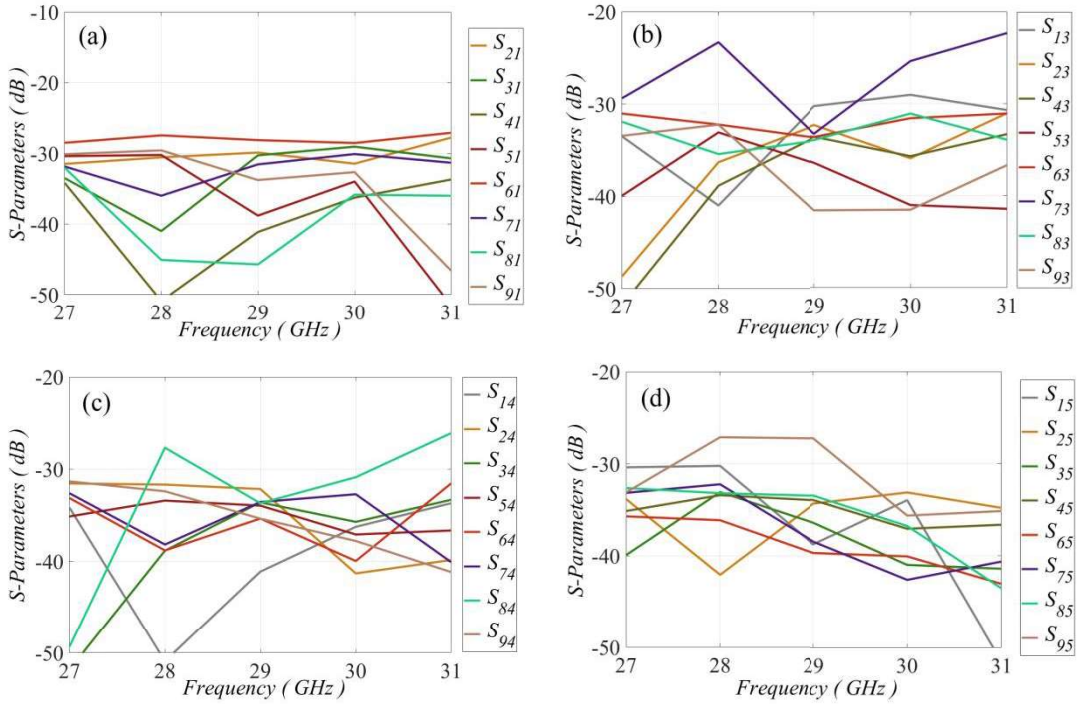

Figure 6.28: Reflection and coupling coefficients of the excitation (a) port 1, (b) port 3, (c) port 4, (d) port 5.

6.6 Conclusions

In this Chapter the all-metal continuous delay line lens with elliptical profiles has been optimized in order to achieve multi-beam fixed radiation patterns that form an isoflux envelope mask. A design method has been implemented on the contour of the lens which is based on the axis inversion of the major and minor axis of the ellipse and has ended up increasing progressively the directivity of the offset beams. An optimization technique has been presented to optimize the lens and has been analysed in four separate stages. The combination of the optimization of the inner and outer profile of the lens, as well as the profile of the transversal ridge, the focal distance and the aperture of the feeds has increased the FOV of the lens up to ±48°. A maximal 1.6 dB difference between the extreme offset

beam and the broadside beam has been attained and the total beams of the lens provide an isoflux envelope mask. However, the single ridge lens provides limited DoFs and it prevents the performance of the lens to reach a maximum 6.2 dB difference between the extreme offset beam and the broadside beam that was our ideal target.

General conclusions

2D-dimentional GRIN Gutman lens antennas have been investigated in the present thesis in order to be applied in low orbit constellation space missions. Periodic structures with glide symmetry have been studied and they present high values of effective index of refraction. The research has shown that all-metal glide symmetry unit-cells with high interleaving between their metal posts induce to high values of effective index of refraction with low dispersion. The latter, allows the design of very compact lenses. A novel design methodology has been analysed to synthesize the GRIN Gutman lenses with the modulated unit-cells. This design methodology can be likewise used to design GRIN lenses with circular symmetry. Two all-metal GRIN Gutman lenses have been designed and both have more compact size compared to the Luneburg lens. The first Gutman lens, has focal distance, $f=R/2$ and is 19% more compact compared to the Luneburg lens. A novel matching methodology has been introduced to match the lens. The lens has been manufactured by Idonial and experimentally tested in the facilities of IETR. The second all-metal GRIN Gutman lens has been designed with focal distance $f=R/2.85$ and it is 25% more compact rather than the Luneburg lens. It has been proved that the Gutman lens has identical FOV compared to the Luneburg lens, although, the SLL level is deteriorated and the scan losses are slightly increased.

The equivalent dielectric Gutman lenses with focal distances, $f=R/2$ and $f=R/2.85$ together with the dielectric Luneburg lens have been designed and synthesized using non-dispersive dielectric layers. A comparison has been provided between the all-metal lenses and the dielectric lenses. It has been shown that the all-metal lenses provide less scan losses. Besides, the dielectric lenses can be used as a preliminary concept to design all-metal GRIN lenses and test the effect of the dispersion of the unit-cells. The simulation time for full-wave simulations on the dielectric lenses is smaller compared to full-wave simulation on the all-metal GRIN lenses.

Concerning the last part of the thesis which underlines the optimization of the delay line lens antennas, elliptical profile equation has been used to design and optimize the lens in order to achieve an envelope mask in the form of an isoflux shape. A design methodology proposed to modify the shape of the transversal ridge of the lens based on the axis inversion of the ellipse. The particular design, allows the desired extreme offset excitation source to exploit larger effective aperture of the profile of the lens and leads to a more directive beam compared to the broadside. The axis inversion technique allows the progressive increase of the directivity of the offset beams in order to attain an isoflux envelope mask. Considering the specifications of this antenna, an optimization technique has been developed. Multiple power mask patterns have been defined to specify the targets of the optimizer for segregate offset beams. A final antenna demonstrator has been designed leading to an isoflux envelope mask where the directivity of the offset beams have been progressively high up to the extreme pointing angle 50°.

Future developments

TO techniques such as quasi-conformal mapping provide transformed lenses with very compact size. However, in order to synthesize GRIN compact lenses we need to design periodic structures with very high effective index of refraction. Interleaved glide symmetry unit-cell can be further investigated with multiple geometries in order to further increase the effective index of refraction and perform low dispersions. More compact lenses with even smaller focal distances can be designed using unit-cells that present high effective index of refraction.

The Luneburg lens together with the Gutman lens can be further examined to optimize the aperture excitation of their feeds. The aperture of the excitation feeds influences the directivity of the radiated beam. Feeds with high apertures lead to low directive beams and on the other hand, feeds with narrower apertures lead to high directive beams. Therefore, by optimizing the excitation feeds of the lenses we can compensate the scan losses.

Traditional milling technology has been used to manufacture the prototype of the Gutman lens with $f=R/2$. AM can be likewise tested to compare the performance of the lenses with the conventional milling technology. It is preferred to manufacture the GRIN Gutman lenses using plastic materials through AM and then metallize it with silver, since the latter perform very high conductivity.

In the present thesis, the transversal ridge of the delay line lens has been optimized using elliptical profile equations. Optimization techniques, with polynomial profile equations can be further investigated in order to enhance the DoFs. Multi-objective optimizations are essential to attain an isoflux envelop mask performance. A combination of the polynomial profile transversal ridge optimization together with the optimization of the focal arc of the lens and the aperture of the feeds can further improve the performance of the lens concerning the isoflux pattern.

The equivalent continuous delay line lens can be designed using metasurfaces in a 2D implementation where the interleaved glide index unit-cell can be used to synthesize the lens. Besides, the delay line lens can be implemented in a 3D configuration to provide beam steering in both E and H-planes where the delay lines can be synthesized by traditional all-metal waveguides with different electrical lengths.

References

[1] P. Lepeltier, P. Bosshard, J. Maurel, C. Labourdette, G. Navarre, and J. David, "Recent achievements and future trends for multiple beam telecommunication antennas," *Int. Symp. on Antenna Tech. Applied Electromagnetics*, pp. 1–6, Jun. 2012.

[2] P. Bosshard *et al*., "Thales Alenia Space HTS/V-HTS Multiple Beam Antennas sub-systems on the right track," in *Proc. 10th Eur. Conf. on Antennas Propag., (EuCAP)*, pp. 1-5, Apr. 2016.

[3] "Iridium NEXT: a constellation of 66 operational satellites that will make history," https://www.thalesgroup.com/en/worldwide/space/press-release/iridium-next-constellation-66 operational-satellites-will-make, accessed: 2018-07-25.

[4] J. C. Lafond *et al*., "Thales Alenia Space multiple beam antennas for telecommunication satellites," in *Proc. 8th Eur. Conf. on Antennas Propag., (EuCAP)*, pp. 186-190, Apr. 2014.

[5] "O3b mPOWER", Fleethttps://boeing.mediaroom.com/2020-08-07-Boeing-to-Build-Four-Additional-702X-Satellites-for-SES.

[6] S. Tubau, F. Vidal, H. Legay, B. Palacin, "Novel multiple beam antenna farms for megaconstellations," *Proc. of the 40th ESA Antenna Workshop,* Oct. 2019.

[7] W. W. Milroy, "The continuous transvere stub (CTS) array: Basic theory, experiment, and application," *in Proc. Antenna Appl. Symp*., vol. 2, 1991, p. 253-283.

[8] M. Ettorre, F. F. Manzillo, M. Casaletti, R. Sauleau, L. Le Coq and N. Capet, "Continuous Transverse Stub Array for Ka-Band Applications," *IEEE Trans. Antennas Propag.*, vol. 63, no. 11, pp. 4792-4800, Nov. 2015.

[9] M. Del Mastro, M. Ettorre and A. Grbic, "Dual-Band, Orthogonally-Polarized LP-to-CP Converter for SatCom Applications," *IEEE Transactions on Antennas and Propagation*, vol. 68, no. 9, pp. 6764-6776, Sept. 2020.

[10] R. K. Luneburg, "*Mathematical theory of optics*," Brown Univ. (1944).

[11] A. S. Gutman, "Modified Luneburg lens," *J. Appl. Phys*., vol. 25, no. 7, pp. 855-859, Jul. 1954.

[12] H. Legay *et al.,* "Multiple beam antenna based on a parallel plate waveguide continuous delay lens beamformer," in *Proc. Int. Symp. Antennas Propag.,* Okinawa, Japan, pp. 118–119, Oct. 2016.

[13] J. A. Dockrey, M. J. Lockyear, S. J. Berry, S. A. R. Horsley, J. R. Sambles, and A. P. Hibbins, "Thin metamaterial Luneburg lens for surface waves," *Phys. Rev. B* 87, 125137, 2013.

[14] Y. L. Loo, Y. Yang, N. Wang, Y. G. Ma, and C. K. Ong, "Broadband microwave Luneburg lens made of gradient index metamaterials," *J. Opt. Soc. Am. A* 29, 426–430, 2012.

[15] Y.-Y. Zhao, Y.-L. Zhang, M.-L. Zheng, X.-Z. Dong, X.-M. Duan, and Z.-S. Zhao, "Three-dimensional Luneburg lens at optical frequencies," *Laser & Photonics Rev*. 10, 665–672, 2016.

[16] S. Tol, F. L. Degertekin, and A. Erturk, "Phononic crystal Luneburg lens for omnidirectional elastic wave focusing and energy harvesting," *Appl. Phys. Lett*. 111, 013503, 2017.

[17] Y. Xie, Y. Fu, and Z. Jia, "Acoustic imaging with metamaterial Luneburg lenses," *Sci. Rep*. 8, 16188, 2018.

References

[18] A. D. Falco, S. C. Kehr, and U. Leonhardt, “Luneburg lens in silicon photonics,” *Opt. Express* 19, 5156-5162, 2011.

[19] Young-Jin Park, A. Herschlein and W. Wiesbeck, "A photonic bandgap (PBG) structure for guiding and suppressing surface waves in millimeter-wave antennas," in *IEEE Trans. Microw. Theory and Techn.*, vol. 49, no. 10, pp. 1854-1859, Oct. 2001.

[20] C. E. Garcia-Ortiz, R. Cortes, J. E. Gómez-Correa, E. Pisano, J. Fiutowski, D. A. Garcia-Ortiz, V. Ruiz-Cortes, H.-G. Rubahn, and V. Coello, “Plasmonic metasurface Luneburg lens,” *Photon. Res.* 7, 1112–1118, 2019.

[21] S. H. Badri and M. M. Gilarlue, “Ultrashort waveguide tapers based on Luneburg lens,” *J. Opt.* 21, 125802, 2019.

[22] S. H. Badri and M. M. Gilarlue, “Coupling silica waveguides to photonic crystal waveguides through a multi-layered Luneburg lens,” *J. Opt. Soc. Am. B* 37, 104-109, 2020.

[23] J. B. Pendry, D. Schurig, and D. R. Smith, “Controlling electromagnetic fields,” *Science* 312, 1780-1782, 2006.

[24] U. Leonhardt, “Optical conformal mapping,” *Science* 312, 1777-1780, 2006.

[25] D. Schurig, J. B. Pendry, and. R. Smith, “Calculation of material properties and ray tracing in transformation media,” *Opt. Express* 14, 9794–9804, 2006.

[26] T. Tyc and U. Leonhardt, “Transmutation of singularities in optical instruments,” *New J. Phys.* 10, 115038, 2008.

[27] J. Yi, S. N. Burokur, and A. de Lustrac, “Conceptual design of a beam steering lens through transformation electromagnetics,” *Opt. Express* 23, 12942–12951, 2015.

[28] S. Li, Z. Zhang, J. Wang, and X. He, “Design of conformal lens by drilling holes materials using quasi-conformal transformation optics,” *Opt. Express* 22, 25455–25465, 2014.

[29] Z. Chang, X. Zhou, J. Hu, and G. Hu, “Design method for quasi-isotropic transformation materials based on inverse laplace’s equation with sliding boundaries,” *Opt. Express* 18, 6089-6096, 2010.

[30] N. Landy, N. Kundtz, and D. Smith, “Designing three-dimensional transformation optical media using quasi-conformal coordinate transformations,” Phys. Rev. Lett 105, 193902, 2010.

[31] H. Ma and T. Cui, “Three-dimensional broadband and broad-angle transformation-optics lens,” *Nat. Com* 1, 124, 2010.

[32] A. Demetriadou and Y. Hao, “Slim Luneburg lens for antenna applications,” *Opt. Express* 19, 19925-19934, 2011.

[33] D. Schurig, “An aberration-free lens with zero F-number,” *New J. Phys* 10, 115034, 2008.

[34] Q. Quevedo-Teruel, W. Tang, and Y. Hao, “Isotropic and non-dispersive planar fed Luneburg lens from Hamiltonian transformation optics,” *Opt. Lett*. 37, 4850-4852, 2012.

[35] O. Bjorkqvist, O. Zetterstrom, and Q. Quevedo-Teruel, “Additive manufactured dielectric Gutman lens,” *Electron. Lett*., 2019.

[36] R. F. Rinehart, “A solution of the problem of rapid scanning for radar antennae,” *J. Appl. Phys.*, vol. 19, no. 9, pp. 860–862, Sep. 1948.

[37] R. F. Rinehart, “A family of designs for rapid scanning radar antennas,” *Proc. IRE*, vol. 40, no. 6, pp. 686–688, Jun. 1952.

References

[38] S. F. Myers, “Parallel plate optics for rapid scanning,” *J. Appl. Phys.*, vol. 18, no. 2, pp. 221–229, Sep. 1947.

[39] R. Rudduck and C. Walter, “A general analysis of geodesic luneberg lenses,” *IRE Trans. Antennas Propag.*, vol. 10, no. 4, pp. 444–449, Jul. 1962.

[40] R. Rudduck, C. Ryan and C. Walter, “Geodesic lenses for aerospace applications,” *IEEE Trans. Aerosp.*, vol. 2, no. 2, pp. 289–293, Apr. 1964.

[41] R. Rudduck, C. Ryan and C. Walter, “Beam elevation positioning in geodesic lenses,” *IEEE Trans. Antennas Propag.*, vol. 12, no. 6, pp. 678–684, Nov. 1964.

[42] G. Thiele and R. Rudduck, C. Ryan and C. Walter, “Geodesic lens antennas for low-angle radiation,” *IEEE Trans. Antennas Propag.*, vol. 13, no. 4, pp. 514–521, Jul. 1965.

[43] C. Liang, J. Dorsey, J. Johnston, and W. Zant, “The design of generalized luneberg geodesic lenses,” *IEEE Antennas Propag. Soc. Int. Symp.*, vol. 4, pp. 220–223, Sep. 1971.

[44] K. S. Kunz, “Propagation of Microwaves between a Parallel Pair of Doubly Curved Conducting Surfaces,” *J. Appl. Phys.*, vol. 25, no. 5, pp. 642–653, May. 1954.

[45] N. J. G. Fonseca and O. Quevedo-Teruel, “Compact parallel plate waveguide geodesic lens for line sources with wide scanning range,” in *Proc. 38th ESA*.

[46] N. J. G. Fonseca and O. Quevedo-Teruel, “The water drop lens: A low-profile geodesic parallel plate waveguide lens antenna for space applications,” in *Proc. 13th Eur. Conf. Antennas Propag. (Eucap),* pp. 1-5, Mar. 2019.

[47] Q. Liao, N. J. G. Fonseca, and O. Quevedo-Teruel, “Compact multibeam fully metallic geodesic Luneburg lens antenna based on non-Euclidean transformation optics,” *IEEE Trans. Antennas Propag.*, vol. 16, no. 12, pp. 7383–7388, Dec. 2018.

[48] N. J. G. Fonseca, Q. Liao and O. Quevedo-Teruel, “Equivalent Planar Lens Ray-Tracing Model to Design Modulated Geodesic Lenses Using Non-Euclidean Transformation Optics, optics,” *IEEE Trans. Antennas Propag.*, vol. 68, no. 5, pp. 3410–3422, May. 2020.

[49] W. Rotman and R. Turner, “Wide-angle microwave lens for line source applications,” *IEEE Trans. Antennas Propag.*, vol. 11, no. 6, pp. 623–632, Nov. 1963.

[50] H. Gent, “The Bootlace Aerial,” *Roy. Radar Establishment J.*, pp. 47–57, Oct. 1957.

[51] O. Kilic and S. J. Weiss, “Rotman lens applications for the US Army: A review of history, present and future,” in *URSI Radio Sci. Bullet.*, vol. 2010, no. 332, pp. 10–23, Jun. 2010.

[52] D. Nussler, H. Fuchs and R. Brauns, “Rotman lens for the millimeter wave frequency range Dirk Nüβler in *European Microw. Conf.,* pp. 696-699, Oct. 2007.

[53] Quevedo-Teruel, M. Ebrahimpouri and M. Ng Mou Kehn, “Ultrawideband Metasurface Lenses Based on Off-Shifted Opposite Layers,” *IEEE Antennas Wireless Propag. Lett.*, vol. 15, pp. 484–487, Dec. 2016.

[54] Young-Jin Park and W. Wiesbeck, "Angular independency of a parallel-plate Luneburg lens with hexagonal lattice and circular metal posts," in *IEEE Antennas and Wireless Propag. Lett.*, vol. 1, pp. 128-130, 2002.

[55] C. D. Diallo, E. Girard, H. Legay and R. Sauleau, “All-metal Ku-band Luneburg lens antenna based on variable parallel plate spacing Fakir bed of nails,” in *Proc. 11th Eur. Conf. Antennas Propag. (Eucap),* pp. 1401-1404, Mar. 2017.

[56] H. Lu, Z. Liu, H. Ni, and X. Lv, "Compact air-filled Luneburg lens antennas based on almost-parallel plate waveguide loaded with equal-sized metallic posts," *IEEE Trans. Antennas Propag.*, vol. 67, no. 11, pp. 6829–6838, Nov. 2019.

[57] Q. Quevedo-Teruel, J. Miao, M. Mattsson, A. Algaba-Brazalez, M. Johansson, and L. Manholm, "Glide-Symmetric Fully Metallic Luneburg Lens for 5G Communications at Ka-Band," *IEEE Antennas Wireless Propag. Lett.*, vol. 17, no. 9, pp. 1588–1592, Sep. 2018.

[58] K. Liu, F. Ghasemifard and O. Quevedo-Teruel, "Broadband metasurface Luneburg lens antenna based on glide-symmetric bed of nails," in *Proc. 11th Eur. Conf. Antennas Propag. (Eucap),* pp. 358-360, Mar. 2017.

[59] H. F. Ma, B. G. Cai, T. X. Zhang, Y. Yang, W. X. Jiang and T. J. Cui, "Three-Dimensional Gradient-Index Materials and Their Applications in Microwave Lens Antennas," *IEEE Trans. Antennas Propag.*, vol. 61, no. 5, pp. 2561–2569, May. 2013.

[60] A. Sayanskiy, S. Glybovski, V. P. Akimov, D. Filonov, P. Belov and I. Meshkovskiy, "Broadband 3-D Luneburg Lenses Based on Metamaterials of Radially Diverging Dielectric Rods," *IEEE Antennas Wireless Propag. Lett.*, vol. 16, pp. 1520–1523, Jan. 2017.

[61] C. Mateo-Segura, A. Dyke, H. Dyke, S. Haq and Y. Hao, "Flat Luneburg Lens via Transformation Optics for Directive Antenna Applications," *IEEE Trans. Antennas Propag.*, vol. 62, no. 4, pp. 1945–1953, Apr. 2014.

[62] F. Caminita *et al*. "A New Double Polarization Isoflux Antenna," in *Proc. 13th Eur. Conf. Antennas Propag. (Eucap),* pp. 1-3, Jun. 2019.

[63] R. Ravanelli, C. Iannicelli, N. Baldecchi and F. Franchinim, "Multi-Objective Optimization of an Isoflux Antenna for LEO Satellite Down-Handling Link," in *Proc. 32th ESA Antenna Workshop,* Noordwijk, The Netherlands, Oct. 2010.

[64] E. Choi, J. W. Lee and T. Lee, "Modified S-Band Satellite Antenna With Isoflux Pattern and Circularly Polarized Wide Beamwidth," *IEEE Antennas Wireless Propag. Lett.*, vol. 12, pp. 1319-1322, Oct. 2013.

[65] J. R. Costa, C. A. Fernandes, G. Godi, R. Sauleau, L. Le Coq and H. Legay, "Compact Ka-Band Lens Antennas for LEO Satellites," *IEEE Trans. Antennas Propag.*, vol. 56, no. 5, pp. 1251–1258, May. 2008.

[66] G. Minatti, S. Maci, P. De Vita, A. Freni and M. Sabbadini, "A Circularly- Polarized Isoflux Antenna Based on Anisotropic Metasurface," *IEEE Trans. Antennas Propag.*, vol. 60, no. 11, pp. 4998–5009, Nov. 2012.

[67] J. M. Tranquilla and S. R. Best, "A study of the quadrifilar helix antenna for global positioning systems (GPS) applications," *IEEE Trans. Antennas Propag.*, vol. 38, no. 10, pp. 1545–1550, Oct. 1990.

[68] P. Rezaei, "Design of quadrifilar helical antenna for use on small satellites," in *Proc. IEEE Antennas Propag. Int. Symp.*, Monterey, CA, vol. 3, pp. 2895–2898, Jun. 2004.

[69] S. Hebib, N. J. G. Fonseca and H. Aubert, "Compact Printed Quadrifilar Helical Antenna With Iso-Flux-Shaped Pattern and High Cross-Polarization Discrimination," *IEEE Trans. Antennas Wireless. Propag. Lett.*, vol. 10, pp. 635–638, Jun. 2011.

[70] M. C. Vigano, G. Toso, G. Caille, C. Mangenot and I. E. Lager, "Spatial density tapered sunflower antenna array," in *Proc. 3th Eur. Conf. Antennas Propag. (Eucap),* pp. 778-782, Jun. 2009.

[71] M. C. Viganò, G. Caille, C. Mangenot, I. E. Lager and G. Toso, "Sunflower sparse array for space applications: From design to manufacturing," in *Proc. 4th Eur. Conf. Antennas Propag. (Eucap),* pp. 1-4, Apr. 2010.

[72] Maria Carolina Viganó, Giovanni Toso, Gerard Caille, Cyril Mangenot, and Ioan E. Lager, "Sunflower Array Antenna with Adjustable Density Taper," *Int. J. Antennas Propag*., 2009.

[73] Alfredo Catalani, Franco Di Paolo, Marzia Migliorelli, Lino Russo, Giovanni Toso and Piero Angeletti, "Ku Band Hemispherical Fully Electronic Antenna for Aircraft in Flight Entertainment," *Int. J. Antennas Propag.*, 2009.

[74] G. Caille, "30 Years Of Agile Antennas Design In Alcatel Then Thales," in *Proc. 38th ESA Antenna Workshop,* Noordwijk, The Netherlands, Oct. 2018.

[75] A. Benini *et al.,* "Phase-Gradient Meta-Dome for Increasing Grating-Lobe-Free Scan Range in Phased Arrays," *IEEE Trans. Antennas Propag.*, vol. 66, no. 8, pp. 3973–3982, Aug. 2018.

[76] F. Silvestri *et al.,* "DragOnFly — Electronically steerable low drag aeronautical antenna," in *Proc. 11th Eur. Conf. Antennas Propag. (Eucap),* pp. 3423-3427, Apr. 2015.

[77] H. Deguchi, H. Kawahara, M. Tsuji and H. Shigesawa*,* "Rotational dielectricdome design for wide-angle scanning applications," in *Proc. IEEE AP-S Conf.,* Washington, DC, pp. 638-641, 2005.

[78] Y. Cailloce, P. Hourlay, F. Lebrun, M. Nadarassin, B. Palacin and C. Romain, "Additive Manufacturing And Thermoplastic Rf Antenna Components for Telecommunication Satellites," in *Proc. 18th ESA Antenna Workshop,* Noordwijk, The Netherlands, Oct. 2018.

[79] H. Lu, Z. Liu, Y. Liu, H. Ni, and X. Lv, "Compact air-filled Luneburg lens antennas based on almost-parallel plate waveguide loaded with equal-sized metallic posts," *IEEE Trans. Antennas Propag*. vol. 67, no. 11, pp. 6829-6838, Nov. 2019.

[80] C. D. Diallo, E. Girard, H. Legay, and R. Sauleau, "All-metal ku-band Luneburg lens antenna based on variable parallel plate spacing fakir bed of nails," in *Proc. 3th Eur. Conf. Antennas Propag. (Eucap)*, pp. 1401–1404, Mar. 2017.

[81] N. Memeletzoglou, C. Sanchez-Cabello, F. Pizarro Torres, and E. Rajo-Iglesias, "Analysis of periodic structures made of pins inside a parallel plate waveguide symmetry," *Symmetry*., vol 11, pp. 82, 2019.

[82] W. Yuan *et al*., "Glide-Symmetric Lens Antenna in Gap Waveguide Technology," *IEEE Trans. Antennas Propag.*, vol. 68, no. 4, pp. 2612-2620, Apr. 2020.

[83] D. M. Pozar, *Microwave Engineering*, 4th Edition.

[84] S. B. Cohn, "Properties of Ridge Wave Guide," *Proc. IRE*, vol. 35, no. 8, pp. 783-788, Aug. 1947.

[85] S. Hopfer, "The Design of Ridged Waveguides," *IRE Trans. Microw. Theory and Techn.*, vol. 3, no. 5, pp. 20-29, Oct. 1955.

[86] S. B. Cohn, "Optimum Design of Stepped Transmission-Line Transformers," *IRE Trans. Microw. Theory and Techn.*, vol. 3, no. 3, pp. 16-20, Apr. 1955.

[87] R. Vincenti Gatti and R. Rossi, "Wideband compact single-ridge waveguide to rectangular waveguide transitions with integrated E-plane bend," in *Elect. Lett.*, vol. 52, no. 20, pp. 1699-1701, Sep. 2016.

[88] Y. Zhang, J. A. Ruiz-Cruz, K. A. Zaki and A. J. Piloto, "A Waveguide to Microstrip Inline Transition With Very Simple Modular Assembly, " in *IEEE Microw. Wireless Compon. Lett.*, vol. 20, no. 9, pp. 480-482, Sept. 2010.

[89] X. Chen, W. Cui, D. Sun and Y. He, "Novel Compact Waveguide Flange Adapter for Passive Intermodulation Measurement Systems," in *Proc. 14th Eur. Conf. on Antennas Propag., (EuCAP)*, pp. 1-4, Mar. 2020.

[90] A. Uz Zaman, T. Vukusic, M. Alexanderson and P. Kildal, "Design of a Simple Transition From Microstrip to Ridge Gap Waveguide Suited for MMIC and Antenna Integration," *IEEE Antennas Wireless Propag. Lett.*, vol. 12, pp. 1558-1561, Dec. 2013.

[91] Hui-Wen Yao, A. Abdelmonem, Ji-Fuh Liang and K. A. Zaki, "Analysis and design of microstrip-to-waveguide transitions," in *IEEE Trans. Microw. Theory and Techn.*, vol. 42, no. 12, pp. 2371-2380, Dec. 1994.

[92] C. D. Diallo, "Study and design of new multibeam antenna architectures in Ku and Ka bands for broadband satellite communication applications," Ph.D. dissertation, University of Rennes 1, 2016.

[93] F. Doucet, N. J. G. Fonseca, E. Girard, H. Legay and R. Sauleau, "Analytical Model and Study of Continuous Parallel Plate Waveguide Lens-like Multiple-Beam Antennas," *IEEE Trans. Antennas Propag.,* vol. 66, no. 9, pp. 4426-4436, Sep. 2018.

[94] F. Doucet, N. J. G. Fonseca, E. Girard, H. Legay and R. Sauleau, "Comparison of optimization procedures for the design of continuous parallel plate waveguide multiple beam lens antennas," in *Proc. 12th Eur. Conf. Antennas Propag. (Eucap),* pp. 1-5, Apr. 2018.

[95] A. L. Peebles, "A dielectric bifocal lens for multibeam antenna applications," *IEEE Trans. Antennas Propag.*, vol. 36, no. 5, pp. 599 - 606, May. 1988.

[96] F. Doucet, "Continuous Parallel Plate Waveguide Lenses for Future Low Cost and High Performances Multiple Beam Antennas," Ph.D. dissertation, University of Rennes 1, 2019.

[97] D. M. Pozar, *Microwave engineering*, 3rd Edition, (Wiley, 2005).

[98] CST Studio Suite, "CST Microwave Studio," 2018.

List of Publications

International conference papers

- P. I. Bantavis , C. Diallo, C. G. Gonzalez, R. Sauleau, G. Goussetis, S. Tubau and H. Legay, “All-Metal Graded Index Gutman Lens Antenna - A More Compact Luneburg Lens,” *14th European Conference on Antennas and Propagation (EUCAP),* Copenhagen, 2020.

Journal papers

- P. I. Bantavis , C. G. Gonzalez, R. Sauleau, G. Goussetis, S. Tubau and H. Legay, “A broadband graded index Gutman lens with wide field of view utilizing artifcial dielectrics - a design methodology,” *Optics Express 10*, pp. 14648-14661, 2020.

- P. I. Bantavis , C. Diallo, C. G. Gonzalez, R. Sauleau, G. Goussetis, S. Tubau and H. Legay, “All- metal Gutman Vs Luneburg Lens in a PPW technology utilizing graded index metasurfaces,” *IEEE Transactions on Antennas and Propagation* (TAP), under preparation.

Biography

Petros Bantavis was born in Larisa, Greece in 1991. He graduated from Democritus University of Thrace (Duth) where he received the Diploma degree in Electrical and Computer Engineering specialized on Space and Telecommunication Engineering (2016). During his Diploma he realized internships in Deusto University at Bilbao, Spain for 6 months and in KEMEA-Center for security studies, Athens, Greece for 2 months working on antennas arrays and RF components. He spent 1 year as an antenna researcher at Lab-STICC, Brest, France (2016-2017). He is currently pursuing the Ph.D. degree in electronics from the Institut d'Electronique et de Télécommunications de Rennes, University of Rennes 1, Rennes, France, in collaboration with Thales Alenia Space, Toulouse and Idonial, Gijon on the REVOLVE project. He is a holder of 4 international conference papers, 2 journal papers and 1 patent. His interests are lens antennas, phased array antennas, beamforming networks and RF components for satellite missions and 5G.

UNIVERSITÉ DE RENNES 1

Titre : Etude et conception d'antennes à lentilles compact formant un faisceau quasi optique dans une technologie de guide d'ondes à plaques parallèles pour les missions de constellation de satellites embarquées

Mots clés : Antenne à Lentille Gutmnan, Index gradué, Métasurfaces, Cellule, Missions de constellation

Résumé : Les travaux présentés dans cette thèse portent sur la conception d'antennes de formation de faisceaux quasi optiques dans une technologie de guide d'ondes à plaques parallèles et trouvent des applications dans les missions de constellation de satellites. La technologie d'antenne qui a été est l'antenne à lentille Gutman à indice gradué dans une technologie PPW. Dans la première partie de la thèse, la lentille Gutman métallique à arc focal f = R / 2 a été analysée, conçue, fabriquée et testée expérimentalement. En outre, un GRIN Gutman lentille tout en métal plus compact avec un arc focal plus petit égal à f = R/2. 85 a été conçu. Les deux lentilles, tout métal Gutman fonctionnent en bande Ku et ont été comparés avec l'antenne à lentille GRIN Luneburg métallique.

Ensuite, les lentilles diélectriques équivalentes, la lentille de Luneburg, la lentille Gutman avec un arc focal f = R / 2 et la lentille Gutman avec l'arc focal f = R / 2.85 ont été conçues en utilisant des couches diélectriques non dispersives. Une comparaison entre les antennes métallique et diélectriques a été présentée.

La dernière partie de la thèse porte sur l'optimisation de l'antenne de lentille à ligne à retard continue métallique dans une technologie PPW. Une méthodologie de conception de la cavité transversale de la lentille a été proposée sur la base de l'inversion d'axe de l'ellipse avec une technique d'optimisation multi-objectif. L'antenne optimisée fournit un masque d'enveloppe isoflux et a un large champ de vision.

.

Title : Study and Design of Compact Quasi Optical Beam Forming Lens Antennas in a Parallel Plate Waveguide Technology for on Board Satellite Constellation Missions

Keywords : Gutmnan lens antenna, Graded index, Metasurfaces, Unit-cell, Constellation missions

Abstract : The activities presented in this Ph. D thesis focus on the design of Quasi Optical Beam Forming (QOBF) antennas in a parallel plate waveguide (PPW) technology and find applications in satellite constellation missions. The antenna technology that has been investigated is the graded index Gutman lens antenna in a PPW technology. In the first part of the thesis the all-metal Gutman lens with focal arc f=R/2 has been analysed, designed, manufactured and experimentally tested. Besides, a more compact all-metal GRIN Gutman lens with smaller focal arc equal to f=R/2.85 has been designed. Both all-metal Gutman lenses operate at Ku-band and have been compared to the all-metal GRIN Luneburg lens.

Next, the equivalent dielectric lenses, Luneburg lens, Gutman lens with focal arc f=R/2 and Gutman lens with focal arc f=R/2.85 have been designed using non-dispersive dielectric layers. A comparison between all-metal and dielectric lenses has been presented.

The last part of the thesis focus on the optimization of the all-metal continuous delay line lens antenna in a PPW technology. A design methodology of the transversal ridge of the lens has been proposed based on the axis inversion of the ellipse together with a multi-objective optimization technique. The optimized lens antenna provides an isoflux envelope mask and has a wide field of view.